

A Simulation-Based Optimisation Method to Evaluate
Dynamic Compensators for the Improvement of
LCC-HVDC Performance in High Source Impedance Power
Systems

Aaron S. C. Leavy

Power Electronics, Drives and Energy Conversion
Department of Electronic and Electrical Engineering
University of Strathclyde, Glasgow

May 2024

This thesis is the result of the author's original research. It has been composed by the author and has not been previously submitted for examination which has led to the award of a degree.

The copyright of this thesis belongs to the author under the terms of the United Kingdom Copyright Acts as qualified by University of Strathclyde Regulation 3.50. Due acknowledgement must always be made of the use of any material contained in, or derived from, this thesis.

Signed:

Date:

Dedicated to my parents

Abstract

Line commutated converter (LCC) high voltage direct current (HVDC) link dynamic performance is negatively affected by low alternating current (AC) system short circuit ratio (SCR) as viewed from the LCC-HVDC link converter stations. This is particularly evident at LCC-HVDC link converter stations operating as inverters subjected to large transient disturbances.

Firstly, this thesis proposes a simulation-based optimisation method to evaluate black-box optimisation solver methods built with mature strategies against alternative solver methods using surrogate model strategies recently proposed in the research literature.

The method uses the problem of tuning LCC-HVDC link controllers considering large transient behaviour modelled via electromagnetic transient (EMT) simulations as the underlying motivating problem on which the solver methods are tested. The results from the applied method confirm the suitability of applying the tested surrogate-based solver methods on LCC-HVDC link controller tuning problems. The surrogate-based solver methods' performances are improved between 45.137% and 72.14% relative to the worst performing solver method using mature strategies.

Secondly, this thesis proposes a method to quantitatively evaluate dynamic compensators' ability to improve the dynamic performance of LCC-HVDC links inverting into low SCR AC systems.

The method uses EMT simulations as part of a simulation-based optimisation using one of the aforementioned surrogate-based optimisation solver methods to make fair

comparisons between different compensator types and compensator ratings. Multiple inverter system short circuit fault locations and inverter system equivalent source impedances are considered in the method. Compensators are evaluated by performance values calculated via performance functions applied to measured time domain variable results from the simulations.

The method is able to successfully quantify and differentiate compensator type and rating superiorities when applied to a set of static VAr compensator (SVC), static synchronous compensator (STATCOM), and synchronous condenser study cases. In particular, the method results show that any type of compensator of any rating typically improves LCC-HVDC link dynamic performance compared to a compensator-less LCC-HVDC link. The best found improvement is 9.2035% relative to the Base study case for the integral square error (ISE) of direct current (DC)-side measured power of the LCC-HVDC link.

The method results also show that synchronous condensers are the most effective compensator, with improvements between 7.5269% and 9.2035% relative to the compensator-less LCC-HVDC link when considering ISE of DC-side measured power. Similarly, SVCs provide improvements between 5.4759%, and 5.7968%, and STATCOMs provide improvements between -0.21144% and 6.9608%. Smaller-rated SVCs and STATCOMs provide better improvements compared with larger-rated SVCs and STATCOMs, using the compensator-less LCC-HVDC link as a baseline.

Acknowledgements

I wish to express my gratitude to my supervisor Professor Lie Xu. He provided thoroughly constructive advice, guidance, and support throughout the course of my doctoral study.

I wish to thank Professor Shaahin Filizadeh and Professor Aniruddha Gole. They ensured that I experienced a welcoming and insightful doctoral research secondment to the University of Manitoba.

Contents

Abstract	i
Acknowledgements	iii
List of Abbreviations	ix
List of Symbols	xii
List of Figures	xix
List of Tables	xxiv
List of Algorithms	xxvi
1 Introduction	1
1.1 Historical Developments in HVDC Transmission	1
1.2 HVDC Transmission Solutions Compared with AC Transmission Solutions	3
1.3 VSC-HVDC Systems Compared with LCC-HVDC Systems	6
1.4 Recent Developments in Power System Generation Patterns	9
1.4.1 Shifts Towards Power Converter Interfaced Generation	9
1.4.2 AC Network Voltage Waveform Sensitivity Considering Widespread Power Converter Interfaced Generation	11
1.5 Research Aim	13
1.6 Research Objectives	14

1.7	Thesis Organisation	14
1.8	Thesis Contributions	16
1.9	Author’s Publication Related to this Thesis	16
2	Literature Review	17
2.1	Research Literature on LCC-HVDC Systems	17
2.1.1	The LCC-HVDC Link Plant and Control Architecture	17
2.1.2	LCC-HVDC Link Susceptibility to AC Network Voltage Sensitivity	23
2.2	Research Literature on Alleviation of LCC-HVDC Link Susceptibility to AC Network Voltage Sensitivity	28
2.2.1	Description of the Research Literature	31
2.2.2	Research Gaps in the Research Literature	36
2.3	Outline of Simulation-Based Optimisation	39
2.3.1	History of Derivative-Free Optimisation	42
2.3.2	Classifications of Derivative-Free Optimisation Methods	43
2.3.3	Global Surrogate-Based Derivative-Free Optimisation Methods .	44
2.4	Research Literature on Power System Engineering Applications of Simulation-Based Optimisation	46
2.4.1	Description of the Research Literature	46
2.4.2	Research Gaps in the Research Literature	48
2.5	Considerations for Simulation-Based Optimisation Solver Method Evaluation	50
2.6	Summary	52
3	Evaluation of Simulation-based Optimisation Solver Methods for LCC-HVDC Link Controller Parameter Selection	54
3.1	Description of Investigated Solver Methods	55
3.1.1	Symmetric Latin Hypercube Experimental Design	56
3.1.2	Solver Method GA	58
3.1.3	Solver Method NM	61
3.1.4	DYCORS	66

3.1.5	Solver Method MARS	70
3.1.6	Solver Method GPR	73
3.1.7	Solver Method Restarts	75
3.1.8	Summary of Solver Method Algorithms	76
3.1.9	Software Implementation	77
3.2	Study Case Plant and Controller Description	78
3.2.1	LCC-HVDC Link and AC System Plant	78
3.2.2	LCC-HVDC Link Controllers	82
3.3	Description of the Simulation-based Optimisation Problems	83
3.3.1	Problem 1: PI Controller Tuning	84
3.3.2	Problem 2: PI Controller and VDCOL Parameter Tuning	85
3.4	Description of the Assessment Strategy for Evaluation of the Solver Methods	87
3.5	Non-parametric Basic Bootstrap	88
3.6	Results and Discussion	90
3.7	Summary	96
4	A Method to Evaluate Dynamic Compensators for the Improvement of LCC-HVDC Link Dynamic Performance	98
4.1	Plant and Controller Architectures for Investigated Study Cases	99
4.1.1	LCC-HVDC Link and AC System Plant	100
4.1.2	LCC-HVDC Link Controllers	105
4.1.3	SVC Plant and Controllers	107
4.1.4	STATCOM Plant and Controllers	109
4.1.5	Synchronous Condenser Plant and Controllers	113
4.2	Simulation-based Optimisation of Study Cases	114
4.2.1	Objective Function	115
4.2.2	Operational SCRs and Fault Locations	116
4.2.3	Dynamic Compensator Ratings	116
4.2.4	Short Circuit Fault Disturbance Application	117
4.2.5	Dynamic Compensator Reactive Power Initialisation	118

4.2.6	Selected Solver Method and Optimisation Problem Variables . . .	118
4.2.7	Optimal Solution Samples	120
4.2.8	Overall Number of Simulations Performed	120
4.3	Measured Variables and Performance Functions	121
4.4	Engineering Feasible Result Screen	122
4.5	Sample Statistics	123
4.5.1	Sample Means and Sample Minima	124
4.5.2	Differences in Sample Means and Sample Minima	124
4.5.3	Ranking of Plant Configurations	125
4.6	Results and Discussion	127
4.6.1	Similarity of Selected Time Domain Variables from Time Domain Plots	128
4.6.2	Observations from Box-plots, Plots of Sample Means, and Plots of Sample Minima	132
4.6.3	Observations from Differences in Sample Means	137
4.6.4	Observations from Differences in Sample Minima	140
4.6.5	Observations from Hypothetical Plant Configuration Rankings based on Sample Means	142
4.6.6	Observations from Hypothetical Plant Configuration Rankings based on Sample Minima	144
4.7	Summary	145
5	Conclusions and Potential Future Research Avenues	148
5.1	Conclusions	148
5.2	Future Research Avenues	149
5.2.1	Specificities of Simulation-based Optimisation	149
5.2.2	Statistical Considerations	150
5.2.3	AC-DC Problem Formulation Considerations	150
	Bibliography	151

A Solver Method Algorithms	160
A.1 Symmetric Latin Hypercube Design	161
A.2 Solver Method GA: Genetic Algorithm	164
A.3 Solver Method NM: Nelder-Mead Simplex	168
A.4 Solver Method MARS and Solver Method GPR: Dynamic Coordinate Search using Response Surfaces	174
B Parameter Values for Solver Method Evaluation Simulations	179
C Parameter Values for Dynamic Compensation Simulations	181
C.1 LCC-HVDC Link Plant, Controller, and Transmission Line Parameters .	182
C.2 SVC including TCR and TSC Plant and Controller Parameters	184
C.3 STATCOM Plant and Controller Parameters	186
C.4 Plant and Controller Parameters of Synchronous Condenser Model . . .	188
D Selected Time Series Plots of Measured Variables	190
E Box-plots	201
E.1 Performance Values of Measured Variables	202
E.2 LCC-HVDC Optimal Controller Parameter Values	207
F Sample Means and Sample Minima of Performance Values	209
G Differences between Sample Means of Performance Values	215
H Differences between Sample Minima of Performance Values	231
I Associations between Proposed Performance Rankings and Observed Performance Values' Rankings of Sample Means	247
J Associations between Proposed Performance Rankings and Observed Performance Values' Rankings of Sample Minima	253

List of Abbreviations

AC	Alternating Current
CBA	Cost-Benefit Analysis
CESCR	Critical Effective Short Circuit Ratio
CFII	Commutation Failure Immunity Index
CFPI	Commutation Failure Probability Index
CI	Confidence Interval
CSCR	Critical Short Circuit Ratio
DC	Direct Current
DFIG	Doubly-Fed Induction Generator
DYCORDS	Dynamic Coordinate Search using Response Surface Models
EMT	Electromagnetic Transient
EMTDC	Electromagnetic Transients including DC
ESCR	Effective Short Circuit Ratio
GA	Genetic Algorithm
GCV	Generalised Cross Validation

GPR	Gaussian Process Regression
HVDC	High Voltage Direct Current
IAE	Integral Absolute Error
IGBT	Insulated Gate Bipolar Transistor
ISE	Integral Square Error
ITAE	Integral Time Absolute Error
LCC	Line Commutated Converter
MARS	Multivariate Adaptive Regression Splines
MCCM	Marginal Current Control Method
MMC	Modular Multilevel Converter
MSC	Mechanically Switched Shunt Capacitor
NETOMAC	Network Torsion Machine Control
PEID	Power Electronics Interfaced Device
PI	Proportional-Integral
PLL	Phase Locked Loop
PSAT	Power System Analysis Toolbox
PSCAD	Power Systems Computer Aided Design
PWM	Pulse Width Modulation
RMS	Root Mean Square
SCR	Short Circuit Ratio
SLHD	Symmetric Latin Hypercube Design
STATCOM	Static Synchronous Compensator

SVC	Static VAR Compensator
TCR	Thyristor Controlled Shunt Reactor
TSC	Thyristor Switched Shunt Capacitor
UPFC	Unified Power Flow Controller
VDCOL	Voltage-Dependent Current Order Limiter
VSC	Voltage Source Converter
VSF	Voltage Stability Factor

List of Symbols

B_L	TCR inductor output susceptance
C	STATCOM DC-side capacitance
C_{SW}^*	Switch signal to switch in or out a TSC stage within an SVC
$C_{i,11}$	Capacitance in single-tuned 11th harmonic LCC-HVDC inverter AC system shunt filter
$C_{i,13}$	Capacitance in single-tuned 13th harmonic LCC-HVDC inverter AC system shunt filter
$C_{i,24}$	Capacitance in high-pass 24th harmonic LCC-HVDC inverter AC system shunt filter
C_{on}	Number of committed TSC stages within an SVC
$C_{r,11}$	Capacitance in single-tuned 11th harmonic LCC-HVDC rectifier AC system shunt filter
$C_{r,13}$	Capacitance in single-tuned 13th harmonic LCC-HVDC rectifier AC system shunt filter
$C_{r,24}$	Capacitance in high-pass 24th harmonic LCC-HVDC rectifier AC system shunt filter
E_F^*	Ordered synchronous condenser field voltage

E_S	Measured synchronous condenser stator power frequency voltage magnitude
F_{fail}	Failure limit in DYCORS algorithm
F_{succ}	Success limit in DYCORS algorithm
F_{tol}	Convergence tolerance in Nelder-Mead simplex algorithm
I_{DC}	Measured DC-side current of an LCC-HVDC link
I_F	Measured synchronous condenser field current
I_{dn}'	LCC-HVDC converter VDCOL ramp down rate limit
I_d^*	Ordered D-axis current in DQ0 frame within a STATCOM controller
I_d	Measured D-axis current in DQ0 frame within a STATCOM controller
I_q^*	Ordered Q-axis current in DQ0 frame within a STATCOM controller
I_q	Measured Q-axis current in DQ0 frame within a STATCOM controller
I_{up}'	LCC-HVDC converter VDCOL ramp up rate limit
K_b	SVC susceptance PI controller proportional gain
K_c	Synchronous condenser voltage PI controller proportional gain
$K_{i,p}$	LCC-HVDC inverter PI controller proportional gain
K_i	STATCOM inner current PI controller proportional gain
K_p	LCC-HVDC converter PI controller proportional gain
$K_{r,p}$	LCC-HVDC rectifier PI controller proportional gain
K_s	STATCOM outer DC-side voltage PI controller proportional gain
K_t	STATCOM outer AC-side voltage magnitude PI controller proportional gain
L	DC-side smoothing reactor inductance of LCC-HVDC link

L_c	STATCOM coupling reactance
$L_{i,11}$	Inductance in single-tuned 11th harmonic LCC-HVDC inverter AC system shunt filter
$L_{i,13}$	Inductance in single-tuned 13th harmonic LCC-HVDC inverter AC system shunt filter
$L_{i,24}$	Inductance in high-pass 24th harmonic LCC-HVDC inverter AC system shunt filter
L_i	Inductance in LCC-HVDC inverter AC system source impedance
$L_{r,11}$	Inductance in single-tuned 11th harmonic LCC-HVDC rectifier AC system shunt filter
$L_{r,13}$	Inductance in single-tuned 13th harmonic LCC-HVDC rectifier AC system shunt filter
$L_{r,24}$	Inductance in high-pass 24th harmonic LCC-HVDC rectifier AC system shunt filter
L_r	Inductance in LCC-HVDC rectifier AC system source impedance
N_{cand}	Number of candidate points in DYCORS algorithm
P_{DC}	Measured DC-side power of an LCC-HVDC link
P_{DC}^*	Ordered DC-side power of an LCC-HVDC link
P_c	Crossover probability in genetic algorithm crossover process
Q_F	Nominal sum of power frequency reactive power injection from fixed shunt filters and fixed reactive compensation at LCC-HVDC link converter station busbar
R_{ESCR}	Effective short circuit ratio
R_{SCR}	Short circuit ratio

$R_{V\text{SF}}$	Voltage stability factor
$R_{i,p}$	Parallel resistance in LCC-HVDC inverter AC system source impedance
$R_{i,11}$	Resistance in single-tuned 11th harmonic LCC-HVDC inverter AC system shunt filter
$R_{i,13}$	Resistance in single-tuned 13th harmonic LCC-HVDC inverter AC system shunt filter
$R_{i,24}$	Resistance in high-pass 24th harmonic LCC-HVDC inverter AC system shunt filter
R_i	Series resistance in LCC-HVDC inverter AC system source impedance
$R_{r,p}$	Parallel resistance in LCC-HVDC rectifier AC system source impedance
$R_{r,11}$	Resistance in single-tuned 11th harmonic LCC-HVDC rectifier AC system shunt filter
$R_{r,13}$	Resistance in single-tuned 13th harmonic LCC-HVDC rectifier AC system shunt filter
$R_{r,24}$	Resistance in high-pass 24th harmonic LCC-HVDC rectifier AC system shunt filter
R_r	Series resistance in LCC-HVDC rectifier AC system source impedance
S_F	Short circuit level at an AC network busbar
T_i	LCC-HVDC inverter transformer
T_r	LCC-HVDC rectifier transformer
T_s	Tournament size in genetic algorithm selection process
V_{DC}	Measured DC-side voltage of an LCC-HVDC link
V_{DC}^*	Ordered DC-side voltage of an LCC-HVDC link

V_T^*	Ordered power frequency voltage magnitude at inverter busbar of LCC-HVDC link
V_T	Measured power frequency voltage magnitude at inverter busbar of LCC-HVDC link
V_d^*	Ordered D-axis voltage in DQ0 frame within a STATCOM controller
V_d	Measured D-axis voltage in DQ0 frame within a STATCOM controller
V_h	LCC-HVDC converter VDCOL upper voltage breakpoint
V_i	LCC-HVDC inverter AC system source alternating voltage magnitude
V_q^*	Ordered Q-axis voltage in DQ0 frame within a STATCOM controller
V_q	Measured Q-axis voltage in DQ0 frame within a STATCOM controller
V_r	LCC-HVDC rectifier AC system source alternating voltage magnitude
V_s^*	Ordered DC-side voltage of STATCOM
V_s	Measured DC-side voltage of STATCOM
$Z_{i,1}$	Transmission line connecting LCC-HVDC inverter busbar to inverter AC system source impedance without line short circuit fault
$Z_{i,2}$	Transmission line connecting LCC-HVDC inverter AC system fault location to inverter AC system source impedance
$Z_{i,3}$	Transmission line connecting LCC-HVDC inverter busbar to inverter AC system fault location
Z_i	Transmission line connecting LCC-HVDC inverter busbar to inverter AC system source impedance
Z_r	Transmission line connecting LCC-HVDC rectifier busbar to rectifier AC system source impedance
Δ	Perturbation coefficient in Nelder-Mead simplex algorithm

ΔI_{DC}	DC-side current margin of an LCC-HVDC link
ΔV_{DC}	DC-side voltage margin of an LCC-HVDC link
α^*	Ordered firing angle of an LCC-HVDC link converter station
α_{SVC}^*	Ordered firing angle of TCR thyristors within an SVC
δ	Success tolerance in DYCORS algorithm
δ_{i}	LCC-HVDC inverter AC system source alternating voltage phase
δ_{r}	LCC-HVDC rectifier AC system source alternating voltage phase
γ	Measured extinction angle of an LCC-HVDC link converter station
γ^*	Ordered extinction angle of an LCC-HVDC link converter station
\mathcal{W}	Exploration-exploitation weight set in DYCORS algorithm
ν	Expansion coefficient in Nelder-Mead simplex algorithm
ψ	Contraction coefficient in Nelder-Mead simplex algorithm
ρ	Reflection coefficient in Nelder-Mead simplex algorithm
σ_{c}	Shrink coefficient in Nelder-Mead simplex algorithm
σ_{init}	Initial perturbation standard deviation in DYCORS algorithm
σ_{max}	Maximum perturbation standard deviation in DYCORS algorithm
σ_{min}	Minimum perturbation standard deviation in DYCORS algorithm
σ_{p}	Perturbation standard deviation in genetic algorithm mutation process
τ_{b}	SVC susceptance PI controller integral time constant
τ_{c}	Synchronous condenser voltage PI controller integral time constant
$\tau_{\text{i,int}}$	LCC-HVDC inverter PI controller integral time constant
τ_{int}	LCC-HVDC converter PI controller integral time constant

τ_i	STATCOM inner current PI controller integral time constant
$\tau_{r,int}$	LCC-HVDC rectifier PI controller integral time constant
τ_s	STATCOM outer DC-side voltage PI controller integral time constant
τ_t	STATCOM outer AC-side voltage magnitude PI controller integral time constant
θ	Perturbation constant in Nelder-Mead simplex algorithm
n_0	Number of points within an experimental design

List of Figures

1.1	HVDC links in Europe.	2
1.2	HVDC links in both East and Southeast Asia.	3
1.3	HVDC links in North America.	4
1.4	HVDC links in both Africa and South America.	4
1.5	HVDC links in both South Asia and the Middle East.	5
1.6	HVDC links in Oceania.	5
1.7	Renewable energy capacity as a share of electricity capacity across worldwide regions.	10
2.1	A twelve-pulse arrangement for a typical LCC-HVDC link, assembled with two six-pulse bridges in one pole.	19
2.2	Control diagram of an LCC-HVDC link converter station using MCCM.	21
2.3	Steady-state voltage-current characteristic of a typical implementation of an LCC-HVDC link using MCCM.	22
2.4	Representation of VSF characteristic with varying AC system ESCR. . .	25
3.1	Flowchart of tested solver methods, with separation between Python interpreter and PSCAD/EMTDC processes.	77
3.2	An LCC-HVDC link interconnecting two AC systems, with shunt filters.	79
3.3	Control diagram of LCC-HVDC link converter controllers.	83
3.4	Difference between solver method mean optimal objective value solutions with 95% confidence interval for Problem 1.	91

3.5	Difference between solver method mean optimal objective value solutions with 95% confidence interval for Problem 2.	92
3.6	Mean convergence curves with 95% confidence intervals for Problem 1. . .	92
3.7	Mean convergence curves with 95% confidence intervals for Problem 2. . .	93
3.8	Measured time series variables corresponding to the best found optimal solutions for each solver method for Problem 1 when ESCR was 3.0. . .	94
3.9	Measured time series variables corresponding to the best found optimal solutions for each solver method for Problem 2 when ESCR was 3.0. . .	95
4.1	An LCC-HVDC link interconnecting two AC systems, with shunt filters, three inverter system transmission lines, and a potential inverter system dynamic compensator.	101
4.2	Control diagram of LCC-HVDC link converter controllers.	106
4.3	System diagram of the SVC within the SVC study case.	108
4.4	Control diagram of the SVC within the SVC study case.	108
4.5	System diagram of the STATCOM within the STATCOM study case. . .	109
4.6	Control diagram of the STATCOM D-axis inner current controller within the STATCOM study case.	109
4.7	Control diagram of the STATCOM Q-axis inner current controller within the STATCOM study case.	110
4.8	Control diagram of the STATCOM D-axis outer controller within the STATCOM study case.	110
4.9	Control diagram of the STATCOM Q-axis outer voltage controller within the STATCOM study case.	110
4.10	Control diagram of the STATCOM PLL and DQ/ABC transformations within the STATCOM study case.	111
4.11	System diagram of the synchronous condenser within the Synchronous Condenser study case.	114
4.12	Control diagram of the synchronous condenser voltage controller within the Synchronous Condenser study case.	114

4.13	DC-side measured power time domain traces for inverter SCR of 1.5. . .	130
4.14	Zoomed view of DC-side measured power time domain traces for inverter SCR of 1.5.	131
4.15	Box-plots of performance values of DC-side measured power.	133
4.16	DC-side measured power sample statistics.	134
4.17	DC-side measured power differences of sample means.	139
4.18	DC-side measured power associations.	143
D.1	DC-side measured power time domain traces for inverter SCR of 1.5. . .	191
D.2	Zoomed view of DC-side measured power time domain traces for inverter SCR of 1.5.	192
D.3	AC-side measured voltage magnitude time domain traces for inverter SCR of 1.5.	193
D.4	DC-side measured voltage time domain traces for inverter SCR of 1.5. .	194
D.5	Zoomed view of DC-side measured voltage time domain traces for inverter SCR of 1.5.	195
D.6	DC-side measured power time domain traces for inverter SCR of 2.0. . .	196
D.7	Zoomed view of DC-side measured power time domain traces for inverter SCR of 2.0.	197
D.8	AC-side measured voltage magnitude time domain traces for inverter SCR of 2.0.	198
D.9	DC-side measured voltage time domain traces for inverter SCR of 2.0. .	199
D.10	Zoomed view of DC-side measured voltage time domain traces for inverter SCR of 2.0.	200
E.1	Box-plots of performance values of DC-side measured power.	202
E.2	Box-plots of performance values of AC-side measured voltage magnitude.	203
E.3	Box-plots of performance values of DC-side measured voltage.	204
E.4	Box-plots of performance values of DC-side measured current.	205
E.5	Box-plots of performance values of measured extinction angle.	206

E.6	Box-plots of LCC-HVDC link PI controller optimal parameter values.	207
E.7	Box-plots of LCC-HVDC link VDCOL optimal parameter values.	208
F.1	DC-side measured power sample statistics.	210
F.2	AC-side measured voltage magnitude sample statistics.	211
F.3	DC-side measured voltage sample statistics.	212
F.4	DC-side measured current sample statistics.	213
F.5	Measured extinction angle sample statistics.	214
G.1	Differences in sample means of measured DC-side measured power.	216
G.2	Differences in sample means of measured DC-side measured power, cont.	217
G.3	Differences in sample means of measured DC-side measured power, cont.	218
G.4	Differences in sample means of measured AC-side measured voltage magnitude.	219
G.5	Differences in sample means of measured AC-side measured voltage magnitude, cont.	220
G.6	Differences in sample means of measured AC-side measured voltage magnitude, cont.	221
G.7	Differences in sample means of measured DC-side measured voltage.	222
G.8	Differences in sample means of measured DC-side measured voltage, cont.	223
G.9	Differences in sample means of measured DC-side measured voltage, cont.	224
G.10	Differences in sample means of measured DC-side measured current.	225
G.11	Differences in sample means of measured DC-side measured current, cont.	226
G.12	Differences in sample means of measured DC-side measured current, cont.	227
G.13	Differences in sample means of measured extinction angle.	228
G.14	Differences in sample means of measured extinction angle, cont.	229
G.15	Differences in sample means of measured extinction angle, cont.	230
H.1	Differences in sample minima of measured DC-side power.	232
H.2	Differences in sample minima of measured DC-side power, cont.	233
H.3	Differences in sample minima of measured DC-side power, cont.	234

H.4	Differences in sample minima of measured AC-side voltage magnitude.	235
H.5	Differences in sample minima of measured AC-side voltage magnitude, cont.	236
H.6	Differences in sample minima of measured AC-side voltage magnitude, cont.	237
H.7	Differences in sample minima of measured DC-side voltage.	238
H.8	Differences in sample minima of measured DC-side voltage, cont.	239
H.9	Differences in sample minima of measured DC-side voltage, cont.	240
H.10	Differences in sample minima of measured DC-side current.	241
H.11	Differences in sample minima of measured DC-side current, cont.	242
H.12	Differences in sample minima of measured DC-side current, cont.	243
H.13	Differences in sample minima of measured extinction angle.	244
H.14	Differences in sample minima of measured extinction angle, cont.	245
H.15	Differences in sample minima of measured extinction angle, cont.	246
I.1	DC-side measured power associations, depending on sample means.	248
I.2	AC-side measured voltage magnitude associations, depending on sample means.	249
I.3	DC-side measured voltage associations, depending on sample means.	250
I.4	DC-side measured current associations, depending on sample means.	251
I.5	Measured extinction angle associations, depending on sample means.	252
J.1	DC-side measured power associations, depending on sample minima.	254
J.2	AC-side measured voltage magnitude associations, depending on sample minima.	255
J.3	DC-side measured voltage associations, depending on sample minima.	256
J.4	DC-side measured current associations, depending on sample minima.	257
J.5	Measured extinction angle associations, depending on sample minima.	258

List of Tables

2.1	Summary of reviewed papers in Section 2.2.	38
2.2	Summary of reviewed papers in Section 2.4.	49
3.1	Parameters used by Solver Method GA.	60
3.2	Parameters used by Solver Method NM.	64
3.3	Parameters used by DYCORDS for both Solver Methods MARS and GPR.	67
3.4	Plant parameter values of the 200 MW LCC-HVDC link.	80
3.5	345 kV rectifier AC-Side impedances.	80
3.6	230 kV inverter AC-Side impedances.	81
3.7	Nominal set-points and parameters for quantities in Figure 3.3.	82
4.1	Plant parameter values of the 200 MW LCC-HVDC link for dynamic compensation simulation studies.	102
4.2	345 kV rectifier AC-Side impedances.	103
4.3	230 kV inverter AC-Side impedances.	104
4.4	Transmission line lengths for each fault location in the 230 kV inverter system.	105
4.5	Nominal set-points and parameters for quantities in Figure 4.2.	106
4.6	Proposed Rankings of plant configurations for both means and minima of performance functions applied over all measured variables.	126
B.1	Transmission line conductor parameters, whole bundle.	179
B.2	Transmission line conductor parameters, cont.	180

B.3	Curve fitting parameters for transmission line frequency dependent phase models.	180
C.1	Transmission line conductor parameters, whole bundle.	182
C.2	Transmission line conductor parameters, cont.	183
C.3	Curve fitting parameters for transmission line frequency dependent phase models.	183
C.4	Parameter values for electrical dynamics model for SVC used in the SVC study case.	184
C.5	Parameter values for SVC controller used in the SVC study case.	185
C.6	Parameter values for STATCOM plant and transformer used in the STATCOM study case.	186
C.7	Parameter values for STATCOM controllers used in the STATCOM study case.	187
C.8	Parameter values for synchronous condenser electrical dynamic model used in the Synchronous Condenser study case.	188
C.9	Parameter values for synchronous condenser transformer and voltage controller used in the Synchronous Condenser study case.	189

List of Algorithms

1	Symmetric Latin Hypercube Design	161
2	Genetic Algorithm	164
3	Nelder-Mead Simplex	168
4	Dynamic Coordinate Search using Response Surfaces	174

Chapter 1

Introduction

1.1 Historical Developments in HVDC Transmission

HVDC links have been deployed for the transportation of electricity since the 1880s [1]. These first systems used electromechanical conversion to transfer energy between AC and DC systems. The use of mercury arc valves for AC-DC conversion as a replacement technology for electromechanical conversion was developed within the first three decades of the 20th century. This led to the Gotland HVDC link, the first commercial mercury arc valve LCC-HVDC link which entered service in 1954 [1]. Mercury arc valve LCC-HVDC links were soon surpassed with thyristor valve LCC-HVDC links from the 1970s onwards [1].

The remainder of the 20th century included continual deployment of HVDC links all over the world. The typical use case for HVDC links in the 20th century was long distance electric power transmission from geographically remote generation to large load centres such as cities [1–3].

In 1999, the first voltage source converter (VSC) HVDC link entered commercial service [1] which utilised the insulated gate bipolar transistor (IGBT) for AC-DC conversion. The first two decades of the 21st century have shown that HVDC transmission remains an economically feasible solution for transmission of

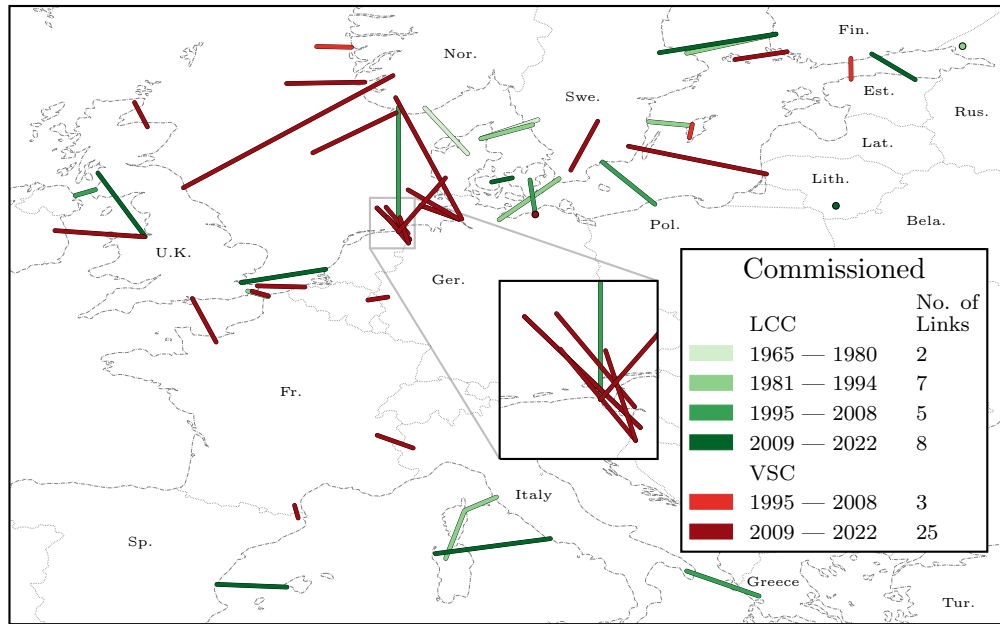


Figure 1.1: HVDC links in Europe.

electrical power [2, 3], with many new HVDC links entering operational service since 2000. VSC-HVDC architectures now allow the economic use of HVDC in circumstances that previously would have required either relatively expensive LCC-HVDC and/or AC solutions.

Figures 1.1–1.6 indicate a sub-set of HVDC links deployed worldwide based upon data in [4–8]. In Figures 1.1–1.6, coloured circle markers indicate back-to-back HVDC links; while coloured lines indicate HVDC links with DC-side overhead lines, underground cables, or undersea cables. Note that “Commissioned” in Figures 1.1–1.6 refers to the earliest period within which a currently in-service HVDC link was commissioned even if that HVDC link has had upgrades or equipment replacements. Where an HVDC link has been completely replaced with another HVDC link in the same vicinity, then the corresponding commissioning period will be for the replacement HVDC link. Note that the set of HVDC links indicated in Figures 1.1–1.6 is not an exhaustive set of all HVDC links in the world; there are additional HVDC links in the world which are not indicated in Figures 1.1–1.6 because they are not included in [4–8]. Also in Figure 1.1,

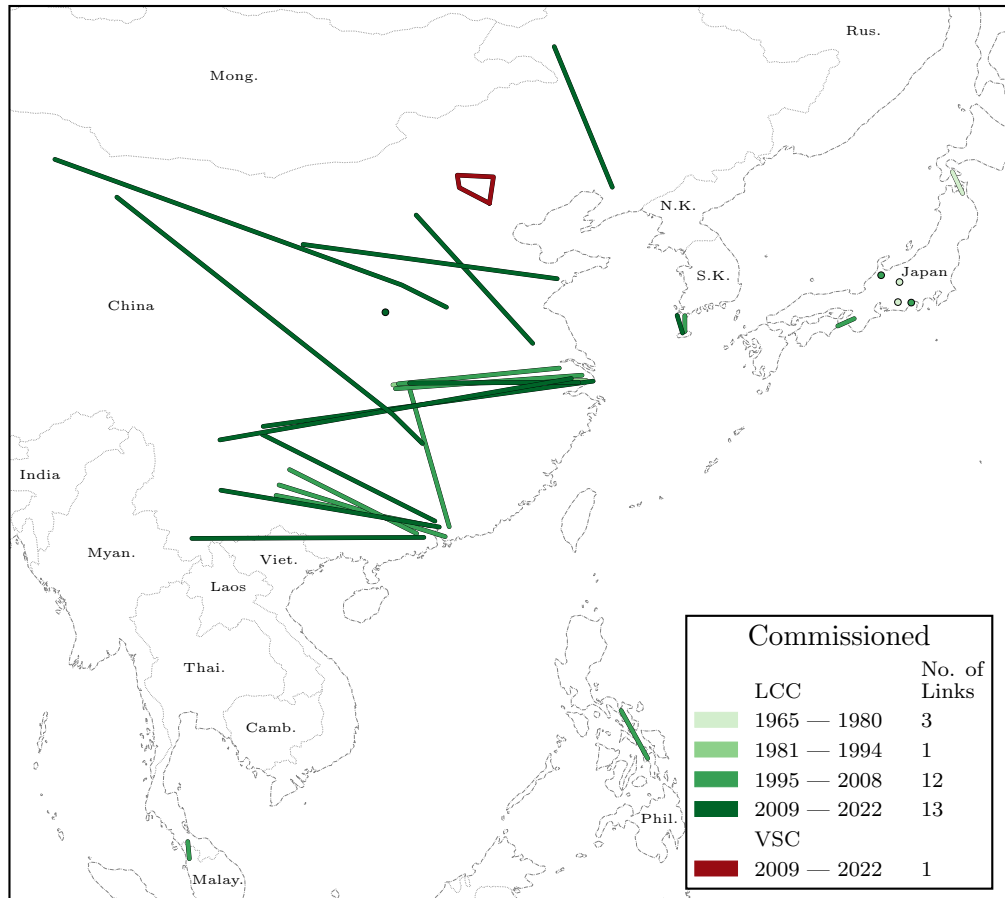


Figure 1.2: HVDC links in both East and Southeast Asia.

some HVDC links connecting offshore wind farms to the German coast have overlapping lines and therefore cannot be visually differentiated; however they are counted in the “Commissioned” legend.

1.2 HVDC Transmission Solutions Compared with AC Transmission Solutions

The decision between choosing AC transmission over HVDC transmission to solve an electrical power transmission problem is a complex question for power system engineers to answer, as evidenced by the discussions in [3, 9].

Chapter 1. Introduction

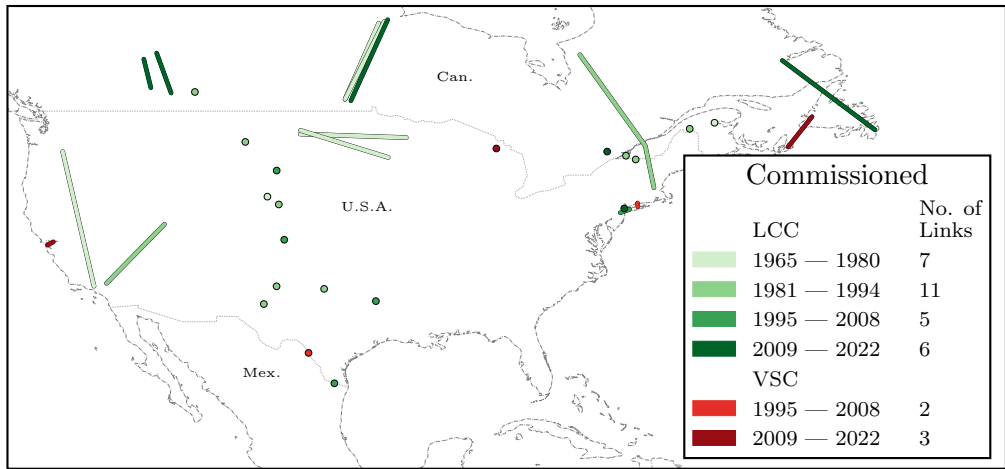


Figure 1.3: HVDC links in North America.

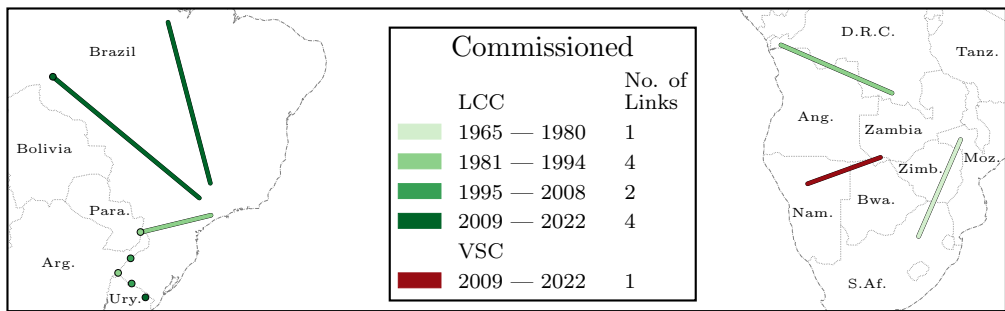


Figure 1.4: HVDC links in both Africa and South America.

The large cost components for HVDC transmission systems are the capital costs of converter stations, whereas substations for AC transmission systems rated for similar power transfer capability are typically much cheaper than HVDC converter stations. When comparing overhead line and underground cable circuit components for HVDC or AC transmission, it is clear that the circuit operational and capital costs per unit of circuit distance are cheaper for HVDC circuits for the same power transfer capability [2, 3, 9].

Chapter 1. Introduction

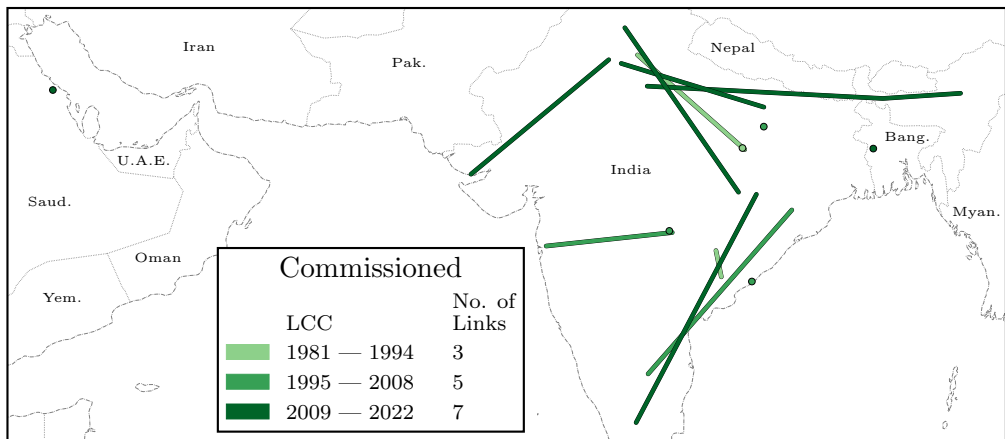


Figure 1.5: HVDC links in both South Asia and the Middle East.

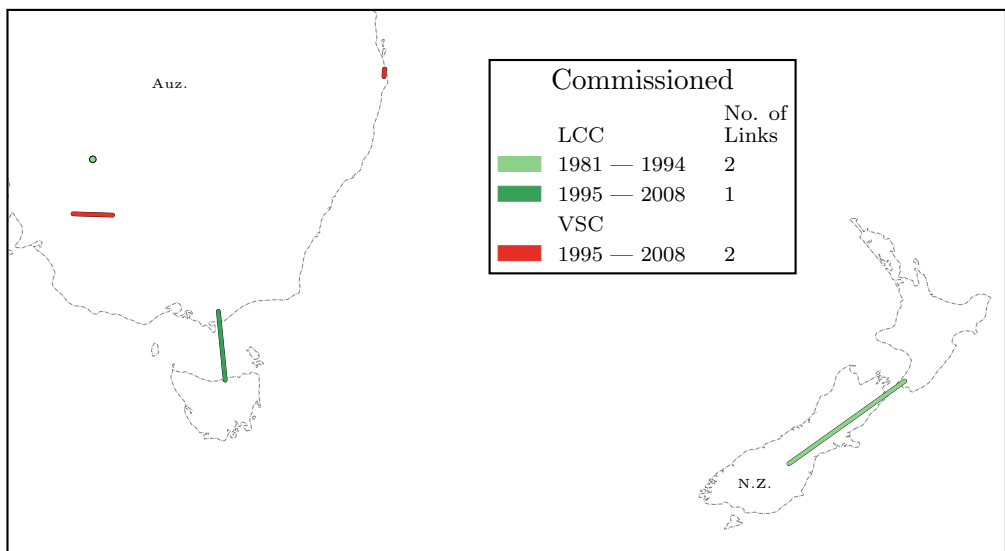


Figure 1.6: HVDC links in Oceania.

For short distance transmission, AC transmission solutions typically have lower total system lifetime cost than HVDC solutions. HVDC is likely to be a more economic choice over long distances compared to AC solutions for large point-to-point power transmission, which explains the wealth of HVDC links deployed instead of AC transmission for this use case since the 1970s until today.

This relationship is complicated by more specific project requirements such as: the need for future power system extensibility, or the existence of power system dynamic problems [9]. AC transmission solutions can allow easier and less invasive future extension or modification compared to HVDC. For example, tapping into a point-to-point AC transmission system to supply a future load centre would typically require less expense in plant than tapping into an existing point-to-point HVDC transmission system. System dynamic issues may favour or disfavour AC transmission compared to HVDC transmission and are therefore project-dependent.

A further complexity with power system dynamic issues is the fact that a power system will likely change in the future and therefore introduce new dynamic issues which were not considered during the design of existing AC or HVDC transmission projects in that power system. A notable subset of system dynamics issues relates to AC system synchronism. Transient stability issues may cause AC transmission to be difficult to manage in some cases, whereas the alternative option of a well-designed HVDC link could be used to alleviate this problem [1]. In other cases, HVDC transmission may be the only option to interconnect two asynchronous AC systems if synchronisation of these systems through an AC transmission link would be expensive to undertake and maintain.

1.3 VSC-HVDC Systems Compared with LCC-HVDC Systems

As discussed in [1], the advent of VSC-HVDC architectures for HVDC systems has expanded the economic feasibility of deploying HVDC solutions to solve power system problems due to some of the technical advantages of VSC-HVDC architectures over LCC-HVDC architectures.

VSC-HVDC architectures generally allow independence of real and reactive power control from short term dynamic timescales in the order of milliseconds, and upwards to longer timescales. LCC-HVDC systems can only achieve some decoupling between real and

Chapter 1. Introduction

reactive power control typically in the order of seconds and longer timescales. This is achieved by coordinated operation of the converters with other items of plant co-located at the converter station, such as: special converter control; converter transformer tap changers; additional dynamic reactive power compensation; and, fast switching of filters and/or shunt capacitors. Faster decoupling in timescales of less than a second between real and reactive power control for LCC-HVDC systems can only be achieved with extra investment in design and plant separate from the LCC-HVDC converters themselves, *e.g.* dynamic compensators.

LCC-HVDC systems maintain some important technical advantages over VSC-HVDC architectures which imply new LCC-HVDC links shall continue to be economically deployed. Both the voltage and current ratings of thyristors are superior to those ratings of IGBTs, and the operational power losses of available VSC-HVDC architectures—including modern IGBT-based modular multilevel converter (MMC) HVDC architectures—are yet to surpass LCC-HVDC systems [2]. These two technical advantages of LCC-HVDC systems imply that LCC-HVDC links should typically be cheaper to construct and operate than similarly rated VSC-HVDC links, assuming the technical advantages particular to VSC-HVDC architectures are not required in the solution of the motivating electric power transmission problem.

A key characteristic of LCC-HVDC links is their dependence on an external arrangement of plant to cause the HVDC link's thyristors to be able to stop conduction and regain forward voltage blocking capability, thus allowing commutation of current between AC phases. In LCC-HVDC links utilising the six-pulse bridge design, this external arrangement is the AC system itself acting in concert with the current source behaviour of the DC-side of the LCC-HVDC link.

The AC system typically behaves as an alternating voltage source behind a substantially inductive impedance, as viewed from the perspective of the six-pulse bridge. This means that orderly operation of an LCC-HVDC converter station and therefore the entire HVDC link is critically dependent on ensuring that the alternating voltage waveform as

Chapter 1. Introduction

applied to the six-pulse bridges by the external AC system remains unperturbed; that is, the voltage waveform should ideally be very insensitive to changing network quantities, including the current from the LCC-HVDC link itself [10].

Failure to ensure insensitive AC system voltage waveforms will result in poor dynamic performance of the LCC-HVDC link; for example, large deviations of LCC-HVDC link power transfer during transient disturbances. Particularly large disturbances such as short circuit faults in the AC system which cause large changes in AC system voltage waveform, may lead to the inability to commutate current between thyristors and ensure forward blocking of thyristors—a condition known as commutation failure [10]. A commutation failure causes power transfer over the LCC-HVDC link to be interrupted, typically for timescales of less than a second; the time taken to recover power transfer after commutation failure is dependant upon the speed and stabilization of AC system voltage magnitude recovery during and after the disturbance.

VSC-HVDC links do not require externally applied alternating voltage from the AC system to cause IGBT turn off, which means VSC-HVDC links are inherently capable of operating with passive AC systems [11]. However VSC-HVDC links connected to active AC systems with high source impedance and thus high AC system voltage waveform sensitivity must be prudently designed to ensure orderly HVDC link control [11]. An LCC-HVDC link would need additional plant such as synchronous condensers in order to be used in a passive AC system. When considering active AC systems with high source impedance, it is still the case that designing an LCC-HVDC link to operate with such a difficult AC system would require additional investment in plant to alleviate the effects of the AC system's high impedance. The five LCC-HVDC links reviewed in [12] demonstrate the range of options that have been used by practitioners to address issues caused by high AC system source impedance relative to those HVDC links' power ratings.

1.4 Recent Developments in Power System Generation Patterns

AC electrical power systems throughout the 20th century were marked by their increasing synchronised interconnection of both generation and demand as electrical energy consumption within societies increased over time. This included the increase in the number of directly connected synchronous machines in the form of large synchronous generators within thermal power stations in order to serve the increasing electrical demands within the AC systems. This meant that AC networks could be generally relied upon to have low equivalent source impedances relative to the power transfers through the networks. Only in certain project-specific instances was this assumption incorrect, such as in those ten LCC-HVDC projects reviewed in [12, 13].

The projects reviewed in [12, 13] are varied in their underlying justifications; although all ten projects were deployed in high source impedance AC networks relative to the LCC-HVDC links' power ratings, the projects include undersea cable links, remote generation interconnection, and asynchronous interconnection between AC networks. These projects indicate two trends by practitioners: to continually interconnect existing network areas that have very few or no existing interconnections; and, to connect remote power generation locations to existing load centres. These trends have not abated. Currently many new HVDC links are being deployed in Asia and South America typically to connect new remote renewable generation [2] such as hydroelectric and wind generation, while further interconnection of existing AC network areas is being pursued in Europe [1].

1.4.1 Shifts Towards Power Converter Interfaced Generation

Since 2000 there has been a shift in generation development internationally, with an increasing share of generation capacity being provided which is reliant upon intermittent renewable energy resources such as wind turbines and solar photovoltaic arrays. In order to make the most efficient use of renewable energy resources, power converters

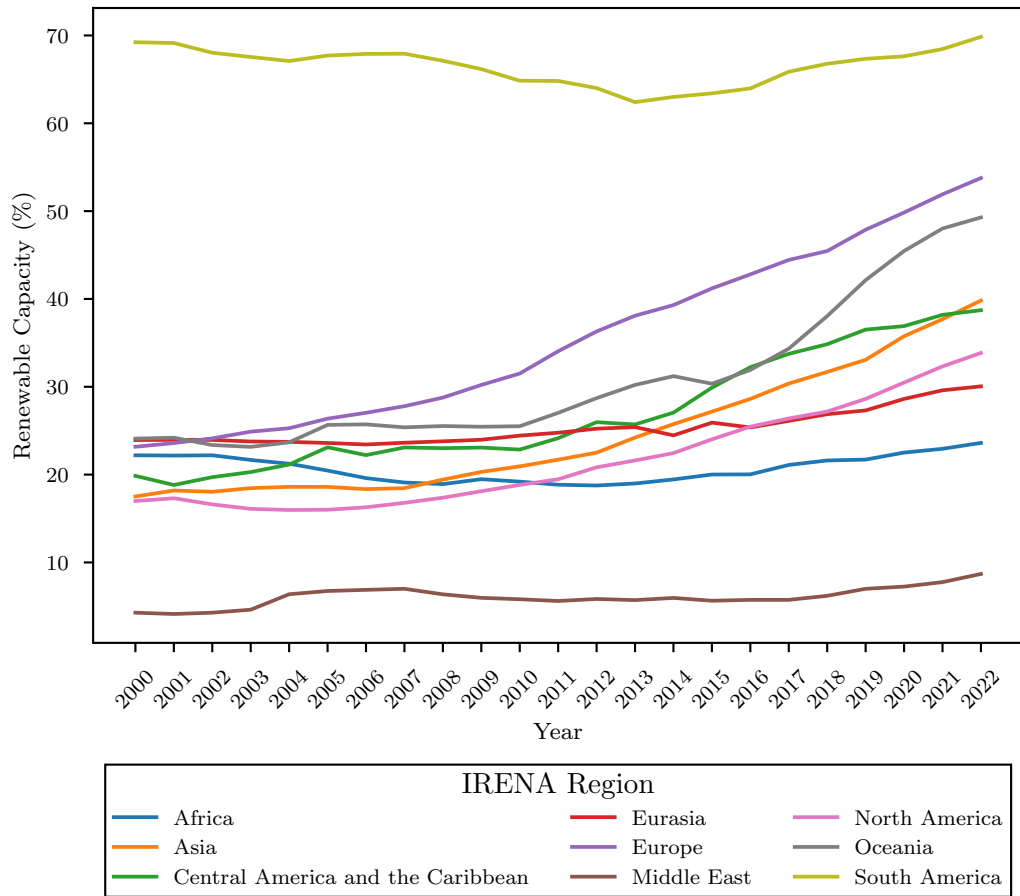


Figure 1.7: Renewable energy capacity as a share of electricity capacity across worldwide regions.

are commonly deployed as part of these renewable energy generation devices in order to interface with the AC network. The increasing shift of world regions’ renewable energy capacity as a proportion of electricity generation capacity is indicated in Figure 1.7 which is drawn from data available in [14].

The shift of the generation fleet from directly connected synchronous machines towards power electronics interfaced devices (PEIDs) will have a major effect on AC system source impedances, leading to high voltage sensitivity issues which will worsen if the trend of increasing PEIDs continues. This trend is envisaged to be the case as many countries are projected to pursue increased utilisation of renewable energy resources

over non-renewable resources which implies an increasing volume of power converter interfaced generation relative to directly connected synchronous generation fed from non-renewable energy sources.

In some circumstances, directly connected synchronous generators are being decommissioned and not replaced as the thermal power stations they were once part of are decommissioned, in line with various governments' policies across the world to increase renewable energy resource utilization.

In summary, economic forces continue to push the deployment of HVDC links in AC networks with high source impedances relative to the HVDC link power ratings. Directly connected synchronous machines are being decommissioned from AC networks, whilst governments' renewable energy policies are increasing the share of power converter interfaced generation in AC networks as a proportion of total generation capacity.

1.4.2 AC Network Voltage Waveform Sensitivity Considering Widespread Power Converter Interfaced Generation

The spread of power converter interfaced generation is an issue for AC network voltage sensitivity because these devices have historically been designed, built, and operated in such a way as to avoid assisting with the control of AC network voltage magnitudes. There are efforts underway by both researchers and practitioners to rectify this situation to allow for the control of AC network voltage magnitudes by power converter interfaced generation.

However it is not yet clear if developments in this area will completely abate the network voltage sensitivity problem. In some cases it may not be economic to do so using geographically dispersed power converter interfaced generation, even if it is technically possible. An additional complexity with the voltage control capability of PEIDs is with respect to how they achieve their voltage control mechanism. This is particularly relevant for VSC-based PEIDs, which are the vast majority of PEIDs in present-day power systems. The example of the application of a short circuit fault within

Chapter 1. Introduction

an AC network will be used to explain this. In synchronous machines, voltage at the machine's terminals and thus wider AC network voltage magnitudes may be affected through three mechanisms.

1. Transiently reduced machine impedance during AC network disturbances which allows greater current flow from the machine into the network, for the same machine internal electromotive force;
2. Field winding current control, which allows internal electromotive force to be increased in response to reduced measured terminal voltage magnitude; and
3. Short term current overload capability, which allows large currents to flow for timescales of tens of milliseconds from the machine into the network during AC network disturbances without machine catastrophic failure, for the same machine internal electromotive force.

However power converter interfaced generation can typically only assist with controlling AC network voltage magnitudes through one mechanism: increasing their reactive power injection as a response to reduced AC network voltage magnitudes measured at their terminals, which is analogous to the second mechanism in the list above. If the disturbance is particularly large such as a short circuit fault in this example, the power converter will limit its current output into the network to comply with the power converter's short term current overload capability which is far smaller than a synchronous machine's short term current overload capability.

The power converter will typically be coupled to the AC network through a coupling impedance which will remain constant during large disturbances like faults, and therefore will not allow increased current to flow for the same voltage applied to the converter side of the coupling impedance by the converter's power electronic devices. During disturbances such as short circuit faults which cause a substantial decrease in AC network equivalent impedance across the terminals of the PEID, the PEID will adjust its operation to ensure that current flow through the device's power electronics is limited in order to avoid damage to the power electronics.

This implies that PEIDs must be dimensioned to provide voltage control capability on par with directly connected synchronous machines, and this dimensioning will imply a potentially significant increase in the cost of the power converter design and plant.

1.5 Research Aim

If trends highlighted in previous sections are to continue; HVDC links will continue to be deployed, and LCC-HVDC links in particular will remain in economic competition with VSC-HVDC links to accomplish this purpose. In the instances where LCC-HVDC links may be proposed, the AC network areas which the LCC-HVDC links may be expected to interface with will have poor voltage sensitivity due to: electrical remoteness; a lack of directly connected synchronous machines; and, relatively insufficient voltage control capability from power converter interfaced generation. Lastly, it is clear that an LCC-HVDC link in this future scenario may become exposed to poor AC network voltage waveform sensitivity during its design life due to larger-than-envisaged displacement of synchronous generation by power converter interfaced generation in the AC system.

As alluded to in [12,13], there exist many possible solutions for addressing different issues caused by poor AC system voltage sensitivity problems with respect to LCC-HVDC links. The more limited scope of inquiry focussing solely on comparing different solutions for ensuring technically favourable power transfer dynamics of an LCC-HVDC link is still a complex problem in itself.

The aim of this thesis is to propose a method to quantitatively evaluate shunt-connected dynamic compensators on their relative capabilities in improving LCC-HVDC link dynamic performance. This thesis also proposes a strategy to evaluate optimisation solver methods to solve simulation-based optimisation problems. A promising solver evaluated via this solver method evaluation strategy is then used as part of the dynamic compensator evaluation method.

1.6 Research Objectives

The research objectives of this thesis are as follows.

1. Propose a method to evaluate simulation-based optimisation solver methods against one another on the problem of LCC-HVDC controller parameter tuning.
2. Evaluate two simulation-based optimisation solver methods using surrogate-model based strategies, against two solver methods using mature strategies, using the method proposed in Objective 1 above.
3. Propose a method to quantitatively evaluate shunt-connected dynamic compensation devices for improving the dynamics of an LCC-HVDC link's power transfer, especially when considering AC system short circuit faults and high AC system source impedance relative to the LCC-HVDC link's power transfer.
4. Evaluate shunt-connected dynamic compensation devices quantitatively against each other by applying the proposed method from Objective 3 above to dynamic compensation study cases modelling: a synchronous condenser, an SVC, and a STATCOM.

1.7 Thesis Organisation

Chapter 1 gives a brief summary of HVDC development, before stating recent developments within power systems involving the increased prevalence of power converter interfaced generation relative to directly connected generation. The Chapter then states thesis aim, objectives, organisation, contributions, and bibliographic details on a publication co-authored by the thesis author and related to the thesis' contents.

Detailed review of prior research literature relevant to this thesis' research objectives are discussed in Chapter 2. Firstly, Chapter 2 summarises the control of the typical LCC-HVDC link during normal operation, before reviewing the specific problem of LCC-HVDC link operation within AC power systems with high equivalent source

Chapter 1. Introduction

impedances relative to the power transfer magnitudes expected to be carried by the LCC-HVDC link. Chapter 2 then investigates research literature on the alleviation of LCC-HVDC operational difficulties in these challenging power system conditions, with gaps in the research literature identified which support the research aim for this thesis. Secondly, Chapter 2 summarises the use of optimisation with computer simulations which is called simulation-based optimisation. Characteristics of optimisation solver methods used for simulation-based optimisation are reviewed. The application of such methods for power system engineering problems in the research literature is then explored, identifying research gaps which support this thesis' consideration of more recent optimisation methods for the solution of power system simulation-based optimisation problems.

Research Objectives 1 and 2 from Section 1.6 are reported on in Chapter 3. Firstly, Chapter 3 proposes a method to statistically evaluate stochastic optimisation solver methods on a particular optimisation problem of LCC-HVDC controller parameter tuning. Chapter 3 then applies the proposed method to two specific versions of the tuning problem in order to evaluate two solver methods using mature solution strategies against two solver methods using surrogate model strategies recently proposed in the research literature.

Research Objectives 3 and 4 from Section 1.6 are reported on in Chapter 4. Firstly, Chapter 4 proposes a method which statistically evaluates dynamic compensators on their improvement of the dynamic performance of an LCC-HVDC link inverting into a low SCR AC system. The method considers different types and ratings of dynamic compensators and different short circuit fault disturbances applied to the LCC-HVDC link's inverter system. Chapter 4 then applies the method to a set of study cases to generate results which show quantitative differences between the different types and ratings of dynamic compensators compared to each other and the basic compensator-less LCC-HVDC link.

Finally Chapter 5 provides conclusions from this thesis, and suggests some avenues of inquiry to future researchers.

1.8 Thesis Contributions

The contributions of this thesis are as follows.

- A new method is proposed which evaluates stochastic black-box optimisation solver methods on their solution of the computationally expensive simulation-based optimisation problem of LCC-HVDC link controller parameter tuning when considering large disturbances and set-point changes.
- A new method is presented which evaluates dynamic compensators on their ability to improve an LCC-HVDC link's dynamic performance when inverting into a high source impedance AC system relative to the LCC-HVDC link's power transfer. The method incorporates simulation-based optimisation and statistical calculations, and considers multiple short circuit fault locations and inverter system SCR values.

1.9 Author's Publication Related to this Thesis

A. S. C. Leavy, L. Xu, S. Filizadeh and A. M. Gole, "Simulation-based Optimisation of LCC-HVDC Controller Parameters using Surrogate Model Solvers," in *20th Workshop on Control and Modeling for Power Electronics (COMPEL)*, Toronto, ON, Canada, Jun. 2019, pp. 1-8.

Abstract. This paper proposes the use of surrogate model optimisation methods to solve box constrained LCC-HVDC controller tuning problems. The tuning problem is the selection of the proportional-integral controller gains and voltage-dependant current order limiter parameters of an LCC-HVDC link subject to two operational scenarios and a set of large-signal disturbances. The solvers using recently proposed surrogate model methods performed either similarly to or significantly better than solvers using mature methods of the types found in PSCAD/EMTDC, thus confirming the suitability of these surrogate model solvers for simulation-based optimisation of LCC-HVDC controllers.

Chapter 2

Literature Review

This chapter introduces the concept of the LCC-HVDC link including its typical control strategy and steady-state characteristic. The problem of high AC system source impedance and corresponding AC system voltage waveform sensitivity to disturbances is discussed, specifically with respect to the negative influence of voltage waveform sensitivity on the dynamic performance of LCC-HVDC links.

This chapter then reviews research literature in two separate subject areas. Firstly, methods to reduce the negative effects of poor AC-side voltage waveform sensitivity on LCC-HVDC link dynamic performance are reviewed. Secondly, simulation-based optimisation and its use in power systems engineering is discussed. Research gaps relevant to the original contributions of this thesis are highlighted in both subject areas.

2.1 Research Literature on LCC-HVDC Systems

2.1.1 The LCC-HVDC Link Plant and Control Architecture

LCC-HVDC links are typically built using thyristors arranged in six-pulse bridges. The bridges are interfaced with the AC network through converter transformers, while the bridges are interfaced with the DC-side circuit through smoothing reactors.

The AC network as viewed from the AC network side of the converter transformers is an

Chapter 2. Literature Review

alternating voltage source behind a mostly inductive source impedance. Although there is some scope for flexibility depending on particular project-dependent requirements, a typical LCC-HVDC link converter station is constructed as a bipole made from two twelve-pulse poles; Figure 2.1 shows a twelve-pulse pole. Note the arrangement of a pair of six-pulse bridges, where one bridge is interfaced with the AC network through a star-star converter transformer and the other bridge interfaced with the AC network through a star-delta transformer. This arrangement allows significant cancellation of some of the characteristic current harmonics introduced into the AC network and characteristic voltage harmonics applied onto the DC-side circuit, both of which occur during operation of the six-pulse bridges.

Harmonic current filters are typically located in the AC network near the converter transformers. These filters are used to reduce the magnitude of voltage harmonics in the alternating voltage waveform at the converter station by allowing a low impedance path for current harmonics from the converters to pass through with small voltage drop. This has two notable consequences: the alternating voltage waveform seen by the thyristor valves is approximately sinusoidal; and, quality of supply to the wider AC network is ensured by maintaining a mostly sinusoidal voltage waveform at other AC network locations in addition to the converter station AC busbar. These harmonic current filters also provide some fundamental frequency reactive power to the converters, as the converters act as consumers of inductive reactive power during operation.

LCC-HVDC link converter control assumes that the DC-side circuit behaves as a direct current source, while the AC-side circuit behaves as an alternating voltage source. These assumptions are approximately held true during operation as follows: the AC-side network is generally a source of alternating voltage to the link as the active sources in the AC-side network are predominantly voltage sources; and, the DC-side circuit is assumed to act as a direct current source due to the substantial inductance of the DC-side smoothing reactors.

The thyristor bridge then acts simultaneously to modulate the AC-side voltage onto

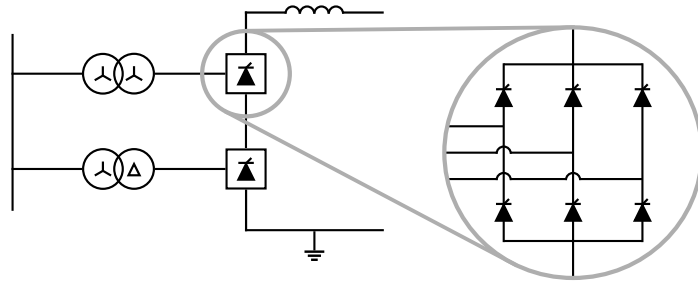


Figure 2.1: A twelve-pulse arrangement for a typical LCC-HVDC link, assembled with two six-pulse bridges in one pole.

the DC-side as a direct voltage, and to modulate the DC-side direct current into the AC-side as an alternating current.

A thyristor will latch into conduction and remain conducting if: a sufficiently large forward voltage is present; a firing pulse is sent to the thyristor gate to trigger it into conduction; and, the circuit causing the forward voltage allows current to start flowing through the thyristor. The thyristor will not allow blocking of forward voltage after having been triggered into conduction until: the current through the thyristor stops flowing due to external circuit conditions; gate pulses are not present at the thyristor gate; and, a reverse voltage is applied for some time to allow recombination within the thyristor.

The thyristor turn-on instant is controllable by manipulating the instant in time when the gate pulse is applied to the thyristor, with respect to the AC system alternating voltage waveform. When analysing LCC-HVDC links, the gate pulse turn-on instant is called the *firing angle* or *delay angle*, and is measured as an angle between 0° and 180° where 0° is the instant at which natural commutation would occur with ideal AC-side three-phase alternating voltage waveforms applied to the six-pulse bridge if the thyristors in the bridge were replaced with diodes.

In a six-pulse bridge, current will commute from one thyristor to another when the forward voltage of the incoming thyristor is larger than the forward voltage of the outgoing thyristor. During commutation, the current through the incoming thyristor will increase

Chapter 2. Literature Review

from zero up to the steady-state value of DC-side current while the current through the outgoing thyristor will simultaneously decrease from the steady-state value of DC-side current down to zero. The commutation process does not complete instantaneously. There is a minimum time taken for commutation to complete; this is due to the magnitude of the commutating inductance. In the arrangement shown in Figure 2.1, the commutating inductance is the leakage inductance of the converter transformer. This period during commutation is known as the overlap period, and is dependent on: AC-side alternating voltage magnitude; DC-side direct current magnitude; commutating inductance; and thyristor turn-on firing angle.

As thyristors can only conduct current in one direction, this means that DC-side current typically flows in the same direction through the point-to-point LCC-HVDC link and only changes in magnitude depending on power transfer dispatch of the LCC-HVDC link. In order to provide bi-directional power transfer over the LCC-HVDC link, the direct voltage applied onto the DC-side from both converter stations is made either positive or negative.

A converter station behaves as a rectifier if its thyristors' firing angles are between 0° and 90° , and will behave as an inverter when the thyristors' firing angles are between 90° and 180° .

The typical control method of point-to-point LCC-HVDC links is the marginal current control method (MCCM); a control diagram of one implementation of MCCM at one converter station in an LCC-HVDC link is shown in Figure 2.2. The variables in Figure 2.2 are defined as follows. P_{DC}^* and V_{DC}^* are the ordered DC-side power and voltage of the LCC-HVDC link, respectively. γ^* and γ are the ordered and measured extinction angles of the specific converter station, respectively. V_{DC} and I_{DC} are the measured DC-side voltage and current of the LCC-HVDC link, respectively. ΔV_{DC} and ΔI_{DC} are the DC-side voltage and current margins of the specific converter station, respectively. α^* is the ordered firing angle sent to all of the thyristors in the specific converter station.

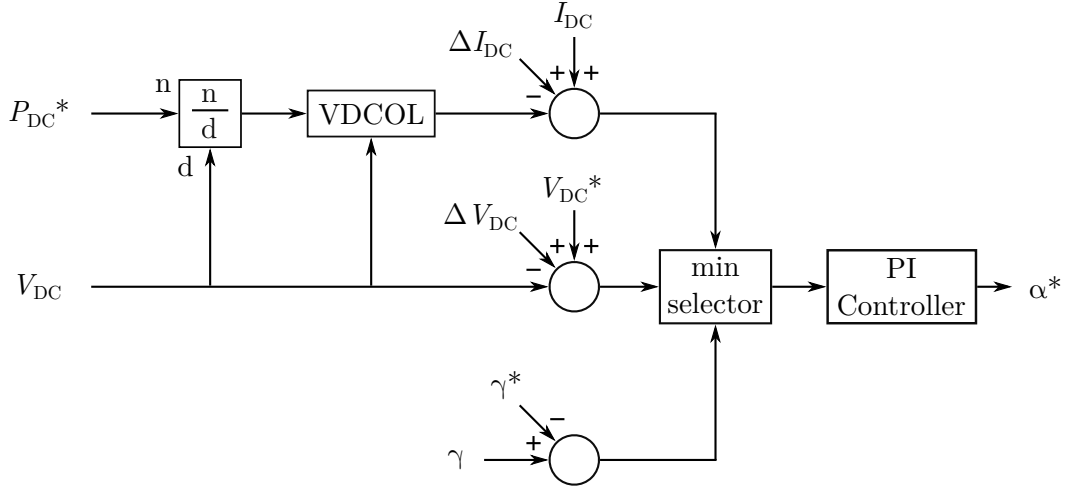


Figure 2.2: Control diagram of an LCC-HVDC link converter station using MCCM.

The MCCM uses the inverting converter station to control DC-side direct voltage magnitude, whilst the other converter station acts as a rectifier and controls DC-side direct current magnitude. Each converter station enacts its control objective by manipulating its own thyristor firing angle. A higher level control scheme is typically used to control LCC-HVDC link power transfer to an ordered value by manipulating the ordered DC-side current of the current-controlling converter station. This control approach makes economically efficient use of nominal voltage and nominal current ratings of the LCC-HVDC link plant. Note that there is generally a need for coordination between converter stations to ensure orderly operation of the LCC-HVDC link. This typically requires a communication link which dispatches at least the ordered DC-side current to both converter stations from the LCC-HVDC link's power control location.

Most LCC-HVDC links employing MCCM have some supplementary control functions to ensure orderly operation during disturbances.

If the rectifier station's AC network voltage magnitude reduces, the MCCM allows the rectifier station to swap from controlling DC-side current to controlling DC-side voltage instead. The inverter station simultaneously swaps from controlling DC-side voltage to controlling DC-side current instead.

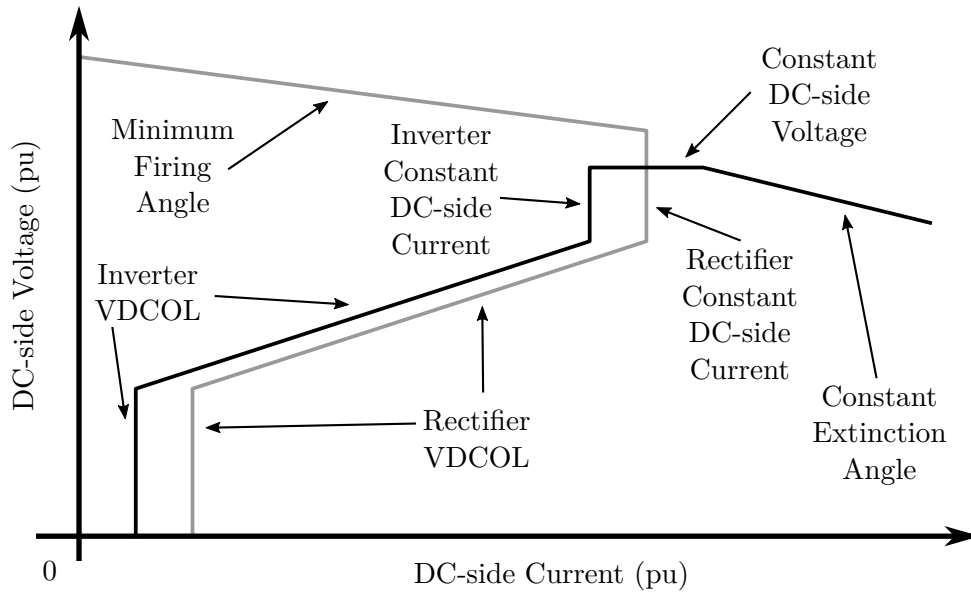


Figure 2.3: Steady-state voltage-current characteristic of a typical implementation of an LCC-HVDC link using MCCM.

Many in-service LCC-HVDC links reduce their ordered DC-side current if measured DC-side voltage or alternatively measured AC-side voltage magnitude decrease. This function can be implemented in many different ways and tends to be project-dependent, however it is typically referred to as a voltage-dependent current order limiter (VDCOL).

The last important aspect of LCC-HVDC link control is the extinction angle controller. This controller ensures that outgoing thyristors during commutation within an inverting six-pulse bridge can complete commutation before the forward voltage across the outgoing thyristor becomes larger than the forward voltage across the incoming thyristor. In such a scenario, the current would fail to reduce to zero in the outgoing thyristor and instead the outgoing thyristor would remain conducting while the incoming thyristor will fail to take over conduction; this is a *commutation failure*.

During inversion, a six-pulse bridge is most economically utilised if the maximum value of direct voltage is being produced across the bridge, which corresponds to ordered thyristor firing angles being closer to 180° than 90° . However thyristor commutation must have completed with some time between the turn-off instant and 180° otherwise

commutation failure will occur, hence some angle headroom is allowed. This headroom is called the *extinction angle*.

The steady-state voltage-current characteristic of an MCCM LCC-HVDC link is shown in Figure 2.3, where the black line indicates the inverter characteristic, and grey line indicates the rectifier characteristic. The intersection of both characteristics represents the steady-state operating point. Note that this characteristic includes DC-side voltage, extinction angle, and DC-side current control segments on the inverter characteristic; and DC-side current and minimum firing angle segments on the rectifier characteristic. Both characteristics employ VDCOL behaviour to reduce ordered DC-side current when DC-side voltage is reduced. Note that there is great variability in the design of VDCOL behaviour and therefore exotic voltage-current characteristics are possible to meet project-specific needs in practical applications.

2.1.2 LCC-HVDC Link Susceptibility to AC Network Voltage Sensitivity

The issue of AC networks with high source impedance relative to desired power transfer levels and their potential corresponding effects on orderly operation of LCC-HVDC links, has been known since the deployment of early LCC-HVDC links into service [15]. However the bulk of the research work undertaken to understand these effects was only completed during the approximate period between 1984 and 1996.

Before this period of research, practitioners and researchers alike tended to use the SCR and the related effective short circuit ratio (ESCR) as indicative measures of relative difficulty in operating an LCC-HVDC link connected to a particular AC network [15].

$$R_{\text{SCR}} = \frac{S_{\text{F}}}{P_{\text{DC}}} \quad (2.1)$$

$$R_{\text{ESCR}} = \frac{S_{\text{F}} - Q_{\text{F}}}{P_{\text{DC}}} \quad (2.2)$$

Chapter 2. Literature Review

In (2.1) and (2.2), S_F is the short circuit level of the AC network as viewed from the converter station AC-side busbar; Q_F is the nominal fundamental frequency reactive power injection from all shunt filters and shunt reactive compensation at the converter station AC-side busbar; P_{DC} is the real power of the converter station; R_{SCR} is the SCR; and R_{ESCR} is the ESCR.

It is clear that S_F , Q_F , and P_{DC} may change during operation of the LCC-HVDC link and the AC system: ordered power transfer over the LCC-HVDC link may be less than the LCC-HVDC link's real power rating; AC network short circuit level will change based upon network state; and, the committed filters and reactive compensation will change as filter banks are switched in and out based primarily upon the LCC-HVDC link ordered power transfer. Therefore researchers and practitioners are often interested in the minimum values of SCR and ESCR that could be expected during the LCC-HVDC link's design life because the minimum values represent the most difficult operational circumstances for the LCC-HVDC link.

As reviewed by [15], researchers have noted that both LCC-HVDC link steady-state and dynamic issues are associated with low values of SCR and ESCR. From the mid-1980s, many authors [16, 17] started to undertake work on proposing more sophisticated approaches and corresponding measures to help with performing indicative analysis of LCC-HVDC link operational difficulty. This work typically focussed on linearised steady-state analysis approaches.

A generalised method of calculating voltage stability factor (VSF) in an AC network with one or more LCC-HVDC link converter stations present within the network was proposed in [16]. For demonstration purposes, the analysis contained within [16] focusses on only one LCC-HVDC link converter station connected to the AC network.

$$R_{VSF} = \left. \frac{\frac{\Delta V}{V}}{\Delta Q} \right|_{P_{DC}} \quad (2.3)$$

In (2.3), V is the voltage magnitude of the AC-side busbar at a converter station; ΔV is

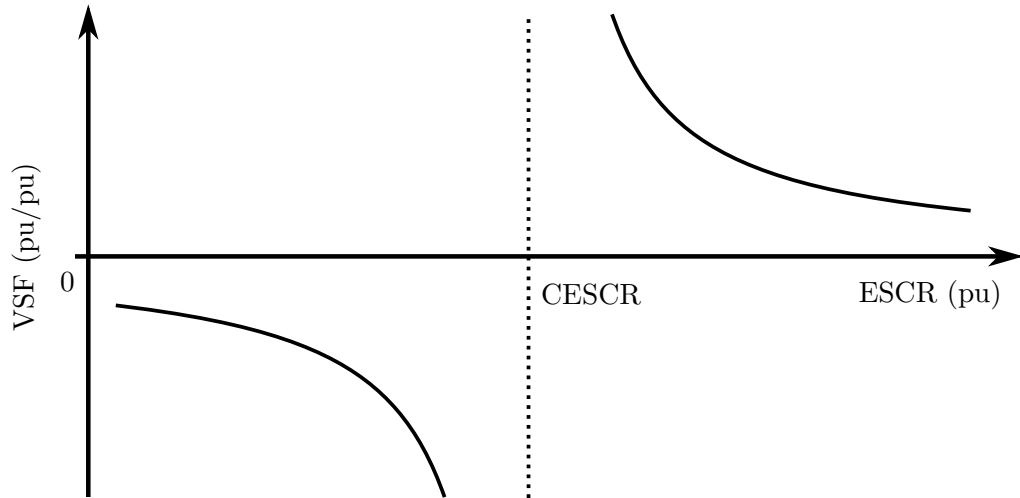


Figure 2.4: Representation of VSF characteristic with varying AC system ESCR.

the incremental change in that voltage magnitude for the increment ΔQ ; ΔQ is an incremental change in the reactive power exchange at the converter station AC-side busbar; and, R_{VSF} is the VSF. The VSF is effectively a measure of sensitivity is evidenced by the incremental quantities in (2.3), and is calculated using elements from a Jacobian matrix formed from linearised steady-state equations. It is therefore clear that the VSF changes depending on the system operational state which is made clear by the inclusion of P_{DC} in (2.3).

The authors of [16] provide plots of VSF considering different ordered power transfers for different LCC-HVDC link control modes, different dynamic compensation approaches, and filter switching. The behaviour of VSF can therefore be summarised as follows, with a representation indicated in Figure 2.4 where the VSF is represented by the black line.

1. Negative values of VSF indicate system steady-state instability; and
2. Positive values of VSF indicate system steady-state stability, however large magnitudes of VSF imply larger control effort to reject disturbances.

In [17], a similar approach of linearised steady-state analysis is undertaken to that

in [16] but with a slightly modified steady-state model incorporating AC network source impedance more explicitly. The authors of [17] then studied the modification of the study system's ESCR while considering: different LCC-HVDC link control modes; converter transformer tap changing; and, the inclusion of an SVC. The work in [17] indicates the existence of the critical effective short circuit ratio (CESCR), which is the value of ESCR for a particular operational scenario at which VSF changes sign. Values of ESCR greater than CESCR for a particular operational scenario indicate system stability and a corresponding positive-valued VSF, *i.e.* the right-hand side of the dotted CESCR line in Figure 2.4. Values of ESCR less than CESCR correspond with negative-valued VSF and indicate system instability, *i.e.* the left-hand side of the dotted CESCR line in Figure 2.4.

Inspection of [16, 17] indicates that operation of LCC-HVDC links with low ESCR is difficult, however this difficulty can be addressed by: selection of alternative control modes for converter stations; or, by manipulating the control of voltage magnitude at the converter station AC-side busbar by addition of dynamic compensation such as synchronous condensers or SVCs [15].

The work in [18] includes a discussion on the effects of transient stability problems associated with LCC-HVDC links. The authors show via time domain simulation results that it is possible for a limit cycle to be created through certain choices of VDCOL and thyristor firing angle controller parameters. The mechanism occurs as follows.

Assume an LCC-HVDC link is operating in a steady-state manner, with rectifier controlling current and inverter controlling extinction angle. An increment in ordered DC-side current is applied to the system. The rectifier increases DC-side current to match the new ordered value. This causes the AC-side voltage magnitude at both converter stations to decrease due to the increased voltage drop because of the increased current from the LCC-HVDC link travelling through mostly inductive source impedances of both AC systems. This correspondingly causes a drop in DC-side voltage. If the measured DC-side voltage drops low enough to activate a VDCOL,

this reduces the ordered DC-side current. The DC-side current is reduced to suit this ordered value from the VDCOL. However the reduced DC-side current causes AC-side voltage magnitude to recover, thus causing DC-side voltage to recover, and therefore the VDCOL to deactivate and allow the ordered DC-side current to resume back to the original incremented value. This then causes the measured DC-side current to increase again. The increased DC-side current then causes the corresponding drop in DC-side measured voltage as explained above, therefore leading to repeated cycles of successive VDCOL activation and deactivation.

This mechanism explained in [18] indicates that attending only to ESCR values calculated from steady-state approach will mask the effect of control system behaviour, potentially hiding detrimental behaviour that only becomes evident when performing transient simulations.

Similar conclusions are evident from inspection of [19], where comparisons are made between steady-state analysis and time domain transient simulations with respect to determination of critical short circuit ratio (CSCR). The authors of [19] found that stable regions of SCR could sometimes be overly optimistic if calculated from steady-state approaches. The apparent point of instability could in fact occur at higher values of SCR as determined from time domain simulations, depending on the choice of control modes at the rectifier and inverter stations in the studied point-to-point LCC-HVDC link.

Commutation failure is a non-linear phenomenon in LCC-HVDC links which is also affected by AC network source impedance as viewed from the LCC-HVDC link. However there are many more influences on the commutation failure mechanism aside from AC network source impedance, as explained in [10]. The work in [10] performed a parametric analysis of commutation failure onset for an idealised model of an LCC-HVDC link connected to a zero impedance AC network. According to [10], low commutating inductance, high smoothing reactance, and high ordered extinction angle can all contribute to avoiding commutation failure onset during reductions in AC-side voltage magnitude.

The analysis in [10] specifically addressed an AC network with zero impedance. The authors of [10] admit that non-zero AC network impedance could result in adverse effects of commutation failure onset compared to those results presented in [10]. In addition, the authors suggest that different controller strategies—apart from increased ordered extinction angle—would be unlikely to reduce the probability of commutation failure during disturbances, and instead controllers are more likely to provide benefit in avoiding subsequent commutation failures and to prudently recover from commutation failures when they occur.

The authors of [20] investigate the commutation failure immunity index (CFII), which attempts to quantify commutation failure onset for LCC-HVDC links in AC systems with either a single LCC-HVDC link or multiple LCC-HVDC links inverting into the AC system. The authors use simulation-based methods rather than the analytical model employed in [10]. High values of CFII indicate that relatively low values of fault inductance may be applied to the LCC-HVDC link AC-side converter busbar to emulate a fault, and the LCC-HVDC link will not suffer a commutation failure. Therefore high CFII for an LCC-HVDC link implies that the LCC-HVDC link can suffer relatively close short circuit faults without suffering a commutation failure. The authors of [20] constructed an EMT time domain simulation model of an LCC-HVDC link and subjected the model to various AC-side disturbances to model faults, over a range of non-zero AC network source impedance values. It is clear from the single-infeed results in [20] that CFII and thus commutation failure inception depends on AC network source impedance.

2.2 Research Literature on Alleviation of LCC-HVDC Link Susceptibility to AC Network Voltage Sensitivity

It is evident from [10, 15–20] that the performance of LCC-HVDC links connected to AC networks with high source impedance relative to LCC-HVDC link power transfer—*i.e.* networks with low SCR—may have their performance improved if

Chapter 2. Literature Review

the AC-side voltage magnitude can be controlled and therefore AC-side voltage sensitivity reduced. This performance would include steady-state stability improvement as well as reduced transient issues such as reduced commutation failure occurrence and improved recovery after commutation failures when they occur.

Dynamic compensators may be employed to reduce the problem of AC-side voltage sensitivity. However, there are different types of dynamic compensators with fundamentally different plant characteristics and associated control methodologies. There may be many potential dynamic compensation options to reduce an AC-side voltage sensitivity problem at an LCC-HVDC converter station. Therefore, an economic appraisal [21,22] of these options is necessary for the transmission network asset owner to select an option to reduce the AC-side voltage sensitivity problem. An economic appraisal is composed of an analysis of these options' economic costs and economic benefits in a coherent manner such that the appraisal's results may be used by a decision maker to select an option to reduce the problem.

The economic appraisal process is often substantially composed of a cost-benefit analysis (CBA). A CBA process [22] typically requires all costs and benefits of investment alternatives to be quantified in common units such as a single currency. These costs and benefits are adjusted to consider the time value of money. Overall, the adjusted costs and benefits of each investment alternative may then be summed together to give that investment alternative's net benefit. The investment alternative with the best net benefit represents the most attractive option for the decision maker to select.

In the case of dynamic compensation options, the investment alternatives are specific combinations of different technologies, plant sizes, and/or controller methodologies. The results of a CBA process employed in this case would allow a decision maker to identify the compensation option which would provide the largest total benefit in assisting LCC-HVDC link dynamic performance, at the least total cost to the asset owner.

A CBA requires three steps to quantify benefits and costs [22].

1. Identification of positive and negative elements of an investment alternative;

Chapter 2. Literature Review

2. Quantification of these elements; and
3. Valuation of the positive and negative elements which taken with their quantification, results in total benefit and total cost for each element.

Valuation of investment alternative costs for dynamic compensation are rare in the open literature [22]. Some open literature sources are cited within [22], however they are not recent and are therefore likely to be inaccurate due to technological and business environment changes [22]. The author of [22] does provide some costs for SVCs and STATCOMs in [22, Table 2] which indicates STATCOMs to be more expensive than SVCs. In addition, the authors of [21] include costs for SVCs and STATCOMs in [21, Table 6] with data from an alternative source not cited within [22]. The data in [21, Table 6] also indicate STATCOMs to be more expensive than SVCs. Furthermore, [23] states that costs for synchronous condensers are much higher than for power electronic compensators.

Overall these indications from [21, Table 6], [22, Table 2], and [23] suggest the following order of dynamic compensator technologies based upon their costs, ordered from highest cost to lowest cost.

1. Synchronous condensers;
2. STATCOMs; then
3. SVCs.

The valuation of investment alternative benefits is also difficult in the power systems domain [22]. This is typically due to inaccuracy of modelling and/or data used to identify and quantify positive elements associated with investment alternatives. In the case of dynamic compensation investment alternatives, plant or controller characteristics may allow compensators with different nominal ratings to reduce the same LCC-HVDC link dynamic performance problem, *i.e.* the options may have the same benefit but with different equipment nominal sizes. Simplistic comparisons based upon nominal ratings are therefore likely to be inaccurate [22].

Alternative comparisons based upon plant parameters and/or proxies are also likely to

be inaccurate for providing benefit information for compensator alternatives due to the unclear technical linkage between these parameters, AC-side voltage waveform sensitivity, and LCC-HVDC link dynamic performance. This is a substantial source of the difficulty encountered in assessing benefits of dynamic compensators which therefore negatively affects decision maker discrimination between compensator investment options' net benefits.

Economic appraisal including a CBA is an important task for decision makers to undertake for assessing dynamic compensators to reduce AC-side voltage sensitivity problems and therefore assist with LCC-HVDC dynamic performance. The CBA results allow coherent comparison between compensation alternatives so that a decision maker may choose an option which has the best net benefit. However, dynamic compensation benefit and cost quantification is difficult for dynamic compensators. A CBA analyst must have good data and/or models to perform these quantifications, but the benefit quantification for dynamic compensators is made especially difficult due to the lack of technical linkage between compensator types and sizes and their effect on LCC-HVDC dynamic performance.

2.2.1 Description of the Research Literature

Reference [24] proposes an AC-side voltage magnitude control loop added to an LCC-HVDC link inverter station to act in conjunction with conventional DC-side current control and extinction angle control. The proposed method is compared with an SVC and a synchronous condenser as alternative methods of dynamic compensation, using both steady-state VSF and non-linear time domain simulations. The results of [24] indicate that the proposed method could achieve superior performance to the alternative methods even with low post-fault SCR values. The authors highlight the proposed method's particular advantage of efficiently utilising reactive injection from additional shunt capacitor banks when coordinated with the switching of those banks. Comparisons between methods were made by visually comparing traces of VSF values plotted with respect to LCC-HVDC link ordered power transfer for steady-state analysis;

and non-linear simulations were used for qualitative comparison of time domain traces of system variables as they evolved during disturbances. Only a single value of base case SCR was studied, although this value varied somewhat depending on dynamic compensation method—synchronous condensers increase system SCR as viewed from an LCC-HVDC link converter station—and also the post-disturbance system state.

In [25] the authors demonstrate that controller modifications of an in-service back-to-back LCC-HVDC link co-located with an SVC could vastly improve the large-signal performance of the link. The authors show that modification of the LCC-HVDC link's VDCOL would allow much-improved damping of AC-side voltage magnitude oscillations and therefore power transfer; and that forcing the inverter into current control as opposed to extinction angle control during disturbances would also avoid AC-side voltage instability issues during low SCR operational scenarios. The proposed controller amendments were compared to the in-place methods via qualitative inspection of time domain responses during large disturbance applications, for only two system conditions chosen for their ability to demonstrate the proposed modifications.

There has been some previous work specifically investigating different types of plant that could be constructed alongside LCC-HVDC links in order to reduce issues associated with low SCR operation. One such paper is [26], which compares the following plant: mechanically switched shunt capacitor (MSC); thyristor switched shunt capacitor (TSC); thyristor controlled shunt reactor (TCR); AC-side series capacitor; and synchronous condenser. The authors of [26] also compared metal oxide varistors, however these could only be used to address transient over-voltage issues rather than completely addressing AC-side voltage magnitude sensitivity problems.

Studies in [26] utilised time domain responses from EMT time domain simulations to qualitatively compare different plant options. Many different disturbances were applied: three-phase and single-phase short circuit faults in both the rectifier and inverter AC systems; a DC circuit short circuit fault; and an LCC-HVDC link power transfer block. The authors of [26] only studied one SCR value of base case LCC-HVDC link, which

varied slightly depending on proposed plant options in a similar manner to [24]. The findings of [26] indicate that the different plant options varied in their speed of control of AC-side voltage magnitude, but all methods apart from the series capacitor could perform similarly when the LCC-HVDC link was recovering after application of short circuit faults. The authors stated that their LCC-HVDC link model was using current control rather than power control, and they expected that results for a constant power control mode would be different.

A similar work to [26] was carried out in [27]. In [27], the authors compared: an SVC incorporating a TSC and a TCR; a synchronous condenser; a base case using MSC only; and a combination of SVC and synchronous condenser together, each with the same rating. As in [26], comparisons in [27] are made via inspection of time domain responses from running EMT time domain simulations, but with some additional quantitative comparisons of metrics derived from inspection of those time domain responses. A similar set of disturbances—primarily short circuit faults—to those in [26], are used in [27]. Only one base case SCR is used as an operational scenario. It should be noted that [27] uses a different AC-DC model and LCC-HVDC link controller arrangement than that of [26], where the model chosen as the base case is a modified version of the model proposed in [28].

The authors of [27] found that an SVC could control transient over-voltages very quickly, but the effect of the TSCs within the SVC acted to worsen AC-side voltage magnitude sensitivity during large transients such as AC-side short circuit faults and thus led to successive commutation failures. These successive commutation failures could be avoided by manipulating the LCC-HVDC link inverter controller, but this would cause slower post-fault recovery and in fact was worse compared to the MSC base case. The synchronous condenser option helped with fast post-disturbance recovery for all disturbances considered. The authors found that the SVC and synchronous condenser combination performed the best of all options for the studied disturbances.

Reference [29] may be regarded as an extension of [27], with similar: base case model;

applied disturbances; and choice of simulation and analysis method. The original contribution of [29] is to compare the same base case and dynamic compensation options of [27] but with an additional STATCOM option. The authors of [29] found the STATCOM option to be superior to all of the other options when comparing post-fault recovery times.

More sophisticated qualitative treatment to compare a STATCOM, a synchronous condenser, and an MSC base case for assisting LCC-HVDC link operation during large disturbances in low SCR AC networks is given in [30]. This work may be regarded as a more specific and detailed subset of the work carried out in [29]: both the set of large signal disturbances and the network model used in [30] are similar to those in [29]. Again, results are generated using EMT time domain simulations. However the specific control architecture of the STATCOM in [30] is different from that used in [29]. Other slight modifications to the base case model are made, for example a VDCOL is added to the model in [30] which was not present in [29].

The qualitative methods used to assess the dynamic compensation options in [30] are different from the methods used in [29]; [30] uses both CFII and commutation failure probability index (CFPI) for comparison purposes. Note that CFPI is defined in [31] but is not referred to explicitly using the term CFPI in that work. The calculation of CFPI involves applying disturbances at different sampling points over one fundamental frequency voltage cycle and calculating the proportion of those observations from the sample which result in a commutation failure. Hence decreasing values of CFPI for an LCC-HVDC link in a particular operational scenario indicate increasing performance of that AC-DC system in avoiding LCC-HVDC link commutation failures. The results from [30] show that the STATCOM either performed similarly or superior to the synchronous condenser alternative when considering: CFII, CFPI; and, recovery times following large signal disturbances.

An even deeper comparison of a base case LCC-HVDC link, synchronous condensers, STATCOMs, and an equally-rated combination of STATCOMs and

synchronous condensers is performed in [32]. Similar to [30], the authors of [32] used EMT time domain simulations to provide raw results upon which values of CFII, post-disturbance recovery time, and CFPI were calculated and used for quantitative comparison of the dynamic compensation options. The underlying AC-DC system model in [32] is different from [30]. The disturbances applied were short circuit faults located at the inverter station busbars, applied through a fault inductance whose value was selected to approximate close-in or remote faults. Many time domain responses were also included to aid in qualitative assessment of the alternative options for post-disturbance recovery, showing AC-side voltage magnitude, measured LCC-HVDC link power transfer, and dynamic compensator reactive injection; in addition, results are shown for CFPI calculated for a range of different short circuit fault inductances.

The results of [32] indicate that the synchronous condensers option outperformed both the STATCOMs only and combined STATCOM and synchronous condenser options in terms of improving post-fault recovery time for relatively severe fault inductances; however all dynamic compensation options were similar for the least severe fault inductance. The combined synchronous condenser and STATCOM option outperformed the STATCOMs only option. All dynamic compensation options improved post-fault recovery for all faults compared to the base case LCC-HVDC link without dynamic compensation. CFPI values with respect to increasing fault severity were improved by: synchronous condensers only; combined synchronous condenser and STATCOM; and STATCOMs only; in order of least improvement to most improvement. All dynamic compensation options improved CFPI compared to the base case.

Reference [33] compares a unified power flow controller (UPFC), an SVC, and a STATCOM for improving CFII of an LCC-HVDC link. Comparisons were performed using results gained from EMT simulations. Consideration was given to: LCC-HVDC link inverter system SCR; compensation ratings; and, fault inductance. The UPFC was connected in series between the LCC-HVDC link inverter AC-side converter busbar and the AC system source impedance. Disturbances of short circuit faults were applied at the inverter AC-side converter busbar via application of a

fault inductance. The authors of [33] conclude that the UPFC vastly improved CFII compared to the SVC and STATCOM over all inverter AC system source impedances, all device ratings, all fault inductances, and over both single-phase and three-phase faults. The authors state that the STATCOM option outperformed the SVC option for three-phase faults, but were similar for single-phase faults.

The descriptive characteristics of [24–27, 29, 30, 32, 33] discussed above are summarised in Table 2.1.

2.2.2 Research Gaps in the Research Literature

It is clear from [24–27, 29, 30, 32, 33] that there exist many possibilities for addressing the steady-state and transient dynamic issues highlighted in [10, 15–20] in relation to the orderly operation of LCC-HVDC links in low SCR AC networks, especially when subjected to disturbances. However there exist some noticeable gaps in the body of work represented by [24–27, 29, 30, 32, 33].

A particularly important gap is the consideration of controller parameter values with respect to LCC-HVDC link performance. The authors in [24, 26, 27, 29, 30, 32, 33] do not directly address this issue by explicitly studying the variation of controller parameters when making their comparisons between dynamic compensation options. The importance of controllers and in particular their parameter value selection is obvious when considering the optimal use of available compensation.

Another gap in [24–27, 29, 30, 32] is the avoidance of studying the effects of multiple SCRs when considering options. Although authors do address this directly in [33] by investigating inverter system AC source impedance, this gap still represents a fruitful avenue of inquiry when considering dynamic compensation strategies.

References [26, 27, 29, 30] investigate different types of large signal disturbances such as three-phase versus single-phase faults; typically only two different fault locations are investigated in the form of close-in and remote faults where fault location is considered. Recent works [30, 32, 33] have attempted to address this gap by approximating fault

Chapter 2. Literature Review

location via applying faults at the inverter AC-side converter busbar through a fault inductance, where increasing value of fault inductance corresponds to increasing fault remoteness. The validity of this fault inductance approach is an open question. There remains a gap here to investigate actual short circuit faults located within the inverter AC network impedance rather than a fault inductance approximation, therefore achieving a closer approximation to practical AC-DC system behaviour.

References [24–27, 29, 30, 32] failed to consider the effect of dynamic compensation rating on assisting with LCC-HVDC link operation. This represents another gap and therefore an avenue of research to investigate the relationship between dynamic compensation technologies' performance differences with respect to device rating.

Another gap in [24–27, 29, 30, 32, 33] is the focus on qualitative comparisons of performance by inspection of time domain plots. Quantitative comparisons are included in more recent papers [27, 29, 30, 32, 33] in addition to qualitative comparisons. In [30, 32, 33], authors have somewhat converged on utilising performance functions such as CFII and CFPI to quantify and compare compensation options' relative performances. Similar to the consideration of SCR when comparing compensation approaches, there remains an avenue for further research in this area. A particular open question is if the multitude of alternative performance functions represent a smallest descriptive set of metrics for comparison between compensation methods. The quantification of the orderly operation of LCC-HVDC links is a pliable concept, yet it may be possible to use alternative performance functions which more directly quantify LCC-HVDC link orderly operation. Such potential performance functions would enable easier comparison between dynamic compensation methods.

All of the papers [24–27, 29, 30, 32, 33] focus on short circuit faults and therefore implicitly consider: the avoidance of commutation failures; the recovery from commutation failures; or, both commutation failure occurrence and recovery. As addressed by [15–19], poor dynamic operation of an LCC-HVDC link is a more general problem than the specific issue of commutation failure occurrence and recovery. There exists a potential gap in the

Table 2.1: Summary of reviewed papers in Section 2.2.

Considerations within the Papers	Relevant Papers
<i>Descriptive characteristics from Section 2.2.1</i>	
Control Loop Influence	[24, 25]
Synchronous Condenser	[24, 26, 27, 29, 30, 32]
SVC	[24, 25, 27, 29, 33]
MSC	TCR/TSC studied separately in [26]
Series Capacitor	[26]
SVC and Synchronous Condenser	[27, 29]
STATCOM	[29, 30, 32, 33]
STATCOM and Synchronous Condenser	[32]
UPFC	[33]
CFII	[30, 32, 33]
CFPI	[30, 32]
Recovery Time	[30, 32]
Set-point Changes	[26, 27, 29, 30, 32, 33]
<i>Characteristics related to research gaps from Section 2.2.2</i>	
Controller Parameter Variation	[25]
Many Explicit SCRs	[33]
Many Fault Locations	[24, 25, 32, 33]
Compensator Rating Variation	[33]
Focus on Qualitative Comparisons	[24–27, 29, 30, 32, 33]
Focus on Short Circuit Faults	[24–27, 29, 30, 32, 33]
Generalisable Contribution(s)	[24]

body of work represented by [24–27, 29, 30, 32, 33] where dynamic compensation could be compared in more general cases where measured variables such as LCC-HVDC link DC-side power transfer fail to correspond to ordered values for any reason brought on by external large or small disturbances. This general approach would also implicitly include both the negative behaviours of commutation failure occurrence and potentially poor commutation failure recoveries.

Lastly, a more general gap exists due to the relatively specific motivating examples used in [25–27, 29, 30, 32, 33], which renders the results from individual papers in this body of work somewhat hard to generalise to other AC-DC systems. Although constructing

a concrete study network and performing analysis on that network in such a way as to produce generalisable results is an extremely difficult task, there is the possibility of producing a generalisable methodology for performing comparisons. Practitioners and researchers alike could be presented with a general approach to be able to perform their own comparisons. In this case, the concrete results would be specific to those practitioners' and researchers' motivating problems yet the mechanism for deriving those results would be in common amongst the practitioners and researchers.

The characteristics of [24–27, 29, 30, 32, 33] linked with research gaps identified above are summarised in Table 2.1.

2.3 Outline of Simulation-Based Optimisation

Simulations performed using computer hardware have become integral to decision making within the engineering design process across many engineering domains [34]. These simulations are typically used to assess the performance of a system or design for a given set of parameters. The inverse problem of finding system parameters which give a specific value of system performance is extremely challenging. The related problem of trying to find system parameters which give an *optimal* system performance is typically addressed by mathematical optimisation. The term *simulation-based optimisation* refers to the case where the forward problem—determining system performance given a set of input system parameters—is a simulation which is used in conjunction with a mathematical optimisation solver method to optimise the inverse problem of finding optimal system parameters to give the best system performance. Alternative phrases include *simulation-optimisation* and *optimisation via simulation* [34].

Power systems contain many items of equipment which incorporate both plant parameters and control system parameters. In the case of LCC-HVDC link controllers, such parameters include: proportional-integral (PI) controller gains; and VDCOL parameters. The dynamic performance of an LCC-HVDC link is strongly affected by the value of these parameters when the LCC-HVDC link is subjected to disturbances and set-point

Chapter 2. Literature Review

changes. The value of these parameters must therefore be carefully selected in order to ensure satisfactory in-service dynamic performance of the LCC-HVDC link.

The choice of method used by engineers to select the values of these controller parameters is not trivial. Two examples of possible approaches to select these PI and VDCOL parameters are: optimal control techniques using linearised state-space models; or, manual tuning via trail-and-error of high fidelity simulations to find feasible parameter values. There are problems with the practicality of these methods: linearised models cannot explicitly model realistic non-linear behaviours such as short circuit faults; while manual tuning methods are inefficient with respect to engineers' time. Simulation-based optimisation represents a feasible alternative method for the selection of LCC-HVDC link controller parameter values whilst explicitly considering large-signal disturbances and non-linearities.

In the case of simulation-based optimisation for LCC-HVDC link controller parameter value selection, the simulation software may be EMT time domain simulation software such as Power Systems Computer Aided Design (PSCAD)/Electromagnetic Transients including DC (EMTDC) while the parameter values are viewed as optimisation problem variables within a mathematical program formulation. Since software such as PSCAD/EMTDC is used directly within the simulation-based optimisation, transient behaviour such as faults and switching events as well as LCC-HVDC plant and controller non-linearities can be explicitly considered within the optimisation process.

A typical strategy for simulation-based optimisation is as follows. The optimisation solver method—the algorithm used to solve a mathematical optimisation program—provides variable values to the underlying simulation software, which then runs a simulation with simulation parameters initialised with those variable values. The raw simulation output is then assessed using a merit function to return a scalar value back to the optimisation solver method, where this scalar value represents the objective function value. A typical solver method uses the variable values and their corresponding objective function value in conjunction with previous evaluated variable values and their corresponding objective

Chapter 2. Literature Review

function values to infer a new set of variable values to test via another simulation evaluation. This iterative process is repeated until solver method convergence conditions are met, where the solver method returns the specific variable values and their objective function value which correspond to the best found objective function value during the solution process.

The underlying simulation process is viewed as an expensive black-box objective function by the optimisation solver method. The simulation is *expensive* due to the substantial computational resources required to execute the simulation relative to the resources required by the optimisation solver method itself. High fidelity simulations such as those performed by PSCAD/EMTDC are an example of expensive simulations, since they will take more time to evaluate than the optimisation solver method's own software process [35].

The simulation is a *black-box* because it cannot be represented by an analytical function mapping simulation input variable values to objective function values [35, 36]. This black-box nature means that the optimisation solver method cannot make use of specific optimisation problem assumptions to aid in the selection of new variable values to evaluate at each solver method iteration. An example of an assumption which cannot be held for black-box functions is the provision of derivative functions of the objective function with respect to input variables. Consequently *black-box optimisation* is often considered to be in the same domain as *derivative-free optimisation* [35]. Black-box problems may also exhibit non-smooth behaviour as well as containing multiple local optima within the feasible region.

Derivative-free optimisation methods are often used to solve black-box problems since these methods typically: consider the whole feasible region and therefore handle multiple optima; and, do not assume smoothness [35]. Derivative-based methods are implied to be inferior to derivative-free methods in terms of computational resource requirements since derivative-based methods often estimate analytically unavailable derivatives by using many additional objective function evaluations; derivative-free optimisation methods do

not have this behaviour and so they are more suited to expensive black-box optimisation problems [35].

The difficult characteristics of black-box problems suggest the utility of feasible region sampling and/or stochastic methods for computing optimal solutions [36]. The difficult characteristics of expensive problems suggest that objective functions evaluations—*e.g.* high fidelity simulations—should be economised by focussing optimisation effort on finding near-optimal solutions within the evaluation budget rather than using a high proportion of the evaluation budget to try to refine solution optimality [36]. Although computing hardware has advanced in recent decades to allow more computations per unit of wall clock time, the hardware computational gains have typically been used to increase the fidelity of simulations [37]. This implies that the economy of expensive simulations when solving simulation-based optimisation problems is still a relevant research problem. This explains why derivative-free optimisation methods continue to be investigated due to their utility with respect to expensive simulation-based optimisation problems [35].

2.3.1 History of Derivative-Free Optimisation

Derivative-free optimisation methods have a mature history: both Hooke-Jeeves and Nelder-Mead methods date from the 1960s [35, 38] whilst the genetic algorithm was proposed in 1975 [38]. The field continues to see attention, and many advances have been made in the decades since the late 1990s [34–36]. The recency of these advances in theory and proposed methods imply the application of these advances in derivative-free optimisation to solve practical optimisation problems is potentially under-explored. An example of a particular area of recent advances is *surrogate-based* derivative-free optimisation methods [37, 38], also referred to as *meta-model-based* derivative-free optimisation methods [34].

There have been many derivative-free optimisation methods proposed in the literature [38] applied to many different types of motivating problems [35, Table 3]. The pedigree of the authors of [35] in the derivative-free optimisation and simulation-based optimisation domains combined with the relative lack of electrical engineering problems

compared to non-electrical engineering problems in [35, Table 3] imply that there is a lack of cross-over of derivative-free optimisation knowledge between engineering disciplines, and therefore a lack of appreciation in electrical engineering of the utility of derivative-free optimisation methods. In particular, the lack of examples of surrogate-based derivative-free optimisation motivating problems in the domain of “energy distribution/generation” [34, Table 2] combined with few electrical engineering problems in [35, Table 3] suggest that researchers within electrical power systems engineering in particular have not notably investigated the potential for surrogate-based derivative-free optimisation methods.

The wealth of characteristics and their combinations to describe derivative-free optimisation methods in [35, Table 3] indicates the abundance of different conceptual approaches for solving derivative-free optimisation problems, which is shown for example in the explanation of solver methods used in [38]—which is only a sample of derivative-free optimisation methods. No derivative-free optimisation method has been found which is generally applicable to black-box problems, and no method to analytically determine better derivative-free optimisation algorithms has been found [36]. Until [38], there had been little work to compare derivative-free optimisation methods on a test suite of problems. Both [36, 38] imply that the performance of derivative-free optimisation methods are heavily application-dependant which suggests that determining a method to use for simulation-based optimisation of LCC-HVDC link controller parameters via PSCAD/EMTDC simulations requires experimental effort to compare optimisation solver methods.

2.3.2 Classifications of Derivative-Free Optimisation Methods

The variety of derivative-free optimisation methods means that general ways of characterising methods are themselves variable and often only approximations. However a common set of orthogonal characteristics for classification of derivative-free optimisation methods [35, 38] are as follows.

1. Local or global;

Chapter 2. Literature Review

2. Direct search (*i.e.* non-surrogate) or surrogate-based; and
3. Deterministic or stochastic.

Local methods do not attempt to search the whole feasible region of the optimisation problem; therefore these methods tend to converge to a local optimum and terminate rather than exploring the feasible region to find a better optimum. Global methods do attempt to find a global optimum in the feasible region. Direct search methods evaluate the objective function directly: to determine the optimality of possible solutions; and, as part of finding an optimal solution. Surrogate-based methods fit a surrogate model to objective function values found via preceding objective function evaluations; this surrogate can then be evaluated at possible solutions as part of finding an optimal solution instead of frequently evaluating the actual objective function. Deterministic methods do not incorporate randomness into their solution algorithm whereas stochastic methods do. Many methods are hybrid methods, involving both classes in one or more of the above three classifications [35], *e.g.* methods which use local search methods to refine promising parts of the feasible region found via a preceding global method step.

2.3.3 Global Surrogate-Based Derivative-Free Optimisation Methods

A typical strategy for surrogate-based derivative-free optimisation is as follows [35].

1. Create an initial sample of points and their corresponding objective function values from the feasible region;
2. Fit a surrogate model to the known observations from the initial sample;
3. Optimise the fitted surrogate to find promising point(s) to evaluate next via the actual objective function;
4. Evaluate promising point(s) from the actual objective function;
5. Re-fit the surrogate model with new point(s) and their objective function value(s); and
6. Repeat Steps 3–5 until convergence criteria are met.

Chapter 2. Literature Review

Surrogate-based methods are very useful for expensive derivative-free optimisation problems because they allow economy of objective function evaluations to find near-optimal solutions quickly [35]. Global methods' most pertinent characteristic according to [37] is the simultaneous consideration of feasible region exploitation and exploration. The term *exploitation* refers to a global method's ability to investigate the neighbourhood of a currently known best found objective value in an attempt to find a more optimal solution. The term *exploration* refers to a global method's consideration of parts of the feasible region which are far away from a current optimal point with the aim of discovering other parts of the feasible region which may contain superior optima. Surrogate-based methods are therefore dependent on the following [35].

1. Type of surrogate model;
2. Method to fit the surrogate model to observations;
3. Method to find suspected optimal points from the fitted surrogate model; and
4. Method of scoring optimal points from the surrogate with respect to objective function favourability, considering exploitation and exploration.

In addition, surrogate-based methods are dependent on the initial sample upon which the surrogate is initially fitted. The initial sample is typically determined via a *design of experiment* method [34]. Methods for the design of experiments are themselves an active research area [36], and the selection of a specific design of experiment and a surrogate model both interact together to affect the best-fitting surrogate model approximation of objective function black-boxes [36].

2.4 Research Literature on Power System Engineering Applications of Simulation-Based Optimisation

2.4.1 Description of the Research Literature

In the specific domain of electrical power systems engineering, simulation-based optimisation is an accepted method and has been in use within software packages for power system studies since at least the late 1990s [39]. In [39], simulation-based optimisation is introduced as a new feature within the simulation program Network Torsion Machine Control (NETOMAC) and demonstrated via four example problems.

The specific case of simulation-based optimisation in PSCAD is demonstrated in [40] which was then expanded upon in [41]. In [40], two example problems are discussed: DC-DC converter PI controller tuning; and, the tuning of an LCC-HVDC link with three PI controllers. Similarly, in [41] two problems are explored. The first problem is the optimisation of switching angles of a three-level VSC. The second problem may be considered an extension of the DC-DC converter problem in [40], where [41] considers selection of plant values and the converter's switching frequency in addition to PI controller gains. In [42], the problem of optimising the PI controller gains and VDCOL parameters of an LCC-HVDC link is considered; this problem may be viewed as an extension of the PI controller tuning problem in [40]. A simulation-based optimisation algorithm is proposed in [43] and is demonstrated on an example problem of tuning PI controller gains of a VSC-HVDC link.

A strategy built upon simulation-based optimisation is proposed in [44] to determine the location, size, and type of voltage compensation devices to be installed in an example network to optimise steady-state and dynamic voltage objectives, using Power System Analysis Toolbox (PSAT) as simulation software. In [45] a control architecture for MMC-HVDC links is proposed based upon a combination of sliding mode and model predictive control. The proposed architecture is compared to PI control and synergetic control. All three control strategies have their controller parameters optimised via

Chapter 2. Literature Review

simulation-based optimisation, with the proposed architecture with optimised parameters performing well in test cases compared to the other two architectures with their own optimised parameters.

A wide-area oscillation damping controller is proposed in [46] for use with doubly-fed induction generator (DFIG) wind turbines to damp inter-area electromechanical oscillations. A conventional method is used to select controller parameter values which are used as initial observations from which a simulation-based optimisation is used to improve the parameter values. Inter-area generator speed deviations were found to settle faster when using optimised parameters compared to parameter values determined via the conventional method.

Neutral reactor architectures and inductances are investigated in [47] to minimise secondary arc currents in multi-circuit overhead line tower arrangements due to coupling effects of the circuits. Simulation-based optimisation is employed to calculate optimal reactor inductance values for different neutral reactor arrangements in order to reduce secondary arc currents in all tower circuits; this therefore constituted a multi-objective optimisation. The optimal inductances are shown using a detailed arc model to be superior to analytically calculated values, demonstrating the utility of the simulation-based optimisation approach.

From inspecting [40–47], objective functions based upon time integrals of functions of error between ordered and measured quantities are common. In particular in [40–43, 45], objective functions made from sums of weighted ISE terms are common where weighting strategies are used to: encourage differential penalisation of error in different parts of time domain responses as in [40, 42]; or, combine together ISE terms of different types of errors between ordered and measured quantities as in [41, 43, 45]. In [44, 46] weighted sums of integral absolute error (IAE) terms over time between ordered and measured quantities constitute the objective functions, and in [47] a root mean square (RMS) over time strategy is used to calculate multiple objective functions.

Another common characteristic seen in [40–42, 46] is the choice of the Nelder-Mead

simplex method [48] to solve the simulation-based optimisation problems. In [44, 45, 47] nature-inspired algorithms are used as optimisation solver methods instead: specifically, genetic algorithm methods in [44, 47] and a particle swarm method in [45].

The complexity of simulation behaviour captured by objective functions in [40–47] is clear. The simulation-based optimisation problems in these works consider: large-transient disturbances in [40, 42, 44, 46, 47] such as short circuit faults; large set-point changes in [40, 42, 43, 45]; small-signal set-point changes in [44, 45]; and small-signal disturbances in [42–44] such as load or system voltage perturbations. In addition, the simulation-based optimisation problems in [42] are performed considering the effect of optimisation variables across two system operational scenarios with differing ESCR. Simulation-based optimisation allows engineers to consider complicated non-linear, non-smooth, and discontinuous relationships between optimisation variables and objective function values whilst allowing relative flexibility in writing software functions which return objective function values for simulation data such as time domain responses.

The descriptive characteristics of [40–47] discussed above are summarised in Table 2.2.

2.4.2 Research Gaps in the Research Literature

It is clear from [39–47] that solving power systems engineering problems by casting them as simulation-based optimisation problems is a mature practice, and provides useful results. The works in [40–43, 45] show that objective functions formed from ISE over time between ordered and measured quantities are valid targets for simulation-based optimisation, while [40–43, 45, 46] demonstrate the validity of simulation-based optimisation to choose controller parameter values to optimise time domain responses of power system plant. Furthermore, performing simulation-based optimisation using PSCAD/EMTDC simulations specifically is shown to be a successful approach in [40–43, 45–47].

There are notable gaps in [40–47] with respect to the topic of simulation-based optimisation. In [40–42, 45–47], authors do not discuss the influence of optimisation

Table 2.2: Summary of reviewed papers in Section 2.4.

Considerations within the Papers	Relevant Papers
<i>Descriptive characteristics from Section 2.4.1</i>	
PSCAD/EMTDC	[40–43, 45–47]
LCC-HVDC	[40, 42]
VSC-HVDC	[41, 43, 45]
PI Controller Tuning	[40–43, 45]
Controller Tuning	[40–43, 45, 46]
Plant Parameter Selection	[41, 44, 47]
ISE-based Objective	[40–43, 45]
Weighting in Objectives	[40–46]
IAE-based Objective	[44, 46]
RMS-based Objective	[47]
Nelder-Mead Simplex Solver Method	[40–42, 46]
Nature-inspired Solver Method	[44, 45, 47]
Large Transient Disturbances	[40, 42, 44, 46, 47]
Large Set-point Changes	[40–44]
<i>Characteristics related to research gaps from Section 2.4.2</i>	
Solver Method Characteristics	[43, 44]
Surrogate-based Solver Method	[43]
Solver Method Initialisation	[43]
Box Constraints	[43]

solver methods’ characteristics with respect to how those characteristics could influence the solution process and solution quality. Only in [44] do authors consider the influence of their genetic algorithm method’s stochastic nature by investigating the convergence and optimal solutions of an additional six independent solution runs. Note that [43] does consider solver method characteristics, which is to be expected since the contribution of [43] is a solver method itself.

Authors of [40–42, 44–47] chose mature optimisation solver methods—Nelder-Mead simplex, genetic algorithms, and particle swarm—to solve their optimisation problems. However these methods do not consider the potential of surrogate-based optimisation methods—only [43] considers surrogates as part of its proposed method. In addition, the authors of [40–42, 44–47] do not highlight the importance of initial optimisation starting

points, *e.g.* initial simplex position in Nelder-Mead or initial population positions in the nature-inspired algorithms; nor do these papers highlight the influence of box constraints or lack thereof on optimisation variables.

Therefore, recent surrogate-based global optimisation methods should be investigated for their utility in power systems engineering simulation-based optimisation problems; particularly with respect to mature solver methods. Furthermore, the effect of initial conditions and solver method stochasticity should be properly considered in this investigation. The characteristics of [40–47] linked with research gaps identified above are summarised in Table 2.2.

2.5 Considerations for Simulation-Based Optimisation Solver Method Evaluation

Section 2.3 highlights the use of derivative-free optimisation on computationally expensive simulation-based optimisation problems to find near-optimal solutions within few objective function evaluations. Section 2.3.1 mentions that the performance of different derivative-free optimisation methods to solve specific simulation-based optimisation problems is heavily problem-dependent. Hence it is important to carefully select derivative-free methods to solve simulation-based optimisation problems [38], such as LCC-HVDC link PI controller tuning using EMT time domain simulations.

An informative approach for evaluating derivative-free optimisation methods is taken in [38]. Stochastic methods studied in [38] required the authors to specify an initial starting point. The authors randomly sampled ten different initial starting points for each test problem assuming uniform distributions for the problem variables. Solver methods were initialised from these different starting points thus giving solver methods ten independent attempts to find an optimum point in the feasible region; each attempt was initialised on each one of the ten initial points, and each attempt was run independently of all the other nine attempts.

Chapter 2. Literature Review

In order to evaluate solver methods with respect to each other, the authors in [38] used two benchmark solver methods to solve all test problems and then used those benchmark solutions as the global solutions to which all tested solver methods' solutions were compared. This approach allowed fair comparison of solver methods to a common base-line of global solutions. To evaluate solution qualities of the tested solver methods from the sample of ten optimal solutions generated one-each from the ten randomly sampled starting points, the work in [38] used two sample statistics to give point statistic values calculated from the samples: best found, *i.e.* a sample maximum or sample minimum depending on the test problem being a maximisation or minimisation; and, sample median.

Reference [38] provides experimental evidence for the claim in [36] that increasing the number of variables in the optimisation problem substantially degrades solver methods' ability to converge to optima. Further, the results in [38] demonstrate that no single solver method dominated the other solver methods across the tested problems, which provides evidence for the strong interaction between derivative-free method choice and the specifics of the optimisation problem. This aligns with [36] which states that derivative-free optimisation methods are often designed to be applied to specific black-box optimisation problems.

It is clear from [35, 36, 38] that there exist many new derivative-free optimisation methods since the Nelder-Mead and genetic algorithm methods were originally proposed, yet PSCAD/EMTDC version 4.6.3 only includes Nelder-Mead and a genetic algorithm for multivariate simulation-based optimisation. Hence there exists a research problem in investigating new derivative-free optimisation methods for their utility in solving LCC-HVDC link controller tuning problems using PSCAD/EMTDC simulations especially when compared to the Nelder-Mead and genetic algorithm methods.

In consideration of both [36, 38], it is also clear that the only approach to diligently choose a derivative-free optimisation method to solve LCC-HVDC link controller tuning problems using PSCAD/EMTDC simulations is to investigate a set of candidate solver

methods experimentally by testing them on actual LCC-HVDC link controller tuning problems and comparing the empirical results. This is because: no comparable work has been observed in the power systems engineering literature; and, the reciprocal interaction between optimisation problem and solver method is so pertinent that inferring a good choice of solver method from other test problems or motivating problems from the research literature is not feasible.

2.6 Summary

This chapter introduced the LCC-HVDC link: the typical arrangement of plant, the MCCM strategy, and the steady-state voltage-current characteristic of a typical MCCM controlled LCC-HVDC link. The specific issue of AC-side voltage waveform sensitivity and its influence on the orderly operation of LCC-HVDC link was then reviewed.

Research literature on methods to alleviate poor sensitivity of AC-side voltage waveform and the corresponding negative influence on LCC-HVDC link dynamic performance has been reviewed. Most of the prior works focus upon different types of dynamic compensators and/or controller modifications to LCC-HVDC links. The gaps in the research literature are identified as follows: the influence of controller tuning, multiple potential SCR operational scenarios, fault modelling choice, and different compensator ratings, are all possible issues to explore. Furthermore, the conceptual re-framing of the specific problem of commutation failure occurrence due to poor AC-side voltage sensitivity towards a more generalisable methodological problem of investigation of poor LCC-HVDC link dynamic performance has also been highlighted.

Simulation-based optimisation was introduced, particularly with respect to expensive black-box simulations. Derivative-free solver methods and their characteristics were also given a brief overview. The use of simulation-based optimisation in power systems engineering research specifically was reviewed, with the research gaps of insufficient treatment of solver method behaviour, strategies, and initial conditions highlighted. Important considerations have been found in the research literature on how derivative-free

Chapter 2. Literature Review

optimisation solver methods may be evaluated. Solver method performance is typically problem-dependent, and therefore their performance evaluation on a specific optimisation problem can only effectively be done via experimental use of the solver methods on the actual optimisation problem at hand. This approach allows solver method superiority to be determined and a solver method definitively selected for the optimisation problem under study.

Chapter 3

Evaluation of Simulation-based Optimisation Solver Methods for LCC-HVDC Link Controller Parameter Selection

This chapter proposes a method to evaluate two optimisation solver methods using surrogate models to solve box-constrained LCC-HVDC link controller tuning problems. The motivating optimisation problem on which the solver methods are tested is the selection of PI controller gains and VDCOL parameters of an LCC-HVDC link, subject to two operational scenarios and a set of large-signal set-point changes and disturbances.

These surrogate-based solver methods are evaluated via statistical comparison with two other solver methods which use mature non-surrogate strategies. These mature solver methods are very similar to optimisation solver methods which are included with PSCAD/EMTDC version 4.6.3. The evaluation is made by testing for statistically significant differences in the sample means of optimal solutions returned by all four solver methods.

The two evaluated surrogate-based solver methods proposed in the research literature performed either similarly to or significantly better than the solver methods using mature strategies. This confirms the suitability of these surrogate model solver methods for simulation-based optimisation of LCC-HVDC link controllers.

3.1 Description of Investigated Solver Methods

Four black-box derivative-free optimisation solver methods are selected for evaluation with respect to each other on solving a simulation-based optimisation problem of tuning the controllers of an LCC-HVDC link via PSCAD/EMTDC simulations. These four solver methods shall be referred to hereafter as:

1. Solver Method MARS
2. Solver Method GPR
3. Solver Method NM
4. Solver Method GA

Solver Methods MARS and GPR are stochastic surrogate-based global optimisation methods. Solver Methods NM and GA are stochastic direct-search global optimisation methods. All four solver methods were initialised by a symmetric Latin hypercube space-filling experimental design. All four solver methods had a termination condition of objective function evaluation budget: the solver methods kept iterating until a specific number of objective function evaluations had been undertaken. In addition, Solver Methods MARS, GPR, and NM could use restarts to use up any remaining evaluation budget if those solver methods' iterations converged early before all of the evaluation budget had been spent.

For brevity, all descriptions and pseudocode algorithms for solver methods have been written to implicitly consider feasible intervals of optimisation variables to be equal to the unit interval, with both boundary enforcement and transformation between the unit interval and the actual feasible intervals of the problem variables being implied.

Although the variables studied within this thesis have feasible intervals outwith the unit interval, all solver method algorithms performed conversions to map variable bounds and variable values to proportionally fall within the unit interval which the solver methods used internally. The solver method internal variable values were mapped back to the problem variables' feasible intervals for evaluation via the objective function.

The symmetric Latin hypercube experimental design will be explained initially, followed by a description of each of the four investigated solver methods.

3.1.1 Symmetric Latin Hypercube Experimental Design

All four solver methods used a symmetric Latin hypercube design (SLHD) [49] of points to initially explore the objective function's feasible region delineated by the problem box constraint bounds. Each point in the SLHD represented a specific combination of optimisation problem variable values where a point had a number of dimensions equal to the number of optimisation variables within the problem. Each element in the point mapped to a scalar-valued optimisation problem variable which would be used to initialise scalar-valued parameters within the underlying PSCAD/EMTDC simulations which constituted the objective function.

An SLHD of points would be evaluated before any solver method iterations occurred. The points in a particular experimental design were all generated at the same time by an SLHD algorithm. The SLHD has an important property from the perspective of global optimisation: the points within the SLHD are generally assumed to be spread evenly throughout the feasible region. This space-filling characteristic ensures good economy of simulation evaluations: for a specific number of points, the SLHD algorithm ensures that the points are spread out within the feasible region. The amount of information about the objective function over the feasible region is therefore maximised for the given number of points within the design, after evaluation of the design's points.

The economy of the SLHD ensured that the proportion of the experimental budget used outwith solver method iterations maximised the initial exploration of the feasible region

of the objective function. This ensured that the solver methods had good coverage of the feasible region from which to start iterations given the initial data from the experimental design.

The pseudocode algorithm used for generating SLHDs is shown in Algorithm 1 in Section A.1 within Appendix A. The pseudocode in Algorithm 1 is a translation of the SLHD construction method implemented as a function in the `pySOT` library [50]. Note that the implementation for SLHD construction in `pySOT` library [50] used in this thesis—and detailed in Algorithm 1—does not select an optimal SLHD as discussed in [49]; only feasible SLHDs are constructed. The authors in [49] recommend that practitioners should focus upon a method for selecting a good enough design with reasonable computational effort rather than an optimal design; this implies that the lack of optimality of a particular SLHD is not a pressing issue.

The algorithm in Algorithm 1 may be summarised as follows.

1. The engineer specifies that an experimental design must be generated with N points where each point has D dimensions and each dimension corresponds to a scalar-valued variable in the optimisation problem.
2. A matrix of N rows and D columns is generated, where the value of each element is initially an integer within the interval $[1, N]$. Each row indicates a specific design point \mathbf{x} ; and, there exists a point which is a reflection of \mathbf{x} through the design centre.
3. The elements in the generated matrix are then divided by N to ensure that all element values are within the interval $[0, 1]$, *i.e.* each point is therefore within the unit hypercube.
4. Lastly, a rank check is performed to ensure that the generated matrix's rank is sufficiently high. If the rank is too low, a new matrix is generated via the method previously described and its rank is checked.
5. Matrices are generated until a matrix of sufficient rank is found, which is then

returned as the SLHD matrix containing the points to be evaluated via the objective function.

3.1.2 Solver Method GA

Solver Method GA was built upon a genetic algorithm (GA) strategy to solve optimisation problems. The GA is a mature framework of methods for solving optimisation problems. GAs can take many specific forms, with different design choices within the overall algorithm giving rise to a specific GA implementation with particular qualities. The typical GA relies upon a *population* of points. This population is evaluated during a *generation* to determine the corresponding objective function values of these points. Once the population's objective function values are known, a set of *operators* are used to create a new population of points to be evaluated in the next generation. The new population's point values are dependent on the operators' interpretation of point values and the associated objective function values of the preceding population.

In this thesis, a real-coded GA is used as mature solver method for solving an expensive black-box optimisation problem; the implementation used is a modification of a specific GA included in `pySOT` [50]. The unmodified GA from `pySOT` uses a similar although not identical collection of strategies as the GA proposed in [51], specifically: tournament *selection*; uniform arithmetical *crossover*; and non-uniform *mutation* operators. The GA proposed in [51] uses a more complex *replacement* strategy than the method used in this thesis which is only an elitist strategy. The elitist strategy employed within this thesis' GA implementation takes the best found point from the previous population generation and retains it into the next generation. In addition, the elitist replacement is performed before the evaluation of the current generation's points, not afterwards as in [51]. Lastly, the non-uniform mutation operator in this thesis uses a perturbation distributed according to a normal distribution rather than the more complex mutation operator used in [51].

The selection operator preferentially selects points from the current population based upon their objective function values into a temporary intermediate population; the

intermediate population is then used as a basis for the next population. Points which have very good objective function values will tend to be selected over worse points, and it is possible for duplicates of points to be made where the total number of duplicates taken is related to relative superiority of the duplicated points' objective function values.

A crossover operator is then applied to the points in the intermediate population. This crossover operator mixes the variable values of pairs of points in the intermediate population to produce new points to be taken forward to the next population. Not all points are necessarily crossed. The resulting population still has the same number of points and same number of dimensions per point as the original population.

The mutation operator applies perturbations to the post-crossover population. Finally, an elitist strategy replaces the first point in the post-mutation, post-crossover, post-selection population with the best known point so far, which ensures that the best known point is retained over all solver method generation iterations. Note that this point is not repeatedly evaluated via the expensive objective function in successive generations, since the objective value is already known and repeatedly evaluating this point would waste objective function evaluations from the evaluation budget. After the elite point replacement is made, the new population of points has now finally been created and can now be evaluated via the objective function. After this, another generation occurs with selection, crossover, mutation, and elite replacement. This process iterates for many generations until the solver method termination criterion is met.

The GA assumes that its initial population of points is initialized via an initial sampling of the objective function: an SLHD as described in Section 3.1.1 is used for this initial sampling. The modifications made to the GA included in `pySOT` as part of the work in this thesis are to allow termination of the algorithm depending on expensive objective function evaluations reaching a user-specific evaluation budget.

Given the above operator explanations, the GA used in this thesis is a global method, using direct search to evaluate points for their objective function values, and is inherently stochastic due to probabilistic mechanisms in the initial SLHD and the selection, crossover,

and mutation operators.

Unlike the solver method implementations Solver Methods NM, MARS, and GPR detailed in Section 3.1.3, Section 3.1.5, and Section 3.1.6 respectively, the GA implementation in this thesis did not depend on restarts. Hence only one SLHD was created and evaluated to fill the population once, and from then on the GA would iterate through generations until the objective function evaluation budget had been reached. At this point, the GA method would report the best found objective function value and the corresponding best found point from the entire expended evaluation budget to the user.

The modified GA method used in this thesis is explained with pseudocode in Algorithm 2 in Section A.2 within Appendix A, and the specific user-specified parameter values used in this thesis are given in Table 3.1.

Table 3.1: Parameters used by Solver Method GA.

Name	Symbol	Value
Experimental design points	n_0	22
Tournament size	T_s	5
Crossover probability	P_c	0.9
Perturbation standard deviation	σ_p	0.2

The pseudocode in Algorithm 2 will now be explained.

1. An initial SLHD of points is created, and all points are evaluated to fill out an initial population.
2. The GA then enters a loop, which repeats until the number of objective function evaluations has reached a user-specified evaluation budget.
3. Within the loop, the tournament selection operator is used to pick promising points for inclusion in the next population to be evaluated.
4. The tournament selection draws a sub-sample of points randomly with replacement from the population, and then selects the point from the sub-sample which has the best objective function value.

5. This selected point is added to the intermediate population. All points in the intermediate population are set as a result of this tournament being applied repeatedly to the existing population. Hence, it is possible for multiple duplicates of better points to appear in the intermediate population, with better points occurring more often.
6. The crossover operator is then applied to the intermediate population, mixing pairs of points together to produce new pairs of points using a crossover probability and random mixing proportions. Some points are not mixed depending the crossover probability.
7. The mutation operator then adds perturbations sampled from a normal distribution to each of the post-crossover points in the intermediate population; perturbations are added to points depending on a mutation probability which is itself dependant on the number of dimensions of the points, *i.e.* the number of scalar-valued input variables to the objective function.
8. The best found point so far is inserted into the intermediate population in-place of the first point, finally giving the new population to evaluate.
9. The new population is then evaluated via the objective function, thus starting a new generation and the loop repeats.
10. When the loop—which started at Step 2 above—finally ends due to the evaluation budget being reached, the GA then returns the best found point and its objective function value back to the user.

3.1.3 Solver Method NM

Solver Method NM was built upon the Nelder-Mead simplex which is a mature method for solving black-box optimisation problems, originally proposed in [48]. In this thesis, a modified version of the Nelder-Mead simplex implementation included in `scipy` [52] is used.

Nelder-Mead simplex relies on a *simplex* of points and their corresponding objective function values, upon which a set of rules are applied to create new points to evaluate and modify the simplex. A simplex is a collection of points; the number of points in the simplex is equal to one plus the number of dimensions in the points. Nelder-Mead simplex is therefore strongly dependent on the choice of points which are used to initially fill the simplex, and is also dependent on the choice of convergence criteria to stop the algorithm and return an optimal solution. In its typical form, Nelder-Mead simplex is a local method, and relies upon direct search of the objective function to evaluate points. It is also a deterministic algorithm as there are no stochastic elements in its algorithm.

The modifications made to create the specific implementation used in this thesis were: to allow termination depending on expensive objective function evaluation budget; and, to allow restarting to use up any remaining evaluation budget if convergence of the simplex caused the Nelder-Mead simplex iterations to terminate early with unspent evaluation budget.

The method in this thesis relied upon an initial SLHD of points—explained in Section 3.1.1—to sample the feasible region of the objective function. These experimental design points were then evaluated, and the best subset of points depending on their objective function value were then selected to construct the initial simplex from which the Nelder-Mead simplex method started iterations. During restarts, all previously evaluated points would be forgotten from the perspective of the algorithm, a new SLHD of points would be created and then evaluated, a new simplex chosen, and then the Nelder-Mead simplex iterations would start from this new sample but with a reduced evaluation budget due to all the evaluations performed before the restart and the new SLHD evaluations. This process ensured that all of the user-specified evaluation budget was used. If a restart occurred with insufficient remaining evaluation budget to fully evaluate a new experimental design, then the Nelder-Mead simplex was restarted with the best found point so far with the initial simplex formed using the original simplex generation rules used in the Nelder-Mead simplex method provided in `scipy`.

The choice of performing an initial SLHD therefore transformed the specific Nelder-Mead simplex algorithm used in this thesis from a local and deterministic method to a global and stochastic method: global because the SLHD explored the entire feasible region and therefore the initial simplex was dependent on this; and, stochastic since the SLHD method is itself stochastic.

$$\mathbf{y}_i = \arcsin \left(2 \cdot \frac{\mathbf{x}_i - \mathbf{X}_i^{\text{LB}}}{\mathbf{X}_i^{\text{UB}} - \mathbf{X}_i^{\text{LB}}} - 1 \right) \quad (3.1)$$

$$\mathbf{x}_i = \frac{\mathbf{X}_i^{\text{UB}} - \mathbf{X}_i^{\text{LB}}}{2} (\sin(\mathbf{y}_i) + 1) + \mathbf{X}_i^{\text{LB}} \quad (3.2)$$

The Nelder-Mead simplex method is also typically an unconstrained method. In order to solve box-constrained optimisation problems, a non-linear variable transformation method was used to transform box-constrained variables to a set of unconstrained auxiliary variables used internally within the Nelder-Mead simplex iterations. Each proposed point from the Nelder-Mead simplex iterations would then be transformed from the auxiliary variables back to the box-constrained variables for evaluation in the objective function. The i -th box-constrained variable \mathbf{x}_i with upper bound \mathbf{X}_i^{UB} and lower bound \mathbf{X}_i^{LB} would be transformed to the unconstrained auxiliary variable \mathbf{y}_i by the transformation in (3.1); and transformed back from \mathbf{y}_i to \mathbf{x}_i by the transformation in (3.2). Note that both \mathbf{x}_i and \mathbf{y}_i are scalar-valued and correspond to scalar-valued input variables in the objective function. Therefore (3.1) and (3.2) would be applied separately to each dimension value within each point in the simplex to transform a box-constrained point to and from the corresponding unconstrained auxiliary point used internally within Nelder-Mead simplex.

These modifications resulted in a global, stochastic, and box-constrained method with an overall termination condition based upon objective function evaluation budget met via possible restarts, which allowed fair comparison with the other three solver methods investigated in this thesis since those other methods were also global, stochastic, and box-constrained. In addition, this fair comparison also acts to strengthen the potential

capability of Nelder-Mead simplex when given access to restarts and experimental designs, *i.e.* the best performance of Nelder-Mead simplex iterative method can be achieved given analogous characteristics to the other tested solver methods.

The high-level pseudocode which explains the specific Nelder-Mead simplex method used in this thesis is given in Algorithm 3 in Section A.3 within Appendix A, and the user-specified parameter values used in the method are given in Table 3.2.

Table 3.2: Parameters used by Solver Method NM.

Name	Symbol	Value
Experimental design points	n_0	22
Simplex perturbation coefficient	Δ	0.05
Simplex perturbation constant	θ	0.00025
Simplex convergence tolerance	F_{tol}	0.01
Reflection coefficient	ρ	1
Expansion coefficient	ν	2
Contraction coefficient	ψ	0.5
Shrink coefficient	σ_c	0.5

The algorithm in Algorithm 3 shall now be described as follows.

1. A loop starts, which only terminates when the evaluation budget has been reached.
2. In this loop, an initial SLHD of points is created and evaluated via the objective function if there is sufficient evaluation budget to do so.
3. The best points are selected from these experimental design points and used to construct the initial simplex. If there is an insufficient evaluation budget, a simplex is constructed using the simplex generation steps used in the original `scipy` Nelder-Mead simplex method. This approach uses an initial point around which the rest of the simplex is constructed; the initial point used is the best point found so far from all evaluations since and including the most recent experimental design. This simplex is then evaluated to get the corresponding objective function values.
4. Another loop embedded within the initial loop at Step 1 now starts, which repeats

Chapter 3. Evaluation of Simulation-based Optimisation Solver Methods for LCC-HVDC Link Controller Parameter Selection

until a convergence criterion is met; the criterion is if the simplex objective function values are all within a certain distance from the best found objective function value, *i.e.* the simplex points' objective function values are all sufficiently close to each other.

5. Within this embedded loop, the points within the simplex are then sorted from best to worst objective function values.
6. The centroid of all of the points except the worst point is then calculated.
7. A reflected point is calculated depending on the centroid and the worst point, and then the reflected point is evaluated.
8. If the reflected point's objective function value is better than the rest of the points in the simplex, another point called the expansion point is calculated depending on the centroid and the worst point in the simplex, and it is then evaluated.
9. If the expansion point is better than the reflected point, then the worst point in the simplex is replaced with the expansion point, otherwise the worst simplex point is replaced with the reflection point.
10. At this stage, the best found simplex point so far is noted, and the embedded loop which started at Step 4 iterates.
11. The actions below are only taken if the reflection point is worse than or equal to the best point in the simplex.
12. If the reflection point is better than the second-worst point in the simplex, then the worst simplex point is replaced with the reflection point, the best found simplex point so far is noted, and the embedded loop started at Step 4 iterates.
13. If the reflection point is worse than or equal to both the best point and second-worst point in the simplex, yet better than the worst point in the simplex: a contraction point is calculated depending upon the centroid and worst point in the simplex, and then it is evaluated. If this contraction point is better than or equal to the

reflection point, then the worst point in the simplex is replaced with the contraction point, the best found simplex point so far is noted, and the embedded loop started at Step 4 iterates; otherwise, a simplex shrink will be performed.

14. If the reflection point is worse than or equal to the best, second-worst, and worst points in the simplex: an inside contraction point is calculated which depends on the centroid and worst point. This inside contraction point is then evaluated: if it is better than the worst point in the simplex, then the worst point is replaced by the inside contraction point, the best found simplex point so far is noted, and the embedded loop started at Step 4 iterates. Otherwise, a simplex shrink operation will be performed.
15. If a shrink operation is to be performed, the simplex points aside from the best point are all drawn closer to the best point's location; and the new points—aside from the best point since it is unchanged—are evaluated. Then the best found simplex point so far is noted, and the embedded loop started at Step 4 iterates.
16. Lastly, the outer loop which started at Step 1 which checks for complete evaluation budget expenditure also iterates.
17. The algorithm can stop within the Nelder-Mead simplex iterations if it reaches the evaluation budget, at which point the best found point over all of the evaluations since the start of the optimisation problem solution process and its objective function value are returned to the user.

3.1.4 DYCORS

The dynamic coordinate search using response surface models (DYCORS) framework is proposed in [53]. The implementation of the DYCORS framework used in this thesis is in pySOT [50].

DYCORS is an algorithm which uses a user-specified surrogate model to optimise expensive black-box objective functions. The algorithm assumes that initial objective function evaluations have been performed and a user-specified surrogate model has been

fitted to those initial evaluations. DYCORS is a global and stochastic method due to its internal design, and is a surrogate-based method.

A high-level pseudocode algorithm explaining the implementation in `pySOT` [50] as used in this thesis is included here as Algorithm 4 in Section A.4 within Appendix A. The user-specified parameter values used in this thesis are given in Table 3.3, where the parameter D is the number of optimisation problem variables.

Table 3.3: Parameters used by DYCORS for both Solver Methods MARS and GPR.

Name	Symbol	Value
Experimental design points	n_0	22
Perturbation standard deviation, initial	σ_{init}	0.2
Perturbation standard deviation, maximum	σ_{max}	0.2
Perturbation standard deviation, minimum	σ_{min}	0.005
Success limit	F_{succ}	3
Failure limit	F_{fail}	$\max(5, D)$
Candidate points	N_{cand}	$100 \cdot D$
Success tolerance	δ	0.001
Exploration-exploitation weight set	\mathcal{W}	$\{0.3, 0.5, 0.8, 0.95\}$

DYCORS starts with a user-specified experimental design—an SLHD is used in this thesis which is explained in Section 3.1.1. These initial variable values from the initial SLHD and their corresponding objective function values are used to fit a surrogate model. In this thesis, two separate surrogate models are tested in conjunction with DYCORS to give two specific optimisation solver methods; the two surrogates are multivariate adaptive regression splines (MARS) and Gaussian process regression (GPR) which are further explained in Section 3.1.5 and Section 3.1.6 respectively. DYCORS is independent of the specific methods used to: choose initial objective function evaluations; and to create a surrogate model to approximate the objective function. DYCORS simply uses the surrogate model as a cheap approximation of the expensive objective function to use in finding a new point to evaluate via the expensive objective function.

The DYCORS algorithm will now be explained.

1. Given a set of initial points and their objective function values from an evaluated

experimental design and an initial surrogate fitted to those points and their objective function values, DYCORDS enters a loop which repeats until a termination condition of sufficiently small perturbation standard deviation is reached.

2. At the start of the loop, a set of candidate points are generated where each candidate point is initially set equal to the best found point observed from the experimental design.
3. A perturbation probability is calculated which depends in the number of objective function evaluations performed so far out of the total evaluation budget but excluding the experimental design evaluations from the first experimental design. However evaluations from any subsequent experimental designs—*e.g.* after solver method restarts—are considered in the perturbation probability calculation.
4. For each dimension coordinate in each candidate point, a perturbation sampled from a normally distributed random variable is added to the dimension coordinate value depending on the perturbation probability; the normal distribution is controlled by the perturbation standard deviation parameter value.
5. Each candidate point is scored based on a weighted combination of: its value returned by evaluating the point on the fitted surrogate; and, its distance to any other points already evaluated in the expensive objective function. The weighting is dependant on the number of evaluations performed so far.
6. The candidate point which scores the best is then chosen for evaluation via the expensive objective function. The best scoring point has the largest distance to any other already evaluated points calculated via a distance metric, and the smallest estimated objective function value from the surrogate.
7. Once the new point has been evaluated, its objective function value is compared with the best objective function value found so far from previous evaluations. If the new point is sufficiently better than the previously best known point, a success counter is incremented by one and a fail counter reset to zero; otherwise, a fail

counter is incremented by one and a success counter is reset to zero instead. If the new point is at all better than the best point, the new point is recorded as the best point.

8. If either of the fail or success counters reaches user-specified limits: the perturbation standard deviation is halved if the success counter is reached its threshold; otherwise the perturbation standard deviation is doubled; then, both of the counters are reset to zero.
9. The new point—whether an improvement over the best found or not—is then added along with its objective function value to the surrogate model along with all previous evaluated points and the surrogate is then re-fitted.
10. At this point, the loop from Step 1 iterates by generating a new set of candidate points above as long as the loop termination condition isn't met.
11. If the loop from Step 1 has ended because the perturbation standard deviation has reached a small enough value, the perturbation standard deviation is reset. At this stage, DYCORS will restart and then repeat the efforts described in Steps 1–10 above, but with: a new SLHD, fitted surrogate, and evaluation budget equal to the overall evaluation budget minus all previous evaluations. The surrogate model and distance metric do not consider evaluated points from before the most recent restart, but all points evaluated via the expensive objective function are still recorded over the course of the overall optimisation.
12. These restarts and corresponding Steps 1–10 loop iterations continue until the total number of objective function evaluations reaches the experimental budget, and then the best found objective function value and the corresponding point from all of the evaluations are returned to the user.

The forgetfulness of the surrogate and distance metric with respect to points before the most recent restart is to encourage exploration of the feasible region. The perturbation probability is used to decrease the number of perturbed dimensions in each new point

to be evaluated as the evaluation budget is spent, which encourages exploitation of the feasible region particularly when the optimisation problem has many input variables.

The choice of weighted scoring of candidate points considering both surrogate value and distance metric is to balance exploration and exploitation of the feasible region. Candidate points which have a high distance metric are far away from other known points, and therefore may be within a part of the feasible region with better objective function values and so should be considered for evaluation from a feasible region exploration perspective. Candidate points which have a low surrogate model value suggest better objective function values and these will typically occur close to known points which are known to have low objective function values, therefore these candidate points should be considered for evaluation from a feasible region exploitation perspective. Overall, a candidate point which has a good weighted score of both distance metric and surrogate is therefore extremely promising for evaluation.

During the course of a DYCORDS run, the weights used in balancing the surrogate value and distance metric for scoring candidate points can be changed depending on the number of evaluations performed. In this thesis, the weights are cycled through a set of values which also encourages a balance of exploration and exploitation of the feasible region.

3.1.5 Solver Method MARS

Solver Method MARS refers to a specific instantiation of DYCORDS as detailed in Section 3.1.4, used in conjunction with a MARS surrogate model. MARS is a method and model to perform a non-linear regression of an output variable with respect to multiple input variables, given a set of training data. Both the MARS model and the method to generate the MARS model are proposed in [54]. The specific implementation of MARS used in this thesis is `py-earth` [55], called via `pySOT` [50]. All parameter values for the surrogate model were set to the default values as specified in `pySOT` version 0.1.36. In this thesis, the fitted MARS model is used as a cheap surrogate for DYCORDS to use in scoring candidate points on their approximate expensive objective function value.

The MARS method generates a model of the form in (3.3).

$$\hat{f}(\mathbf{x}) = \sum_{i=1}^M c_i B_i(\mathbf{x}) \quad (3.3)$$

The model in (3.3) is a sum of basis functions B_i multiplied by weights c_i . In MARS, there are three forms of basis function:

1. a constant 1 (the unity basis function), which must appear once and only once;
2. a hinge function; or
3. a product of two or more hinge functions.

A hinge function $\max(0, x - b)$ or $\max(0, b - x)$ for a scalar-valued input variable x and scalar-valued parameter b returns 0 on one side of a hinge point or *knot*, and a linear-like behaviour on the other side of the knot. The value of b specifies the location of the knot. In MARS, hinge functions are initially considered in pairs, *i.e.* both $\max(0, x - b)$ and $\max(0, b - x)$ are added the model during forward pass loop iterations and only in the backward pass may one of the individual hinge functions be effectively removed; this will be explained in more detail below.

Given a set of data with input vector-valued variable \mathbf{x} and output scalar-valued function evaluations $f(\mathbf{x})$, MARS attempts to construct a model $\hat{f}(\mathbf{x})$ by choosing:

1. the number of weighted sum terms as in (3.3);
2. the value of weights c_i in each of those terms;
3. the choice of basis function in those terms;
4. the choice of scalar-valued dimension within \mathbf{x} evaluated in the hinge function(s) in those terms if the chosen basis function is a hinge or product of hinges; and
5. the knot values in those terms' hinge function(s).

The MARS method to fit a model comprises two steps: a forward pass, and a backward

pass. The method will be explained as follows.

1. Initially, the model is constructed with the unity basis function with a weight calculated via a least squares method.
2. The forward pass then starts a loop: during each loop iteration, a new pair of basis functions are added which multiply a selected basis function from the earlier loop iterations—referred to here as the parent basis function—and a new pair of hinge functions which include one of the problem variables as arguments; these new basis function terms are added in addition to all earlier parent terms. The variable in the new hinge pair cannot already be represented in the parent basis function. Note that the parent basis function could be the unity basis function; if so, this allows a hinge function pair on a new previously unmodelled variable to be introduced to the model. Parent basis functions which are themselves hinge functions (or products of hinge functions) which are then multiplied by the new hinge pair allow the introduction of interaction effects to the model between variable(s) in the parent basis functions and the variable in the new hinge pair.
3. At each iteration, the choice of which parent basis function, which input variable to select for the new hinge pair, and that variable's knot location in the new hinge pair, are determined from linear least squares programs solved independently for all combinations of all parent basis functions, all input variables, and all of each variable's observations substituted into the new hinge pair, with the least squares method selecting optimal weightings of all terms in each independent combination solution.
4. The optimal knot, input variable, and parent basis function from the combinations are then selected for the new basis function terms to be used in the next loop iteration. The hinge functions in a pair are mirrored: they may have different weights calculated by the least square method, but the hinge input variable and knot locations are the same.
5. The loop iterations continue, progressively adding terms until the total number of

added terms has reached a user-specified threshold, or the improvement in least squares residual error at each iteration is not sufficiently large.

6. When the forward pass has terminated, the backward pass begins.
7. The backward pass loops over the terms in the model, selecting a term to remove at each loop iteration which gives a sub-model with the smallest residual sum of squares.
8. This sub-model is then used in the next iteration where another term is removed. The backward pass therefore provides a number of sub-models equal to the number of terms which was originally proposed at the end of forward pass.
9. Each sub-model's generalised cross validation (GCV) is calculated, and the model with the smallest GCV is selected as the optimal fitted MARS model returned by the MARS method. Note that the simplest sub-model is a single term with the unity basis function, *i.e.* the backward pass cannot remove the unity basis function. The GCV trades off sub-model fit as represented by the residual sum of squares of the sub-model, against sub-model complexity as represented by the number of remaining terms in the sub-model. The aim of the backward pass is to select a model which has better generalisability to unseen data compared to the typically over-fit model generated by the forward pass.

3.1.6 Solver Method GPR

Solver Method GPR refers to a specific instantiation of DYCORS as detailed in Section 3.1.4, used in conjunction with a GPR surrogate model. GPR can be used to perform a non-linear regression of an output variable with respect to multiple input variables, given a set of training data.

An explanation of the GPR strategy is given in [56]. The specific implementation of GPR used in this thesis is in `scikit-learn` [57], called via `pySOT` [50]. All parameter values for the surrogate model were set to the default values as specified in `pySOT` version 0.1.36. The GPR implementation in `scikit-learn` is based upon the algorithm in [58]. In this

thesis, the fitted GPR model is used as a cheap surrogate for DYCORDS to use in scoring candidate points on their approximate expensive objective function value.

An explanation of the GPR method will now be given as follows.

1. A matrix of evaluated points \mathbf{X} and a column vector \mathbf{f} corresponding to the objective function values of the points in \mathbf{X} are generated from known points and their objective function evaluations, *i.e.* by an experimental design.
2. Each row in \mathbf{X} corresponds to a point, and the objective function value in \mathbf{f} at a specific row index value corresponds to the point in \mathbf{X} with the same row index value.
3. The surrogate model using GPR can return an approximate objective function value $\hat{f}(\mathbf{x})$ for an unknown point \mathbf{x} by applying (3.4).

$$\left[\hat{f}(\mathbf{x}) \right] = \mathbf{K}_*^T [\mathbf{K} + \sigma_n \mathbf{I}]^{-1} \mathbf{f} \quad (3.4)$$

In (3.4), σ_n is a small scalar noise term, \mathbf{I} is the identity matrix, \mathbf{K} is a matrix with elements composed of a kernel function κ as in (3.5), and \mathbf{K}_*^T is a row vector with elements composed of function κ as in (3.6). In (3.5) and (3.6), points \mathbf{x}_1 to \mathbf{x}_n are taken from the matrix \mathbf{X} with n rows, *i.e.* n observed points have already been evaluated from the objective function. For two different points \mathbf{z} and \mathbf{y} , the kernel function κ used in this thesis is given in (3.7), where $\|\cdot\|$ is the Euclidean norm.

$$\mathbf{K} = \begin{bmatrix} \kappa(\mathbf{x}_1, \mathbf{x}_1) & \dots & \kappa(\mathbf{x}_1, \mathbf{x}_n) \\ \vdots & \ddots & \vdots \\ \kappa(\mathbf{x}_n, \mathbf{x}_1) & \dots & \kappa(\mathbf{x}_n, \mathbf{x}_n) \end{bmatrix} \quad (3.5)$$

$$\mathbf{K}_*^T = \left[\kappa(\mathbf{x}_1, \mathbf{x}) \quad \dots \quad \kappa(\mathbf{x}_n, \mathbf{x}) \right] \quad (3.6)$$

$$\kappa(\mathbf{z}, \mathbf{y}) = e^{-0.5 \cdot \|\mathbf{z} - \mathbf{y}\|^2} \quad (3.7)$$

3.1.7 Solver Method Restarts

Solver Methods MARS, GPR, and NM could terminate with local optima before using up all of a specified simulation evaluation budget, *e.g.* due to convergence towards a small threshold value of relative improvement. In order to ensure a fair comparison between solver methods as well as matching the goal of finding near-optimal solutions within a limited expensive simulation budget, all solver methods were required to use up their simulation budget via restarts. This resulted in equal-length sets of best found objective function values per solver method optimisation run.

During a solver method restart the solver method database of evaluated points and their corresponding objective function values were forgotten by the solver method algorithm, although they were retained for use by the user to determine the best found point over the entire optimisation process. A new random experimental design was then generated, and used to initialise the solver methods' point database. Finally, the solver method was allowed to adaptively iterate using this database as before. Crucially, the evaluation budget for each restart and succeeding adaptive iterations was set equal to the total evaluation budget minus the count of all evaluations performed before the current restart.

A following example will explain this behaviour.

1. A budget of 200 evaluations is specified.
2. A solver method evaluates a 50 point experimental design, then adaptively iterates for a further 40 points before terminating early.
3. A restart is performed with a new budget of 110 evaluations due to 90 evaluations of the total budget already being performed. Thus, a new experimental design of 50 is evaluated.
4. A phase of adaptive sampling is performed and the solver method converges within 30 points after the second experimental design.

5. At this stage, 170 evaluations have been performed and therefore 30 evaluations remain.
6. A new experimental design of 50 points is created, and the first 30 points of that design are evaluated before terminating due to the total evaluations performed now reaching the budget of 200.

The best found objective function value—and its corresponding solution—found since the beginning of the solver method run were accumulated over all of the evaluations, therefore allowing evaluation of solver method convergence over all 200 evaluations. Lastly, the best found objective function value from all 200 evaluations was also stored for use in the subsequent assessment of solver methods.

3.1.8 Summary of Solver Method Algorithms

Solver Methods NM and GA were built using mature algorithms. Both solvers were direct search methods. In addition, both implementations within this thesis were global methods, were stochastic, and used SLHDs for sampling the objective function. Solver Method NM could restart during solver iterations, but Solver Method GA could not.

Solver Methods MARS and GPR were stochastic methods built using surrogate-based strategies recently proposed in the research literature. Both used the DYCORDS algorithm internally, and differed by the specific choice of surrogate model used to approximate the optimisation problem objective function. Both also relied upon SLHDs for sampling the objective function, and could perform restarts.

All four solver methods were therefore similar in the following ways: they were all global methods; they were all stochastic; and they all used SLHDs. The solver methods differed by: their dependency or lack thereof on surrogate models; and, their ability to restart or not during solver method iterations.

3.1.9 Software Implementation

The general approach of the solver method solution process for all four solver methods is shown in the diagram in Figure 3.1.

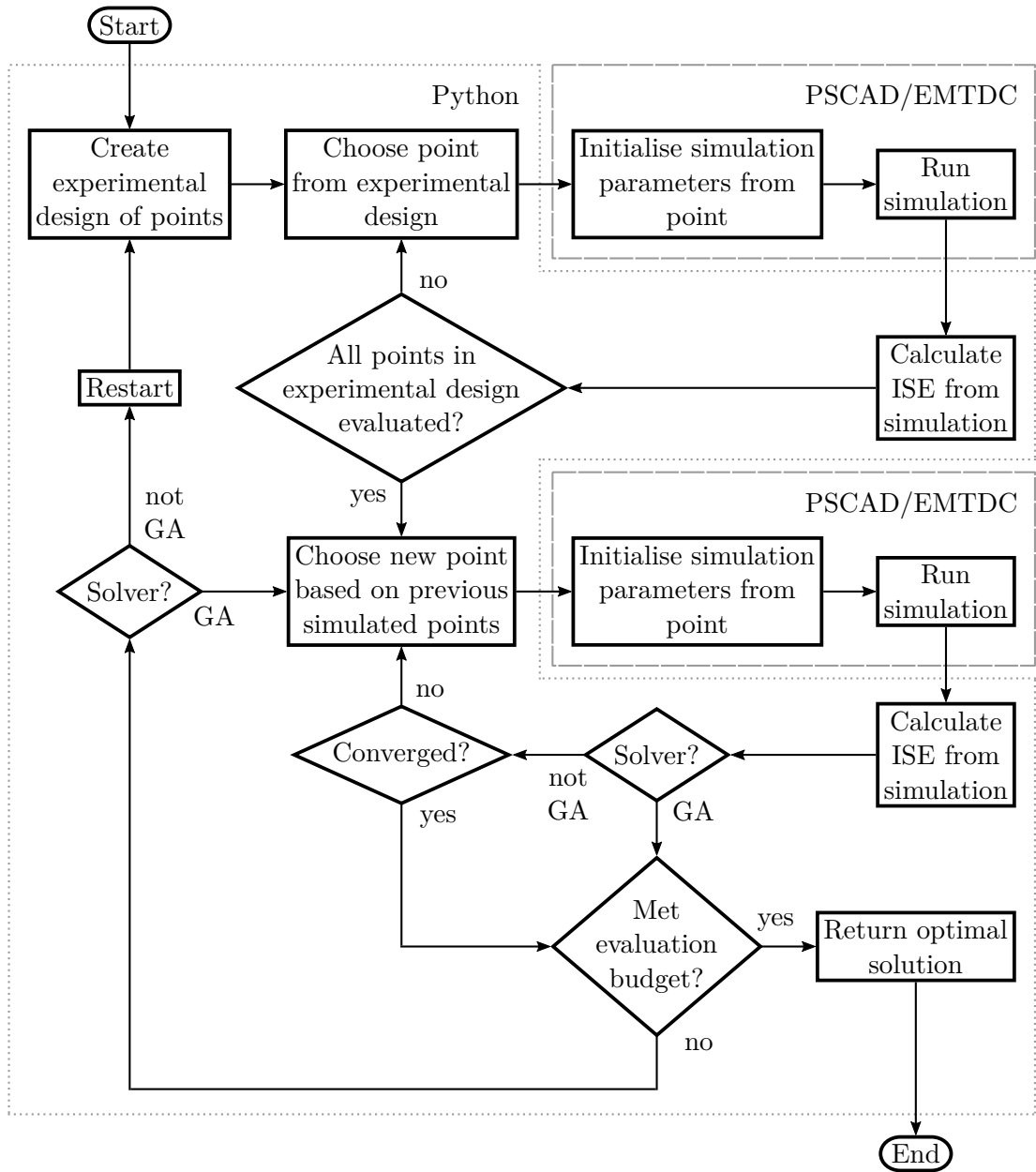


Figure 3.1: Flowchart of tested solver methods, with separation between Python interpreter and PSCAD/EMTDC processes.

Initially, the solver method will run an experimental design of variable values to observe objective function values corresponding to these experimental design points. PSCAD/EMTDC simulations are fed proposed variable values from an optimisation solver method. These variable values are treated as parameter values within the PSCAD/EMTDC simulations. The PSCAD/EMTDC time domain simulations are then run, and time series results are recorded. The time series results are input to a merit function—integral-square-error (ISE) of LCC-HVDC link measured DC-side power compared to an initial steady-state ordered power in this case—to calculate a scalar objective function value which is returned to the solver method. When the initial experimental design has been completed, the solver method iterations can then begin; subsequent experimental designs may also be performed depending on the specific solver method. The best found objective function value within the specified evaluation budget is returned along with the corresponding best found variable values.

Apart from the underlying PSCAD/EMTDC simulations, all other aspects of the study used Python software and libraries. The entire study was written in Python, and all solver methods were implemented in Python version 3.7.11 using Python software libraries.

3.2 Study Case Plant and Controller Description

This section shall detail the specific simulation study case constructed to represent an example of the motivating problem of optimisation of LCC-HVDC link controller parameter values via simulation-based optimisation. The study case was subsequently used to evaluate different expensive black-box optimisation methods on their performance on solving such types of simulation-based optimisation problems.

3.2.1 LCC-HVDC Link and AC System Plant

The study case comprised a PSCAD/EMTDC EMT simulation modelling an LCC-HVDC link interconnecting two AC systems. The two AC systems were modelled as controlled

Chapter 3. Evaluation of Simulation-based Optimisation Solver Methods for LCC-HVDC Link Controller Parameter Selection

three-phase voltage sources with source impedances, connected to the LCC-HVDC link's converter busbars via transmission lines. One AC system's nominal voltage was 230 kV RMS phase to phase, and the other system was 345 kV. In all scenarios modelled, the LCC-HVDC link's power dispatch was 200 MW from the 345 kV rectifier system towards the 230 kV inverter system. Both systems nominal frequencies were 60 Hz. This AC-DC system is based upon the model within [42]. The single line diagram of the LCC-HVDC link plant and the AC-side systems are shown in Figure 3.2, where $V_r = 1.0$ pu and $\delta_r = 0.0^\circ$ during all simulations.

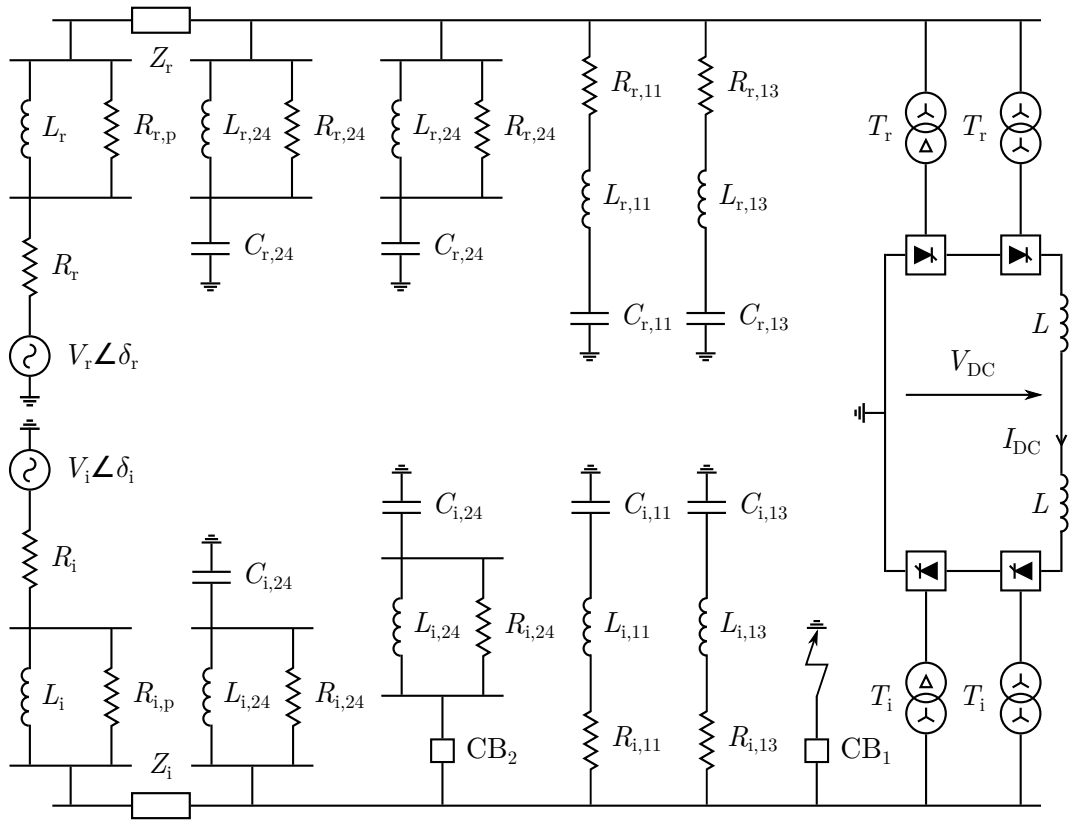


Figure 3.2: An LCC-HVDC link interconnecting two AC systems, with shunt filters.

The LCC-HVDC link's DC-side nominal voltage was 83.3 kV, and the its nominal power rating was 200 MW. The link was a monopole with thyristor bridges arranged in a twelve-pulse format. The parameter values describing the link and its converter transformers are given in Table 3.4.

The LCC-HVDC link also had shunt filters connected at both of its AC converter busbars to filter characteristic harmonics generated by the LCC-HVDC link commutation process and to compensate reactive power consumption. In each AC system, there were four filter banks each rated to provide 30 MVAR at nominal AC voltage magnitude and nominal 60 Hz frequency; two filters were single-tuned arrangements, one targeting the 11th harmonic and the other targeting the 13th harmonic; and two filters were high-pass arrangements both targeting the 24th harmonic. The resistances, inductances, and capacitances for the AC-side filters are given in Table 3.5 for the 345 kV rectifier system, and Table 3.6 for the 230 kV inverter system.

Table 3.4: Plant parameter values of the 200 MW LCC-HVDC link.

	Transformers T_r	Transformers T_i	Smoothing Reactors L
AC-side Winding Voltage (nominal)	345 kV	230 kV	—
Valve-side Winding Voltage (nominal)	36.5 kV	36.5 kV	—
Power Rating	120 MVA	120 MVA	—
Series Impedance (on transformer power rating)	12%	12%	—
Series Inductance	—	—	29.5 mH

Table 3.5: 345 kV rectifier AC-Side impedances.

Resistances (Ω)		Inductances (mH)		Capacitances (μF)	
<i>AC-side Source</i>					
R_r	1.4759	L_r	104.4	—	—
$R_{r,p}$	3150	—	—	—	—
<i>AC-side Filters</i>					
$R_{r,11}$	0.66125	$L_{r,11}$	87.701	$C_{r,11}$	0.66305
$R_{r,13}$	0.47232	$L_{r,13}$	62.644	$C_{r,13}$	0.66462
$R_{r,24}$	496.79	$L_{r,24}$	18.303	$C_{r,24}$	0.66742

Each of the AC systems included a transmission line to connect the relevant LCC-HVDC

Table 3.6: 230 kV inverter AC-Side impedances.

Resistances (Ω)		Inductances (mH)		Capacitances (μF)	
<i>AC-side Source, ESCR = 1.9</i>					
R_i	1.1483	L_i	2452.9	—	—
$R_{i,p}$	81.294	—	—	—	—
<i>AC-side Source, ESCR = 3.0</i>					
R_i	0.056035	L_i	121.73	—	—
$R_{i,p}$	4.0344	—	—	—	—
<i>AC-side Source Filters</i>					
$R_{i,11}$	0.29389	$L_{i,11}$	38.978	$C_{i,11}$	1.4919
$R_{i,13}$	0.20992	$L_{i,13}$	27.842	$C_{i,13}$	1.4954
$R_{i,24}$	220.8	$L_{i,24}$	8.1346	$C_{i,24}$	1.5017

link’s converter busbar to that AC system’s controlled voltage source and source impedance. In the 230 kV system, transmission line Z_i was 160 km long, while transmission line Z_r in the 345 kV system was 200 km long.

The resistances and inductances of the AC system source impedances were selected such that the overall impedance of the transmission lines in conjunction with the AC system source impedances resulted in an ESCR of 4.62 at the 345 kV rectifier system converter busbar, and an ESCR of either 1.9 or 3.0 at the 230 kV inverter system converter busbar depending on the commitment of a filter bank. All ESCR values were calculated using the LCC-HVDC link’s 200 MW dispatch as the denominator. The source resistances and inductances for the 345 kV rectifier system are given in Table 3.5, while the analogous values for the 230 kV inverter system are given in Table 3.6.

The parameters specifying the transmission lines in the 345 kV rectifier and 230 kV inverter systems are specified in both Table B.1 and Table B.2 in Appendix B. Both transmission lines were frequency dependent phase models within PSCAD/EMTDC and solved using PSCAD’s line constants program using parameters given in Table B.3 in Appendix B.

Note the two circuit breakers CB_1 and CB_2 in Figure 3.2. CB_1 was used to apply and

remove short circuit faults to the 230 kV inverter system busbar during time domain simulations in PSCAD/EMTDC; therefore CB_1 was normally open until the fault-on period during the time domain simulations. CB_2 was used to control the ESCR of the 230 kV inverter system for different operational scenarios. When the 230 kV inverter system ESCR was 1.9, CB_2 was closed, *i.e.* both high-pass 24th harmonic filters in the inverter system were in service. When the 230 kV inverter system ESCR was 3.0, CB_2 was open, *i.e.* only one high-pass 24th harmonic filter in the inverter system was in service.

3.2.2 LCC-HVDC Link Controllers

The converter control of both the rectifier and inverter ends of the LCC-HVDC link within the study case used a conventional MCCM with extinction angle, DC-side voltage, and DC-side current loops; and, minimum-error selector for control mode selection. The control diagram for both rectifier and inverter ends is shown in Figure 3.3, with parameter values for some of the parameters in Figure 3.3 given in Table 3.7. In Figure 3.3 the measured extinction angle γ was the minimum of the extinction angles measured from that particular converter station's thyristor bridges. The ordered firing angle α^* for a particular converter station was sent to both thyristor bridges of that converter station.

Table 3.7: Nominal set-points and parameters for quantities in Figure 3.3.

Parameter Name	Symbol	Rectifier Value	Inverter Value
Ordered DC-side Power (pu)	P_{DC}^*	1	1
Ordered DC-side Voltage (pu)	V_{DC}^*	1	1
Ordered Extinction Angle (rad)	γ^*	$0.1 \cdot \pi$	$0.1 \cdot \pi$
DC-side Voltage Margin (pu)	ΔV_{DC}	2	0
DC-side Current Margin (rad)	ΔI_{DC}	0	0.1
Ordered Firing Angle Upper Bound (rad)	α^{UB}	$0.5 \cdot \pi$	π
Ordered Firing Angle Lower Bound (rad)	α^{LB}	$\frac{1}{36} \cdot \pi$	$0.5 \cdot \pi$

The LCC-HVDC link controllers also contained VDCOLs at both ends. The VDCOL characteristics for the converter stations had identical shapes to those indicated in

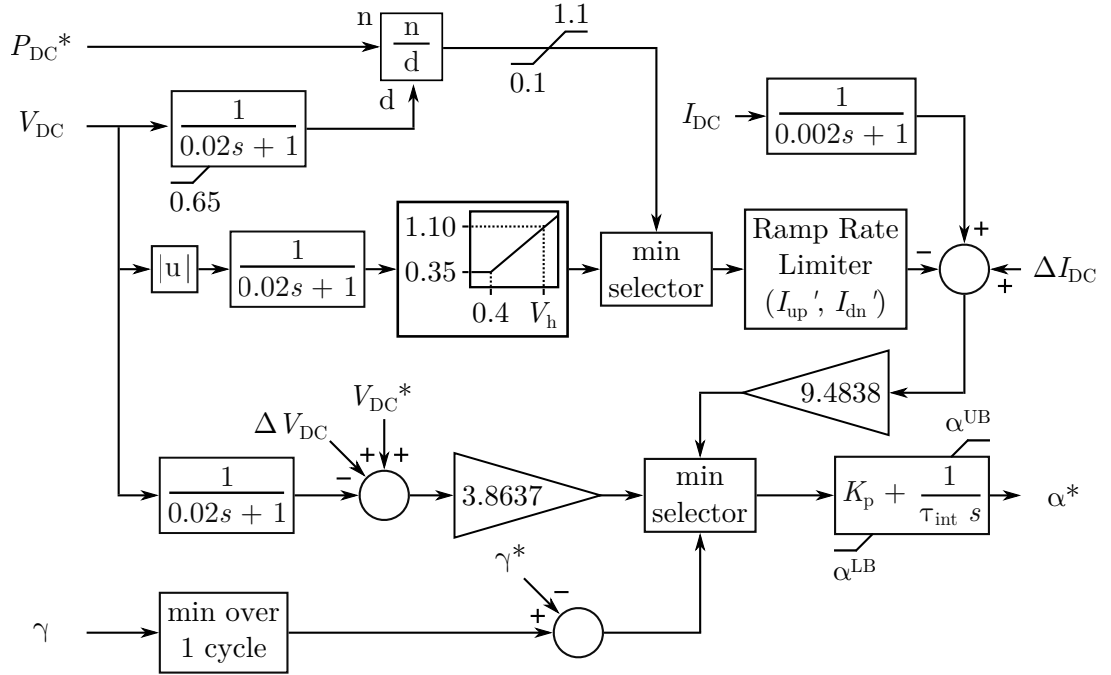


Figure 3.3: Control diagram of LCC-HVDC link converter controllers.

Figure 2.3. In each converter controller, the VDCOL reduced ordered DC-side current at that converter station if the local measured DC-side voltage reduced below a threshold value. Both LCC-HVDC link converter stations' VDCOL characteristics were identical, with the current margin set-points on both converter stations' current controllers used to separate each converter stations' VDCOL characteristics to ensure one steady-state operating point for the LCC-HVDC link. The VDCOL characteristics used ramp rate limiters to control the rate of change of ordered current during VDCOL activation. The voltage-current relationships of the VDCOLs were formed of piecewise-linear segments.

3.3 Description of the Simulation-based Optimisation Problems

The study case described in Section 3.2 was used as part of two controller tuning problems, similar to those found in [42]. These two controller tuning problems were used to generate the results which were then used for the eventual evaluation of the four

different black-box optimisation solver methods. The two Problems were:

1. Problem 1, which tuned the PI controllers of the LCC-HVDC link; and
2. Problem 2, which tuned the PI controllers and the VDCOL parameters of the LCC-HVDC link.

Both tuning Problems were considered as box-constrained, expensive, black-box, simulation-based optimisation problems.

The objective functions of both Problems were similar: both considered the ISE between ordered and measured DC-side power. The measured power was constructed from the product of the measured DC-side voltage and measured DC-side current indicated by V_{DC} and I_{DC} respectively in Figure 3.2. The error in DC-side power was output from the PSCAD/EMTDC simulation as a time series, which was then squared and integrated using trapezoidal integration of the time series values to result in a scalar value of ISE.

Both Problems considered two different operational scenarios: one where the ESCR of the 230 kV inverter was 1.9, and another scenario where ESCR was 3.0.

These two scenarios were modelled by two separate PSCAD/EMTDC simulations which ran in parallel and were identical aside from the inverter system ESCR; both simulations received the same parameter values from the solver method to simulate and produce DC-side power error. The ISE of the DC-side power for each individual ESCR scenario were calculated separately, and then the sum of the two ISE values was returned back to the optimisation solver method as the objective function value corresponding to the input variable values suggested by the solver method.

3.3.1 Problem 1: PI Controller Tuning

In this Problem, four optimisation variables were optimally tuned.

1. Rectifier proportional gain $K_{r,p}$;
2. Inverter proportional gain $K_{i,p}$;

3. Rectifier integral time constant $\tau_{r,int}$; and
4. Inverter integral time constant $\tau_{i,int}$.

The rectifier and inverter proportional gains $K_{r,p}$ and $K_{i,p}$ are indicated by K_p in Figure 3.3; the rectifier and inverter integral time constants $\tau_{r,int}$ and $\tau_{i,int}$ are indicated by τ_{int} in Figure 3.3.

The optimisation was performed considering power set-point changes and disturbances embedded within the PSCAD/EMTDC study case simulations. These set-point changes and disturbances are given below, in conjunction with the time step t in the simulation at which the set-point change or disturbance occurred.

1. $t = 0.1$ s, $\delta_i = -7.5$ deg;
2. $t = 0.6$ s, $\delta_i = 0.0$ deg;
3. $t = 1.1$ s, $V_i = 0.93$ pu;
4. $t = 1.6$ s, $V_i = 1.0$ pu;
5. $t = 2.1$ s, $P_{DC}^* = 0.5$ pu; and
6. $t = 2.6$ s, $P_{DC}^* = 1.0$ pu.

The bounds of all four of the optimisation variables were as follows: all lower bounds set to 0.01; and all upper bounds set to 1.0.

3.3.2 Problem 2: PI Controller and VDCOL Parameter Tuning

In this Problem, seven optimisation variables were tuned.

1. Rectifier proportional gain $K_{r,p}$;
2. Inverter proportional gain $K_{i,p}$;
3. Rectifier integral time constant $\tau_{r,int}$;
4. Inverter integral time constant $\tau_{i,int}$;

5. VDCOL upper voltage breakpoint V_h ;
6. VDCOL ramp up rate limit I_{up}' ; and
7. VDCOL ramp down rate limit I_{dn}' .

The rectifier and inverter proportional gains and integral time constants are indicated in Figure 3.3 in the same as manner as in Section 3.3.1. In addition, VDCOL upper voltage breakpoint V_h , ramp up rate limit I_{up}' , and ramp down rate limit I_{dn}' are also optimisation variables in Problem 2. Note that the rectifier and inverter proportional gains and integral time constants are independent for each converter station, but the three VDCOL parameters are shared by the VDCOLs at both converter stations.

As in Problem 1, power set-point changes and disturbances were embedded within the the PSCAD/EMTDC study case simulations. These set-point changes and disturbances were the same as in Problem 1, in conjunction with additional disturbances linked with a short circuit fault applied at the 230 kV inverter system converter station busbar.

1. $t = 0.1 \text{ s}$: $\delta_i = -7.5 \text{ deg}$;
2. $t = 0.6 \text{ s}$: $\delta_i = 0.0 \text{ deg}$;
3. $t = 1.1 \text{ s}$: $V_i = 0.93 \text{ pu}$;
4. $t = 1.6 \text{ s}$: $V_i = 1.0 \text{ pu}$;
5. $t = 2.1 \text{ s}$: $P_{DC}^* = 0.5 \text{ pu}$;
6. $t = 2.6 \text{ s}$: $P_{DC}^* = 1.0 \text{ pu}$;
7. $t = 4.0 \text{ s}$: CB_1 closed;
8. $t = 4.01667 \text{ s}$: $P_{DC}^* = 0.0 \text{ pu}$;
9. $t = 4.05 \text{ s}$: CB_1 opened; and
10. $t = 4.05667 \text{ s}$: $P_{DC}^* = 1.0 \text{ pu}$.

The bounds of the rectifier and inverter proportional gain and integral time constant

optimisation variables were as follows: all lower bounds set to 0.01; and all upper bounds set to 1.0. The lower and upper bounds of the VDCOL upper voltage breakpoint were 0.52 and 0.95 respectively. For both the ramp up and ramp down rate limits, the lower and upper bounds of both were 0.667 and 66.7 respectively.

Note that the applied short circuit fault was applied and then cleared by simply removing the fault from the AC-side converter station busbar of the inverter end of the link using circuit breaker CB_1 . The converter station busbar itself was not switched out of service when clearing the fault.

3.4 Description of the Assessment Strategy for Evaluation of the Solver Methods

The four solver methods described in Section 3.1 were all stochastic, *i.e.* optimal solutions returned by the solver methods would in general be different over repeated independent solution runs of the solver method on the same optimisation problem with identical parameters and experimental budget. This therefore meant that the solver method performance had to be evaluated via statistical methods.

The strategy is as follows. A sample of optimal solutions were drawn for each solver method, where each observation in the sample was the best found objective function value from an independent solution run of the solver method on one of the optimisation Problems described in Section 3.3. For pairs of solver methods, an independent two-sample comparison was made by calculating a sample statistic of difference in sample mean between the two samples. The sample statistic 95% confidence interval was then estimated via a non-parametric basic bootstrapping method with a 95% confidence level. If the confidence interval for the sample statistic did not include zero, then it was assumed that there was a significant difference in the means of the two samples and therefore a significant difference in the ability of the two solver methods to find superior solutions, *i.e.* one solver method was inferred to find better optimal solutions than the other solver method.

Since four solver methods were tested, there were six pairs of two-sample comparisons; these were performed separately for both Problems.

Each sample included 30 independent observations, and each Problem was solved by the solver method with an experimental budget of 200 evaluations, *i.e.* 200 sets of PSCAD/EMTDC simulations, or 400 simulations in total for each Problem due to the two studied ESCR scenarios.

The solution time of the optimisation problems was overwhelmingly due to the PSCAD/EMTDC simulation wall clock time, *i.e.* the solver methods' software did not consume much wall clock time. Therefore statistically significant differences in sample means between pairs of solver methods implied that one solver method would be superior to another and would not take more time to find those superior solutions.

3.5 Non-parametric Basic Bootstrap

The difference in two sample means for a pair of samples taken from two different solver methods will be indicated in this section by δ .

The purpose of the bootstrap was to assist in the estimation of the population difference δ in mean optimal solutions μ , given the sample difference $\hat{\delta}$ in mean optimal solutions $\hat{\mu}$ found from the two drawn samples. If multiple independent samples were drawn for both solver methods and 95% confidence intervals estimated for the sample difference in means for each independent pair of samples, the proportion of the 95% confidence intervals which included the true—but unknown—population difference in means would approach 95%. Bootstrapping allows the estimation of a confidence interval for a one-sample statistic—such as the mean—using only a single sample of data rather than repeatedly drawing samples. For two-sample statistics such as difference in means used in this thesis, one sample from each solver method can be drawn and used with the bootstrapping approach.

Firstly, assume the optimal solution objective function value of a particular solver method

for a Problem is a random variable W , with an unknown distribution F , and an expected value $E[W] = \mu_1$; and secondly, assume another solver method applied to the same Problem returns an optimal solution objective function value which is another random variable V , with its own unknown distribution G , and an expected value $E[V] = \mu_2$.

The population difference between the solver methods' means is $\delta = \mu_1 - \mu_2$, but μ_1, μ_2 , and therefore δ are population parameters and therefore cannot be known with surety. Hence samples drawn for the two different solver methods can be used in conjunction with bootstrapping to estimate δ with confidence intervals, where six different estimated δ with confidence intervals were calculated—one for each pair of solver method comparisons.

A sample \mathcal{W} of optimal solution objective function values for one solver method is drawn from F by running independent solution runs of that solver method and recording the best found objective function value for each solution run. The sample \mathcal{W} is therefore a multiset, where $\mathcal{W} = \{w_k : k \in \mathcal{N}\}$, $\mathcal{N} = \{1, 2, \dots, n\}$, and $n = 30$ due to the 30 independent solver method solution runs. For the other solver method, a sample \mathcal{V} of optimal solution objective function values is drawn by sampling from G . The sample \mathcal{V} is also a multiset, where $\mathcal{V} = \{v_k : k \in \mathcal{N}\}$.

A multiset \mathcal{W}^* is created with a large number B of re-samples \mathcal{W}_b^* of \mathcal{W} by uniform re-sampling with replacement; where $B = 10^5$, \mathcal{W}_b^* is the b -th re-sample of \mathcal{W} , and $\mathcal{W}^* = \{\mathcal{W}_1^*, \mathcal{W}_2^*, \dots, \mathcal{W}_B^*\}$. A similar multiset \mathcal{V}^* of re-samples \mathcal{V}_b^* is generated from \mathcal{V} . Each \mathcal{W}_b^* and \mathcal{V}_b^* are of cardinality n , *i.e.* they contain 30 observations due to the 30 observations originally drawn from F and G .

A multiset \mathcal{Q}^* of statistics calculated from sets \mathcal{W} , \mathcal{V} , \mathcal{W}^* and \mathcal{V}^* via (3.8).

$$\mathcal{Q}^* = \left\{ \frac{1}{n} \left(\sum \mathcal{W}_b^* - \sum \mathcal{V}_b^* \right) - \frac{1}{n} \left(\sum \mathcal{W} - \sum \mathcal{V} \right) : b \in \{1, 2, \dots, B\} \right\} \quad (3.8)$$

A quantile function $\hat{J}(p)$ is defined which returns the quantile for a specified probability p using a linear interpolation method on the empirical cumulative distribution of the values in the multiset \mathcal{Q}^* . The linear interpolation method is *Definition 7* from [59]. $\hat{J}(p)$ can be used to estimate a confidence interval for δ . The estimated 95% confidence level lower δ_{LB} and upper δ_{UB} bounds of δ for a 95% confidence level are given by (3.9) and (3.10) respectively.

$$\delta_{LB} = \frac{1}{n} \left(\sum \mathcal{W} - \sum \mathcal{V} \right) - \hat{J}(0.975) \quad (3.9)$$

$$\delta_{UB} = \frac{1}{n} \left(\sum \mathcal{W} - \sum \mathcal{V} \right) - \hat{J}(0.025) \quad (3.10)$$

If both δ_{LB} and δ_{UB} are greater than zero, this implies the solver method which generated sample \mathcal{V} provides superior optimal solutions than the solver method which generated sample multiset \mathcal{W} . If both δ_{LB} and δ_{UB} are less than zero, this implies the solver method which generated sample \mathcal{W} provides superior optimal solutions than the solver method which generated sample multiset \mathcal{V} .

3.6 Results and Discussion

Figures 3.4 and 3.5 show the sample mean difference with 95% confidence intervals estimated via bootstrapping for Problem 1 and Problem 2 respectively. In both Figures 3.4 and 3.5, the x-axis tick labels should be read as follows: the optimal solutions for the Solver Method with its name closest to the x-axis corresponds to multiset \mathcal{W} in Section 3.5, while the other named Solver Method corresponds to multiset \mathcal{V} in Section 3.5.

For Problem 1, Solver Methods GPR and MARS outperformed Solver Method GA. However Solver Methods MARS and GPR were similar to each other, and Solver Methods GA, GPR, and MARS were all similar to Solver Method NM.

For Problem 2, Solver Method MARS outperformed all other solver methods. Solver

Chapter 3. Evaluation of Simulation-based Optimisation Solver Methods for LCC-HVDC Link Controller Parameter Selection

Methods GA and GPR outperformed Solver Method NM, while Solver Methods GA and GPR were similar to each other.

This implies qualitatively that for Problem 1, Solver Methods GPR, MARS, and NM could be chosen for finding good optimal solutions compared to Solver Method GA.

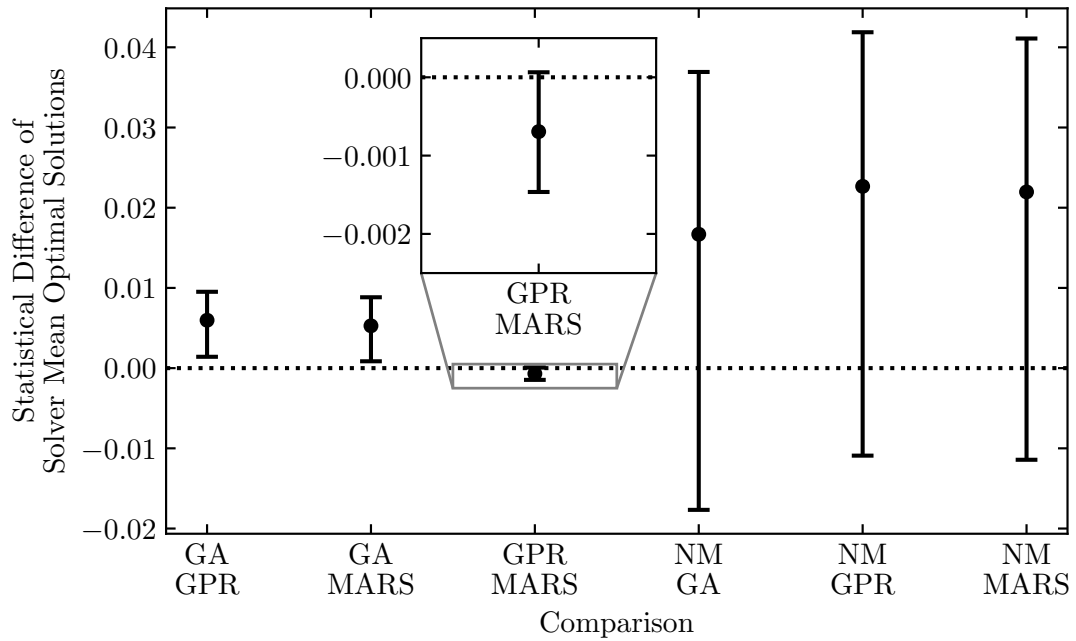


Figure 3.4: Difference between solver method mean optimal objective value solutions with 95% confidence interval for Problem 1.

Chapter 3. Evaluation of Simulation-based Optimisation Solver Methods for LCC-HVDC Link Controller Parameter Selection

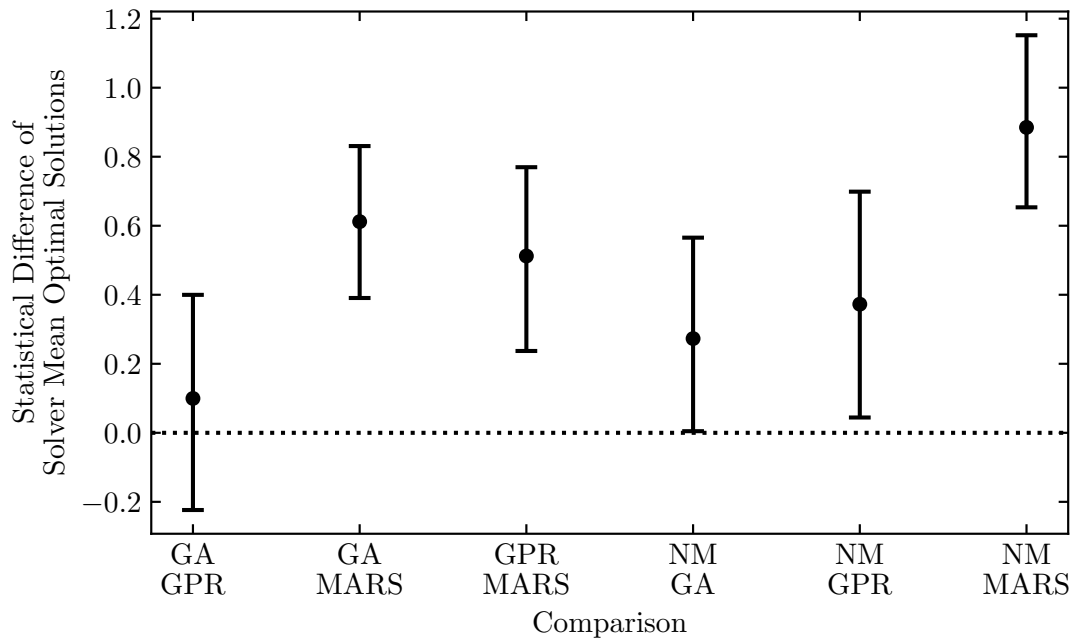


Figure 3.5: Difference between solver method mean optimal objective value solutions with 95% confidence interval for Problem 2.

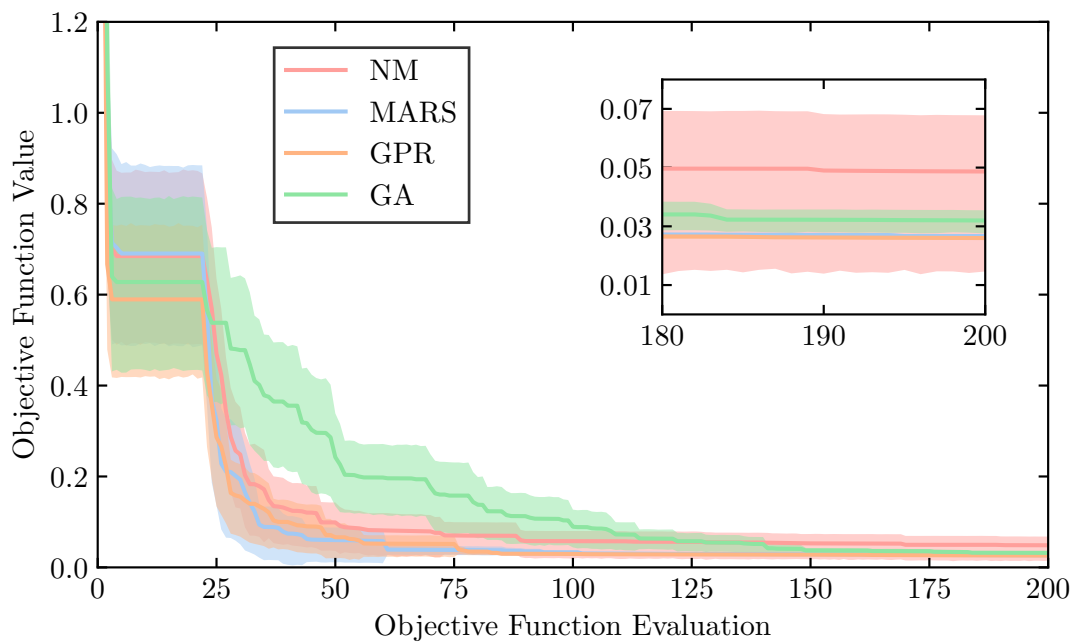


Figure 3.6: Mean convergence curves with 95% confidence intervals for Problem 1.

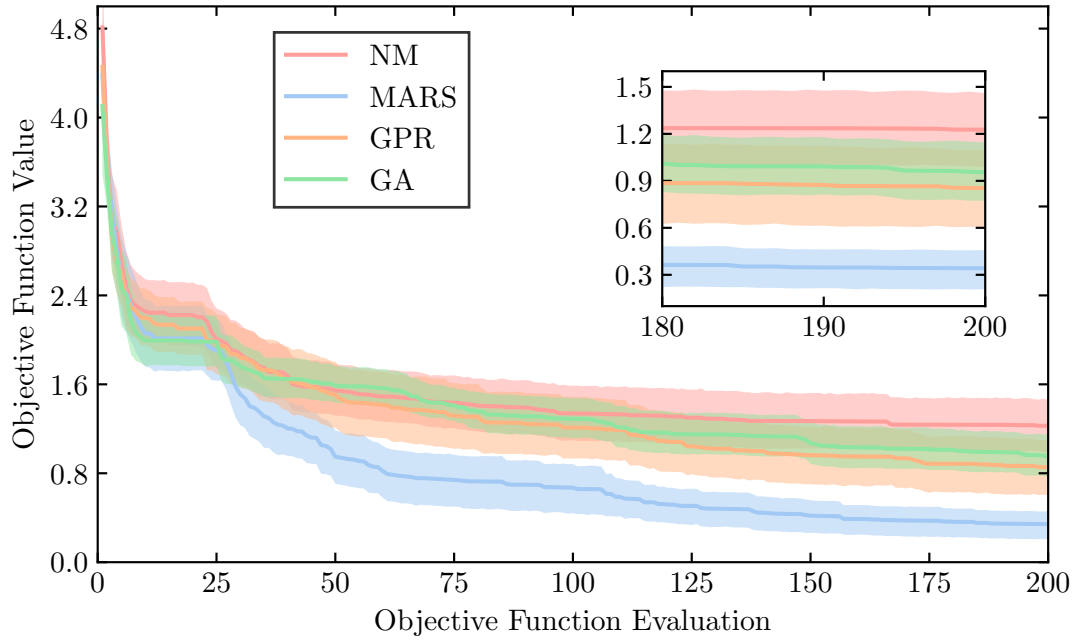


Figure 3.7: Mean convergence curves with 95% confidence intervals for Problem 2.

As for Problem 2, Solver Method MARS is superior to all other solver methods and therefore represents the best choice of solver method for this Problem.

Overall, the proposed methods of Solver Method MARS and GPR perform no worse than the mature methods of Solver Method NM and GA for solving Problem 1. With respect to Problem 2, the proposed methods of Solver Method MARS and GPR perform similar to or better than the mature methods.

Figures 3.6 and 3.7 show the convergence curves of the best solutions found over the course of the evaluation budget expenditure for Problem 1 and Problem 2 respectively. The curves are composed of a line representing the sample mean of best found optimal solutions up to a particular x-axis evaluation number, with a 95% confidence interval for the sample mean represented by the shaded areas around the sample mean line. The 95% confidence intervals for the sample means were calculated using a bootstrapping method similar to the method detailed in Section 3.5.

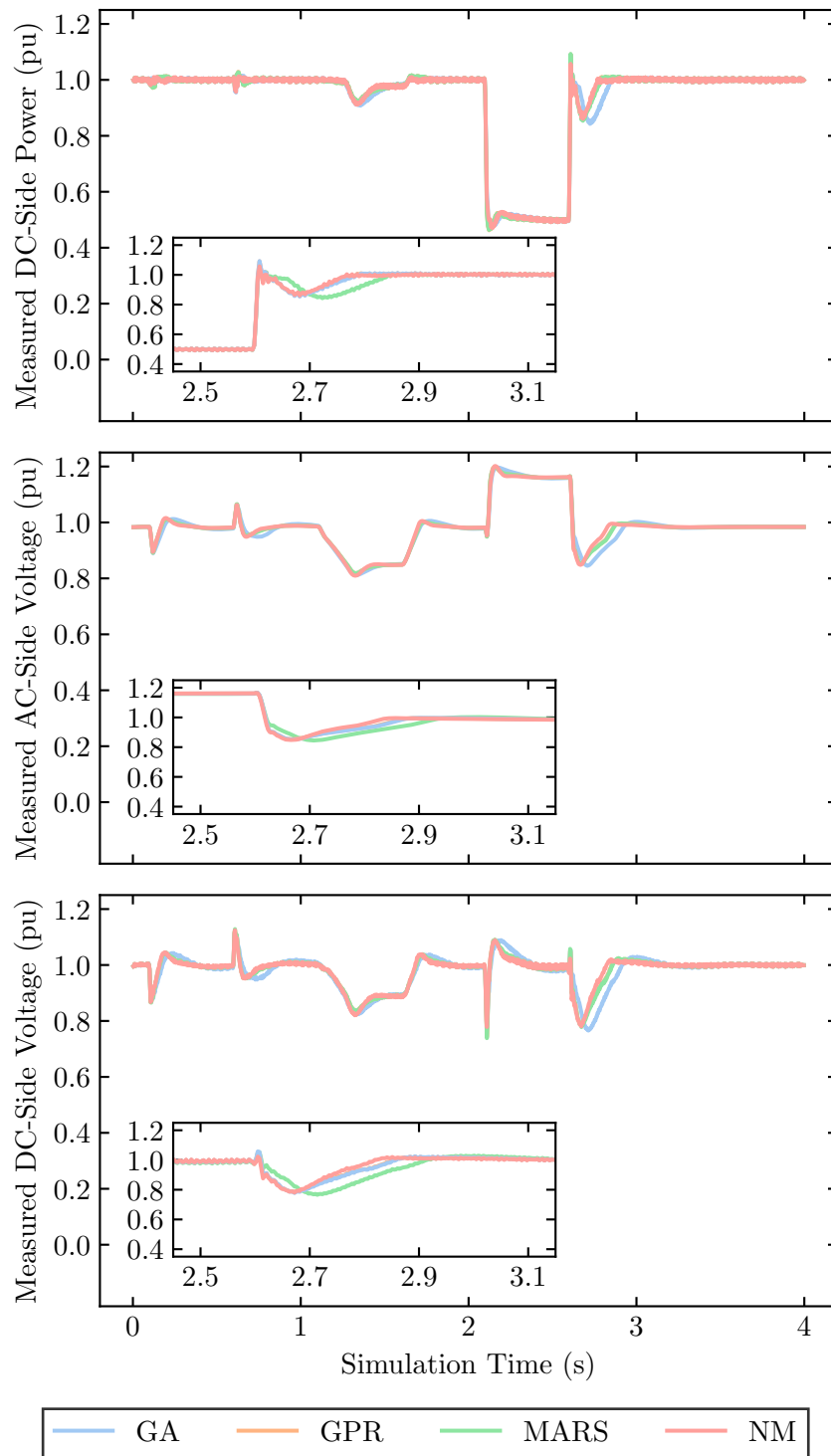


Figure 3.8: Measured time series variables corresponding to the best found optimal solutions for each solver method for Problem 1 when ESCR was 3.0.

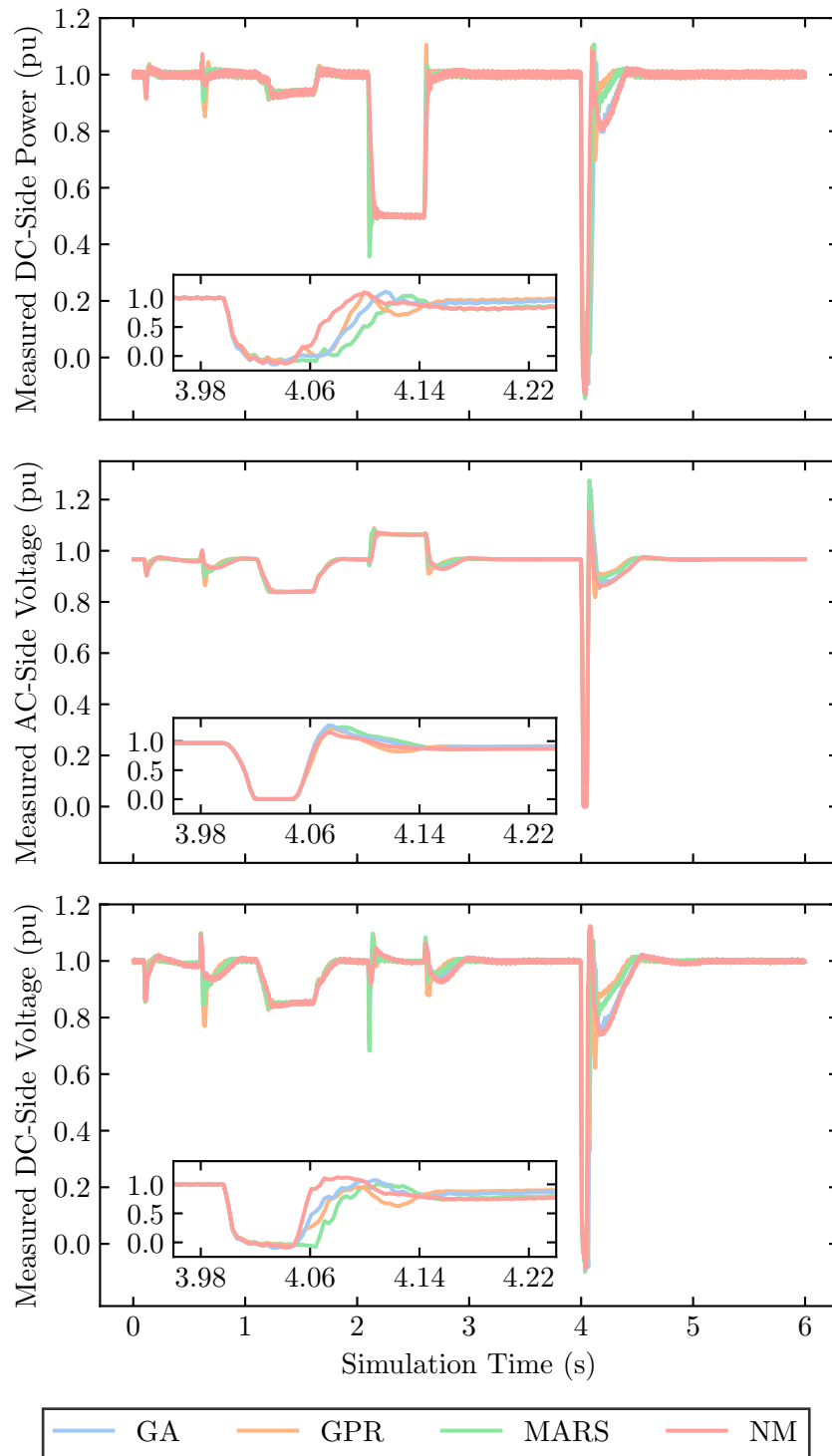


Figure 3.9: Measured time series variables corresponding to the best found optimal solutions for each solver method for Problem 2 when ESCR was 3.0.

Figures 3.8 and 3.9 show the measured time series traces of three system variables for the scenario where ESCR was equal to 3.0, corresponding to the best found objective function value in the sample of 30 observations drawn for each Solver Method. DC-side measured power, AC-side measured voltage, and DC-side measured voltage are shown in both Figures 3.8 and 3.9. The measured time series traces for Problem 1 are shown specifically in Figure 3.8; similarly, the time series traces for Problem 2 are shown in Figure 3.9.

3.7 Summary

In this chapter, optimisation solver methods using surrogate-based strategies recently proposed in the research literature have been evaluated with respect to mature strategies on the problem of tuning LCC-HVDC link controller parameters. The controller tuning problem was represented as two similar box-constrained, expensive, black-box, simulation-based optimisation Problems considering PI controller and VDCOL parameters, set-point changes and disturbances. These Problems were then successfully solved by the four solver methods independently.

The evaluation method uses a statistical approach to address the stochastic nature of the optimisation solver methods. This evaluation method uses differences in sample means of best-found optimal solution objective values with estimated confidence intervals to infer population parameters and find statistically significant differences in optimal solution quality between the solver methods.

The two solver methods using recently proposed strategies were found to perform no worse than either of the mature solvers on both Problems, and in some cases perform significantly better than the mature methods.

Using the observed mean ISE values for both Problems: Solver Methods GA, GPR, and MARS mean ISE are reduced by 34.291%, 46.562%, and 45.137% relative to Solver Method NM for Problem 1; and, Solver Methods GA, GPR, and MARS mean ISE are reduced by 22.259%, 30.38%, and 72.14% relative to Solver Method NM for Problem 2.

Chapter 3. Evaluation of Simulation-based Optimisation Solver Methods for LCC-HVDC Link Controller Parameter Selection

The work in this chapter shows that either Solver Method GPR or Solver Method MARS can successfully be deployed for solving the expensive black-box simulation-based optimisation problem of tuning LCC-HVDC controller parameters, particularly when considering disturbances and set-point changes, modelled using underlying PSCAD/EMTDC EMT time domain simulations.

Chapter 4

A Method to Evaluate Dynamic Compensators for the Improvement of LCC-HVDC Link Dynamic Performance

This chapter describes a proposed simulation-based optimisation method to evaluate dynamic compensators' capabilities for assisting the dynamic performance of an LCC-HVDC link.

LCC-HVDC link technical performance is adversely affected by disturbances to alternating voltage waveforms at the LCC-HVDC link's converter station busbars. Deleterious effects at the inverting end of the LCC-HVDC link may include commutation failure occurrence and poor recovery after commutation failure, particularly during large transient disturbances such as short circuit faults. These effects are generally more severe in inverter AC systems with high source impedance relative to the LCC-HVDC link's power transfer dispatch, *i.e.* low SCR systems as viewed from the inverter station. Adding dynamic reactive compensation to the inverter AC system near the LCC-HVDC

link inverter station might improve the dynamic behaviour of the LCC-HVDC link to recover steady-state operation quickly after a fault. The difference between compensators in terms of their plant or control imply that they may have different capabilities from each other to quantitatively improve LCC-HVDC link dynamic performance.

The proposed method considers optimal selection of LCC-HVDC link controller parameter values and dynamic compensator voltage controller parameter values via simulation-based optimisation to ensure fair comparison between compensators and the compensator-less LCC-HVDC link configuration. The method uses statistical approaches to consider the stochasticity of the simulation-based optimisation solver method, which means the method is useful in studies with random sampling such as sampling from many possible operational scenarios. The method also investigates multiple measured variables and engineer-defined performance functions, which are affected by the presence of dynamic compensators and plant controller tuning.

The proposed method is demonstrated on four study cases: a configuration of the LCC-HVDC link without any compensator; and, configurations of the LCC-HVDC link with three different compensator types. The compensator types studied are the SVC, the STATCOM, and the synchronous condenser; in addition, three different possible reactive power ratings are studied for each different compensator type.

4.1 Plant and Controller Architectures for Investigated Study Cases

This section details plant and controllers of an LCC-HVDC link and dynamic reactive power compensators used within study case simulations. These simulations are part of the motivating problem of optimisation of LCC-HVDC link controller and potential dynamic compensation voltage controller parameter values via simulation-based optimisation, subject to: inverter system short circuit faults at multiple possible locations; and, multiple inverter system SCRs.

The simulations are split into four individual study cases: a Base study case with no connected dynamic compensator, a Synchronous Condenser study case, a STATCOM study case, and a SVC study case. All four study cases were subjected to the same sets of short circuit disturbance locations and inverter SCRs. The Synchronous Condenser, STATCOM, and SVC study cases all investigated the same set of values of dynamic compensation equipment rating.

All four study cases included the LCC-HVDC link plant and controllers described in Sections 4.1.1 and 4.1.2. The SVC, STATCOM, and synchronous condenser study cases additionally included the plant and controllers described in Sections 4.1.3, 4.1.4, and 4.1.5 respectively.

4.1.1 LCC-HVDC Link and AC System Plant

The Base study case was composed of PSCAD/EMTDC EMT simulations modelling an LCC-HVDC link interconnecting two AC systems. The AC systems were modelled as three-phase alternating voltage sources with source impedances, with each source connected to one of the LCC-HVDC link's converter busbars via source impedances and transmission lines. The single line diagram of the LCC-HVDC link plant and the AC-side systems are shown in Figure 4.1. One AC system's nominal voltage was 230 kV RMS phase to phase, and the other system was 345 kV. In all scenarios modelled, the LCC-HVDC link's power dispatch was 200 MW from the 345 kV rectifier system towards the 230 kV inverter system. Both systems nominal frequencies were 60 Hz. The AC-DC system used within the Base study case was therefore very similar to the AC-DC system used within Chapter 3, but with some important modifications. In Figure 4.1, note that $V_r = 1.0$ pu, $V_i = 1.0$ pu, $\delta_r = 0.0^\circ$, and $\delta_i = 0.0^\circ$ during all simulations.

The dynamic compensator study cases were identical to the Base study case except they also included the relevant dynamic compensator, which was connected via circuit breaker CB₃. During simulations with either a synchronous condenser, SVC, or STATCOM, CB₃ was always closed to connect the relevant compensator to the inverter system. During the Base study case, CB₃ was always open, *i.e.* no compensator existed in the system.

Chapter 4. A Method to Evaluate Dynamic Compensators for the Improvement of LCC-HVDC Link Dynamic Performance

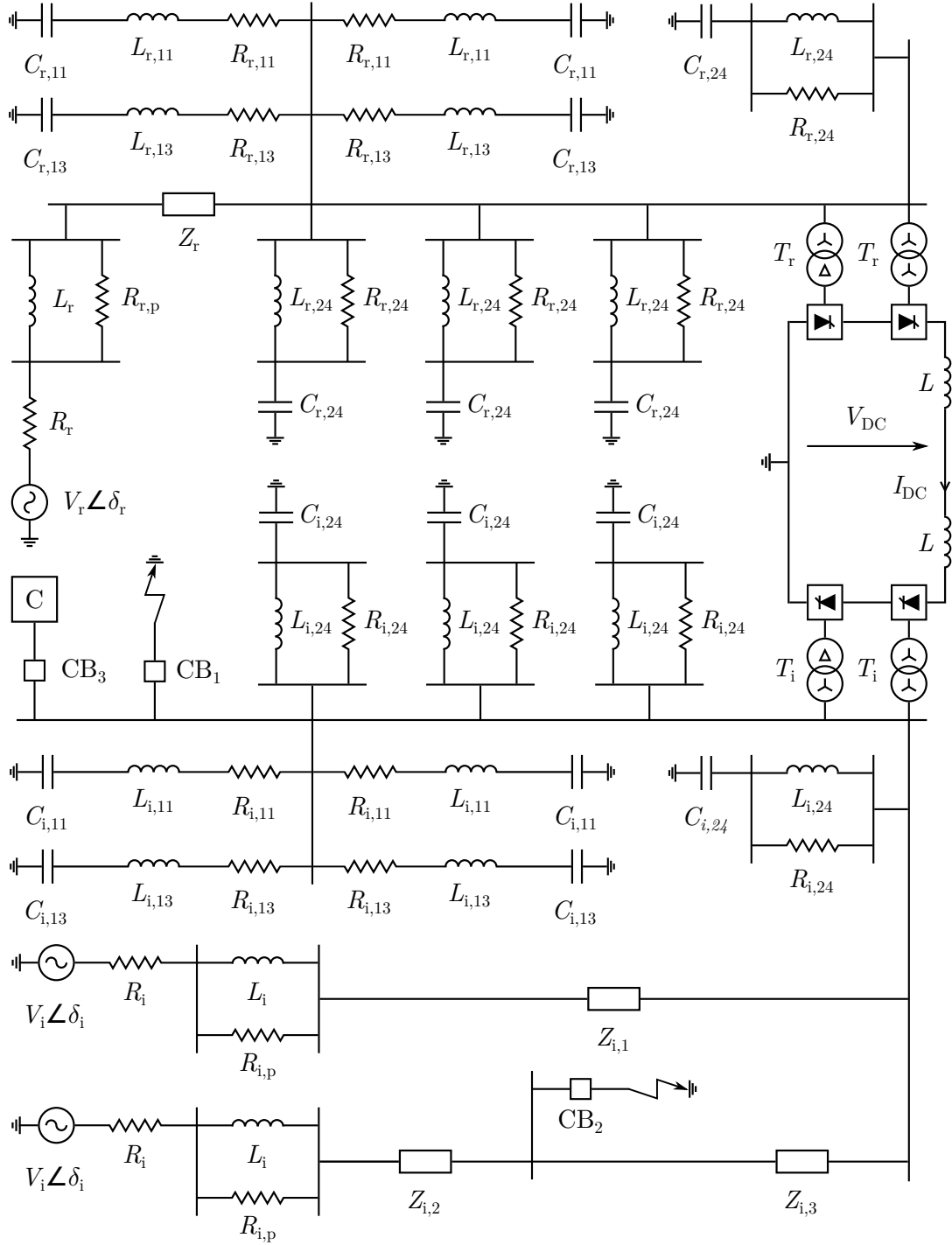


Figure 4.1: An LCC-HVDC link interconnecting two AC systems, with shunt filters, three inverter system transmission lines, and a potential inverter system dynamic compensator.

Table 4.1: Plant parameter values of the 200 MW LCC-HVDC link for dynamic compensation simulation studies.

	Transformers	Transformers	Smoothing Reactors
	T_r	T_i	L
AC-side Winding Voltage (nominal)	345 kV	230 kV	—
Valve-side Winding Voltage (nominal)	30.853 kV	30.853 kV	—
AC-side Tap Setting	0.91917	0.91921	—
Power Rating	120 MVA	120 MVA	—
Series Impedance (on transformer power rating)	12%	12%	—
Series Inductance	—	—	29.5 mH

The LCC-HVDC link's DC-side nominal voltage was 83.3 kV, and the its nominal power rating was 200 MW. The LCC-HVDC link was a monopole with thyristor bridges arranged in a twelve-pulse layout. The parameter values describing the LCC-HVDC link and its converter transformers are given in Table 4.1.

At each AC-side converter busbar, there were eight filter banks each rated to provide 7.12 MVar of reactive power at nominal AC voltage magnitude and nominal 60 Hz frequency. Each converter station had: two single-tuned filters tuned to the 11th harmonic; two single-tuned filters tuned to the 13th harmonic; and four high-pass filters tuned to the 24th harmonic. The resistances, inductances, and capacitances for the AC-side filters are given in Table 4.2 for the 345 kV rectifier system, and Table 4.3 for the 230 kV inverter system.

Each AC system contained at least one transmission line to connect the relevant LCC-HVDC link converter busbar to that AC system's controlled voltage source(s) and source impedance(s). In the 230 kV system the transmission line $Z_{i,1}$ was 320 km long, and the sum of transmission lines $Z_{i,2}$ and $Z_{i,3}$ was also 320 km. The transmission line Z_r in the 345 kV system was 200 km long. Note that the inverter system was modelled via two separate voltage sources and impedances, interconnected together only via the

Table 4.2: 345 kV rectifier AC-Side impedances.

Resistances (Ω)		Inductances (mH)		Capacitances (μF)	
<i>AC-side Source</i>					
R_r	2.0316	L_r	107.84	—	—
$R_{r,p}$	2441.2	—	—	—	—
<i>AC-side Filters</i>					
$R_{r,11}$	30.647	$L_{r,11}$	369.52	$C_{r,11}$	0.15736
$R_{r,13}$	25.87	$L_{r,13}$	263.95	$C_{r,13}$	0.15774
$R_{r,24}$	2088.1	$L_{r,24}$	76.927	$C_{r,24}$	0.1588

long transmission lines connecting the sources' impedances to the inverter station AC-side busbar. Although this is a somewhat synthetic scenario since most research literature models an inverter system using a single voltage source behind a source impedance, the representation adopted in this thesis with two separated sources was selected for the following reason. This two-source representation allows fault locations to be investigated on the interconnecting transmission lines such that AC-side steady-state fault-on voltage magnitudes at the inverter station busbar—*i.e.* retained voltages—during the short circuit faults would take values in a more varied manner within the interval 0.0 pu to 1.0 pu than could otherwise be achieved with a single inverter system voltage source representation.

The parameters specifying the transmission lines in the 345 kV rectifier and 230 kV inverter systems are specified in both Tables C.1 and C.2 in Appendix C. Both transmission lines were frequency dependent phase models within PSCAD/EMTDC and solved using PSCAD's line constants program using parameters given in Table C.3 in Appendix C.

The resistances and inductances of the AC system source impedances were selected such that the overall impedance of the transmission lines in conjunction with the AC system source impedances at power frequency resulted in an SCR of 5.22 at the 345 kV rectifier system converter busbar, and an SCR of either 1.5, 1.625, 1.75, 1.875, or 2.0 at the 230 kV inverter system converter busbar. All SCRs were calculated using the

Table 4.3: 230 kV inverter AC-Side impedances.

Resistances (Ω)		Inductances (mH)		Capacitances (μF)	
<i>AC-side Source, SCR = 1.5</i>					
R_i	11.215	L_i	594.96	—	—
$R_{i,p}$	13469	—	—	—	—
<i>AC-side Source, SCR = 1.625</i>					
R_i	9.7352	L_i	516.47	—	—
$R_{i,p}$	11692	—	—	—	—
<i>AC-side Source, SCR = 1.75</i>					
R_i	8.467	L_i	449.19	—	—
$R_{i,p}$	10169	—	—	—	—
<i>AC-side Source, SCR = 1.875</i>					
R_i	7.3678	L_i	390.88	—	—
$R_{i,p}$	8848.8	—	—	—	—
<i>AC-side Source, SCR = 2.0</i>					
R_i	6.406	L_i	339.85	—	—
$R_{i,p}$	7693.6	—	—	—	—
<i>AC-side Source Filters</i>					
$R_{i,11}$	13.621	$L_{i,11}$	164.23	$C_{i,11}$	0.35407
$R_{i,13}$	11.498	$L_{i,13}$	117.31	$C_{i,13}$	0.35491
$R_{i,24}$	928.03	$L_{i,24}$	34.19	$C_{i,24}$	0.35729

LCC-HVDC link's 200 MW dispatch as the denominator, and did not include the effect of any compensator. The source resistances and inductances for the 345 kV rectifier system are given in Table 4.2, while the analogous values for the 230 kV inverter system are given in Table 4.3.

Circuit breakers CB_1 and CB_2 in Figure 4.1 were used to apply three-phase short circuit faults to the inverter system during time domain simulations in PSCAD/EMTDC. CB_1 was used to apply and remove short circuit faults to the 230 kV inverter system busbar when studying Fault Location 1 in Table 4.4, while CB_2 applied short circuit faults at different locations along one of the inverter system transmission lines when studying Fault Locations 2–5 in Table 4.4. Therefore CB_1 and CB_2 were open from simulation

Table 4.4: Transmission line lengths for each fault location in the 230 kV inverter system.

Fault Location	Fault-On Steady-State Voltage (pu)	$Z_{i,2}$ Length (km)	$Z_{i,3}$ Length (km)
1	0.0	160	160
2	0.075	270.42	49.584
3	0.15	197.4	122.6
4	0.225	157.26	162.74
5	0.3	57.542	262.46

start until the fault-on period during the time domain simulation where one of them would close during the fault-on period to introduce the specific short circuit fault to the system, then they would open at the end of the fault-on period to remove the fault and would remain open until the end of the simulation. The faulted equipment was not removed during fault clearance. This allowed the pre-disturbance and post-disturbance steady-states to be the same and therefore ensured that any differences in study case results would not be due to pre- versus post-disturbance steady-states.

The specific location of the fault during Fault Locations 2–5 was determined by specifying the lengths of both $Z_{i,2}$ and $Z_{i,3}$ transmission lines. The fault-on steady-state retained voltage magnitudes at the inverter station converter busbar, and corresponding $Z_{i,2}$ and $Z_{i,3}$ line lengths are given for each of the five studied fault locations in Table 4.4. Note that transmission line $Z_{i,1}$ maintained a constant length of 320 km in all simulation studies.

4.1.2 LCC-HVDC Link Controllers

The converter control of both the rectifier and inverter ends of the LCC-HVDC link within the simulations used a conventional MCCM with extinction angle control loop and minimum-error selector for control mode selection, in conjunction with DC-side voltage and DC-side current control loops. The control diagram for both rectifier and inverter ends is shown in Figure 4.2. The LCC-HVDC link controllers also contained VDCOLs at both ends.

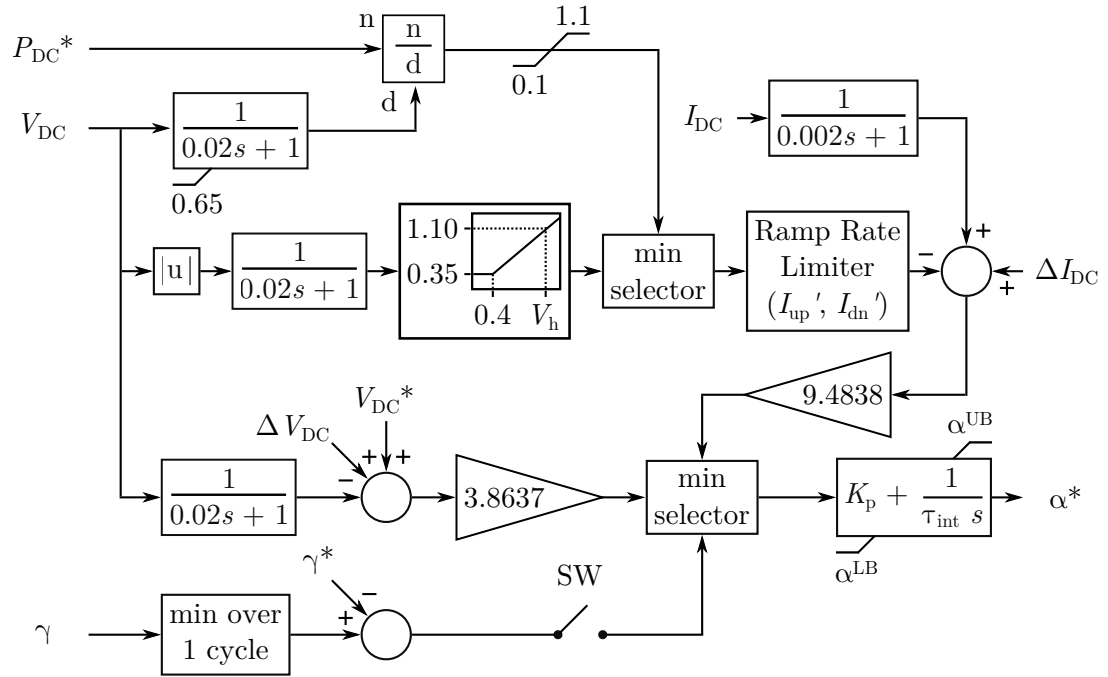


Figure 4.2: Control diagram of LCC-HVDC link converter controllers.

Table 4.5: Nominal set-points and parameters for quantities in Figure 4.2.

Parameter Name	Symbol	Rectifier Value	Inverter Value
Ordered DC-side Power (pu)	P_{DC}^*	1	1
Ordered DC-side Voltage (pu)	V_{DC}^*	1	1
Ordered Extinction Angle (rad)	γ^*	N/A	$0.1 \cdot \pi$
DC-side Voltage Margin (pu)	ΔV_{DC}	2	0
DC-side Current Margin (rad)	ΔI_{DC}	0	0.1
Ordered Firing Angle Upper Bound (rad)	α^{UB}	$0.5 \cdot \pi$	π
Ordered Firing Angle Lower Bound (rad)	α^{LB}	$\frac{1}{36} \cdot \pi$	$0.5 \cdot \pi$

In Figure 4.2, the variables and parameter values which are in common with Figure 3.3 are defined in the same way as for Figure 3.3 in Chapter 3. Switch SW was closed for the inverter station controller, and open for the rectifier station controller, *i.e.* the rectifier controller did not include a extinction angle controller whilst the inverter station controller did.

The parameter values for the constant-valued parameters in Figure 4.2 are given in Table 4.5. Controller parameter values which were optimised during the simulation-based optimisation were: VDCOL upper breakpoint voltage V_h ; VDCOL ramp up and ramp down rate limits I_{up}' and I_{dn}' ; rectifier and inverter PI controller proportional gains $K_{r,p}$ and $K_{i,p}$ indicated by K_p in Figure 4.2; and, rectifier and inverter PI controller integral time constants $\tau_{r,int}$ and $\tau_{i,int}$ indicated by τ_{int} in Figure 4.2.

4.1.3 SVC Plant and Controllers

The SVC study case used an SVC connected via circuit breaker CB_3 in Figure 4.1. The SVC model used components included within the PSCAD/EMTDC Master Library. The model includes an electrical dynamics model first proposed in [60] which models the SVC as a twelve-pulse arrangement with both TSC and TCR elements spread equally between low voltage windings of a three-phase three winding transformer whose high voltage winding connects to CB_3 in Figure 4.1. The system and controller diagrams for the SVC are detailed in Figures 4.3 and 4.4 respectively, where: C_{on} was the number of capacitor stages committed; C_{sw}^* was a capacitor switch signal to switch in or out another TSC element in the SVC electrical dynamics component; B_L was the TCR inductor output susceptance; B^{LB} and B^{UB} were lower and upper bounds on total ordered SVC susceptance; V_T and V_T^* were the measured and ordered power frequency voltage magnitude at the inverter 230 kV busbar of the LCC-HVDC link; and, α_{SVC}^* was the ordered firing angle for the TCR elements within the SVC electrical dynamics component. The PI controller proportional gain K_b and integral time constant τ_b were optimised during the simulation-based optimisation process.

The parameter values for the SVC electrical dynamics model are given in Table C.4 in Appendix C, while the parameter values for the controller in Figure 4.4 are given in Table C.5 in Appendix C. Note that the controller architecture in Figure 4.4 and parameter values in Table C.5 corresponds to an Example Workspace included with PSCAD/EMTDC version 4.6.3 used to demonstrate the SVC model.

4.1.4 STATCOM Plant and Controllers

The STATCOM study case used a two-level VSC-based STATCOM connected via circuit breaker CB_3 in Figure 4.1. The STATCOM model used components included within the PSCAD/EMTDC Master Library, including a transformer model to couple the STATCOM to the inverter 230 kV busbar via CB_3 . The system diagram for the STATCOM is given in Figure 4.5.

The inner current controllers for the STATCOM are detailed in Figures 4.6 and 4.7. The outer controllers for the STATCOM are detailed in Figures 4.8 and 4.9. The DQ/ABC transformations and associated phase locked loop (PLL) are indicated in Figure 4.10.

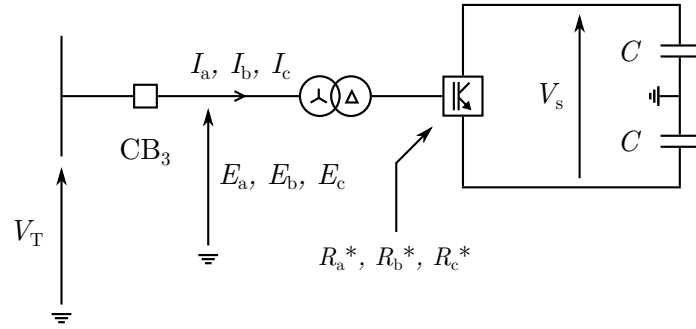


Figure 4.5: System diagram of the STATCOM within the STATCOM study case.

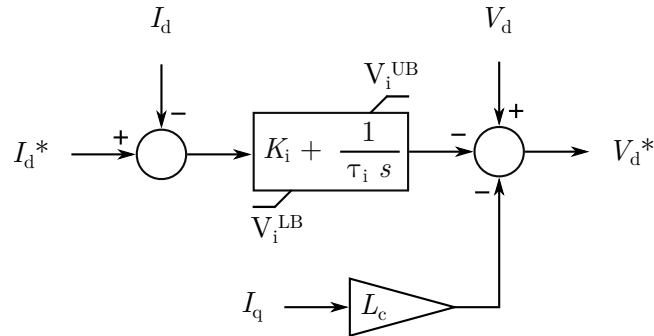


Figure 4.6: Control diagram of the STATCOM D-axis inner current controller within the STATCOM study case.

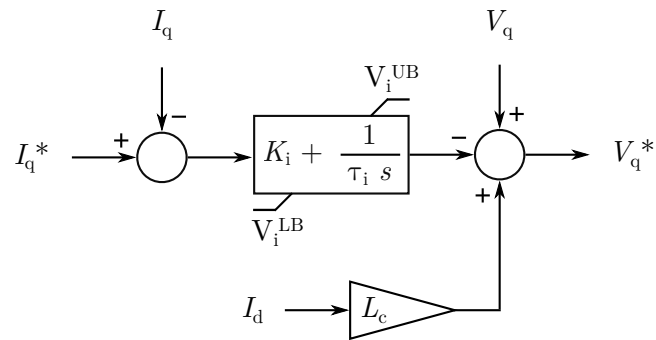


Figure 4.7: Control diagram of the STATCOM Q-axis inner current controller within the STATCOM study case.

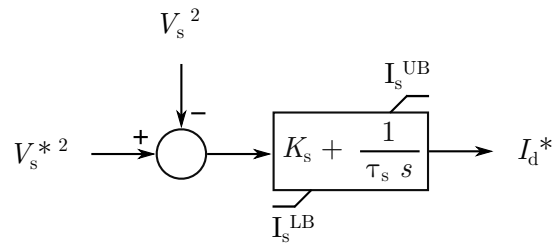


Figure 4.8: Control diagram of the STATCOM D-axis outer controller within the STATCOM study case.

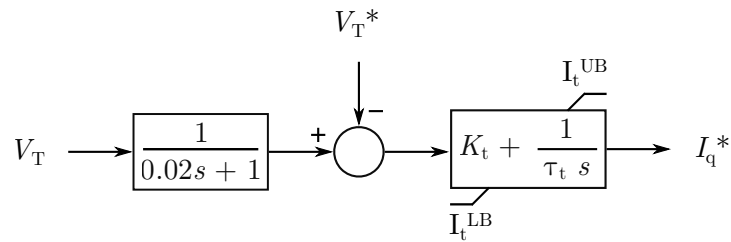


Figure 4.9: Control diagram of the STATCOM Q-axis outer voltage controller within the STATCOM study case.

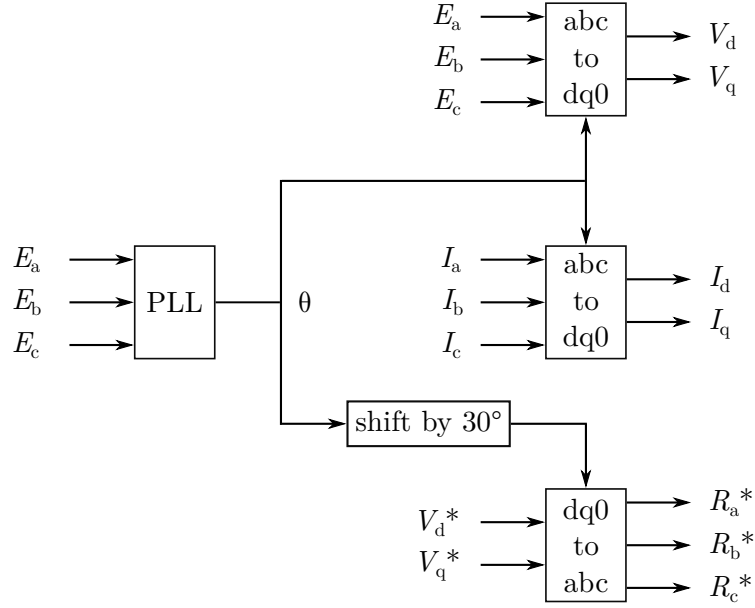


Figure 4.10: Control diagram of the STATCOM PLL and DQ/ABC transformations within the STATCOM study case.

In Figures 4.5–4.10, the following variables are defined. E_a , E_b , and E_c were instantaneous phase-to-earth voltages; and, I_a , I_b , and I_c were instantaneous phase currents. R_a^* , R_b^* , and R_c^* were ordered phase-to-earth reference waveforms sent to the IGBT pulse width modulation (PWM) control. θ was the reference angle locked to the 230 kV inverter busbar voltage A phase. I_d^* and I_d were ordered and measured D-axis currents; V_d^* and V_d were ordered and measured D-axis voltages; I_q^* and I_q were ordered and measured Q-axis currents; V_q^* and V_q were ordered and measured Q-axis voltages; V_s^* and V_s were ordered and measured STATCOM DC-side total voltage; and, V_T^* and V_T were ordered and measured power frequency voltage magnitude at the inverter 230 kV busbar of the LCC-HVDC link.

In Figures 4.5–4.9, the following parameters are defined. Inner current controller D-/Q-axis voltage lower and upper bounds were V_i^{LB} and V_i^{UB} . Outer DC-side voltage controller lower and upper bounds were I_s^{LB} and I_s^{UB} , while outer inverter busbar voltage controller lower and upper bounds were I_t^{LB} and I_t^{UB} . Inner current PI controller

proportional gain and integral time constant were K_i and τ_i ; and, outer DC-side voltage PI controller proportional gain and integral time constant were K_s and τ_s . C was the capacitance between each DC-side conductor and earth. Lastly, L_c was the value of the coupling transformer series reactance through which the STATCOM IGBTs connected to the LCC-HVDC link inverter 230 kV busbar.

Outer inverter busbar voltage PI controller proportional gain K_t and integral time constant τ_t were optimised during the simulation-based optimisation.

The STATCOM plant and control architecture was modified from a model detailed in [61] of a two-level VSC for a solar farm, produced by the software vendor of PSCAD/EMTDC. The STATCOM DC-side was composed of a total DC-side capacitance, split into two equally-sized series-connected capacitors with a mid-point earth connection. Miscellaneous parameter values for the STATCOM plant are detailed in Table C.6 in Appendix C; controller parameter values for the STATCOM are given in Table C.7 in Appendix C.

The inner current PI controller proportional gain and integral time constant K_i and τ_i were selected using the internal model control method [62], assuming a bandwidth of 10% of the VSC switching frequency and a coupling reactance X/R ratio of 20, although the coupling impedance in the simulations was modelled as a simple reactance with no resistance. The outer DC-side voltage PI controller proportional gain and integral time constant K_s and τ_s were selected as follows. Firstly, the DC-side capacitor was assumed to have a transfer function $P(s)$ in (4.1) and the DC-side voltage controller was assumed to have a transfer function $C(s)$ in (4.2).

$$P(s) = \frac{1}{Hs} \quad (4.1)$$

$$C(s) = K_s + \frac{1}{\tau_s s} \quad (4.2)$$

The overall closed-loop system of (4.1) and (4.2) with unity negative feedback is given by $G(s)$ in (4.3).

$$\begin{aligned} G(s) &= \frac{P(s)C(s)}{1 + P(s)C(s)} \\ &= \frac{\frac{K_s}{H}s + \frac{1}{\tau_s H}}{s^2 + \frac{K_s}{H}s + \frac{1}{\tau_s H}} \end{aligned} \quad (4.3)$$

Assuming a damping ratio of $\frac{1}{\sqrt{2}}$, a DC-side energy storage coefficient H value of 0.005, and a closed-loop damped natural angular frequency ω_b of 10% of the inner current controller bandwidth, K_s and τ_s were calculated via (4.4) and (4.5).

$$K_s = \sqrt{2}\omega_b H \quad (4.4)$$

$$\tau_s = \frac{1}{\omega_b^2 H} \quad (4.5)$$

4.1.5 Synchronous Condenser Plant and Controllers

The Synchronous Condenser study case used a synchronous condenser connected via circuit breaker CB_3 in Figure 4.1. The synchronous condenser model used components from the PSCAD/EMTDC Master Library, including the PSCAD/EMTDC synchronous machine electrical dynamics model and a transformer model to couple the synchronous condenser to the inverter 230 kV busbar via CB_3 .

The system diagram and voltage controller for the synchronous condenser are detailed in Figure 4.11 and 4.12 respectively, where: V_T^* and V_T were ordered and measured power frequency voltage magnitude at the inverter 230 kV busbar of the LCC-HVDC link; E_S was the measured power frequency voltage magnitude at the machine's stator; I_F was the measured machine field current; E_F^* was the ordered machine field voltage; and, V_c^{LB} and V_c^{UB} were the exciter voltage controller lower and upper bounds. The voltage

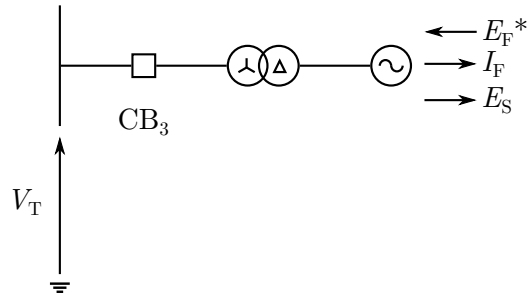


Figure 4.11: System diagram of the synchronous condenser within the Synchronous Condenser study case.

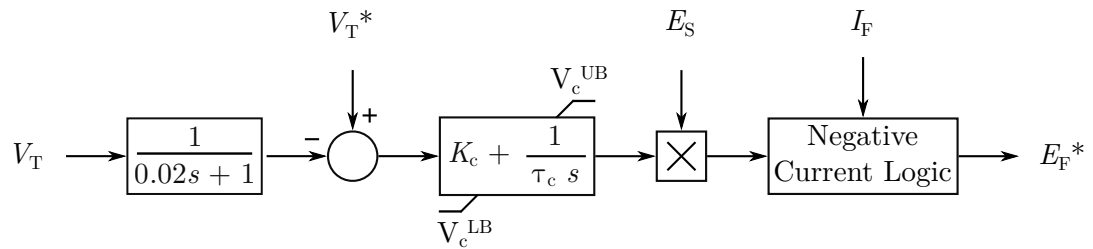


Figure 4.12: Control diagram of the synchronous condenser voltage controller within the Synchronous Condenser study case.

PI controller proportional gain K_c and integral time constant τ_c were optimised during the simulation-based optimisation. The voltage controller included negative current logic which ensured the field current could not be negative. The voltage controller is based upon an “SCRX” excitation model included within the PSCAD/EMTDC Master Library. Machine parameters for the synchronous condenser are given in Table C.8 in Appendix C, and other miscellaneous parameters are given in Table C.9 in Appendix C.

4.2 Simulation-based Optimisation of Study Cases

The study cases described in Section 4.1 were used as part of a controller tuning simulation-based optimisation problem, similar to Problem 2 described in Section 3.3.2. The controller tuning problem was used to evaluate the three different types of dynamic compensators described in Sections 4.1.3, 4.1.4, and 4.1.5 in conjunction with an

LCC-HVDC link described by Sections 4.1.1 and 4.1.2; and, a Base study case described by Sections 4.1.1 and 4.1.2 only.

The controller tuning problem optimised the parameter values of the controllers of the LCC-HVDC link and dynamic compensator voltage controllers where modelled, to reduce the error in the LCC-HVDC link's power transfer during inverter system short circuit faults at different locations over multiple inverter system SCRs. The controller tuning problem ensured that optimal controller values were found for the LCC-HVDC PI controllers and VDCOL parameters, and also the dynamic compensator PI voltage controller where appropriate. These optimal values would ensure a fair comparison amongst the three different dynamic compensator study cases and the Base study case by reducing the influence of bad controller tuning on causing differences in dynamic performance between the study cases.

The tuning problem was considered as a box-constrained, expensive, black-box, simulation-based, optimisation problem. This is because of the necessity of using PSCAD/EMTDC simulations to appropriately model large transient behaviour—*i.e.* the inverter system short circuit faults—as well as the non-linear behaviour of the LCC-HVDC link controllers and plant when subjected to these large transients.

4.2.1 Objective Function

The objective function of the tuning problem considered the ISE between ordered and measured DC-side power of the LCC-HVDC link. The measured power was constructed from the product of the LCC-HVDC link's measured DC-side voltage and measured DC-side current indicated by V_{DC} and I_{DC} respectively in Figure 4.1. The ordered power was a constant of 200 MW during the entire simulation time.

The error in DC-side power was output from the PSCAD/EMTDC simulation as a time series, which was then squared and integrated using trapezoidal integration of the time series values to result in a scalar value of ISE. The scalar values of ISE from multiple simulations were summed together, with the sum being returned to the optimisation

solver method as the objective function. The multiple simulations were due to the cross product of many different inverter AC system fault locations and SCR values; these will be explained in Section 4.2.2.

4.2.2 Operational SCRs and Fault Locations

The tuning problem considered five different operational scenarios: inverter system SCR values of 1.5, 1.625, 1.75, 1.875, and 2.0. In addition, the tuning problem also considered five different inverter system three-phase short circuit fault locations indicated by their steady-state fault-on AC-side voltage magnitude at the inverter station busbar: 0.0 pu, 0.075 pu, 0.15 pu, 0.225 pu, and 0.3 pu. This means that twenty-five simulations were performed for each objective function evaluation, where the set of twenty-five simulations was formed from the cross product of the five inverter system SCR values and the five inverter system fault locations. These twenty-five simulations ran in parallel and were identical to each other apart from the aforementioned inverter system SCR values and fault locations; during each objective function evaluation each of the twenty-five simulations received the same controller parameter values from the solver method to simulate and produce DC-side power error. The ISE of the power for each individual simulation was calculated separately, and then the sum of the twenty-five ISE values was returned back to the optimisation solver method as the objective function value corresponding to the variable values suggested by the solver method for the controller parameter values. Minimisation of this sum of ISEs is equivalent to minimisation of the mean ISE across the twenty-five simulations.

4.2.3 Dynamic Compensator Ratings

For each dynamic compensator study case, three different ratings of the dynamic compensator were studied: 0.2 pu, 0.4 pu, and 0.6 pu. These ratings were on a power base of 200 MVar, *i.e.* a 0.2 pu rating for a compensator corresponded to 40 MVar power rating. The Base study case did not include a compensator therefore compensator rating was irrelevant for the Base study case. Therefore, a total of ten different plant

configurations were studied: the Base study case with no compensator; three different STATCOM configurations of 0.2 pu, 0.4 pu, and 0.6 pu rating in the STATCOM study case; three different SVC configurations of 0.2 pu, 0.4 pu, and 0.6 pu rating in the SVC study case; and, three different synchronous condenser configurations of 0.2 pu, 0.4 pu, and 0.6 pu rating in the Synchronous Condenser study case.

Each plant configuration was solved independently of all other plant configurations, and each plant configuration considered the same twenty-five pairs of inverter system SCR and fault locations.

4.2.4 Short Circuit Fault Disturbance Application

The short circuit fault disturbances were embedded within the PSCAD/EMTDC study case simulations, with the events during the simulation occurring at the following time stamps:

1. $t = 0.10\text{ s}$: CB_1 closed if modelling Fault Location 1, otherwise CB_2 closed; and
2. $t = 0.15\text{ s}$: CB_1 opened if modelling Fault Location 1, otherwise CB_2 opened.

Every simulation was 2.1 s long: an initial 0.1 s to ensure pre-fault steady-state operation could be demonstrated; followed by a three-cycle short circuit fault; and then ending with a further 1.95 s of simulation run time to ensure asymptotic post-fault recovery back to a post-fault steady-state. The time series of the measured DC-side power over the entire simulation of 2.1 s was used as part of the objective function calculation described previously.

Note that the applied short circuit fault was applied and then cleared by simply adding and then removing the fault from the inverter system using circuit breakers CB_1 or CB_2 ; the equipment to which the fault was connected was not itself switched out of service when clearing the fault.

4.2.5 Dynamic Compensator Reactive Power Initialisation

In order to ensure a fair comparison, the simulations were initialised in such a way that the dynamic compensators did not exchange any reactive power with the inverter system in the pre-fault steady-state. Since the faults were modelled by switching in and out of a fault without the simultaneous disconnection of any faulted equipment, this meant that the post-fault steady-state would be equal to the pre-fault steady-state; except where controller tuning due to a particular set of controller parameter values being evaluated by the optimisation solver method may have prevented this. Therefore, quantitative differences in results between plant configurations would only be the result of the compensator type, size, and optimal controller tuning rather than due to different pre-fault steady-state reactive power exchanges from the compensators.

4.2.6 Selected Solver Method and Optimisation Problem Variables

The optimisation solver method selected for the tuning problem was Solver Method MARS as described in Section 3.1.5. The same parameter values in Section 3.1.5 for the solver method algorithm were used over all study cases in this Chapter.

Up to nine optimisation variables were tuned in the controller tuning problem: seven variables in the Base study case; and nine in the dynamic compensator study cases. The dynamic compensator study cases included all seven of the Base study case variables, and an additional two variables for the PI voltage controller for the dynamic compensator.

The seven optimisation variables shared amongst all four study cases—Base, Synchronous Condenser, STATCOM, and SVC—are:

1. Rectifier proportional gain $K_{r,p}$;
2. Inverter proportional gain $K_{i,p}$;
3. Rectifier integral time constant $\tau_{r,int}$;
4. Inverter integral time constant $\tau_{i,int}$;
5. VDCOL upper voltage breakpoint V_h ;

6. VDCOL ramp up rate limit I_{up}' ; and
7. VDCOL ramp down rate limit I_{dn}' .

The eighth and ninth optimisation variables in the three dynamic compensator study cases—Synchronous Condenser, STATCOM, and SVC—are as follows:

- exciter proportional gain K_c , and exciter integral time constant τ_c in the Synchronous Condenser study case;
- voltage controller proportional gain K_b , and voltage controller integral time constant τ_b in the SVC study case; and,
- outer Q-axis voltage controller proportional gain K_t , and outer Q-axis voltage controller integral time constant τ_t in the STATCOM study case.

The LCC-HVDC link rectifier and inverter proportional gains and integral time constants, and VDCOL upper voltage breakpoint V_h , ramp up rate limit I_{up}' , and ramp down rate limit I_{dn}' parameters are indicated in Figure 4.2. Note that the rectifier and inverter proportional gains and integral time constants are independent for each converter station, but the three VDCOL parameters are shared by the VDCOLs at both converter stations. The voltage controller proportional gain K_b and voltage controller integral time constant τ_b in the SVC study case are indicated in Figure 4.4. The outer Q-axis voltage controller proportional gain K_t and outer Q-axis voltage controller integral time constant τ_t in the STATCOM study case are indicated in Figure 4.9. The exciter proportional gain K_c and exciter integral time constant τ_c in the Synchronous Condenser study case are indicated in Figure 4.12.

In all four study cases, the bounds of the rectifier and inverter proportional gain and integral time constant optimisation variables were as follows: all lower bounds set to 0.01; and all upper bounds set to 1.0. The lower and upper bounds of the VDCOL upper voltage breakpoint were 0.52 and 0.95 respectively. For both the ramp up and ramp down rate limits, the lower and upper bounds of both were 0.667 and 21.091 respectively. In the Synchronous Condenser study case, the exciter proportional gain upper and lower

bounds were set to 1000 and 10 respectively, while the exciter integral time constant upper and lower bounds were set to 1 and 0.01 respectively. In the STATCOM study case, the outer Q-axis voltage controller proportional gain and integral time constant upper and lower bounds were set to 1 and 0.01 respectively. In the SVC study case, the voltage controller proportional gain upper and lower bounds were set to 3.1623 and 0.031623 respectively, while the voltage controller integral time constant upper and lower bounds were set to 1 and 0.01 respectively.

4.2.7 Optimal Solution Samples

The selected Solver Method MARS was a stochastic solver method, *i.e.* optimal solutions returned by the solver method would in general be different over repeated independent solution runs of the solver method on the same optimisation problem with identical parameters and experimental budget. A sample of optimal solutions was drawn for a plant configuration from the set of 10 possible plant configurations, where each observation in the sample was the best found objective function value from an independent solution run of the solver method on the controller tuning problem.

When all 10 samples were drawn—1 for each plant configuration where each sample comprised multiple independent observations—then sample statistics were calculated and confidence intervals for those sample statistics estimated where appropriate.

4.2.8 Overall Number of Simulations Performed

Each sample included 30 independent observations, and each plant configuration was solved by the solver method with an experimental budget of 200 evaluations, *i.e.* 200 sets of PSCAD/EMTDC simulations. Overall, 1500000 simulations in total were performed due to the product of: 5 inverter system SCR scenarios; 5 inverter system fault locations; 30 independent solver method runs; 200 evaluations per solver method run; and 10 different plant configurations created from 1 Base study case and 3 dynamic compensator study cases with 3 different compensator ratings.

4.3 Measured Variables and Performance Functions

In each simulation, 5 time domain variables were measured over the entire length of the 2.1 s simulation. These variables were:

1. inverter system power frequency AC-side voltage magnitude at converter busbar V_T ;
2. DC-side voltage magnitude of the LCC-HVDC link V_{DC} ;
3. DC-side current magnitude of the LCC-HVDC link I_{DC} ;
4. DC-side power of the LCC-HVDC link P_{DC} ; and
5. extinction angle of the LCC-HVDC link inverter γ .

For each of the 5 measured variables' time series, 6 performance functions were applied in order to calculate 6 scalar-valued performance values per measured variable time series. These performance values could then be used for quantitative evaluation purposes.

These performance values were:

1. recovery time after fault clearance of a measured variable to above 0.8 pu of the measured variable's pre-fault steady-state value;
2. settling time after fault clearance of a measured variable to within 0.9 pu and 1.1 pu of the measured variable's pre-fault steady-state value;
3. overshoot of a measured variable after fault clearance;
4. ISE of a measured variable compared to the measured variable's pre-fault steady-state value;
5. IAE of a measured variable compared to the measured variable's pre-fault steady-state value; and
6. integral time absolute error (ITAE) of a measured variable compared to the measured variable's pre-fault steady-state value.

Therefore, each simulation generated 30 performance values, calculated using

the 6 performance functions applied to each of the 5 measured time domain variables recorded from the simulation.

Although only 1 of the 30 performance values was used by the optimisation solver method—ISE of DC-side power of the LCC-HVDC link as explained in Section 4.2.1—as part of the objective function to choose different control system parameters to evaluate, the other 29 performance values would in general also be affected by the choice of controller system values.

4.4 Engineering Feasible Result Screen

In order to make fair comparisons between different plant configurations, a screen was applied to time domain results from each sample of 30 observations to generate a variable length sub-sample of *engineering feasible* results. Note that this engineering feasible term is used to describe a sub-sample of the solutions provided by the solver method as being qualitatively acceptable to an engineer, rather than mathematically feasible from the perspective of the box constraints with which the solver method complied. This sub-set was selected since the mathematical optimisation problem could result in mathematically feasible solutions which had unacceptable qualitative time domain behaviour of measured variables as assessed by engineering judgement and therefore were regarded as not being engineering feasible in this thesis.

In the Base study case, all observations where the measured DC-side power settled to within 0.9 pu and 1.1 pu of the pre-fault steady-state DC-side power value within 1.5 s of the fault application for all fault locations and inverter system SCRs were regarded as being within the engineering feasible sub-set.

In any of the dynamic compensator study cases, the engineering feasible sub-set of observations for all fault locations and inverter system SCRs was where those observations resulted in both: the measured DC-side power settling to within 0.9 pu and 1.1 pu of the pre-fault steady-state DC-side power value within 1.5 s of the fault application; and, the measured reactive power exchange from the dynamic compensator to the inverter

station busbar settling to within -0.1 pu and 0.1 pu within 1.5 s of the fault application.

These engineering feasible sub-sets therefore ensure that results evaluated within this thesis are qualitatively closer to those that would be expected by an engineer; *i.e.* these engineering feasible results are those where the controller values selected by the stochastic solver method did not result in an excessively slow HVDC link power recovery, and did not result in a long transient exchange of reactive power from dynamic compensators with the inverter AC system within the dynamic compensator study cases. In the pre- and post-disturbance states, the compensator steady-state reactive power exchange was zero; therefore reactive power would only be exchanged to any significant degree due to power system and controller dynamics associated with the fault application and clearance.

4.5 Sample Statistics

In this thesis, 6 different sample statistics are considered for each of the 30 performance values. These sample statistics are as follows, with sections explaining the sample statistics specified in brackets:

1. sample minimum (Section 4.5.1);
2. sample mean (Section 4.5.1);
3. difference in sample means between two independent samples (Section 4.5.2);
4. difference in sample minima between two independent samples (Section 4.5.2);
5. Kendall's Tau-c association between ranks of sample means, and a proposed hypothetical Ranking (Section 4.5.3); and
6. Kendall's Tau-c association between ranks of sample minima, and a proposed hypothetical Ranking (Section 4.5.3).

Note that the statistic representing the difference in sample means between two independent samples is the same statistic used in Section 3.5.

Each of the 6 sample statistics above were subjected to the same basic bootstrap computational procedure as described in Section 3.5 in-place of the difference between means sample statistic described in Section 3.5. This bootstrap procedure was used to estimate a 95% confidence interval to indicate an estimated range of values for the population parameter corresponding to the relevant sample statistic.

4.5.1 Sample Means and Sample Minima

Since the engineering feasible samples include multiple observations drawn from random variables where the randomness is due to the stochastic optimisation solver method, there is a statistical question as to what sample statistics calculated on these samples should be used to inform engineers about a plant configuration's capabilities with respect to dynamic compensation of an LCC-HVDC link.

In this thesis, 2 of the 6 sample statistics are sample means and sample minima. The means are considered due to the pedigree of sample means within the subject area of statistics. The minima are recorded since they are more interesting to engineers when assessing the minimisation of the results of the 6 performance functions applied to each of the 5 measured variables for the different plant configurations. Note that 95% confidence intervals (CIs) are only estimated via bootstrapping for the sample mean and not for the sample minima. Only the observed sample minima is included. This is because basic bootstrapping does not provide useful CIs for sample minima.

4.5.2 Differences in Sample Means and Sample Minima

Sample statistics of mean and minima are not sufficient to determine which plant configurations are superior with respect to different performance values. Differences in sample means, and differences in sample minima, are two additional sample statistics recorded with 95% CIs to infer population differences between plant configurations. Differences in sample means is the the same strategy used in Section 3.5 to infer population differences in solver method optimisation superiority.

4.5.3 Ranking of Plant Configurations

Kendall's Tau-c associations [63] are calculated to evaluate observed ranks of plant configuration sample statistics—both means and minima are assessed separately—with hypothetical Rankings derived from engineering judgment.

Kendall's Tau-c is a scalar value within the interval $[-1, 1]$ which measures the strength of association between two samples of scalar values. In this thesis, Kendall's Tau-c association values are used to score how much a hypothetical Ranking of plant configurations agrees with the actual ranking observed from the result data for some sample statistic, applied for each performance function applied to each measured variable.

A Kendall's Tau-c value closer to 1 indicates strong association between the observed ranking and hypothetical Ranking, while a value closer to -1 indicates strong anti-association between the observed ranking and hypothetical Ranking. A value close to 0 indicates minimal or even no association between the observed ranking and hypothetical Ranking. Therefore association values of high magnitude regardless of sign indicate that a hypothetical rank order is a good association or anti-association match compared to observed ranks of sample statistics from the plant configurations' result data. The sign indicates if there is an association or anti-association between the proposed Ranking and the observed ranking from the data.

In this thesis, 8 different hypothetical Rankings of the 10 plant configurations are modelled. These are listed in Table 4.6 where Rank 1 is asserted to be the best and the highest rank value being asserted to be the worst. In each Ranking, ranks are arranged in ascending order from best to worst, *i.e.* smallest value of a performance function sample mean or sample minima is given rank 1. Multiple plant configurations per rank indicate those configurations are asserted as equal in rank in that specific hypothetical Ranking, *i.e.* they are asserted to have equal ranks of sample statistics calculated from observations of performance values.

Rankings A–D all assume the plant configurations never share ranks. Ranking A assumes

Table 4.6: Proposed Rankings of plant configurations for both means and minima of performance functions applied over all measured variables.

Plant Configuration		Proposed Rankings							
Compensator Type	Compensator Rating (pu)	A	B	C	D	E	F	G	H
SC	0.6	1	1	1	1	1	1	1	1
SC	0.4	4	4	2	2	1	2	2	2
SC	0.2	7	7	3	3	1	3	3	3
STATCOM	0.6	2	3	4	7	3	1	4	6
STATCOM	0.4	5	6	5	8	3	2	4	5
STATCOM	0.2	8	9	6	9	3	3	4	4
SVC	0.6	3	2	7	4	2	1	4	5
SVC	0.4	6	5	8	5	2	2	4	5
SVC	0.2	9	8	9	6	2	3	4	4
Base (no compensator)	N/A	10	10	10	10	4	4	5	7

dynamic compensator rating is most important for minimising performance values, and compensator type is of secondary importance. Ranking B is similar to Ranking A but with SVCs being ranked more importantly than STATCOMs for similar ratings.

Rankings C and D are similar to Rankings A and B respectively, except the compensator type takes primary importance while the compensator size is of secondary importance.

Rankings E and F rank plant configurations by only compensator type or only compensator size, respectively.

Ranking G and H are derived from manual visual inspection of the performance value box-plots in Appendix E, and the sample statistic and differences in sample statistics in Appendices F, G, and H. Ranking G assumes that synchronous condensers outperform all other plant configurations, with larger synchronous condensers performing better than smaller condensers; meanwhile all of the SVC and STATCOM plant configurations are all similar and only outperform the Base study case. Similar to Ranking G, Ranking H also assumes that synchronous condensers outperform all other plant configurations, with larger synchronous condensers performing better than smaller condensers. Ranking H then assumes with increasing inferiority: a small STATCOM ranks similarly to a small

SVC; intermediate and large SVC ratings rank similarly to an intermediate STATCOM; followed penultimately by a large STATCOM. Lastly, the Base study case is assumed inferior to the aforementioned dynamic compensators in Ranking H.

Since Kendall's Tau-c is a sample statistic calculated between two samples, there is a corresponding unknown population parameter which may be inferred from the Kendall's Tau-c sample statistic and its corresponding 95% CI. The CI was calculated from bootstrapping of the observed rank data; the proposed hypothetical Rankings were not bootstrapped since they are not random.

4.6 Results and Discussion

All elements of this discussion should be understood as referring to results which have been optimised considering a single objective of minimising mean LCC-HVDC link DC-side power ISE over a set of inverter AC system fault locations and SCRs. This means that although there are statistical differences between plant configurations for the 4 measured variables other than LCC-HVDC link DC-side measured power, this does not mean that differences between plant configurations for those measured variables will remain constant under all circumstances. For example, plant configurations may exhibit different relative performances from those results found in this thesis if: an alternative controller optimisation objective other than minimising LCC-HVDC link DC-side power ISE is selected; or, if multi-objective optimisation is performed considering optimisation of many measured variable errors simultaneously.

In addition, this discussion is also predicated on results generated from the particular study cases modelled in this thesis, which typically used somewhat simplistic representations of plant controllers than may be encountered in practical applications especially in low SCR AC systems. The importance of this discussion is in demonstrating the variety of complex behaviours of the performance values which have been elicited from the proposed dynamic compensation evaluation strategy using stochastic simulation-based optimisation. In practical settings, this methodology would help

engineers discover quantitative differences between engineer-specified plant configurations over many different engineer-specified measured variables and performance functions, specific to the engineer's particular problem under consideration.

Therefore the only generalisable result to practical systems which may be gleaned from these study case results generated from the proposed evaluation methodology is as follows. Engineers must be careful with their choice of plant configurations to be evaluated, and what aspects of those designs should be measured and quantified using performance functions which are aligned with the engineer's specific dynamic compensation problem and the engineer's value system for optimally solving that engineering problem.

It is clear that qualitative differences exist depending on the choice of sample statistic used to describe some aspect of random samples: in many causes, plant configurations rank differently on the same performance function for the same measured variable when assessing means instead of minima. This implies that a key issue with engineering design solution methodologies incorporating stochastic mechanisms is the selection of suitable sample statistics which are aligned with the engineer's motivations. These stochastic mechanisms could arise due to stochastic optimisation solver methods—which is the case in this thesis—or due to random sampling of power system operational scenarios, for example.

4.6.1 Similarity of Selected Time Domain Variables from Time Domain Plots

Some time domain plots are provided in this thesis which show the progression of selected measured variables over time during selected inverter system SCR and inverter fault location situations. Three measured variables are included: DC-side measured power; AC-side measured voltage magnitude at the inverter busbar; and DC-side measured voltage. Plots are drawn for two fault locations named by their steady-state fault-on retained voltage at the inverter AC-side busbar: 0.0 pu, *i.e.* fault at the inverter busbar; and, 0.3 pu, *i.e.* fault furthest away from the inverter station. Plots are drawn for two inverter system SCRs as seen at the inverter AC-side busbar: 1.5 and 2.0. The plots are

included in Appendix D.

The purpose of including the time domain plots in Appendix D is to show the qualitative similarity of best found engineering feasible optimal solutions amongst all plant configurations, with respect to the different measured variables over time. Although there are substantial differences between plant configurations across Figures D.1–D.10 during the transient period immediately following inverter system short circuit fault clearance, all of the plant configurations asymptotically converge to post-fault steady-states which are the same as the pre-fault steady-states. This is shown by example in Figures 4.13 and 4.14 which are copies of Figures D.1 and D.2 respectively in Appendix D.

Figures 4.13 and 4.14 show measured DC-side power through the LCC-HVDC link over the entire simulation time during short circuit fault application and clearance when the inverter AC system SCR was equal to 1.5. Plot columns in Figures 4.13 and 4.14 correspond to 2 of the 5 different fault locations, specifically the most remote fault—with steady-state fault-on retained voltage of 0.3 pu—and the closest fault—with steady-state fault-on retained voltage of 0.0 pu, *i.e.* at the inverter station busbar. Plot rows in Figures 4.13 and 4.14 correspond to the three different possible dynamic compensator ratings studied; note that the “Base” study case results are the same across all three dynamic compensator ratings.

Note that the traces in Figures 4.13 and 4.14 all start and end with a steady-state DC-side power transfer; yet the actual responses of the best found optimal parameter selections for the “Base” study case and the three different compensators are qualitatively different during the transient recovery period immediately after fault clearance. The responses from all plant configurations are generally worse during the fault at the inverter AC-side busbar compared with the remote fault location, yet it is difficult to firmly declare which compensator ratings and types between SVC and STATCOM give typically superior responses. These facts confirm the need for quantitative evaluation between the compensators by statistical comparison.

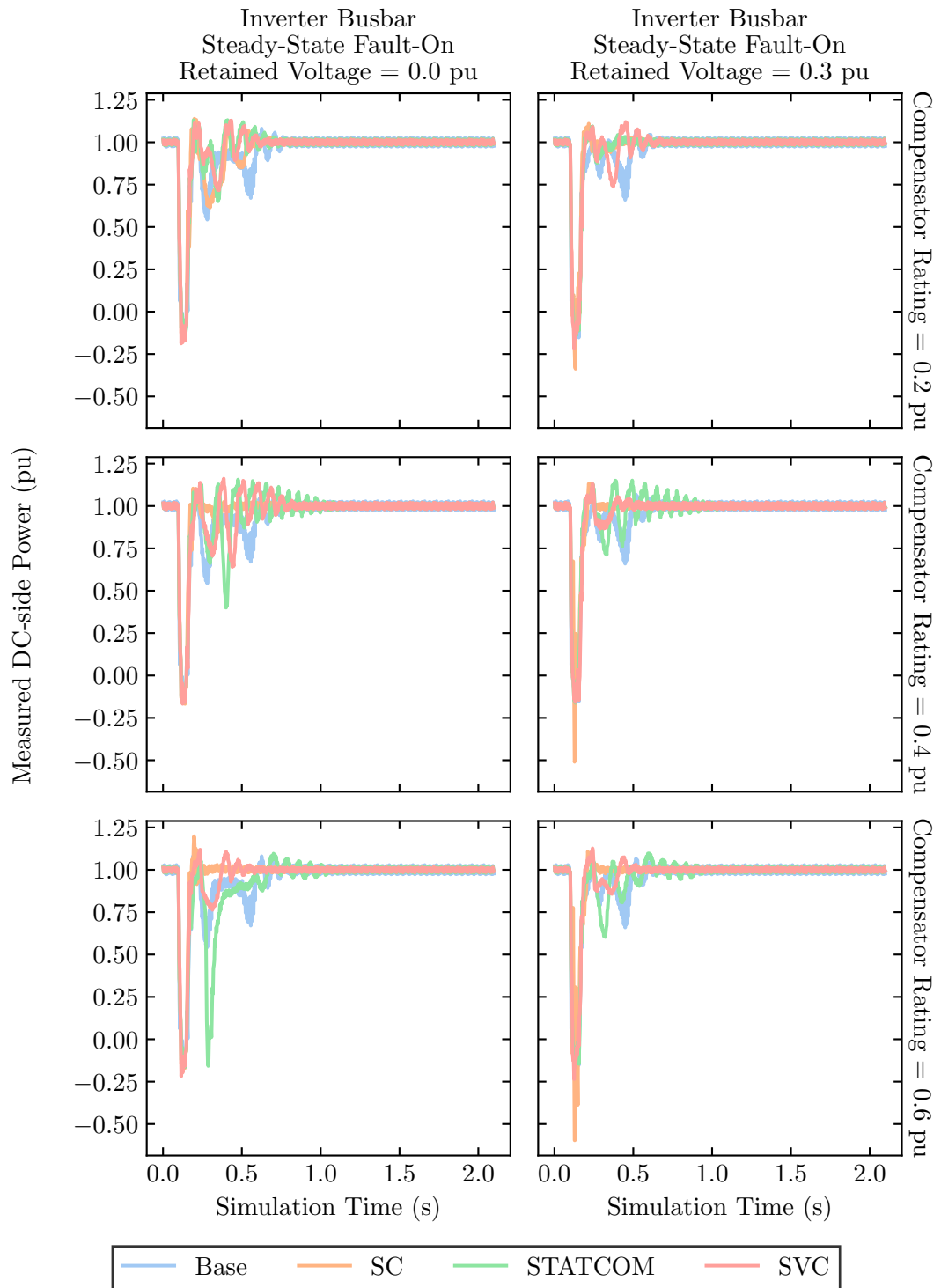


Figure 4.13: DC-side measured power time domain traces for inverter SCR of 1.5.

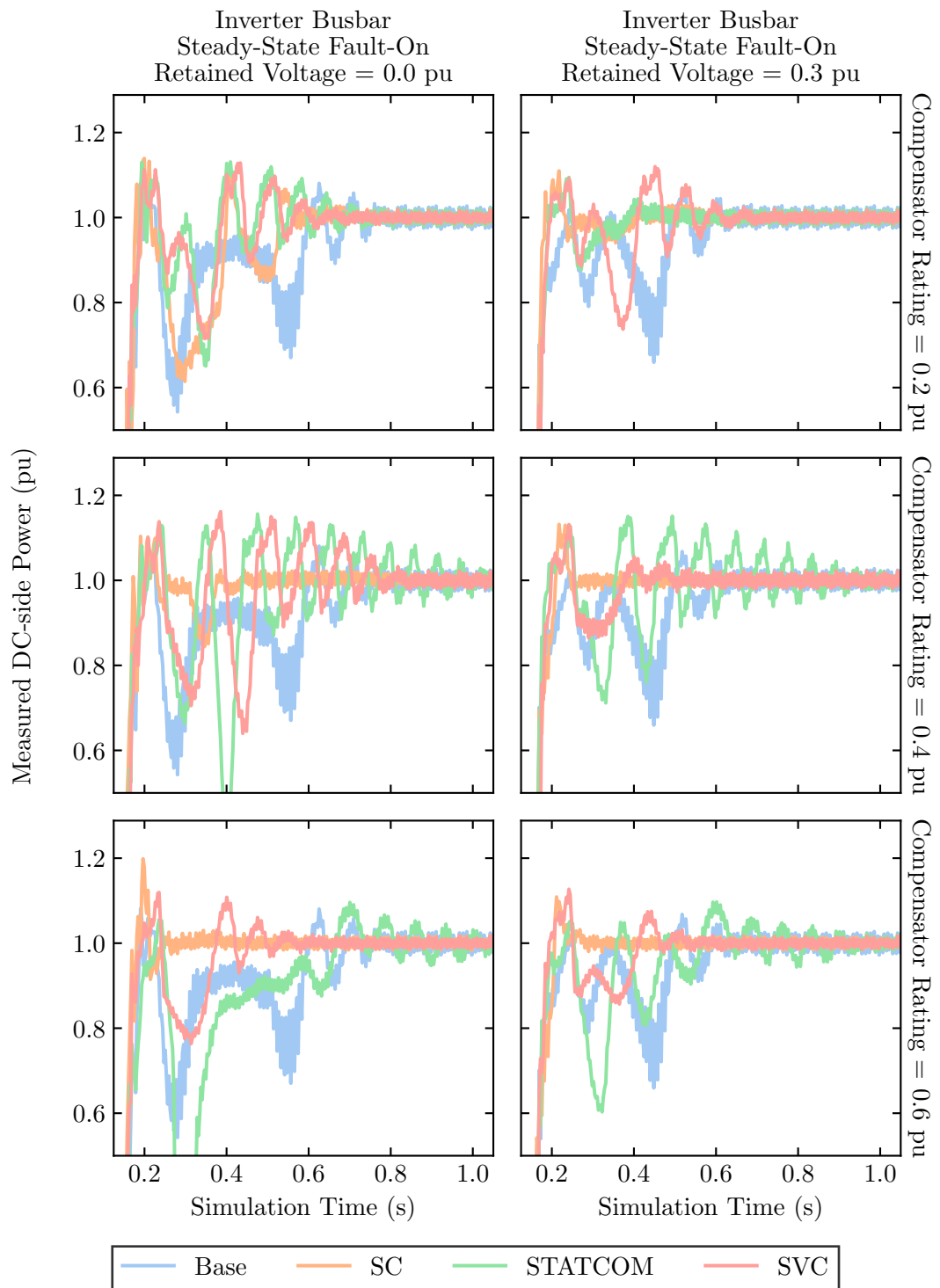


Figure 4.14: Zoomed view of DC-side measured power time domain traces for inverter SCR of 1.5.

4.6.2 Observations from Box-plots, Plots of Sample Means, and Plots of Sample Minima

Descriptive statistical information for all of the plant configurations is provided via box-plots for: the 30 specific performance values; and the 7 LCC-HVDC link controller parameter values returned by the optimisation solver method. The data in both types of box-plots correspond to the engineering feasible sub-sets screened from the samples of 30 optimal solutions returned by the solver method. The box-plots are included in Appendix E: the performance value box-plots specifically are included in Section E.1; while the LCC-HVDC link controller parameter value box-plots specifically are included in Section E.2.

Figure 4.15 is a copy of Figure E.1 in Section E.1. Figure 4.15 shows both the individual engineering feasible observations and the descriptive box-plots of those samples of observations for the 6 different performance functions applied to the measured DC-side power of the LCC-HVDC. Each plot in Figure 4.15 corresponds to the performance values calculated via one of the performance functions. By visual inspection of Figure 4.15, is clear that there are qualitative differences between the samples drawn for each of the plant configurations. Some boxes are locationally different from others, while many box-plots have different dispersions of observations within their sample.

These same observations are shared with the box-plots in Figures E.1–E.5 for all 5 measured time domain variables; differences in the box-plots provide more evidence that quantitative methods to evaluate plant configuration performances are necessary, since it is difficult to infer population differences between plant configurations by visual inspection of the boxes in Figure 4.15.

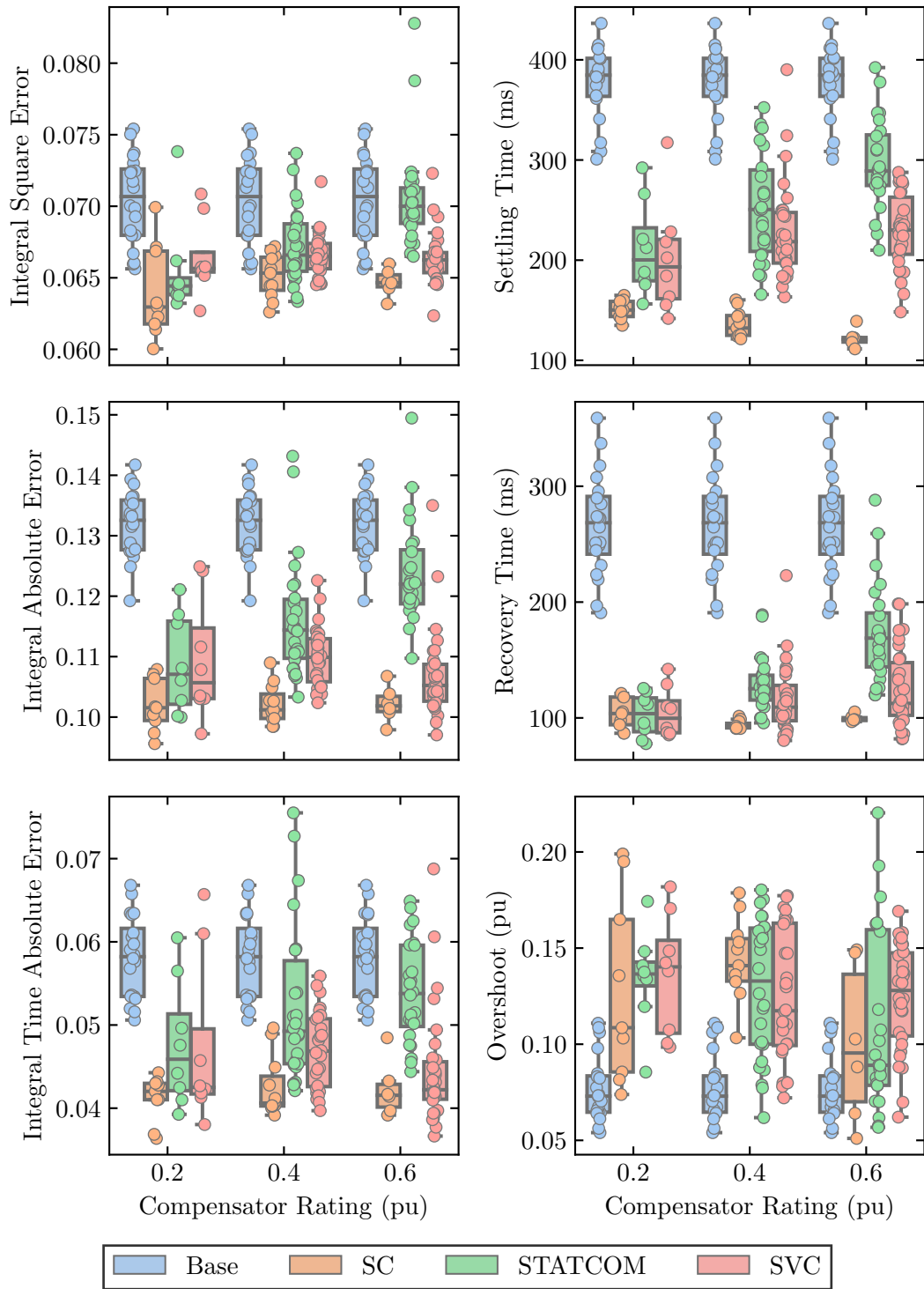
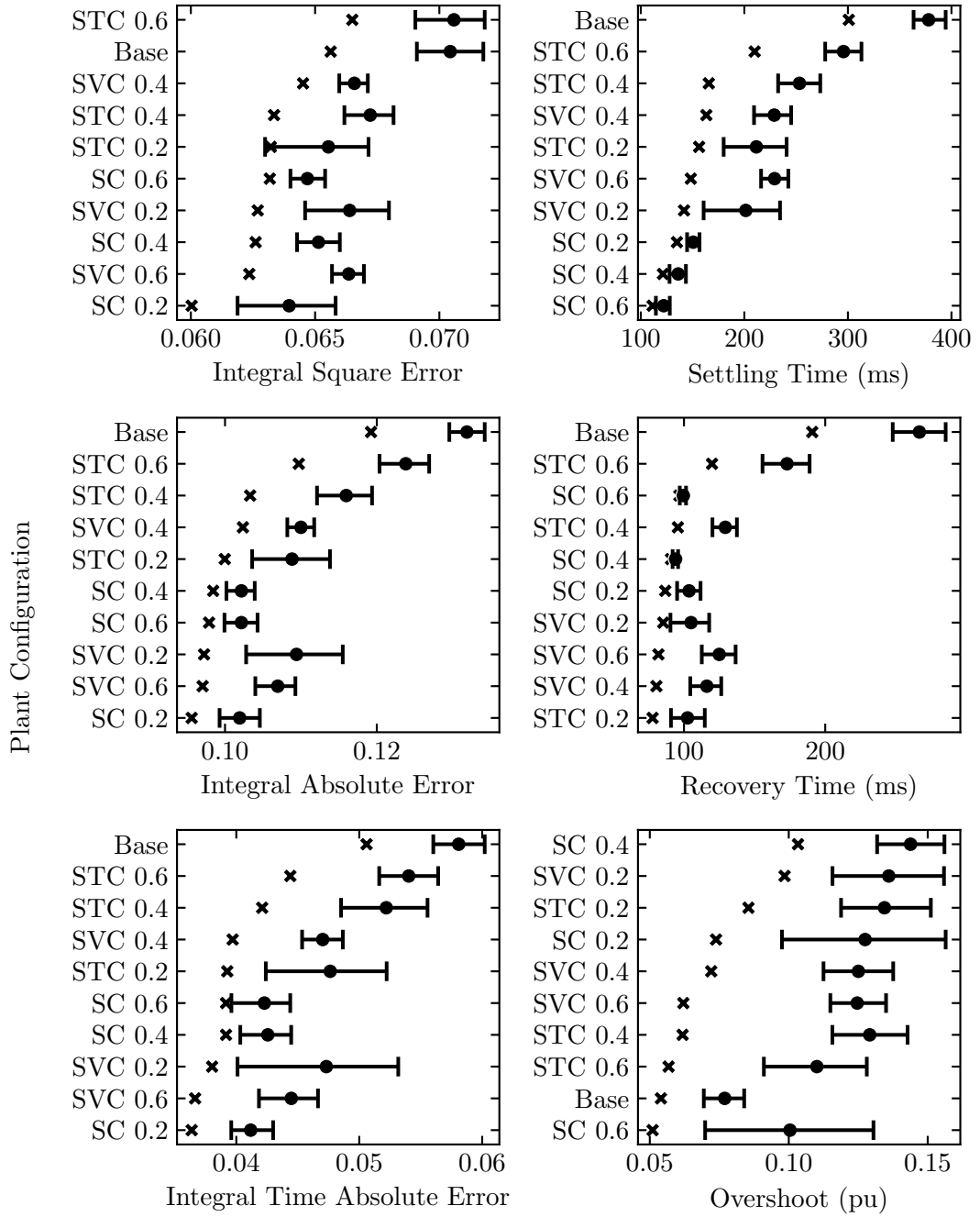


Figure 4.15: Box-plots of performance values of DC-side measured power.



Plant Configuration Sample Means (with 95% CI), and Sample Minima

Figure 4.16: DC-side measured power sample statistics.

Chapter 4. A Method to Evaluate Dynamic Compensators for the Improvement of LCC-HVDC Link Dynamic Performance

Plots of the sample means and sample minima are included in Appendix F. Figure 4.16 is a copy of Figure F.1, and shows sample minima and sample means of the performance values calculated via the 6 different performance functions applied to measured DC-side power of the LCC-HVDC link. Round markers indicate observed sample means, and cross markers indicated observed sample minima. Furthermore, 95% CIs are provided for the population mean estimated via bootstrapping.

Note that plant configurations on the y-axes in Figure 4.16 are labelled as follows: compensator type, then compensator size. In this circumstance compensator type may include “Base”, *i.e.* the Base study case results with no compensator actually connected. For example “SC 0.2” corresponds to a synchronous condenser of 0.2 pu rating defined using a 200 MVar base power. Note that the “STC” compensator is the STATCOM.

In Figure 4.16 it is clear that although there is somewhat of a visual association between sample minima and sample means, there are circumstances where some plant configurations have sample minima closer in value to their sample means, *e.g.* synchronous condenser settling time results. Furthermore, there is a variety of lengths of 95% CIs across the plant configurations. The results in Figure 4.16 provide more direct evidence of differences in plant configurations’ performance values than can be seen in Figures 4.13–4.15, but it is still not quantitatively clear which plant configurations can be assumed to have significant differences between each other. This is indicated by some plant configurations’ 95% CIs overlapping each other even when those configurations’ sample means are different.

Some qualitative observations can be noted from visual inspection of measured variables’ performance values in Appendix E and sample mean and minima statistics in Appendix F.

A theme common across many—although not all—of the performance values over all box-plot Figures E.1–E.5 and over all sample mean and minima Figures F.1–F.5 is that any type of dynamic compensator helps to improve dynamic performance of the Base study case LCC-HVDC link.

A frequent exception to this theme is in the case of overshoot, where dynamic compensator

plant configurations typically exhibited larger overshoots than what otherwise occurred in the Base study case as can be seen for example by the relative positions of “Base” labels on y-axes across Figures F.1–F.5. Another exception is measured extinction angle in Figures E.5 and F.5, where the Base study case often had good performance for performance values compared to dynamic compensators—apart from recovery time of extinction angle.

A possible explanation for the larger overshoots in compensator results compared with the Base study case is the transient injection of reactive power from the compensators causing high AC-side voltages, before the compensator feedback control can regulate reactive power injection sufficiently to regulate AC-side voltage towards the set-point.

As for the relatively good extinction angle performance values’ in the Base study case compared to the compensators, the compensator reactive power injection is closely associated with the LCC-HVDC link extinction angle. An excess reactive power injection from the compensator could be counteracted from a DC-side power transfer perspective via the LCC-HVDC link transiently operating at a higher extinction angle and therefore resulting in acceptably regulated power transfer from the perspective of the simulation-based optimisation solver method. In this case, there is little incentive to the optimisation solver method to tune controllers to preferentially force the compensator to regulate its reactive power transfer in consideration of inverter AC-side voltage deviations instead of allowing variable extinction angle control of the LCC-HVDC link to do so. This is due to the single optimisation objective which only considers LCC-HVDC link real power transfer.

Note that the difficulty in determining significant differences between plant configurations for different performance values and measured variables via visual inspection of plots in Figures E.1–E.5 and F.1–F.5 in Appendices E and F is what motivates the effort to statistically analyse differences in these sample statistics, with the results given in Appendices G and H and discussion provided below.

4.6.3 Observations from Differences in Sample Means

Two-sample comparisons using differences between sample means via 95% CI, between all 10 different plant configurations for each performance function result and for each measured variable are included in Appendix G. An example of such two-sample comparisons is provided in Figure 4.17 which is a copy of Figure G.1.

Figure 4.17 shows differences between sample means, and the associated 95% CIs for two performance functions for measured DC-side power of the LCC-HVDC link. Plant configurations on the y-axis should be read as follows: “compensator 1 type, compensator 1 rating — compensator 2 type, compensator 2 rating”. In this circumstance compensator 1 type and compensator 2 type may include “Base”, *i.e.* the Base study case results with no compensator actually connected. For example, “Base — STC 0.2” corresponds to the subtraction of the STATCOM sample mean from the Base sample mean specifically where the STATCOM rating is 0.2 pu of a defined base power of 200 MVar. Results marked with an asterisk are statistically significant, *i.e.* where the 95% CIs does not include zero. Therefore, intervals which lie to the right of zero indicate compensator 2 had a statistically significant small magnitude sample mean compared to compensator 1 sample mean. Intervals which lie to the left of zero indicate compensator 2 had a statistically significant large magnitude sample mean compared to compensator 1 sample mean.

In the case of “Base — STC 0.2” IAE in Figure 4.17, the interval is wholly to the right-hand side of the x-axis zero line and so the 0.2 pu STATCOM can be inferred to have smaller population mean IAE than the population mean IAE of the Base LCC-HVDC link with no compensator, specifically when considering IAE of the measured DC-side power of the LCC-HVDC link. In the case of “SC 0.2 — STC 0.2” in Figure 4.17, the CI of IAE difference in means is wholly to the left-hand side of x-axis zero implying the 0.2 pu synchronous condenser to typically provide smaller IAE values than the 0.2 pu STATCOM because the population mean of 0.2 pu synchronous condenser is inferred to be smaller than the 0.2 pu STATCOM population mean; but, the CI of ISE for

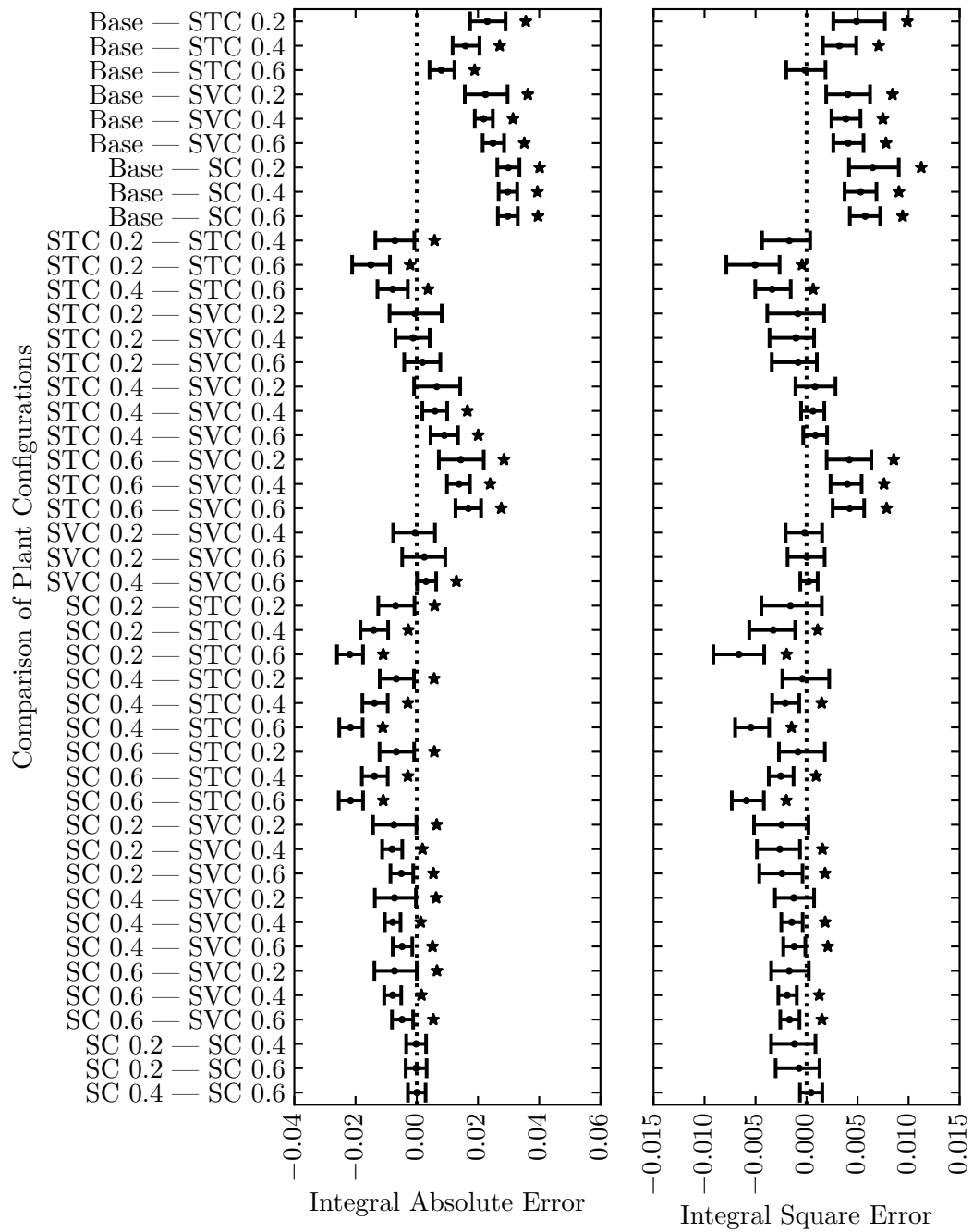
“SC 0.2 — STC 0.2” includes zero which infers that no difference in population means can be assumed in the case of ISE. This means that significant difference between 0.2 pu synchronous condenser and STATCOM means has been detected for the IAE performance function but not the ISE performance function, specifically when considering measured DC-side power of the LCC-HVDC link.

The differences in sample means of plant configurations included in Appendix G provide quantitative information about statistically significant differences between plant configurations, where statistical significance in this thesis is assumed when the value 0 is not within a 95% CI for a difference in a sample mean.

Via inspection of difference in means in Appendix G, the following performance values and measured variables have large sets of non-significant differences between dynamic compensators: overshoot of DC-side power from Figure G.2; and, ISE, IAE, ITAE, overshoot, and recovery time of DC-side current from Figures G.10–G.12. All performance values for AC-side voltage magnitude (Figures G.4–G.6), DC-side voltage (Figures G.7–G.9), and extinction angle (Figures G.13–G.15) indicate many significant differences between dynamic compensator plant configurations.

More generally, the claim from manual inspection of the plots in Figures E.1–E.5 and F.1–F.5 in Appendices E and F that dynamic compensators of any configuration generally had superior performance values (except overshoot) over all of the measured variables—except from extinction angle (Figures E.5 and F.5)—compared with the Base study case is refined in two ways via inspection of the results in Appendix G.

Firstly, the aforementioned claim is incorrect where many compensator plant configurations are found to be non-significantly different to the Base study case for: IAE and ITAE of AC-side measured voltage magnitude in Figures G.4 and G.5; and, ISE of DC-side current in Figure G.10.



Differences of Plant Configuration Sample Means

Figure 4.17: DC-side measured power differences of sample means.

Secondly, the synchronous condenser plant configurations are demonstrated to have superior performance over the Base study case and the SVC and STATCOM plant configurations for the performance values particularly in the case of DC-side power (Figures G.1–G.3 except when considering DC-side power overshoot in Figure G.2), AC-side voltage magnitude (Figures G.4–G.6), and DC-side voltage (Figures G.7–G.9). Results are more mixed in the case of DC-side current (Figures G.10–G.12) and extinction angle (Figures G.13–G.15). For extinction angle performance values, the synchronous condenser configurations are typically superior to the SVC and STATCOM configurations apart from recovery time in Figure G.15, yet mixed inferiority, superiority, or similarity compared to the Base study case depending on the specific performance values. For DC-side measured current, synchronous condenser configuration performance values are mostly similar to SVC and STATCOM configurations.

Also notable is the number of non-significant differences amongst compensator plant configurations in the case of DC-side current (Figures G.10–G.12), except from settling time in Figure G.12 where many more differences between compensators are found.

4.6.4 Observations from Differences in Sample Minima

Similar to Appendix G, two-sample comparisons using differences between sample minima via 95% CI are provided in Appendix H, between all 10 different plant configurations for each performance function result and for each measured variable.

From inspection of difference in minima in Appendix H, the following performance values and measured variables have large sets of non-significant differences between dynamic compensators: IAE and ITAE of DC-side current in Figures H.10 and H.11 respectively; and, recovery time of extinction angle in Figure H.15. These are different sets from the analogous observation from differences in sample means where there were more performance values with non-significant difference amongst the dynamic compensator configurations: overshoot of DC-side power from Figure G.2; and, ISE, IAE, ITAE, overshoot, and recovery time of DC-side current from Figures G.10–G.12. Similar to differences in sample means, differences in sample minima of performance values for

AC-side voltage magnitude (Figures H.4–H.6), DC-side voltage (Figures H.7–H.9), and extinction angle (Figures H.13–H.15) indicated many significant differences between dynamic compensator plant configurations.

Also similar to differences in sample means, the differences in sample minima indicated that addition of any compensators gave superior results compared to the Base study case, except from: overshoots of measured variables; extinction angle performance values (Figures H.13–H.15); ISE, IAE, ITAE, and recovery time of AC-side measured voltage magnitude (Figures H.4–H.6); and, ISE and ITAE of DC-side current in Figures H.10 and H.11.

Synchronous condenser plant configurations also tended to have superior performance values—apart from overshoot—compared to the other compensators and the Base study case for DC-side power (Figures H.1–H.3 except when considering DC-side power overshoot in Figure H.2), AC-side voltage magnitude (Figures H.4–H.6), and DC-side voltage (Figures H.7–H.9), similar to the differences in sample means. However recovery time of DC-side power and AC-side voltage magnitude in Figures H.3 and H.6 respectively tended to be worse for synchronous condensers compared to the other dynamic compensators when considering differences between sample minima, but were superior when considering differences between sample means in Figures G.3 and G.6 in Appendix G.

Results for extinction angle (Figures H.13–H.15) and DC-side current (Figures H.10–H.12) performance values of synchronous condensers compared to the Base study case and the other compensators are also mixed for differences in sample minima, similar to differences in sample means (Figures G.13–G.15 and G.10–G.12). Note that performance values of DC-side current had many significant differences between sample minima for different SVC and STATCOM configurations (Figures H.10–H.12) when compared to synchronous condenser configurations, whereas there were many non-significant differences in the case of differences in sample means (Figures G.10–G.12).

4.6.5 Observations from Hypothetical Plant Configuration Rankings based on Sample Means

It is clear from the descriptive box-plots of the performance values in Figures E.1–E.5 that plant configurations rank differently in their minimisation of performance values. Even when considering one specific performance value for one specific measured variable, the observed rank of plant configuration minima may be different from the observed rank of plant configuration mean.

Plots of Kendall’s Tau-c associations with 95% CI for scoring strengths of proposed hypothetical Rankings compared to the observed ranks of sample means from the data are included for each performance function’s results and for each measured variable are included in Appendix I.

Kendall’s Tau-c associations between Rankings described in Section 4.5.3 and observed means of performance values calculated via all 6 performance functions for measured DC-side power in the LCC-HVDC are shown in Figure 4.18 which is a copy of Figure I.1. The sample statistics are indicated along with 95% CIs. Note that all possible Rankings are associated with observed ITAE sample means with statistical significance as indicated by the 95% CIs of all Rankings being wholly to the right-hands side of the x-axis zero line. As for sample mean of overshoots, Ranking H has a statistically significant anti-association, while Ranking A has a statistically significant association, and Ranking C has no statistically significant association.

When considering proposed plant configuration Rankings compared to observed ranks of sample means from the data via the plots in Figures I.1–I.5 in Appendix I, the Rankings H, E, G, and D persistently scored highly—especially Rankings H and E—with high Kendall’s Tau-c associations for almost all performance values for all measured variables. The exceptions are: overshoot of DC-side measured power in Figure I.1; all performance values apart from settling time for DC-side measured current in Figure I.4; and, recovery time of measured extinction angle in Figure I.5. Ranking H was created by engineering judgement via inspection of the observed results.

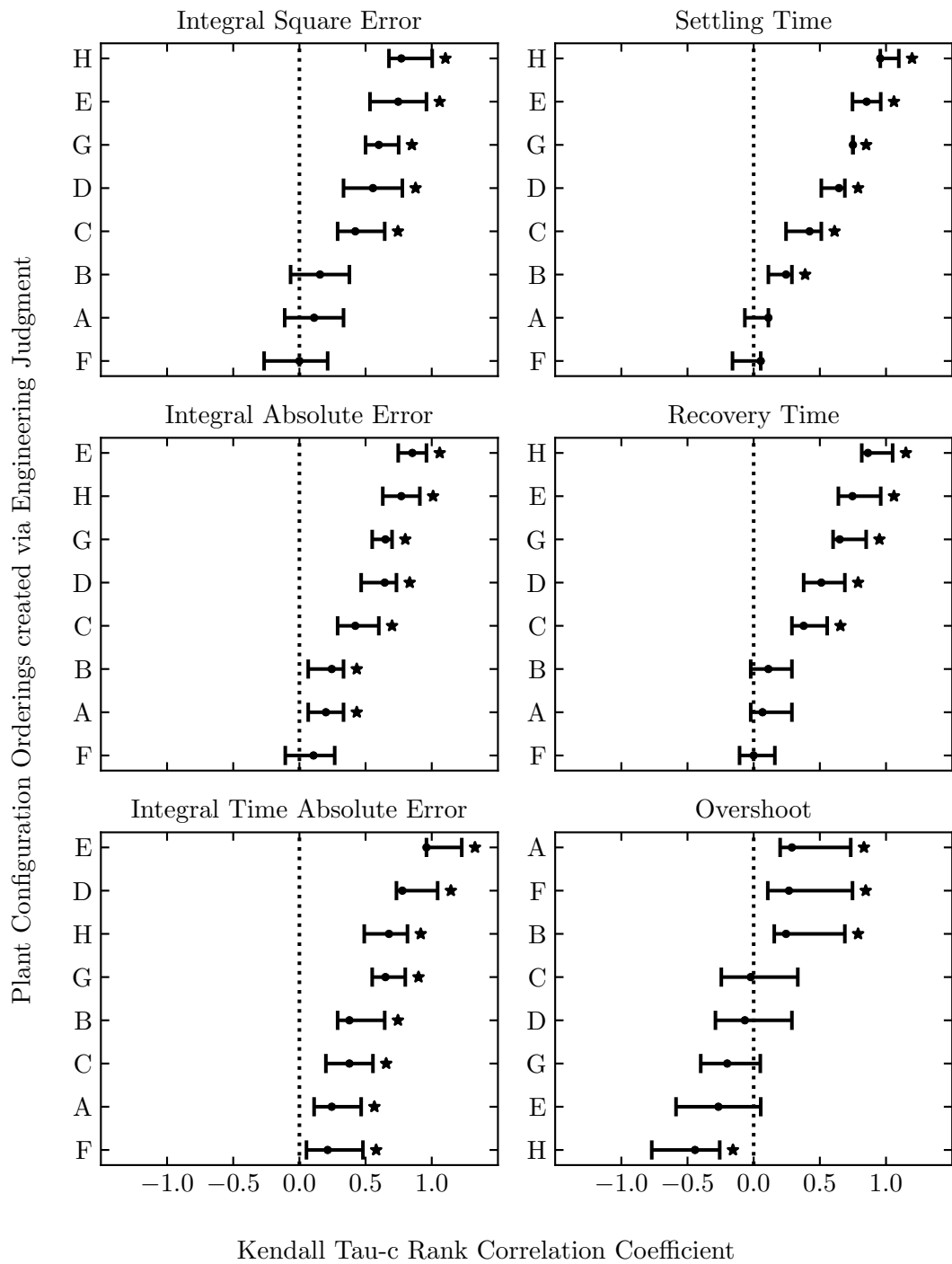


Figure 4.18: DC-side measured power associations.

Ranking E assumed that ratings of compensators were irrelevant, and that compensator type was most important for influencing ranks of performance values' sample means. Ranking H did include some consideration of ratings particularly in the case of synchronous condensers, but SVC and STATCOM were viewed as being somewhat equal for similar ratings.

Rankings F, A, and B are persistently low scoring Rankings compared to the observed data, except where these Rankings had notable anti-associations in the case of: recovery time of AC-side voltage magnitude in Figure I.2; and, ITAE and settling time of extinction angle in Figure I.5. These three Rankings were often either statistically insignificant, *i.e.* their confidence intervals overlapped 0, or otherwise had low score magnitudes. Rankings A and B are very similar because they only swapped the proposed ranks of similarly sized SVCs and STATCOMs. Fundamentally, Rankings F, A, and B all assumed that compensator rating was the most important variable for ranking plant configurations, with compensator type of secondary importance—in the case of Rankings A and B—or no importance in the case of Ranking F.

These observations of Rankings H, E, G, and D versus Rankings F, A, and B imply that compensator type is very important to consider when considering plant configurations ranks of sample means for performance values. However choosing to also rank by compensator rating as a secondary ordering after a primary ordering based upon compensator type—Ranking D—suggests a worse model compared to only ordering based upon compensator type—Ranking E—due to how often Ranking E is scored more highly compared to Ranking D from qualitative inspection of the plots in Appendix I.

4.6.6 Observations from Hypothetical Plant Configuration Rankings based on Sample Minima

In Appendix J, Rankings H, E, G, and D persistently scored highly—especially Rankings H and E—for Kendall's Tau-c associations depending on sample minima across Figures J.1–J.5, with the exceptions being: overshoot and recovery time of DC-side measured power in Figure J.1; ITAE, recovery time, and settling time for

DC-side measured current in Figure J.4; and, ITAE of measured extinction angle in Figure J.5. In some situations, Rankings H, E, G, and D had very low scores below 0, suggesting strong anti-association between the proposed Ranking and the observed ranking from the sample minima. These situations are: recovery time of AC-side voltage magnitude in Figure J.2; ISE, IAE, and overshoot of DC-side current in Figure J.4; and, recovery time of extinction angle in Figure J.5. This also suggests that these Rankings are useful for those performance values as well.

Rankings F, A, and B are persistently low scoring Rankings compared to the observed data for the Tau-c associations based upon sample minima, similar to the low scoring ranks for Tau-c associations based upon sample means. The exceptions to this are: overshoot of DC-side measured power in Figure J.1; and, recovery time and settling time of DC-side measured current in Figure J.4. In these exceptions, Rankings F, A, and B score with high magnitude.

Therefore, Rankings H, E, G, and D versus Rankings F, A, and B imply that compensator type is very important in the case of comparing hypothetical proposed Rankings with observed ranks from sample minima, *i.e.* a qualitative agreement with the observations of Rankings H, E, G, and D versus Rankings F, A, and B when considering ranks from observed sample means. However the results are not exactly the same between the ranks depending on the two different types of sample statistics—sample mean or sample minimum.

4.7 Summary

A method has been proposed which makes fair comparisons between dynamic compensator plant configurations of different types and sizes. The method uses simulation-based optimisation to find optimal controller parameter values of SVCs, STATCOMs and synchronous condensers to assist LCC-HVDC link dynamic operation in low SCR inverter systems subjected to short circuit faults. The method uses EMT simulations to inherently incorporate large transient and non-linear behaviour within

the optimisation problem.

The method uses statistical approaches to find statistically significant differences between plant configurations for a range of engineer-specified measured variables and engineer-specified performance functions. Two fundamental sample statistics were investigated: sample means, and sample minima. Sample statistics representing independent two-sample differences in sample means and independent two-sample differences in sample minima were also investigated.

The method also uses the Kendall's Tau-c association statistic to evaluate proposed Rankings of plant configurations for their superiority on performance values against the observed ranks from the simulation-based optimisation results.

When applied to the particular study cases investigated and using a simulation-based optimisation objective of minimisation of ISE of LCC-HVDC link DC-side power, the method has qualitatively determined that adding dynamic compensators is overwhelmingly associated with improved dynamic performance of the LCC-HVDC link. Specifically, synchronous condensers are very effective at improving LCC-HVDC link performance, followed by small SVCs and STATCOMs. Larger SVCs and STATCOMs are qualitatively associated with inferior performance values when compared with smaller SVCs and STATCOMs, and any synchronous condensers.

Focussing on observed values of ISE of DC-side measured power as an example, the addition of dynamic compensators reduces the mean ISE by as much as 9.2035% relative to the Base study case. The only deterioration in mean ISE occurs in the addition of a 0.2 pu STATCOM which worsens the mean ISE by 0.21144% relative to the Base study case. The addition of synchronous condensers reduces the mean ISE by 9.2035%, 7.5269%, and 8.1618% relative to the Base study case for the 0.2 pu, 0.4 pu, and 0.6 pu synchronous condensers respectively. Meanwhile, the addition of SVCs of 0.2 pu, 0.4 pu, and 0.6 pu reduces mean ISE by 5.7476%, 5.4759%, and 5.7968% respectively relative to the Base study case. Lastly, the addition of 0.2 pu, 0.4 pu, and 0.6 pu STATCOMs reduces mean ISE by 6.9608%, 4.5703%, and -0.21144% respectively relative to the Base

study case.

It is not clear from the method's results why differences in performance values are found between larger SVCs and STATCOMs compared with smaller SVCs and STATCOMs. A possible explanation may be associated with the high source impedance of the inverter AC system which is associated with high magnitude VSF, therefore highly fluctuating time domain responses, and therefore worse performance values from the six performance values studied in this Chapter. In this scenario, only the precisely tuned and designed feedback control of the compensators would mitigate the natural tendency of the combined AC-DC and dynamic compensator system to give highly fluctuating time domain responses associated with a high VSF magnitude system.

There is a theoretical explanation as to why synchronous condenser results are so strongly favourable compared to the SVC and STATCOM results. A synchronous condenser is a voltage source as seen within the AC-DC system, and its voltage source characteristic is overwhelmingly independent of any closed-loop control. This means that during large disturbances such as close-in short circuit faults, the synchronous condenser will still appear as a voltage source with significant voltage magnitude behind its machine impedance as viewed from the AC network. In the cases of STATCOMs and SVCs, these devices do not act as significant voltage sources during close-in faults: a STATCOM will be forced to apply low-valued voltage magnitudes to force currents from the STATCOM to remain within its own current limits; and, an SVC is fundamentally a susceptance rather than a voltage source. Furthermore, both the STATCOM and SVC are dependent on robust closed-loop control in order for them to contribute in any significant and useful way to assist network voltage waveform quality during disturbances such as short circuit faults.

These fundamental differences between the STATCOM, SVC and the synchronous condenser provide the qualitative explanation for why the synchronous condenser should provide more favourable LCC-HVDC link dynamic performance compared to STATCOMs and SVCs.

Chapter 5

Conclusions and Potential Future Research Avenues

5.1 Conclusions

This thesis has focussed upon the problem of evaluating dynamic compensation devices for the purpose of improving the dynamic performance of LCC-HVDC links operating in inverter AC systems with high equivalent source impedance relative to the LCC-HVDC links' power transfers.

Firstly, this thesis proposed a method to evaluate different optimisation solver methods on their solution performance of an LCC-HVDC link controller tuning problem. The method was applied to four solver methods: two solver methods using mature strategies similar to those included in PSCAD/EMTDC version 4.6.3; and two solver methods using surrogate-based strategies recently proposed in the research literature.

The proposed method identified the surrogate-based solver methods as performing better than or no worse than the mature strategies, depending on the specific controller tuning problem study case and the specific pairing of solver methods being evaluated within the set of four solver methods.

Secondly, this thesis proposed a method to quantitatively evaluate dynamic compensation devices for their effect on LCC-HVDC link performance. The method considered: different types and different sizes of the compensators; multiple potential values of inverter system equivalent source impedances; and, multiple potential short circuit fault disturbances within the inverter system.

The method determined quantitative differences between the compensator type and size configurations of SVC, a STATCOM, and a synchronous condenser, using a conventional compensator-less LCC-HVDC link with an in-built inverter DC-side voltage control loop as a baseline. The results from applying the method to the particular study cases show dynamic compensators can help with LCC-HVDC link dynamic performance. In particular, synchronous condensers help substantially compared to SVCs and STATCOMs; and, smaller-rated SVCs and STATCOMs tend to help more than larger-rated SVCs and STATCOMs.

5.2 Future Research Avenues

There are many aspects of the presented work in this thesis which are amenable to further research and analysis.

1. Aspects related to the deployment of simulation-based optimisation;
2. Statistical considerations; and,
3. AC-DC power system engineering design problem formulations using simulation-based optimisation.

These three domains will now be explained further.

5.2.1 Specificities of Simulation-based Optimisation

The specific form of box-constrained optimisation problems investigated in this thesis are only one type of mathematical formulation which could feasibly model the problem faced by the engineer. The choice of optimisation problem constraints could help or

hinder the engineer in their problem solving task.

- Initial linearised models could be used to analytically determine values for upper and lower bounds of variables used in a follow-on simulation-based optimisation problem.
- Additional objective functions could be modelled, therefore making the problem a multi-objective optimisation. This would allow the evaluation of multiple performance values simultaneously.
- Black-box constraint functions could be modelled, which would allow the modelling of feasible envelopes within time domain responses.
- Alternative merit functions and measured variables within the optimisation problem could be investigated.
- Hyper-parameter optimisation could be performed, which optimally selects solver method parameters to ensure good solver method performance on a particular optimisation problem.
- The influence of solver method parameters on the outputs of the dynamic compensator evaluation method could be investigated.

5.2.2 Statistical Considerations

This thesis has used statistical methods to prudently evaluate sets of optimal solutions provided by stochastic solver methods. This leads to further research avenues.

- Different types of sample statistics could be investigated.
- Alternative distributions of random variables could be investigated, for example distributions for extreme values such as minima.

5.2.3 AC-DC Problem Formulation Considerations

Only three types of compensators have been investigated in this thesis. The architectures used to model these devices are in line with general modelling approaches in the research

Chapter 5. Conclusions and Potential Future Research Avenues

literature. However the choice of architecture for the specific problem of dynamic compensation of LCC-HVDC for large disturbances is an open question.

- Alternative dynamic compensator control or plant architectures could be investigated.
- Selection of specific controller parameters to optimise could be studied, aside from the PI controller gains and VDCOL parameters studied in this thesis.
- Consideration could be given to the inclusion of plant and/or controller layouts within the optimisation problem, encoded via additional optimisation problem choice variables to select the alternative layouts.
- Risk-based or cost-benefit analysis formulations of the dynamic compensator selection problem for LCC-HVDC link dynamic performance could be studied, made possible by strategies for both sampling operational scenarios and for handling the stochasticity of the scenario sampling.

Bibliography

- [1] M. Barnes, D. Van Hertem, S. P. Teeuwsen, and M. Callavik, “HVDC systems in smart grids,” *Proceedings of the IEEE*, vol. 105, no. 11, pp. 2082–2098, Nov. 2017.
- [2] A. Alassi, S. Bañales, O. Ellabban, G. Adam, and C. MacIver, “HVDC transmission: Technology review, market trends and future outlook,” *Renewable and Sustainable Energy Reviews*, vol. 112, pp. 530–554, Sep. 2019.
- [3] A. Kalair, N. Abas, and N. Khan, “Comparative study of HVAC and HVDC transmission systems,” *Renewable and Sustainable Energy Reviews*, vol. 59, pp. 1653–1675, Jun. 2016.
- [4] Advisory Group B4.04, “Compendium of HVDC schemes throughout the World,” CIGRE, Tech. Rep., 2009.
- [5] “High Voltage Direct Current Systems,” GE Grid Solutions, Reference List GEA-31971, Aug. 2017.
- [6] “HVDC Classic Reference List,” Hitachi Energy, Reference List POW0013 rev 31, Aug. 2023.
- [7] “HVDC Light Reference List,” Hitachi Energy, Reference List POW0027 rev 42, Jun. 2023.
- [8] “HVDC References,” Siemens Energy, Reference List PTSO-T10005-00-76DE, Nov. 2021.

Bibliography

- [9] C. C. Diemond *et al.*, “AC-DC economics and alternatives - 1987 panel session report,” *IEEE Transactions on Power Delivery*, vol. 5, no. 4, pp. 1956–1976, Nov. 1990.
- [10] C. V. Thio, J. B. Davies, and K. L. Kent, “Commutation failures in HVDC transmission systems,” *IEEE Transactions on Power Delivery*, vol. 11, no. 2, pp. 946–957, Apr. 1996.
- [11] J. Khazaei, P. Idowu, A. Asrari, A. B. Shafaye, and L. Piyasinghe, “Review of HVDC control in weak AC grids,” *Electric Power Systems Research*, vol. 162, pp. 194–206, Sep. 2018.
- [12] P. C. S. Krishnayya, R. J. Piwko, T. L. Weaver, M. P. Bahrman, and A. E. Hammad, “DC transmission terminating at low short circuit ratio locations,” *IEEE Transactions on Power Delivery*, vol. 1, no. 3, pp. 308–318, Jul. 1986.
- [13] R. S. Thallam, “Review of the design and performance features of HVDC systems connected to low short circuit ratio AC systems,” *IEEE Transactions on Power Delivery*, vol. 7, no. 4, pp. 2065–2073, Oct. 1992.
- [14] International Renewable Energy Agency (IRENA), “Renewable Capacity Statistics,” Abu Dhabi, Jul. 2023.
- [15] A. Gavrilović, “AC/DC system strength as indicated by short circuit ratios,” in *5th International Conference on AC and DC Power Transmission*, London, UK, Sep. 1991, pp. 27–32.
- [16] A. E. Hammad and W. Kuhn, “A computation algorithm for assessing voltage stability at AC/DC interconnections,” *IEEE Transactions on Power Systems*, vol. 1, no. 1, pp. 209–215, Feb. 1986.
- [17] B. Frankén and G. Andersson, “Analysis of HVDC converters connected to weak AC systems,” *IEEE Transactions on Power Systems*, vol. 5, no. 1, pp. 235–242, Feb. 1990.

Bibliography

- [18] L. S. Pilotto, M. Szechtman, and A. E. Hammad, "Transient AC voltage related phenomena for HVDC schemes connected to weak AC systems," *IEEE Transactions on Power Delivery*, vol. 7, no. 3, pp. 1396–1404, Jul. 1992.
- [19] K. R. Padiyar and S. S. Rao, "Dynamic analysis of voltage instability in AC-DC systems," *International Journal of Electrical Power & Energy Systems*, vol. 18, no. 1, pp. 11–18, Jan. 1996.
- [20] X. Chen, A. M. Gole, and C. Guo, "A fast calculation method for the local commutation failure immunity indices in single- and multi-infeed HVDC systems," in *11th International Conference on AC and DC Power Transmission*, Birmingham, UK, Feb. 2015, pp. 1–6.
- [21] F. H. Gandoman *et al.*, "Review of FACTS technologies and applications for power quality in smart grids with renewable energy systems," *Renewable and Sustainable Energy Reviews*, vol. 82, pp. 502–514, Feb. 2018.
- [22] "Chapter 16: Economic Appraisal and Cost-Benefit Analysis," in *Flexible AC Transmission Systems: FACTS*, ser. CIGRE Green Books, B. R. Andersen and S. L. Nilsson, Eds. Cham, CH: Springer International Publishing, 2020, pp. 709–751.
- [23] J. Dixon, L. Moran, J. Rodriguez, and R. Domke, "Reactive power compensation technologies: State-of-the-art review," *Proceedings of the IEEE*, vol. 93, no. 12, pp. 2144–2164, Dec. 2005.
- [24] A. Hammad, K. Sadek, H. Koelsch, and G. Gueth, "Advanced scheme for AC voltage control at HVDC converter terminals," *IEEE Transactions on Power Apparatus and Systems*, vol. 104, no. 3, pp. 697–703, Mar. 1985.
- [25] A. E. Hammad, J. Gagnon, and D. McCallum, "Improving the dynamic performance of a complex AC/DC system by HVDC control modifications," *IEEE Transactions on Power Delivery*, vol. 5, no. 4, pp. 1934–1943, Nov. 1990.

Bibliography

- [26] S. Nyati, S. Atmuri, D. Gordon, V. Koschik, and R. Mathur, "Comparison of voltage control devices at HVDC converter stations connected to weak AC systems," *IEEE Transactions on Power Delivery*, vol. 3, no. 2, pp. 684–693, Apr. 1988.
- [27] O. B. Nayak, A. M. Gole, D. G. Chapman, and J. B. Davies, "Dynamic performance of static and synchronous compensators at an HVDC inverter bus in a very weak AC system," *IEEE Transactions on Power Systems*, vol. 9, no. 3, pp. 1350–1358, Aug. 1994.
- [28] M. Szechtman, T. Wess, and C. V. Thio, "A benchmark model for HVDC system studies," in *5th International Conference on AC and DC Power Transmission*, London, UK, Sep. 1991, pp. 374–378.
- [29] Y. Zhuang, R. W. Menzies, O. B. Nayak, and H. M. Turanli, "Dynamic performance of a STATCON at an HVDC inverter feeding a very weak AC system," *IEEE Transactions on Power Delivery*, vol. 11, no. 2, pp. 958–964, Apr. 1996.
- [30] Y. Zhang and A. M. Gole, "Comparison of the transient performance of STATCOM and synchronous condenser at HVDC converter stations," in *11th International Conference on AC and DC Power Transmission*, Birmingham, UK, Feb. 2015, pp. 1–8.
- [31] E. Rahimi, A. M. Gole, J. B. Davies, I. T. Fernando, and K. L. Kent, "Commutation failure analysis in multi-infeed HVDC systems," *IEEE Transactions on Power Delivery*, vol. 26, no. 1, pp. 378–384, Jan. 2011.
- [32] A. U. Rehman, C. Guo, C. Zhao, and W. Jiang, "Comparative performance study of dynamic reactive power compensators on operating characteristics of LCC based UHVDC system under hierarchical connection mode," *Journal of Electrical Engineering & Technology*, vol. 14, no. 2, pp. 535–547, Mar. 2019.
- [33] Y. Lei *et al.*, "Comparison of UPFC, SVC and STATCOM in improving commutation failure immunity of LCC-HVDC systems," *IEEE Access*, vol. 8, pp. 135 298–135 307, Aug. 2020.

Bibliography

- [34] J. V. Soares do Amaral, J. A. B. Montevechi, R. d. C. Miranda, and W. T. d. S. Junior, “Metamodel-based simulation optimization: A systematic literature review,” *Simulation Modelling Practice and Theory*, vol. 114, pp. 1–21, Jan. 2022.
- [35] F. Boukouvala, R. Misener, and C. A. Floudas, “Global optimization advances in mixed-integer nonlinear programming, MINLP, and constrained derivative-free optimization, CDFO,” *European Journal of Operational Research*, vol. 252, no. 3, pp. 701–727, Aug. 2016.
- [36] S. Shan and G. G. Wang, “Survey of modeling and optimization strategies to solve high-dimensional design problems with computationally-expensive black-box functions,” *Structural and Multidisciplinary Optimization*, vol. 41, no. 2, pp. 219–241, Mar. 2010.
- [37] R. T. Haftka, D. Villanueva, and A. Chaudhuri, “Parallel surrogate-assisted global optimization with expensive functions - a survey,” *Structural and Multidisciplinary Optimization*, vol. 54, no. 1, pp. 3–13, Jul. 2016.
- [38] L. M. Rios and N. V. Sahinidis, “Derivative-free optimization: A review of algorithms and comparison of software implementations,” *Journal of Global Optimization*, vol. 56, no. 3, pp. 1247–1293, Jul. 2013.
- [39] X. Lei, E. Lerch, D. Povh, and B. Kulicke, “Optimization - a new tool in a simulation program system,” *IEEE Transactions on Power Systems*, vol. 12, no. 2, pp. 598–604, May 1997.
- [40] A. M. Gole, S. Filizadeh, R. W. Menzies, and P. L. Wilson, “Electromagnetic transients simulation as an objective function evaluator for optimization of power system performance,” in *International Conference on Power Systems Transients*, New Orleans, LA, USA, Sep.-Oct. 2003, pp. 1–6.
- [41] A. M. Gole, S. Filizadeh, R. W. Menzies, and P. L. Wilson, “Optimization-enabled electromagnetic transient simulation,” *IEEE Transactions on Power Delivery*, vol. 20, no. 1, pp. 512–518, Jan. 2005.

Bibliography

- [42] S. Filizadeh, A. M. Gole, D. A. Woodford, and G. D. Irwin, “An optimization-enabled electromagnetic transient simulation-based methodology for HVDC controller design,” *IEEE Transactions on Power Delivery*, vol. 22, no. 4, pp. 2559–2566, Oct. 2007.
- [43] A. Y. Goharrizi, R. Singh, A. M. Gole, S. Filizadeh, J. C. Muller, and R. P. Jayasinghe, “A parallel multimodal optimization algorithm for simulation-based design of power systems,” *IEEE Transactions on Power Delivery*, vol. 30, no. 5, pp. 2128–2137, Oct. 2015.
- [44] A. M. Tahboub, M. S. El Moursi, W. L. Woon, and J. L. Kirtley, “Multiobjective dynamic VAR planning strategy with different shunt compensation technologies,” *IEEE Transactions on Power Systems*, vol. 33, no. 3, pp. 2429–2439, May 2018.
- [45] A. Musa, L. R. Sabug Jr., and A. Monti, “Robust predictive sliding mode control for multiterminal HVDC grids,” *IEEE Transactions on Power Delivery*, vol. 33, no. 4, pp. 1545–1555, Aug. 2018.
- [46] L. Simon, K. S. Swarup, and J. Ravishankar, “Wide area oscillation damping controller for DFIG using WAMS with delay compensation,” *IET Renewable Power Generation*, vol. 13, no. 1, pp. 128–137, Jan. 2019.
- [47] J. S. Acosta, M. C. Tavares, and A. M. Gole, “Neutral reactor structures for improved single phase auto reclosing in multi-circuit multi-voltage transmission lines,” *IEEE Transactions on Power Delivery*, vol. 37, no. 1, pp. 298–307, Feb. 2022.
- [48] J. A. Nelder and R. Mead, “A simplex method for function minimization,” *The Computer Journal*, vol. 7, no. 4, pp. 308–313, Jan. 1965.
- [49] K. Q. Ye, W. Li, and A. Sudjianto, “Algorithmic construction of optimal symmetric Latin hypercube designs,” *Journal of Statistical Planning and Inference*, vol. 90, no. 1, pp. 145–159, Sep. 2000.
- [50] D. Eriksson, D. Bindel, and C. A. Shoemaker, “pySOT and POAP: An event-driven asynchronous framework for surrogate optimization,” *arXiv:1908.00420v1*, Jul. 2019.

Bibliography

- [51] T.-D. Tran and G.-G. Jin, “Real-coded genetic algorithm benchmarked on noiseless black-box optimization testbed,” in *Proceedings of the 12th Annual Conference Companion on Genetic and Evolutionary Computation*. Portland, OR, USA: Association for Computing Machinery, Jul. 2010, pp. 1731–1738.
- [52] P. Virtanen *et al.*, “SciPy 1.0: Fundamental algorithms for scientific computing in Python,” *Nature Methods*, vol. 17, no. 3, pp. 261–272, Mar. 2020.
- [53] R. G. Regis and C. A. Shoemaker, “Combining radial basis function surrogates and dynamic coordinate search in high-dimensional expensive black-box optimization,” *Engineering Optimization*, vol. 45, no. 5, pp. 529–555, May 2013.
- [54] J. H. Friedman, “Multivariate adaptive regression splines,” *The Annals of Statistics*, vol. 19, no. 1, pp. 1–67, Mar. 1991.
- [55] “Py-Earth: A Python implementation of Jerome Friedman’s multivariate adaptive regression splines,” 2017. [Online]. Available: <https://github.com/scikit-learn-contrib/py-earth>
- [56] E. Schulz, M. Speekenbrink, and A. Krause, “A tutorial on Gaussian process regression: Modelling, exploring, and exploiting functions,” *Journal of Mathematical Psychology*, vol. 85, pp. 1–16, Aug. 2018.
- [57] F. Pedregosa *et al.*, “Scikit-learn: Machine learning in Python,” *Journal of Machine Learning Research*, vol. 12, pp. 2825–2830, Nov. 2011.
- [58] C. E. Rasmussen and C. K. I. Williams, “Algorithm 2.1,” in *Gaussian Processes for Machine Learning*. MIT Press, 2006, p. 19.
- [59] R. J. Hyndman and Y. Fan, “Sample quantiles in statistical packages,” *The American Statistician*, vol. 50, no. 4, pp. 361–365, Nov. 1996.
- [60] A. M. Gole and V. K. Sood, “A static compensator model for use with electromagnetic transients simulation programs,” *IEEE Transactions on Power Delivery*, vol. 5, no. 3, pp. 1398–1407, Jul. 1990.

- [61] “2-quadrant AC-DC conversion using VSC: The active rectifier scheme,” MHI, PSCAD Application Note Revision 1, Sep. 2018. [Online]. Available: <https://www.pscad.com/knowledge-base/article/256>
- [62] L. Harnefors and H.-P. Nee, “Model-based current control of AC machines using the internal model control method,” *IEEE Transactions on Industry Applications*, vol. 34, no. 1, pp. 133–141, Jan.-Feb. 1998.
- [63] A. Stuart, “The estimation and comparison of strengths of association in contingency tables,” *Biometrika*, vol. 40, no. 1/2, pp. 105–110, Jun. 1953.

Appendix A

Solver Method Algorithms

A.1 Symmetric Latin Hypercube Design

Algorithm 1 Symmetric Latin Hypercube Design

```
1: procedure GENERATESLHD
2:   Set rank  $R$  to 0.
3:   while  $R \neq D + 1$  do
4:     Create an empty matrix  $\mathbf{D}$  of  $N$  rows and  $D$  columns, where each row indicates
       a point in the feasible region to be evaluated and each column represents
       a dimension of each point, i.e. each column corresponds to a scalar-valued
       optimisation problem variable.
5:     Set a counter  $i = 1$ .
6:     for each element  $d$  in the first column of  $\mathbf{D}$  do
7:       Set the value of  $d$  equal to  $i$ .
8:       Increment  $i$  by 1.
9:     end for
10:    if number of points  $N$  is odd then
11:      Calculate the index of the middle row in  $\mathbf{D}$ ,  $m = \frac{N+1}{2}$ .
12:      Set all elements in the  $m$ -th row in  $\mathbf{D}$  to equal the value  $m$ .
13:    end if
```

Algorithm 1 continued

```

14:     Calculate  $k = \lfloor \frac{N}{2} \rfloor$ , which is the index of either: the last row in the top half
        of  $\mathbf{D}$  if  $N$  is even; or, the row before the middle row if  $N$  is odd.
15:     for column  $c$  in  $\mathbf{D}$ , counting from the second column onwards do
16:         Set a counter  $i = 1$ .
17:         for row  $r$  in  $\mathbf{D}$ , counting up to and including row  $k$  do
18:             Draw a single sample  $l$  from a uniformly distributed random number
                on the interval  $[0, 1]$ .
19:             if  $l < 0.5$  then
20:                 Set the element at row  $r$  and column  $c$  to equal  $N - i - 1$ .
21:             else
22:                 Set the element at row  $r$  and column  $c$  to equal  $i$ .
23:             end if
24:             Increment the counter  $i$  by 1.
25:         end for
26:         Randomly shuffle all of the elements in column  $c$  between the first row
                and row  $k$ , inclusive.
27:     end for
28:     for column  $c$  in  $\mathbf{D}$ , counting from the second column onwards do
29:         Set a counter  $i = k + 1$ .
30:         for row  $r$  in  $\mathbf{D}$ , counting from the  $(k + 1)$ -th row onwards, inclusive do
31:             Temporarily copy the value of the element at row  $N - i + 1$  and column
                 $c$ , and store as value  $t$ .
32:             Set the element at row  $r$  and column  $c$  to equal  $N + 1 - t$ .
33:             Increment the counter  $i$  by 1.
34:         end for
35:     end for

```

Appendix A. Solver Method Algorithms

Algorithm 1 continued

36: **for** each element d in \mathbf{D} **do**
37: Take the value at d and store as t .
38: Calculate $\frac{t}{N}$ and store to d .
39: **end for**
40: Create a new matrix \mathbf{E} which is equal to matrix \mathbf{D} but with an additional
 prepended column, where all element values in the prepended column are
 equal to 1.
41: Calculate the rank of matrix \mathbf{E} and store to R .
42: **end while**
43: **return** Experimental design matrix, \mathbf{D} .
44: **end procedure**

A.2 Solver Method GA: Genetic Algorithm

Algorithm 2 Genetic Algorithm

- 1: **procedure** RUNGAOPTIMISATION
 - 2: Set evaluation counter n to 0.
 - 3: Create an empty set \mathcal{E} to store evaluated points and their corresponding objective function values.
 - 4: Generate an initial experimental design \mathbf{D} of N points, where each point contains D dimensions, $N = n_0 + n_0 \bmod 2$, and n_0 is the user-specified population size.
 - 5: Evaluate all points from the initial experimental design \mathbf{D} via the objective function f , incrementing n with each objective function evaluation. If n reaches N_{\max} stop evaluating design points. N_{\max} is the user-specified evaluation budget.
 - 6: Find best objective function value f^* and corresponding point \mathbf{x}^* from the initial evaluations.
 - 7: Create an empty matrix \mathbf{P} to store the population of points.
 - 8: Create an empty vector \mathbf{f} to store the objective function value of each point from the matrix \mathbf{P} .
 - 9: Copy all experimental design points and their objective function values to set \mathcal{E} , *i.e.* $\mathcal{E} \leftarrow \{(\mathbf{x}, f(\mathbf{x})) : \mathbf{x} = \text{row}_i(\mathbf{D}_{N \times D}), i \in \{1, 2, \dots, N\}\}$.
 - 10: Copy all experimental design points to the matrix \mathbf{P} , and each point's corresponding objective function value to vector \mathbf{f} . A point's variable values and objective function value are stored at the same row indices in \mathbf{P} and \mathbf{f} , respectively.
 - 11: **while** $n < N_{\max}$ **do**
 - 12: Create a temporary empty set \mathcal{G} to store evaluated points and their corresponding objective function values during the tournament selection.
 - 13: **for** each point in the population \mathbf{P} **do**
 - 14: Create a temporary empty set \mathcal{S} .
 - 15: **for** index i in $\{1, 2, \dots, T_s\}$ **do**
-

Algorithm 2 continued

16: Randomly pick an index j from $\{1, 2, \dots, N\}$.

17: Find $f = \text{row}_j(\mathbf{f}_N)$ and $\mathbf{p} = \text{row}_j(\mathbf{P}_{N \times D})$, respectively.

18: Create member $s = (\mathbf{p}, f(\mathbf{p}))$, and add s to \mathcal{S} .

19: **end for**

20: Find the member s_{\min} from \mathcal{S} which has the smallest objective function value of all T_s members in \mathcal{S} . Add the point \mathbf{p} of member s_{\min} to set \mathcal{G} , *i.e.* $\mathcal{G} \leftarrow \mathcal{G} \cup \{\mathbf{p}\}$ where $s_{\min} = (\mathbf{p}, f(\mathbf{p}))$ and $s_{\min} \in \mathcal{S}$.

21: **end for**

22: Take half of the points in \mathcal{G} and store them as rows in a matrix $\mathbf{A}_{\frac{N}{2} \times D}$.

23: Take remaining half of the points in \mathcal{G} and store them as rows in a matrix $\mathbf{B}_{\frac{N}{2} \times D}$.

24: **for** index i in $\{1, 2, \dots, \frac{N}{2}\}$ **do**

25: Randomly sample a scalar number l from a uniformly distributed random number on the interval $[0, 1]$.

26: **if** $l < \sigma_p$ **then**

27: Find the points $\mathbf{q} = \text{row}_i(\mathbf{A})$ and $\mathbf{v} = \text{row}_i(\mathbf{B})$.

28: Randomly sample a scalar number m from a uniformly distributed random number on the interval $[0, 1]$.

29: **for** for each element index j in $\{1, 2, \dots, D\}$ **do**

30: Calculate $\mathbf{t}_{i,j} = m\mathbf{q}_{i,j} + (1 - m)\mathbf{v}_{i,j}$

31: Calculate $\mathbf{u}_{i,j} = m\mathbf{v}_{i,j} + (1 - m)\mathbf{q}_{i,j}$

32: **end for**

33: Set the points $\text{row}_i(\mathbf{A}) \leftarrow \text{row}_i(\mathbf{t})$, and $\text{row}_i(\mathbf{B}) \leftarrow \text{row}_i(\mathbf{u})$.

34: **end if**

35: **end for**

Algorithm 2 continued

36: Overwrite matrix \mathbf{P} by taking all points from both \mathbf{A} and \mathbf{B} , and storing them all into matrix \mathbf{P} as concatenation of points from matrices \mathbf{A} and \mathbf{B} . All points from \mathbf{A} and \mathbf{B} are now in \mathbf{P} .

37: **for** each element p in \mathbf{P} **do**

38: Randomly sample a scalar number k from a uniformly distributed random number on the interval $[0, 1]$.

39: **if** $k < \frac{1}{D}$ **then**

40: Randomly sample a scalar number h from a normally distributed random number with mean 0 and perturbation standard deviation σ_p .

41: Add the value of element p to h , and store the sum temporarily as the scalar t .

42: **If** $t > 1$, set $t \leftarrow 1$. **If** $t < 0$, set $t = 0$.

43: Store the value of t to the element p .

44: **end if**

45: **end for**

46: Store \mathbf{x}^* in the place of the first point in \mathbf{P} .

47: Store f^* in the place of the first objective function value in \mathbf{f} .

48: **for** i in $\{2, 3, \dots, N\}$ **do**

49: **if** $n < N_{\max}$ **then**

50: Evaluate point $\mathbf{p} = \text{row}_i(\mathbf{P})$ from \mathbf{P} via the objective function f .

51: Store $\mathbf{f}_i = f(\mathbf{p})$.

52: Store $\mathcal{E} \leftarrow \mathcal{E} \cup \{(\mathbf{p}, f(\mathbf{p}))\}$.

53: Increment counter n by 1.

54: **end if**

55: **end for**

56: Find and store best objective function value f^* and corresponding point \mathbf{x}^* from \mathbf{f} and \mathbf{P} , respectively.

Algorithm 2 continued

57: **end while**

58: Find smallest objective function value in \mathcal{E} and store as f_{best} .

59: Store the point \mathbf{x}_{best} from \mathcal{E} where $f_{\text{best}} = f(\mathbf{x}_{\text{best}})$.

60: **return** \mathbf{x}_{best} and f_{best} ; the best found solution and its corresponding objective function value respectively.

61: **end procedure**

A.3 Solver Method NM: Nelder-Mead Simplex

Algorithm 3 Nelder-Mead Simplex

- 1: **procedure** RUNNMOPTIMISATION
 - 2: Set evaluation counter n to 0.
 - 3: Create an empty set \mathcal{E} to store evaluated points and their corresponding objective function values.
 - 4: **while** $n < N_{\max}$ **do**
 - 5: Create an empty matrix $\mathbf{P}_{(D+1) \times D}$ to store the simplex of $D + 1$ points, where \mathbf{P} has $D + 1$ rows (each row corresponds to a point) and D columns (each column corresponds to a dimension, *i.e.* a scalar optimisation problem variable).
 - 6: Create an empty vector \mathbf{f} of $D + 1$ rows to store the objective function value of each point from the simplex \mathbf{P} .
 - 7: **if** $N_{\max} - n \geq n_0$ **then**
 - 8: Generate an initial experimental design, $\mathbf{D}_{n_0 \times D}$, with n_0 points and each point containing D dimensions.
 - 9: Evaluate all points from the initial experimental design \mathbf{D} via the objective function f , incrementing n with each objective function evaluation. If n reaches N_{\max} stop evaluating design points.
 - 10: Copy all experimental design points and their objective function values to set \mathcal{E} , *i.e.* $\mathcal{E} \leftarrow \mathcal{E} \cup \{(\mathbf{x}, f(\mathbf{x})) : \mathbf{x} = \text{row}_i(\mathbf{D}_{n_0 \times D}), i \in \{1, 2, \dots, n_0\}\}$.
 - 11: Copy the $D + 1$ experimental design points with the smallest objective function values to the matrix \mathbf{P} , and each of those point's corresponding objective function value to vector \mathbf{f} . A point's variable values and objective function value are stored at the same row indices in \mathbf{P} and \mathbf{f} , respectively.
 - 12: **else**
 - 13: Copy \mathbf{x}^* and store as the first point in \mathbf{P} .
 - 14: **for** $i \in \{1, \dots, D\}$ **do**
 - 15: Copy \mathbf{x}^* and store temporarily as \mathbf{y} .
-

Algorithm 3 continued

```

16:         if the  $i$ -th element in point  $\mathbf{y}$  has the value 0 then
17:             Store the value  $\theta$  to the  $i$ -th element in point  $\mathbf{y}$ .
18:         else
19:             Temporarily store the value of the  $i$ -th element in point  $\mathbf{y}$  as  $k$ , i.e.
                 $k \leftarrow \mathbf{y}_i$ .
20:             Multiply  $k$  by  $(1 + \Delta)$  and store the product back to  $k$ .
21:             Store  $k$  back to the  $i$ -th element in point  $\mathbf{y}$ .
22:         end if
23:         Copy  $\mathbf{y}$  and store as the  $(i + 1)$ -th point in  $\mathbf{P}$ .
24:     end for
25:     Evaluate all points in  $\mathbf{P}$  except the first via the objective function  $f$ ,
        incrementing  $n$  with each objective function evaluation. If  $n$  reaches  $N_{\max}$ 
        stop evaluating design points. For each point, store the returned objective
        function value in  $\mathbf{f}$  in the same order of execution.
26:     Copy each evaluated point  $\mathbf{p}$  from  $\mathbf{P}$  and its corresponding objective
        function value in  $\mathbf{f}$  to set  $\mathcal{E}$ , i.e.
        
$$\mathcal{E} \leftarrow \mathcal{E} \cup \{(\mathbf{p}, f(\mathbf{p})) : \mathbf{p} = \text{row}_i(\mathbf{P}_{(D+1) \times D}), i \in \{1, 2, \dots, D + 1\}\}.$$

27:     end if
28:     while  $n < N_{\max}$  do
29:         Calculate  $d$ , the largest magnitude difference between the best objective
            function value  $f^*$  in  $\mathbf{f}$ , and all other objective function values in  $\mathbf{f}$  aside
            from  $f^*$  itself.
30:         if  $d \leq F_{\text{tol}}$  then
31:             break while
32:         end if

```

Algorithm 3 continued

```

33:         Sort both  $\mathbf{P}$  and  $\mathbf{f}$ ; rows are ordered from smallest objective value in  $\mathbf{f}$  to
           largest objective value in  $\mathbf{f}$ ; and the points within  $\mathbf{P}$  are ordered to match
           each point's row position with its objective function value row position
           from the sorted objective value order in  $\mathbf{f}$ .
34:         Temporarily store the last point  $\mathbf{p}$  from  $\mathbf{P}$  as  $\mathbf{l}$ , i.e.  $\mathbf{l} \leftarrow \mathbf{p}$ .
35:         Calculate  $\bar{\mathbf{x}}$ , the centroid of all points in  $\mathbf{P}$  except from the last point in
            $\mathbf{P}$  (i.e. the point with the largest objective function value in  $\mathbf{f}$ ).
36:         Create an empty point  $\mathbf{r}$  with  $D$  elements.
37:         for  $i \in \{1, \dots, D\}$  do
38:             Calculate  $\mathbf{r}_i \leftarrow (1 + \rho) \bar{\mathbf{x}}_i - \rho \mathbf{l}_i$ 
39:         end for
40:         if  $n < N_{\max}$  then
41:             Evaluate  $\mathbf{r}$  via  $f$ , i.e.  $f_{\mathbf{r}} \leftarrow f(\mathbf{r})$ .
42:             Increment evaluation counter  $n$  by 1.
43:             Record evaluation  $\mathcal{E} \leftarrow \mathcal{E} \cup \{(\mathbf{r}, f_{\mathbf{r}})\}$ 
44:         else
45:             break while
46:         end if
47:         Set  $Q \leftarrow 0$ .
48:         if  $f_{\mathbf{r}}$  is smaller than the first value in  $\mathbf{f}$  then
49:             Create an empty point  $\mathbf{e}$  with  $D$  elements.
50:             for  $i \in \{1, \dots, D\}$  do
51:                 Calculate  $\mathbf{e}_i \leftarrow (1 + \rho\nu) \bar{\mathbf{x}}_i - \rho\nu \mathbf{l}_i$ .
52:             end for
53:             if  $n < N_{\max}$  then
54:                 Evaluate  $\mathbf{e}$  via  $f$ , i.e.  $f_{\mathbf{e}} \leftarrow f(\mathbf{e})$ .
55:                 Increment evaluation counter  $n$  by 1.
56:                 Record evaluation  $\mathcal{E} \leftarrow \mathcal{E} \cup \{(\mathbf{e}, f_{\mathbf{e}})\}$ 

```

Algorithm 3 continued

```

57:         else
58:             break while
59:         end if
60:         if  $f_e < f_r$  then
61:             Replace the last point in  $\mathbf{P}$  with  $\mathbf{e}$  and the last value in  $\mathbf{f}$  by  $f_e$ .
62:         else
63:             Replace the last point in  $\mathbf{P}$  with  $\mathbf{r}$  and the last value in  $\mathbf{f}$  by  $f_r$ .
64:         end if
65:     else
66:         if  $f_r$  is smaller than the second last value in  $\mathbf{f}$  then
67:             Replace the last point in  $\mathbf{P}$  with  $\mathbf{r}$  and the last value in  $\mathbf{f}$  by  $f_r$ .
68:         else
69:             if  $f_r$  is smaller than the last value in  $\mathbf{f}$  then
70:                 Create an empty point  $\mathbf{c}$  with  $D$  elements.
71:                 for  $i \in \{1, \dots, D\}$  do
72:                     Calculate  $\mathbf{c}_i \leftarrow (1 + \rho\psi) \bar{\mathbf{x}}_i - \rho\psi \mathbf{l}_i$ .
73:                 end for
74:                 if  $n < N_{\max}$  then
75:                     Evaluate  $\mathbf{c}$  via  $f$ , i.e.  $f_c \leftarrow f(\mathbf{c})$ .
76:                     Increment evaluation counter  $n$  by 1.
77:                     Record evaluation  $\mathcal{E} \leftarrow \mathcal{E} \cup \{(\mathbf{c}, f_c)\}$ 
78:                 else
79:                     break while
80:                 end if
81:                 if  $f_c \leq f_r$  then
82:                     Replace the last point in  $\mathbf{P}$  with  $\mathbf{c}$  and the last value in  $\mathbf{f}$ 
                        by  $f_c$ .
83:                 else

```

Algorithm 3 continued

```

84:             Set  $Q \leftarrow 1$ .
85:         end if
86:     else
87:         Create an empty point  $\mathbf{d}$  with  $D$  elements.
88:         for  $i \in \{1, \dots, D\}$  do
89:             Calculate  $\mathbf{d}_i \leftarrow (1 - \psi) \bar{\mathbf{x}}_i + \psi \mathbf{l}_i$ 
90:         end for
91:         if  $n < N_{\max}$  then
92:             Evaluate  $\mathbf{d}$  via  $f$ , i.e.  $f_{\mathbf{d}} \leftarrow f(\mathbf{d})$ .
93:             Increment evaluation counter  $n$  by 1.
94:             Record evaluation  $\mathcal{E} \leftarrow \mathcal{E} \cup \{(\mathbf{d}, f_{\mathbf{d}})\}$ 
95:         else
96:             break while
97:         end if
98:         if  $f_{\mathbf{d}}$  is smaller than the last value in  $\mathbf{f}$  then
99:             Replace the last point in  $\mathbf{P}$  with  $\mathbf{d}$  and the last value in  $\mathbf{f}$ 
            by  $f_{\mathbf{d}}$ .
100:        else
101:            Set  $Q \leftarrow 1$ .
102:        end if
103:    end if
104:    if  $Q = 1$  then
105:        Temporarily store the first point in  $\mathbf{P}$  as  $\mathbf{s}$ .
106:        for  $i$  in  $\{2, 3, \dots, D - 1\}$  do
107:            Temporarily store the  $i$ -th point in  $\mathbf{P}$  as  $\mathbf{u}$ .
108:            Create an empty point  $\mathbf{k}$  with  $D$  elements.
109:            for  $j \in \{1, \dots, D\}$  do

```

Algorithm 3 continued

```

110:             Calculate  $\mathbf{k}_j \leftarrow \mathbf{s}_j + \sigma_c(\mathbf{u}_j - \mathbf{s}_j)$ 
111:         end for
112:         if  $n < N_{\max}$  then
113:             Evaluate  $\mathbf{k}$  via  $f$ , i.e.  $f_{\mathbf{k}} \leftarrow f(\mathbf{k})$ .
114:             Increment evaluation counter  $n$  by 1.
115:             Record evaluation  $\mathcal{E} \leftarrow \mathcal{E} \cup \{(\mathbf{k}, f_{\mathbf{k}})\}$ 
116:         else
117:             break while
118:         end if
119:             Store  $\mathbf{k}$  at the  $i$ -th location in  $\mathbf{P}$ .
120:             Store  $f_{\mathbf{k}}$  at the  $i$ -th location in  $\mathbf{f}$ .
121:         end for
122:     end if
123: end if
124: end if
125:     Find and store the point  $\mathbf{x}^*$  from  $\mathbf{P}$  which corresponds to the
        best objective function value found so far.
126: end while
127: end while
128: Find smallest objective function value in  $\mathcal{E}$  and store as  $f_{\text{best}}$ .
129: Store the point  $\mathbf{x}_{\text{best}}$  from  $\mathcal{E}$  where  $f_{\text{best}} = f(\mathbf{x}_{\text{best}})$ .
130: return  $\mathbf{x}_{\text{best}}$  and  $f_{\text{best}}$ ; the best found solution and its corresponding objective
        function value respectively.
131: end procedure

```

A.4 Solver Method MARS and Solver Method GPR: Dynamic Coordinate Search using Response Surfaces

Algorithm 4 Dynamic Coordinate Search using Response Surfaces

- 1: **procedure** RUNDYCORSOPTIMISATION
 - 2: Set evaluation counter n to 0, and σ to σ_{init} .
 - 3: Create an empty set \mathcal{E} to store evaluated points and their corresponding objective function values.
 - 4: **while** $n < N_{\text{max}}$ **do**
 - 5: Generate an initial experimental design, $\mathbf{D}_{n_0 \times D}$, with n_0 points and each point containing D dimensions.
 - 6: Evaluate all points from the initial experimental design \mathbf{D} via the objective function f , incrementing n with each objective function evaluation. If n reaches N_{max} stop evaluating design points.
 - 7: Find best objective function value f^* and corresponding point \mathbf{x}^* from the initial evaluations.
 - 8: Create a temporary empty set \mathcal{G} to store evaluated points and their corresponding objective function values during this loop iteration.
 - 9: Copy all experimental design points and their objective function values to both sets \mathcal{E} and \mathcal{G} , *i.e.* $\mathcal{E} \leftarrow \mathcal{E} \cup \{(\mathbf{x}, f(\mathbf{x})) : \mathbf{x} = \text{row}_i(\mathbf{D}_{n_0 \times D}), i \in \{1, 2, \dots, n_0\}\}$ and $\mathcal{G} \leftarrow \mathcal{G} \cup \{(\mathbf{x}, f(\mathbf{x})) : \mathbf{x} = \text{row}_i(\mathbf{D}_{n_0 \times D}), i \in \{1, 2, \dots, n_0\}\}$.
 - 10: Fit either a MARS or a GPR surrogate model \hat{f} to the initial points and their objective function values from \mathcal{G} .
 - 11: Set fail counter C_{fail} to 0 and success counter C_{succ} to 0.
 - 12: Set weight counter e to 1.
 - 13: **while** $n < N_{\text{max}}$ and $\sigma \geq \sigma_{\text{min}}$ **do**
-

Algorithm 4 continued

14: Create a set $\mathbf{S}_{N_{\text{cand}} \times D}$ of candidate points, where each row in \mathbf{S} corresponds to a point \mathbf{s} . All points \mathbf{S} are initially set equal to a copy of the variable values which give the current best known objective function value, *i.e.* $\text{row}_i(\mathbf{S}_{N_{\text{cand}} \times D}) \leftarrow \mathbf{x}^*, i \in \{1, 2, \dots, N_{\text{cand}}\}$.

15: **if** weight counter $e \leq |\mathcal{W}|$ **then**

16: Set weight ω to equal the e -th weight value in \mathcal{W} , *i.e.* $\omega = w_e$, where $\omega_e \in \mathcal{W}$.

17: **else**

18: Reset weight counter e to 1.

19: Set weight ω to equal the first weight value in \mathcal{W} , *i.e.* $\omega = w_1$.

20: **end if**

21: Increment weight counter e by 1.

22: Calculate variable dimension perturbation probability p from $p = \min\left(\frac{20}{D}, 1\right) \cdot \left(1 - \frac{\log(n-n_0+1)}{\log(N_{\text{max}}-n_0)}\right)$, where D is the number of optimisation problem variables, n is the number of objective function evaluations performed so far (including evaluations due to the initial experimental design), and N_{max} is the evaluation budget.

23: Create an empty set \mathcal{I} .

24: Draw a sample \mathcal{K} of D uniformly distributed random numbers each within the interval $[0, 1]$.

25: **for** each i in the set $\{1, 2, \dots, |\mathcal{K}|\}$ **do**

26: Mark dimension i to be perturbed by adding i to \mathcal{I} if the value of k_i in \mathcal{K} is less than p .

27: **end for**

28: **if** no dimensions have been marked for perturbation **then**

29: Randomly select a dimension i from $\{1, 2, \dots, |\mathcal{K}|\}$ to be perturbed and store in \mathcal{I} .

30: **end if**

Algorithm 4 continued

```

31:         for each point (i.e. row)  $\mathbf{s}$  in  $\mathbf{S}$  do
32:             for each element index  $j$  in  $\{1, 2, \dots, |\mathcal{K}|\}$  do
33:                 if the index  $j$  is a dimension to be perturbed, i.e.  $j \in \mathcal{I}$  then
34:                     Draw a single observation  $y$  from a normal distributed random
                       number with mean 0 and standard deviation  $\sigma$ .
35:                     Add  $y$  to the value of  $\mathbf{s}_j$  and store in a temporary variable  $\mathbf{u}$ ,
                       i.e.  $\mathbf{u}_j \leftarrow \mathbf{s}_j + y$ .
36:                     Store  $\mathbf{u}_j$  to  $\mathbf{s}$  in  $\mathbf{S}$ , i.e.  $\mathbf{s}_j \leftarrow \mathbf{u}_j$ .
37:                 else
38:                     Leave the value of  $\mathbf{s}_j$  from  $\mathbf{s}$  in  $\mathbf{S}$  unchanged.
39:                 end if
40:             end for
41:             Ensure the elements of  $\mathbf{s}$  are within the interval  $[0, 1]$ , i.e. they will
                       not infringe upon the optimisation problem's box constraints.
42:         end for
43:         Find and store maximum and minimum surrogate values  $g_{\max}$  and  $g_{\min}$ 
                       respectively of all candidate points' surrogate values  $\hat{f}(\mathbf{s})$  by evaluating
                       them via  $\hat{f}$ .
44:         Find and store maximum and minimum shortest Euclidean distance values
                        $h_{\max}$  and  $h_{\min}$  respectively of all candidate points' shortest Euclidean
                       distances to any of the evaluated points within  $\mathcal{G}$ .
45:         for  $i$  in  $\{1, 2, \dots, N_{\text{cand}}\}$  do
46:             Select the  $i$ -th point from  $\mathbf{S}$ , i.e.  $\mathbf{s} = \text{row}_i(\mathbf{S})$ .
47:             Evaluate point  $\mathbf{s}$  on fitted surrogate model  $\hat{f}$  and store the surrogate
                       value  $\hat{f}(\mathbf{s})$ .

```

Algorithm 4 continued

48: Calculate candidate point's surrogate value $\hat{f}(\mathbf{s})$ within the $[0, 1]$ interval by $v_{i,e} = \frac{\hat{f}(\mathbf{s}) - g_{\min}}{g_{\max} - g_{\min}}$. If $g_{\max} = g_{\min}$, set $v_{i,e} = 1$.

49: Calculate shortest Euclidean distance between the candidate point \mathbf{s} and any of the evaluated points within \mathcal{G} and store as $L(\mathbf{s})$.

50: Calculate candidate point's shortest Euclidean distance value $L(\mathbf{s})$ within the $[0, 1]$ interval by $v_{i,l} = \frac{h_{\max} - L(\mathbf{s})}{h_{\max} - h_{\min}}$. If $h_{\max} = h_{\min}$, set $v_{i,l} = 1$.

51: Calculate overall candidate point score $t_i = \omega v_{i,e} + (1 - \omega) v_{i,l}$

52: **end for**

53: Select candidate point \mathbf{s} from \mathbf{S} with smallest overall score t_i , and store as \mathbf{x}_{next} .

54: Evaluate \mathbf{x}_{next} via the objective function f , and increment n by 1.

55: Add point \mathbf{x}_{next} and its objective function value $f(\mathbf{x}_{\text{next}})$ to both sets \mathcal{E} and \mathcal{G} , *i.e.* $\mathcal{E} \leftarrow \mathcal{E} \cup \{(\mathbf{x}_{\text{next}}, f(\mathbf{x}_{\text{next}}))\}$ and $\mathcal{G} \leftarrow \mathcal{G} \cup \{(\mathbf{x}_{\text{next}}, f(\mathbf{x}_{\text{next}}))\}$.

56: **if** $f(\mathbf{x}_{\text{next}}) < f^*$ **then**

57: **if** $f(\mathbf{x}_{\text{next}}) < f^* - \delta |f^*|$ **then**

58: Set fail counter C_{fail} to 0, and increment success counter C_{succ} by 1.

59: **end if**

60: Store $f(\mathbf{x}_{\text{next}})$ and \mathbf{x}_{next} as the new f^* and \mathbf{x}^* , *i.e.* $f^* \leftarrow f(\mathbf{x}_{\text{next}})$ and $\mathbf{x}^* \leftarrow \mathbf{x}_{\text{next}}$.

61: **else**

62: Set success counter C_{succ} to 0, and increment fail counter C_{fail} by 1.

63: **end if**

64: **if** either $C_{\text{succ}} = F_{\text{succ}}$ or $C_{\text{fail}} = F_{\text{fail}}$ **then**

65: **if** $C_{\text{succ}} = F_{\text{succ}}$ **then**

Algorithm 4 continued

66: Double perturbation standard deviation σ , within limit σ_{\max} , *i.e.*
 $\sigma \leftarrow \min(2\sigma, \sigma_{\max})$.

67: **else**

68: Halve perturbation standard deviation σ , *i.e.* $\sigma \leftarrow 0.5\sigma$.

69: **end if**

70: Reset both success C_{succ} and fail C_{fail} counters to 0.

71: **end if**

72: Update surrogate model \hat{f} by re-fitting with all points and their objective
 function values from \mathcal{G} .

73: **end while**

74: **if** $n < N_{\max}$ and $\sigma < \sigma_{\min}$ **then**

75: Set σ to σ_{init} .

76: **end if**

77: **end while**

78: Find smallest objective function value in \mathcal{E} and store as f_{best} .

79: Store the point \mathbf{x}_{best} from \mathcal{E} where $f_{\text{best}} = f(\mathbf{x}_{\text{best}})$.

80: **return** \mathbf{x}_{best} and f_{best} ; the best found solution and its corresponding objective
 function value respectively.

81: **end procedure**

Appendix B

Parameter Values for Solver Method Evaluation Simulations

Table B.1: Transmission line conductor parameters, whole bundle.

Conductor Name	DC Resistance (Ω/km)	Outside Radius (cm)	Horizontal Distance (m)	Vertical Distance (m)
<i>Rectifier AC-side Line, Z_r</i>				
Earth Wire 1	3.4	0.4763	-4.115	27.12
Earth Wire 2	3.4	0.4763	4.115	27.12
Phase A	0.0696	1.407	-8.23	20.19
Phase B	0.0696	1.407	0	20.19
Phase C	0.0696	1.407	8.23	20.19
<i>Inverter AC-side Line, Z_i</i>				
Earth Wire 1	4.046	0.4572	-3.125	12.8
Earth Wire 1	4.046	0.4572	3.125	12.8
Phase A	0.0449	1.7551	-5.64	7.62
Phase B	0.0449	1.7551	0	7.62
Phase C	0.0449	1.7551	5.64	7.62

Appendix B. Parameter Values for Solver Method Evaluation Simulations

Table B.2: Transmission line conductor parameters, cont.

Conductor Name	No. Conductors in Bundle (m)	Mid-point Sag (m)	Conductor Spacing in Bundle
<i>Rectifier AC-side Line, Z_r</i>			
Earth Wire 1	1	3.9	N/A
Earth Wire 2	1	3.9	N/A
Phase A	2	7.71	0.4572
Phase B	2	7.71	0.4572
Phase C	2	7.71	0.4572
<i>Inverter AC-side Line, Z_i</i>			
Earth Wire 1	1	0	N/A
Earth Wire 1	1	0	N/A
Phase A	1	0	N/A
Phase B	1	0	N/A
Phase C	1	0	N/A

Table B.3: Curve fitting parameters for transmission line frequency dependent phase models.

Parameter Name	Value
Lower Limit (Hz)	0.5
Upper Limit (MHz)	1
Total Solution Increments	100
Maximum Poles per Column	20
Maximum Final Fitting Error, characteristic admittance (%)	2
Weighting factor, 0 to F0	100
Weighting factor, F0	1000
Weighting factor, F0 to Fmax	1
Maximum Poles per Delay Group	20
Maximum Final Fitting Error, propagation function (%)	2
Maximum Residue/Pole Ratio Tolerance	100

Appendix C

Parameter Values for Dynamic Compensation Simulations

Note that in Tables C.4–C.6 and C.8–C.9, parameter $m \in \{0.2, 0.4, 0.6\}$ depending on the specific dynamic compensation rating under study for a particular simulation.

C.1 LCC-HVDC Link Plant, Controller, and Transmission Line Parameters

Table C.1: Transmission line conductor parameters, whole bundle.

Conductor Name	DC Resistance (Ω/km)	Outside Radius (cm)	Horizontal Distance (m)	Vertical Distance (m)
<i>Rectifier AC-side Line, Z_r</i>				
Earth Wire 1	3.4	0.4763	-4.115	27.12
Earth Wire 2	3.4	0.4763	4.115	27.12
Phase A	0.0696	1.407	-8.23	20.19
Phase B	0.0696	1.407	0	20.19
Phase C	0.0696	1.407	8.23	20.19
<i>Inverter AC-side Lines, $Z_{i,1}$, $Z_{i,2}$, and $Z_{i,3}$</i>				
Earth Wire 1	4.046	0.4572	-3.125	12.8
Earth Wire 1	4.046	0.4572	3.125	12.8
Phase A	0.0449	1.7551	-5.64	7.62
Phase B	0.0449	1.7551	0	7.62
Phase C	0.0449	1.7551	5.64	7.62

Appendix C. Parameter Values for Dynamic Compensation Simulations

Table C.2: Transmission line conductor parameters, cont.

Conductor Name	No. Conductors in Bundle (m)	Mid-point Sag (m)	Conductor Spacing in Bundle
<i>Rectifier AC-side Line, Z_r</i>			
Earth Wire 1	1	3.9	N/A
Earth Wire 2	1	3.9	N/A
Phase A	2	7.71	0.4572
Phase B	2	7.71	0.4572
Phase C	2	7.71	0.4572
<i>Inverter AC-side Lines, $Z_{i,1}$, $Z_{i,2}$, and $Z_{i,3}$</i>			
Earth Wire 1	1	0	N/A
Earth Wire 1	1	0	N/A
Phase A	1	0	N/A
Phase B	1	0	N/A
Phase C	1	0	N/A

Table C.3: Curve fitting parameters for transmission line frequency dependent phase models.

Parameter Name	Value
Lower Limit (Hz)	0.5
Upper Limit (MHz)	1
Total Solution Increments	100
Maximum Poles per Column	20
Maximum Final Fitting Error, characteristic admittance (%)	2
Weighting factor, 0 to F0	100
Weighting factor, F0	1000
Weighting factor, F0 to Fmax	1
Maximum Poles per Delay Group	20
Maximum Final Fitting Error, propagation function (%)	2
Maximum Residue/Pole Ratio Tolerance	100

C.2 SVC including TCR and TSC Plant and Controller Parameters

Table C.4: Parameter values for electrical dynamics model for SVC used in the SVC study case.

Parameter Name	Value
Transformer Rating (MVA)	$m \cdot 200$
Steps per Main Time Step	20
Steps per NS1 during Switching	5
Number of Capacitor Stages	10
Initial Number of TSC Stages Committed	5
PLO Proportional Gain	100
PLO Integral Gain	900
Leakage Reactance (Primary-Star) (pu)	0.12
Leakage Reactance (Primary-Delta) (pu)	0.12
Leakage Reactance (Star-Delta) (pu)	0.014824
Total Inductive Reactive Power of TCR (MVar)	$m \cdot 200$
Combined Reactive Power of All Capacitor Stages (MVar)	$m \cdot 200$
Parallel Resistance across each Capacitor Stage (Ω)	500
Minimum Total Capacitive Reactive Power (MVar)	0.001
Rated Primary Voltage Phase-Phase (kV)	230
Primary Magnetizing Current (%)	0.0001
Rated Secondary Voltage Phase-Phase (kV)	17
Secondary Star Magnetizing Current (%)	0.0001
Secondary Delta Magnetizing Current (%)	0.0001
Air Core Reactance (pu)	1
In Rush Decay Time Constant (s)	0.001
Knee Voltage (pu)	10
Shunt Loss Conductance (S)	0

Appendix C. Parameter Values for Dynamic Compensation Simulations

Table C.5: Parameter values for SVC controller used in the SVC study case.

Parameter Name	Value
<i>PI Controller Output Bounds</i>	
SVC Susceptance Order Upper Bound B^{UB} (pu)	1.0
SVC Susceptance Order Lower Bound B^{LB} (pu)	-1.0
<i>Non-Linear Susceptance Characteristic</i>	
Transformer MVA	$m \cdot 200$
Transformer Leakage Reactance (Primary-Secondary) (pu)	0.12
Maximum Inductive Reactive Power (MVA _r)	$m \cdot 200$
Total Reactive Power of All Capacitor Stages (MVA _r)	$m \cdot 200$
Total Number of Capacitor Stages	10
<i>Capacitor Switching Logic</i>	
Total Number of Capacitor Stages	10
Minimum Time between Switchings (s)	0.01667
<i>Schmitt Trigger Thresholds</i>	
Logic One Input Level (pu)	0
Logic Zero Input Level (pu)	-0.1
<i>Non-Linear Gain (input: pu, output: deg)</i>	
Point 1	(-0.1, 180)
Point 2	(0, 180)
Point 3	(0.015, 161.89)
Point 4	(0.05, 149.79)
Point 5	(0.15, 138.08)
Point 6	(0.25, 128.94)
Point 7	(0.4, 119.5)
Point 8	(0.6, 108.32)
Point 9	(1, 90)
Point 10	(1.5, 90)

C.3 STATCOM Plant and Controller Parameters

Table C.6: Parameter values for STATCOM plant and transformer used in the STATCOM study case.

Parameter Name	Value
<i>STATCOM Misc. Parameters</i>	
PLL Proportional Gain	10
PLL Integral Gain	50
Offset Angle to PLL (rad)	$0.5 \cdot \pi$
ABC to DQ0 Transformation DQ Sequence	Q-axis Lagging
Converter PWM	1980
Switching Frequency (Hz)	1980
Total Converter DC-side Capacitance (μF)	$\frac{m \cdot 200 \cdot 30000}{14450}$
<i>Coupling Transformer</i>	
Transformer Rating (MVA)	$m \cdot 200$
Winding 1	Star
Winding 2	Delta
Leakage Reactance (pu)	0.12
Eddy Current Losses (pu)	0
Copper Losses (pu)	0
Winding 1 Voltage Phase-to-Phase (kV)	230
Winding 2 Voltage Phase-to-Phase (kV)	17
Saturation Enabled	No

Appendix C. Parameter Values for Dynamic Compensation Simulations

Table C.7: Parameter values for STATCOM controllers used in the STATCOM study case.

Parameter Name	Value
<i>Inner Current PI Controllers</i>	
Voltage Order Upper Bound V_i^{UB} (pu)	1.0
Voltage Order Lower Bound V_i^{LB} (pu)	-1.0
Proportional Gain K_i	0.396
Integral Time Constant τ_i (s)	0.13397
Coupling Transformer Series Reactance L_c (pu)	0.12
<i>Outer PI Controllers</i>	
D-axis Current Order Upper Bound I_s^{UB} (pu)	0.45826
D-axis Current Order Lower Bound I_s^{LB} (pu)	-0.45826
Q-axis Current Order Upper Bound I_t^{UB} (pu)	1.0
Q-axis Current Order Lower Bound I_t^{LB} (pu)	-1.0
D-axis Proportional Gain K_s	0.87969
D-axis Integral Time Constant τ_s (s)	0.012922

C.4 Plant and Controller Parameters of Synchronous Condenser Model

Table C.8: Parameter values for synchronous condenser electrical dynamic model used in the Synchronous Condenser study case.

Parameter Name	Value
<i>Synchronous Condenser Electrical Dynamic Model</i>	
Number of Q-axis Damper Windings	1
Multi-mass Interface	Disabled
D-axis Saturation	Disabled
Rated RMS Phase-to-Neutral Voltage (kV)	9.815
Rated RMS Phase Current (kA)	$\frac{m \cdot 200}{29.445}$
Base Angular Frequency (rad/s)	376.99
Inertia Constant (s)	2
Mechanical Friction and Windage (pu)	0
Neutral Series Resistance (pu)	0
Neutral Series Reactance (pu)	0
Iron Loss Resistance (pu)	0
Armature Time Constant (s)	0.17
Potier Reactance (pu)	0.2
D-axis Unsaturated Reactance (pu)	1.8
D-axis Unsaturated Transient Reactance (pu)	0.4
D-axis Unsaturated Transient Time Open (s)	9
D-axis Unsaturated Sub-transient Reactance (pu)	0.25
D-axis Unsaturated Sub-transient Time Open (s)	0.035
Q-axis Unsaturated Reactance (pu)	1.15
Q-axis Unsaturated Sub-transient Reactance (pu)	0.3
Q-axis Unsaturated Sub-transient Time Open (s)	0.035
Air Gap Factor	1

Appendix C. Parameter Values for Dynamic Compensation Simulations

Table C.9: Parameter values for synchronous condenser transformer and voltage controller used in the Synchronous Condenser study case.

Parameter Name	Value
<i>Coupling Transformer</i>	
Transformer Rating (MVA)	$m \cdot 200$
Winding 1	Star
Winding 2	Delta
Leakage Reactance (pu)	0.12
Eddy Current Losses (pu)	0
Copper Losses (pu)	0
Winding 1 Voltage Phase-to-Phase (kV)	230
Winding 2 Voltage Phase-to-Phase (kV)	17
Saturation Enabled	No
<i>PI Controller Output Bounds</i>	
Exciter Voltage Order Upper Bound V_c^{UB} (pu)	10.0
Exciter Voltage Order Lower Bound V_c^{LB} (pu)	-10.0

Appendix D

Selected Time Series Plots of Measured Variables

These time domain plots are drawn for the best optimal objective function values found in each engineering feasible set of results for each plant configuration.

Appendix D. Selected Time Series Plots of Measured Variables

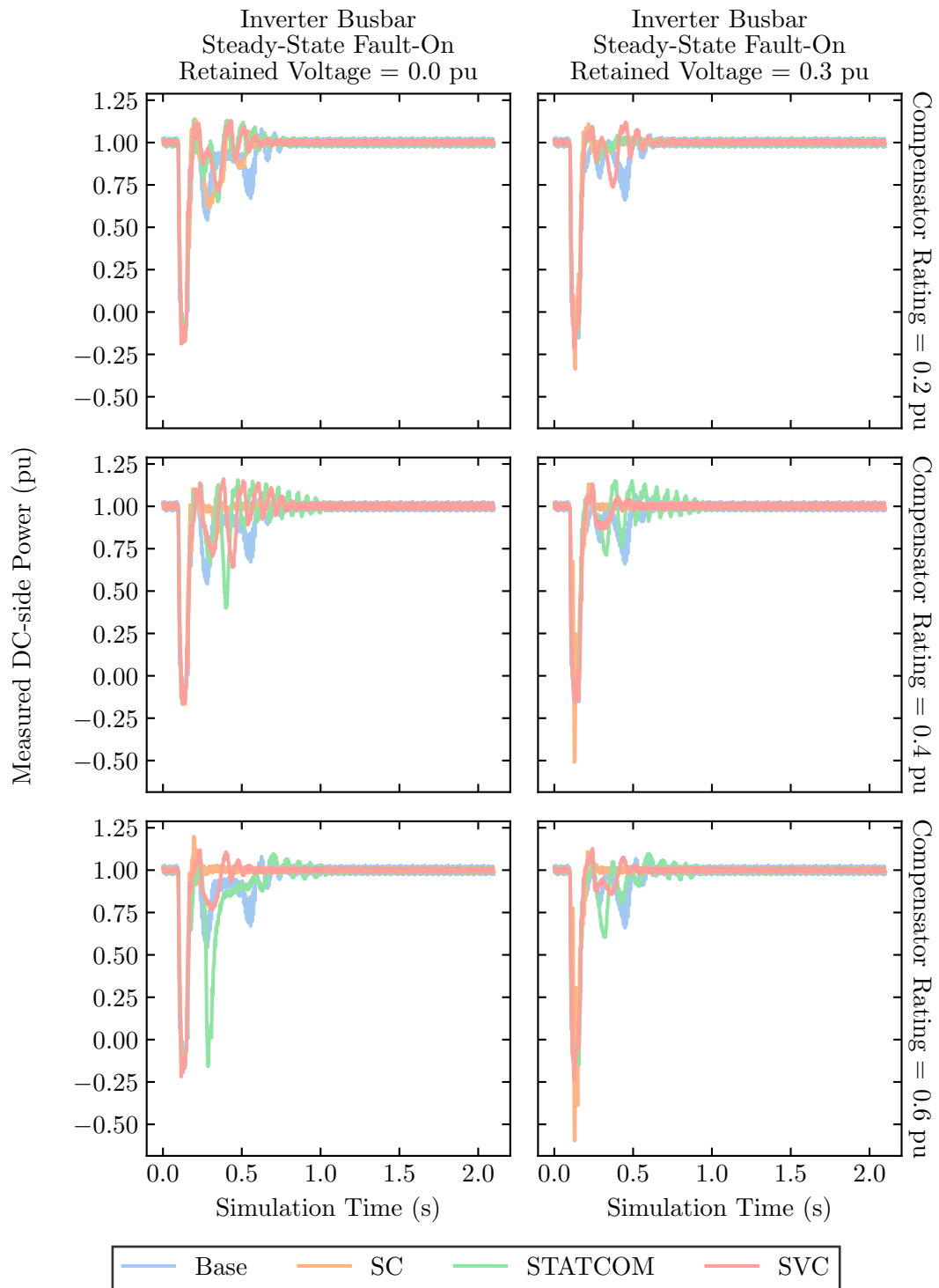


Figure D.1: DC-side measured power time domain traces for inverter SCR of 1.5.

Appendix D. Selected Time Series Plots of Measured Variables

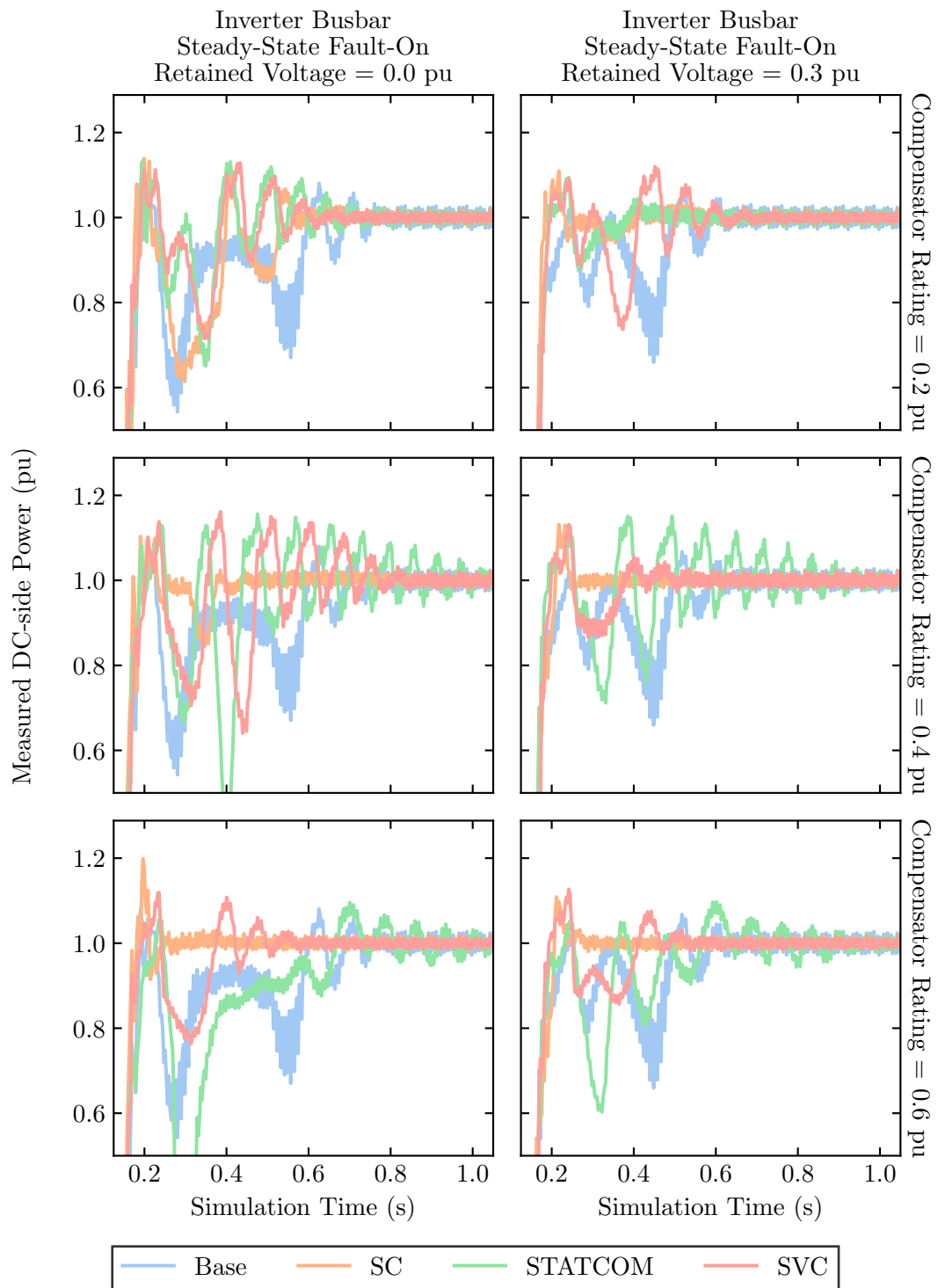


Figure D.2: Zoomed view of DC-side measured power time domain traces for inverter SCR of 1.5.

Appendix D. Selected Time Series Plots of Measured Variables

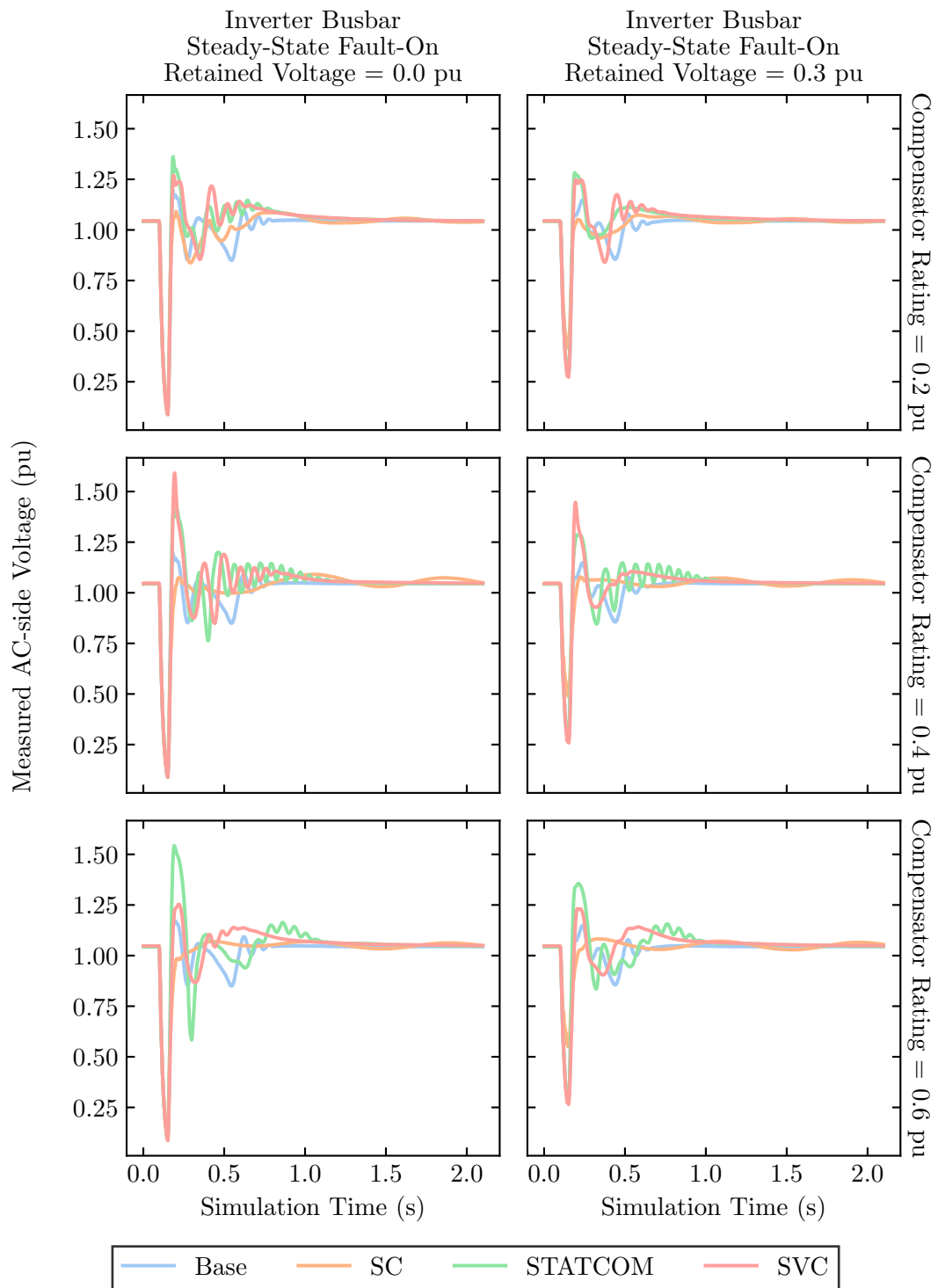


Figure D.3: AC-side measured voltage magnitude time domain traces for inverter SCR of 1.5.

Appendix D. Selected Time Series Plots of Measured Variables

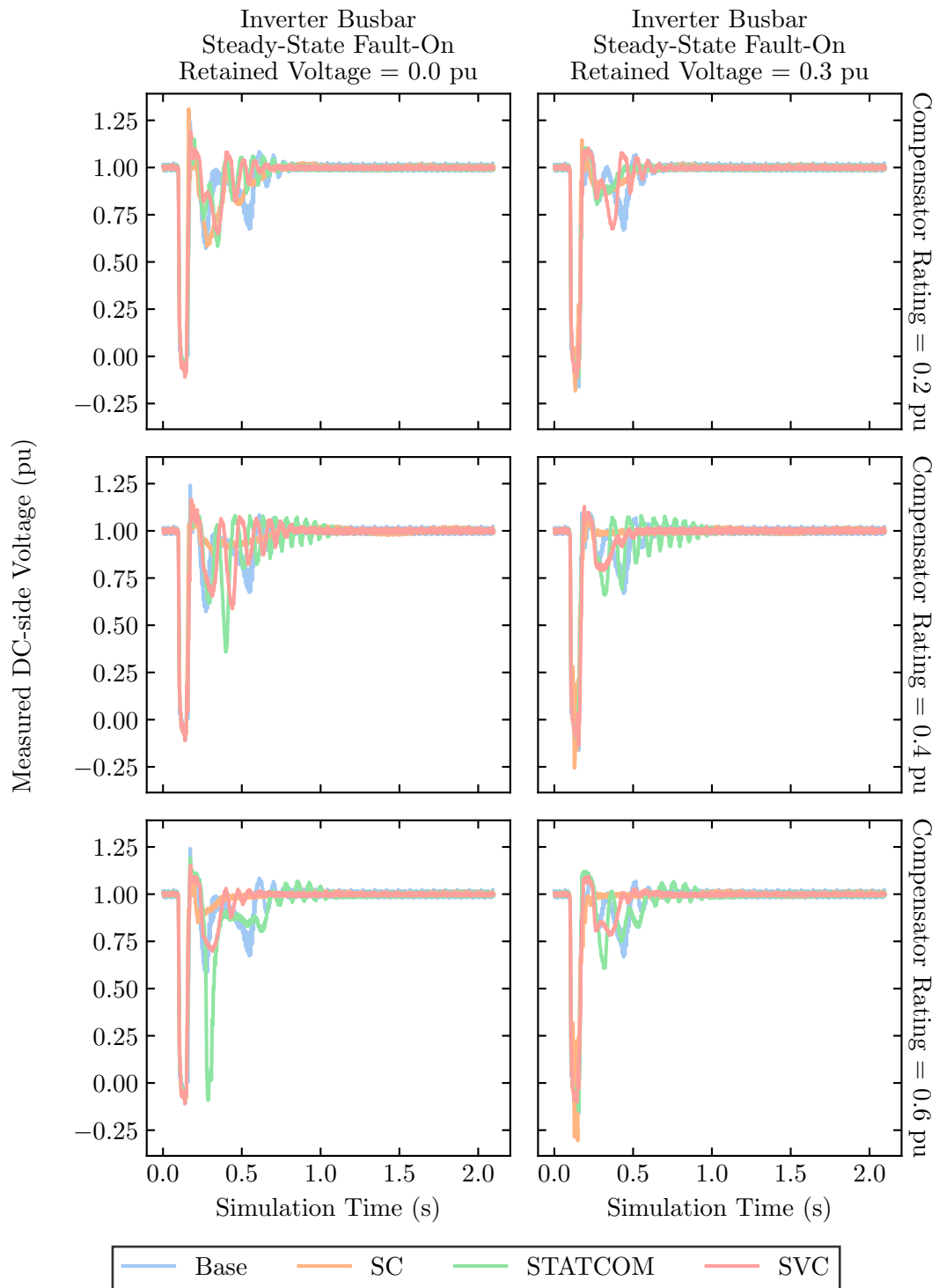


Figure D.4: DC-side measured voltage time domain traces for inverter SCR of 1.5.

Appendix D. Selected Time Series Plots of Measured Variables

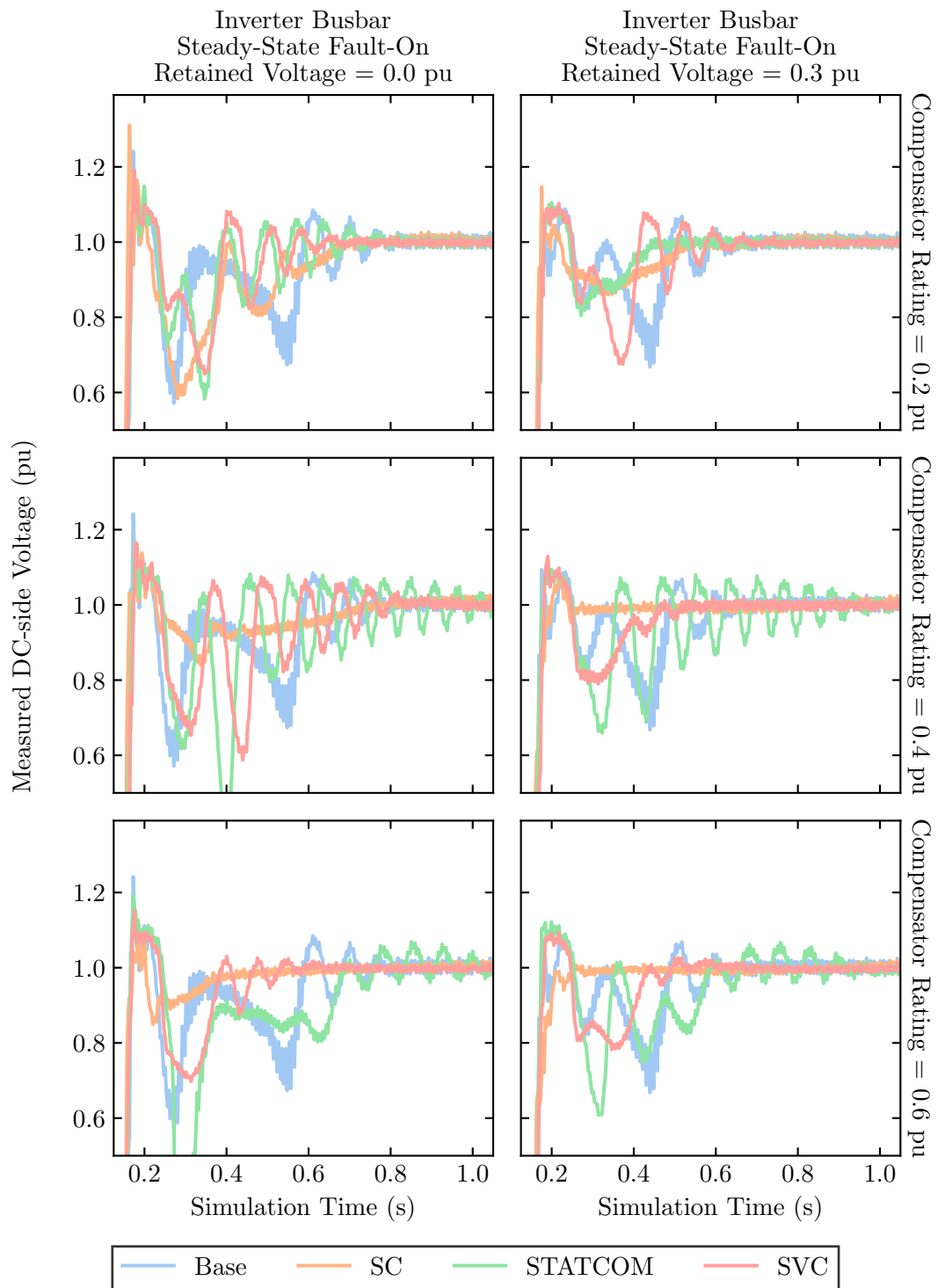


Figure D.5: Zoomed view of DC-side measured voltage time domain traces for inverter SCR of 1.5.

Appendix D. Selected Time Series Plots of Measured Variables

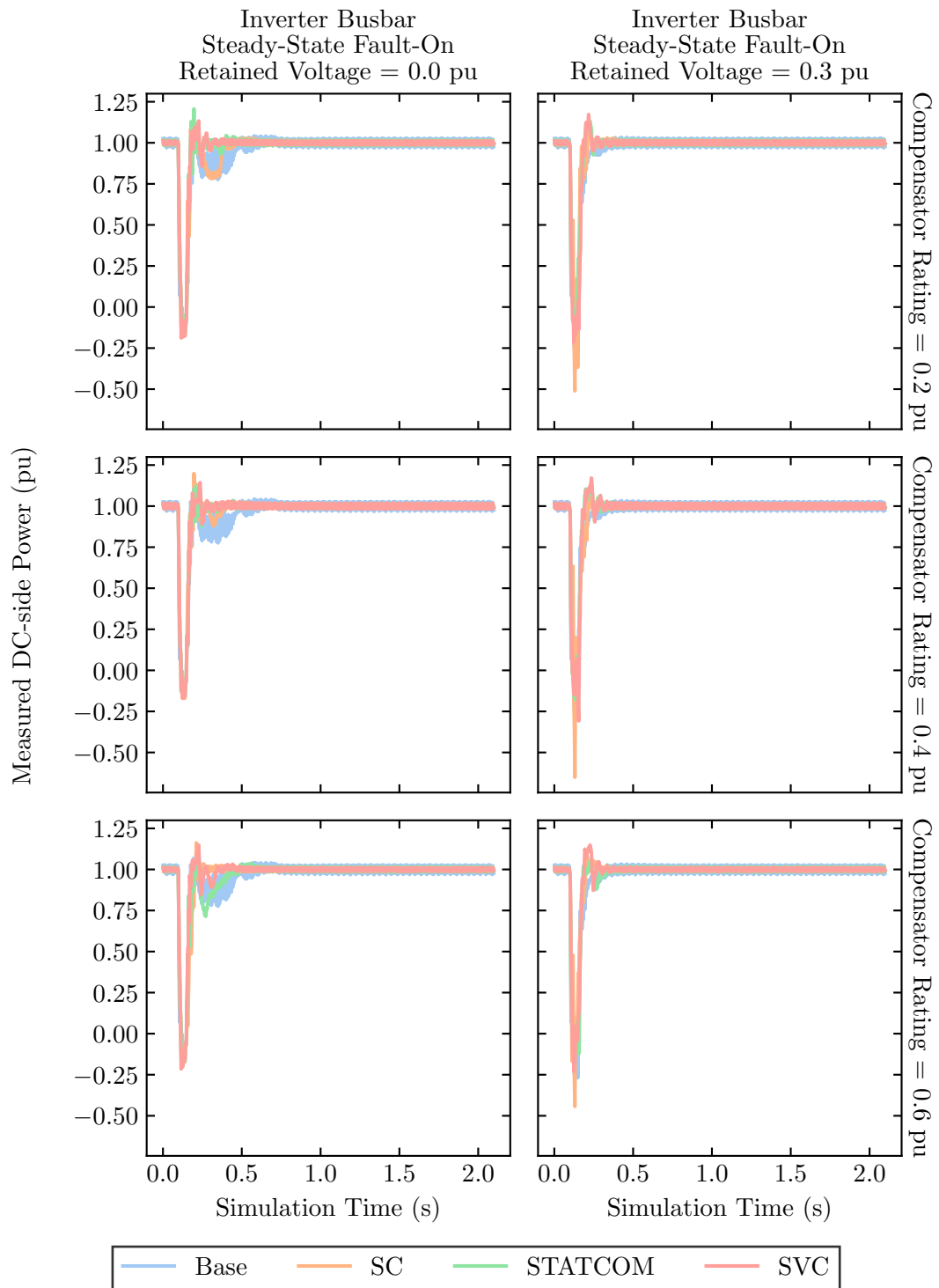


Figure D.6: DC-side measured power time domain traces for inverter SCR of 2.0.

Appendix D. Selected Time Series Plots of Measured Variables

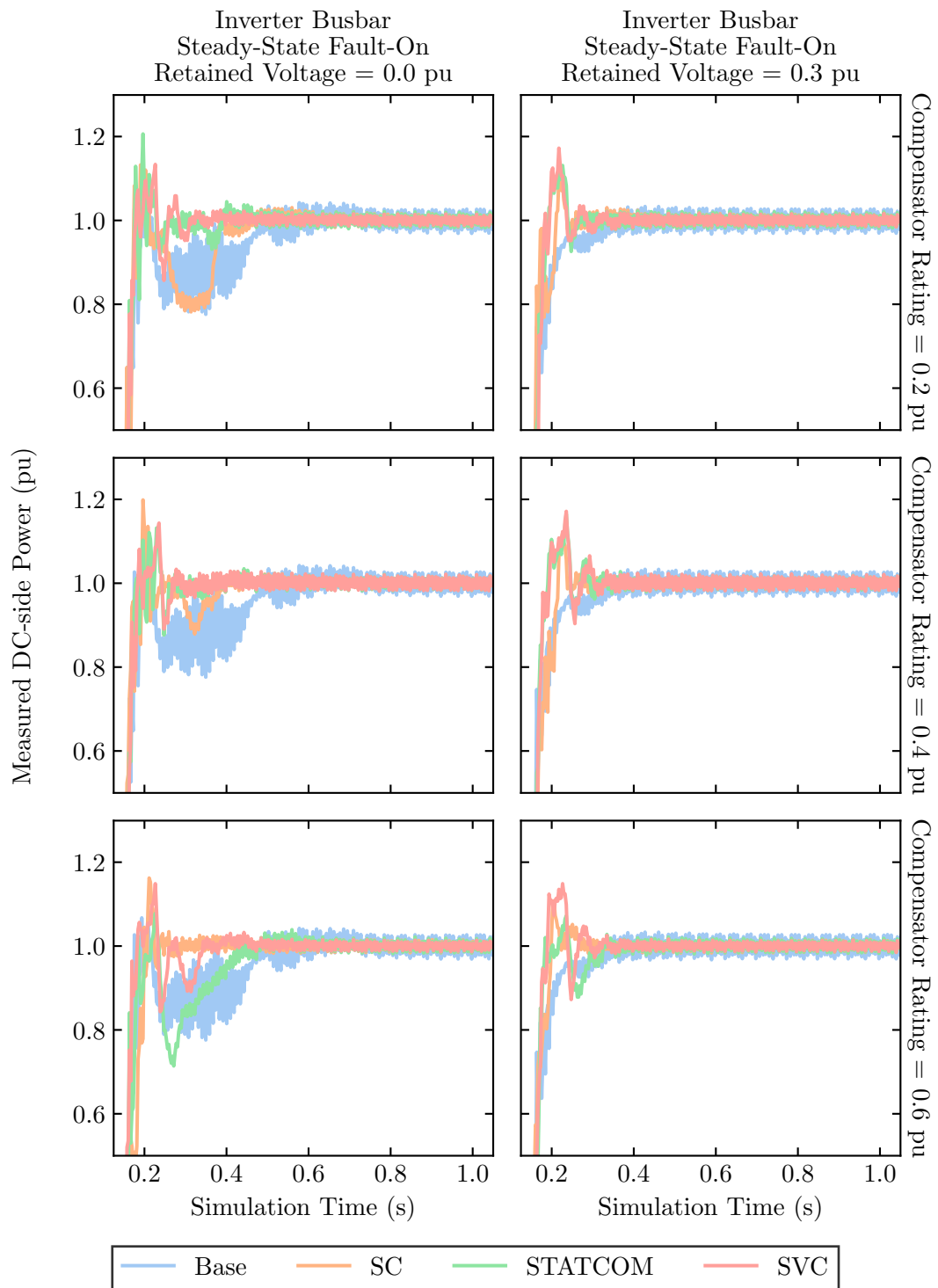


Figure D.7: Zoomed view of DC-side measured power time domain traces for inverter SCR of 2.0.

Appendix D. Selected Time Series Plots of Measured Variables

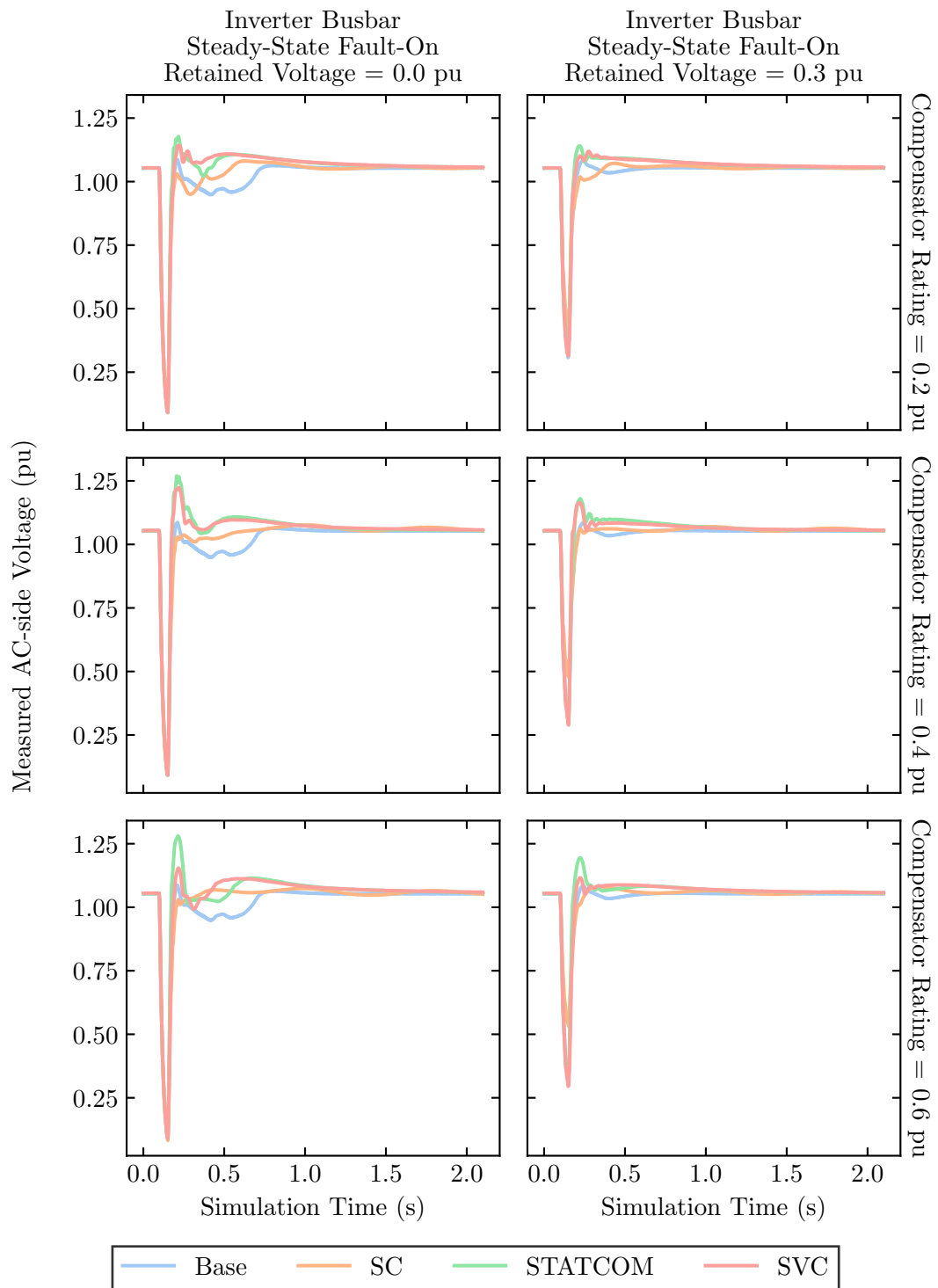


Figure D.8: AC-side measured voltage magnitude time domain traces for inverter SCR of 2.0.

Appendix D. Selected Time Series Plots of Measured Variables

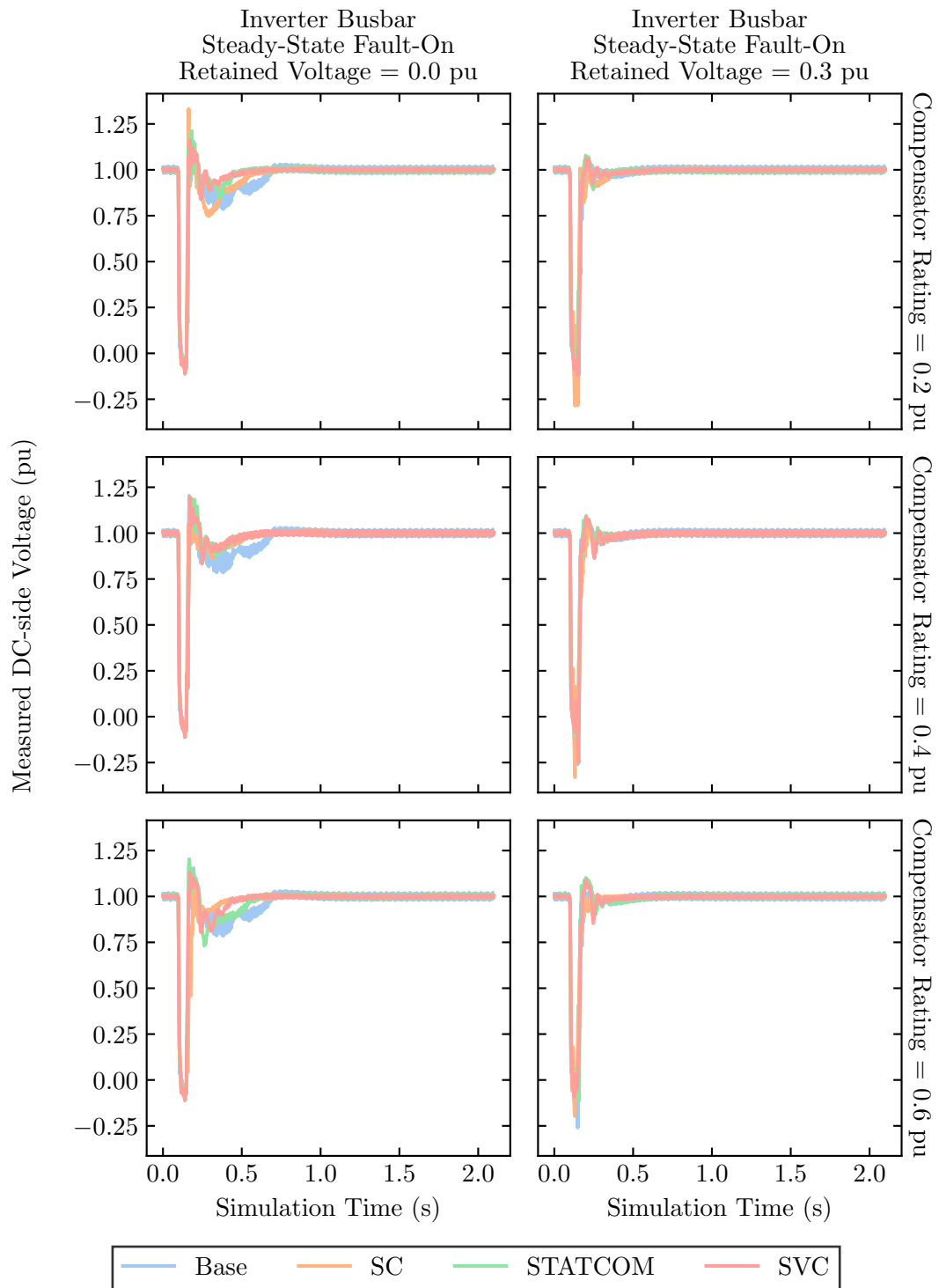


Figure D.9: DC-side measured voltage time domain traces for inverter SCR of 2.0.

Appendix D. Selected Time Series Plots of Measured Variables

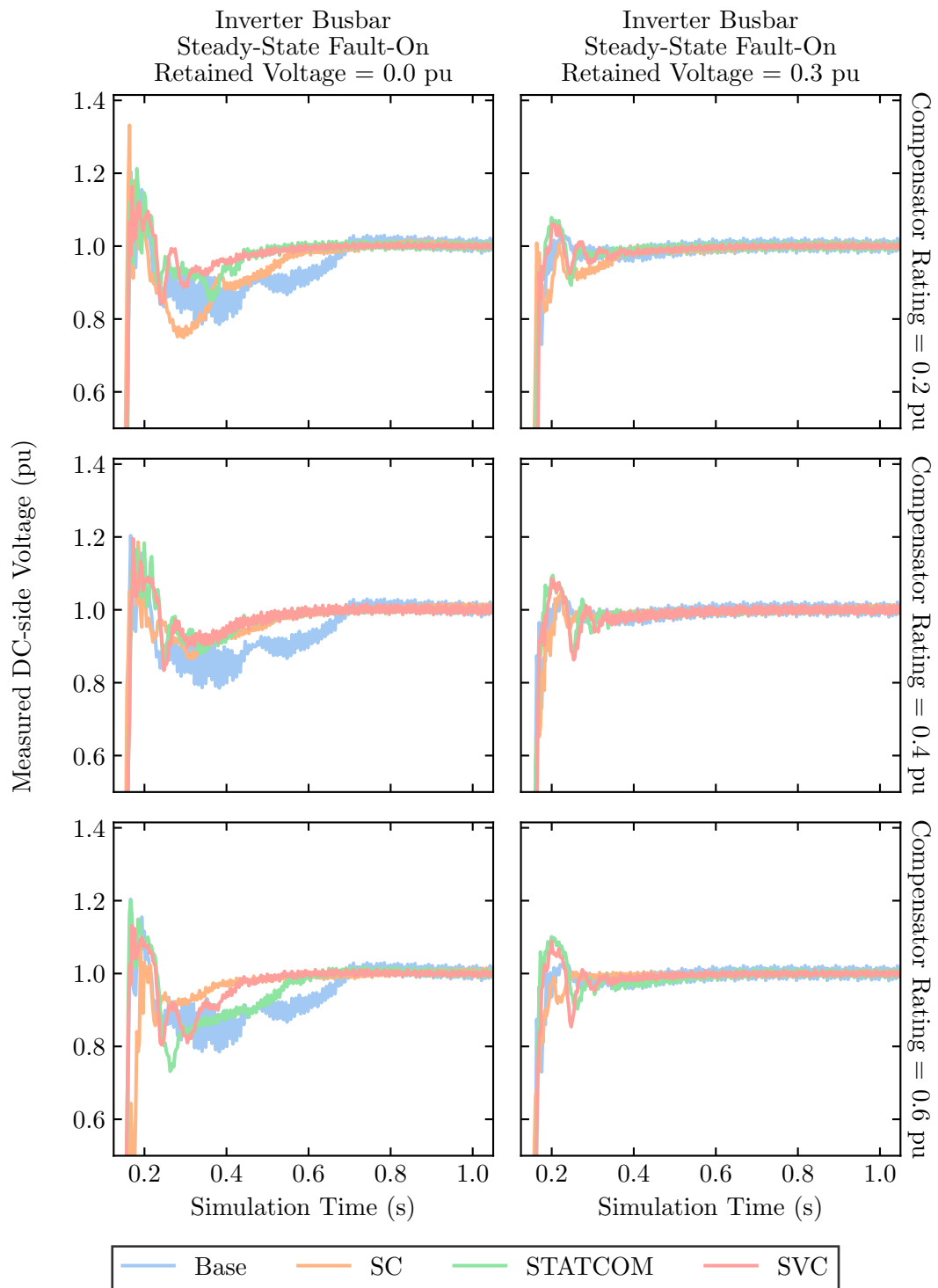


Figure D.10: Zoomed view of DC-side measured voltage time domain traces for inverter SCR of 2.0.

Appendix E

Box-plots

The box-plots are drawn with respect to engineering feasible samples. The box-plots indicate median and interquartile range and the box-plot whiskers correspond to a maximum range of one-and-a-half times the interquartile range with whiskers extending to the furthest data point within that maximum range. Furthermore, the individual observations within the samples are explicitly overlaid in top of the box-plots.

E.1 Performance Values of Measured Variables

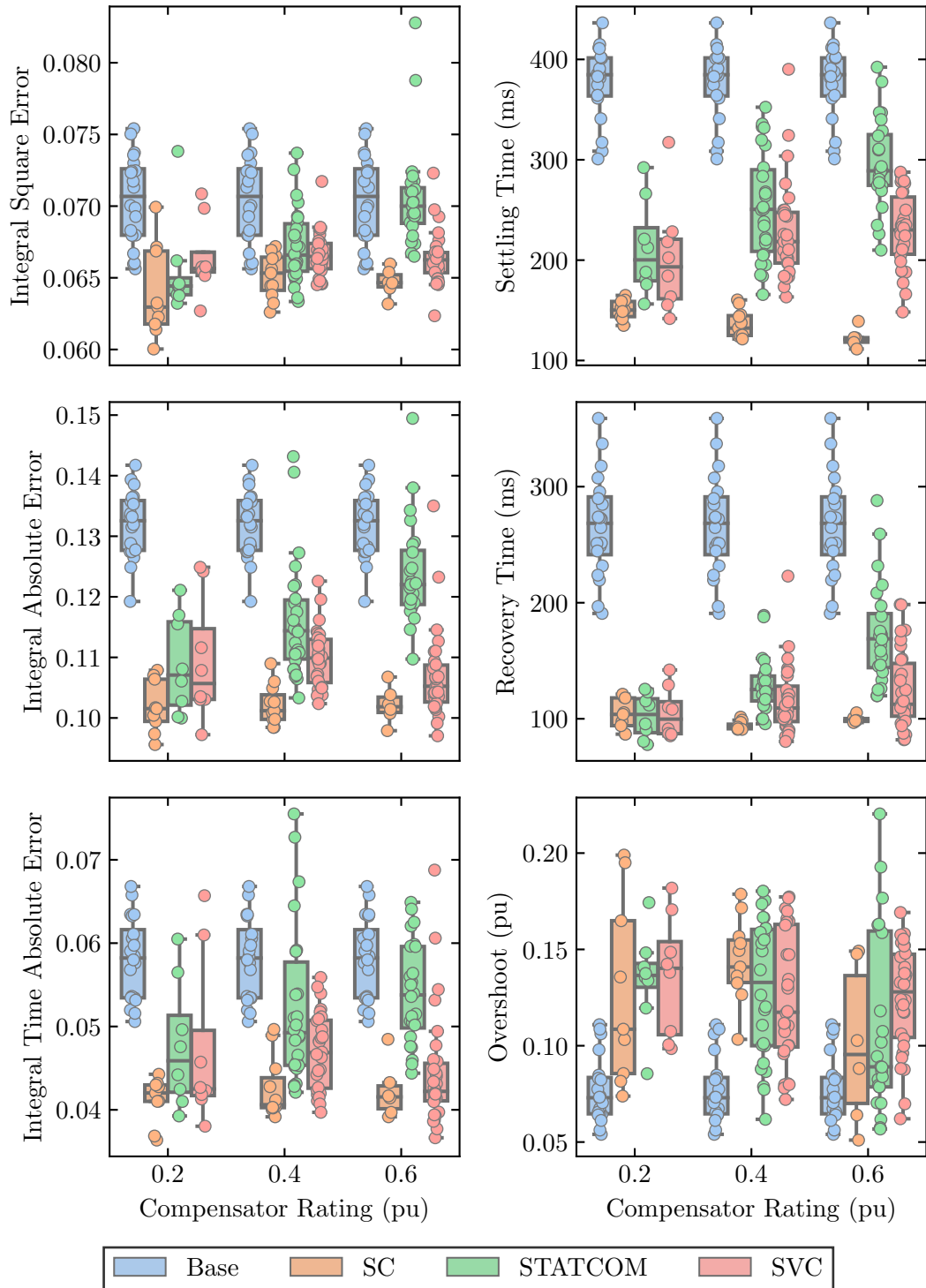


Figure E.1: Box-plots of performance values of DC-side measured power.

Appendix E. Box-plots

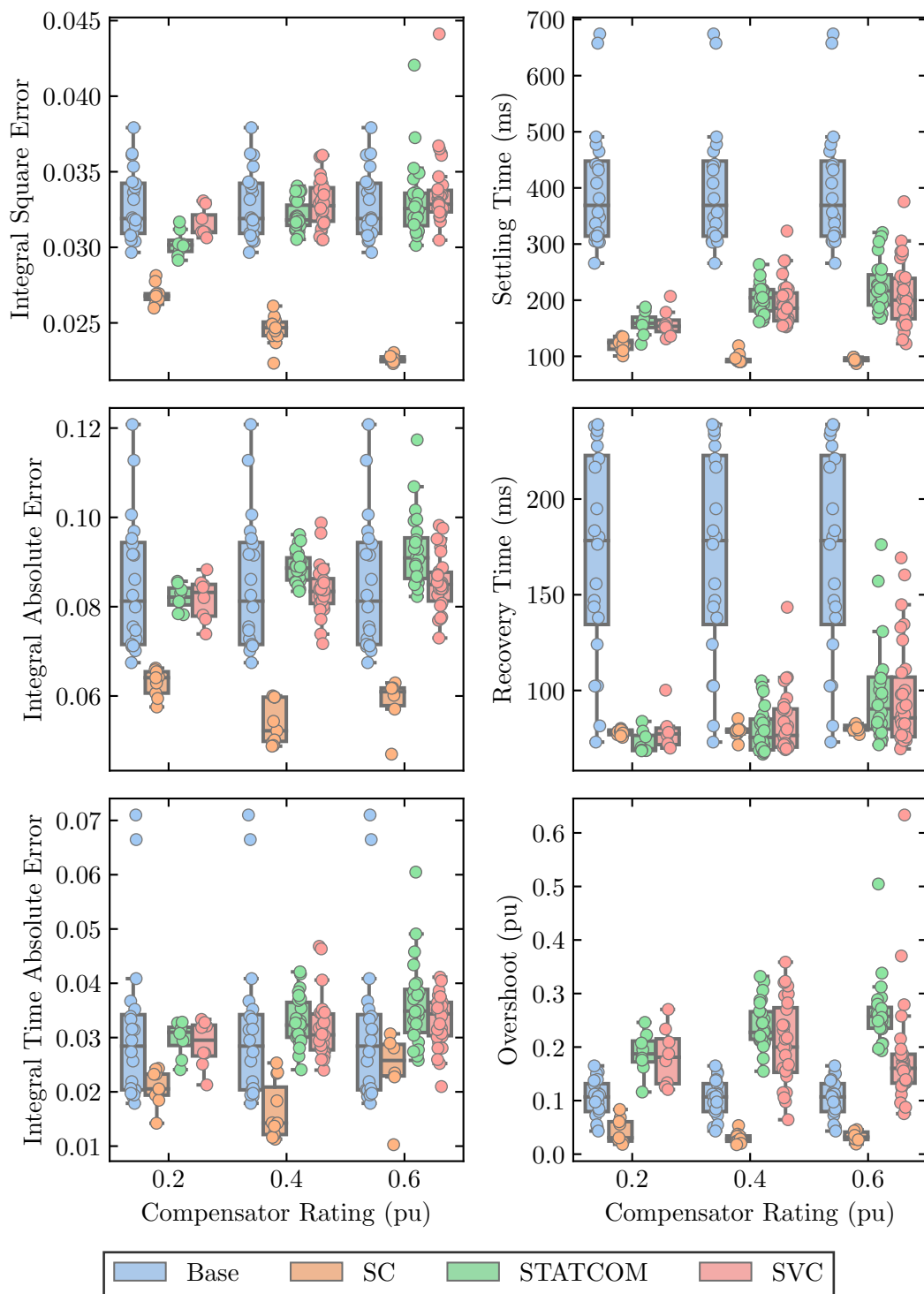


Figure E.2: Box-plots of performance values of AC-side measured voltage magnitude.

Appendix E. Box-plots

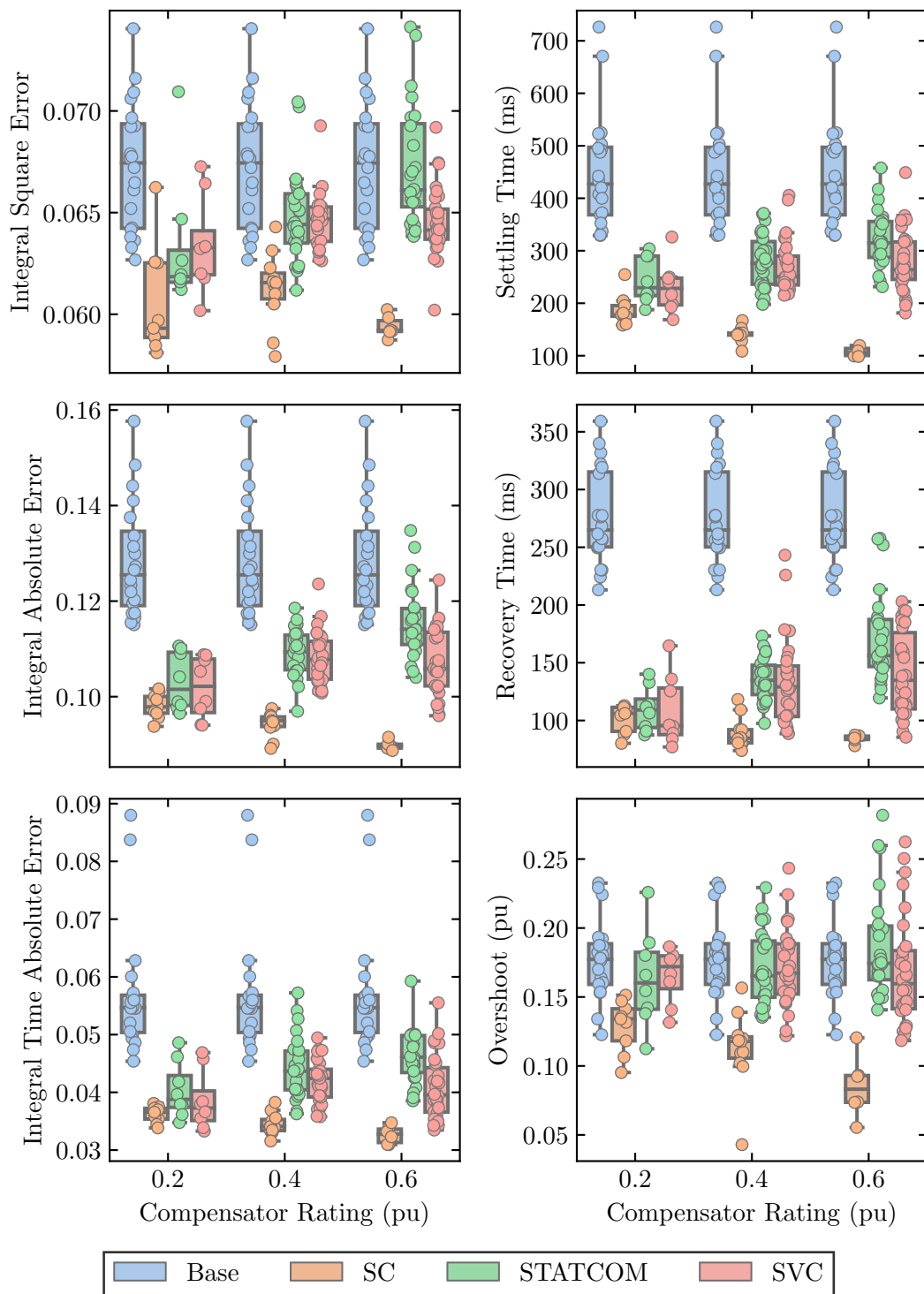


Figure E.3: Box-plots of performance values of DC-side measured voltage.

Appendix E. Box-plots

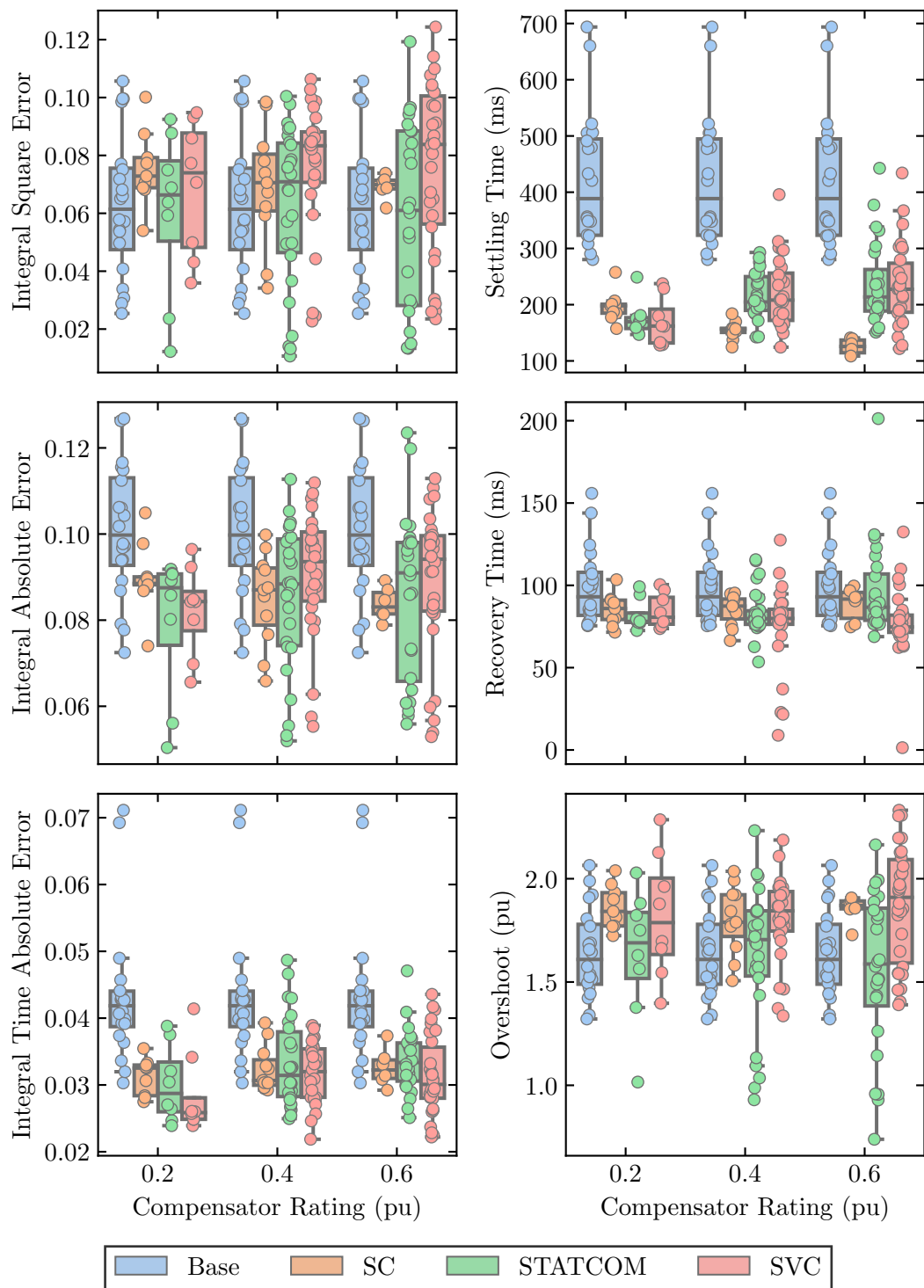


Figure E.4: Box-plots of performance values of DC-side measured current.

Appendix E. Box-plots

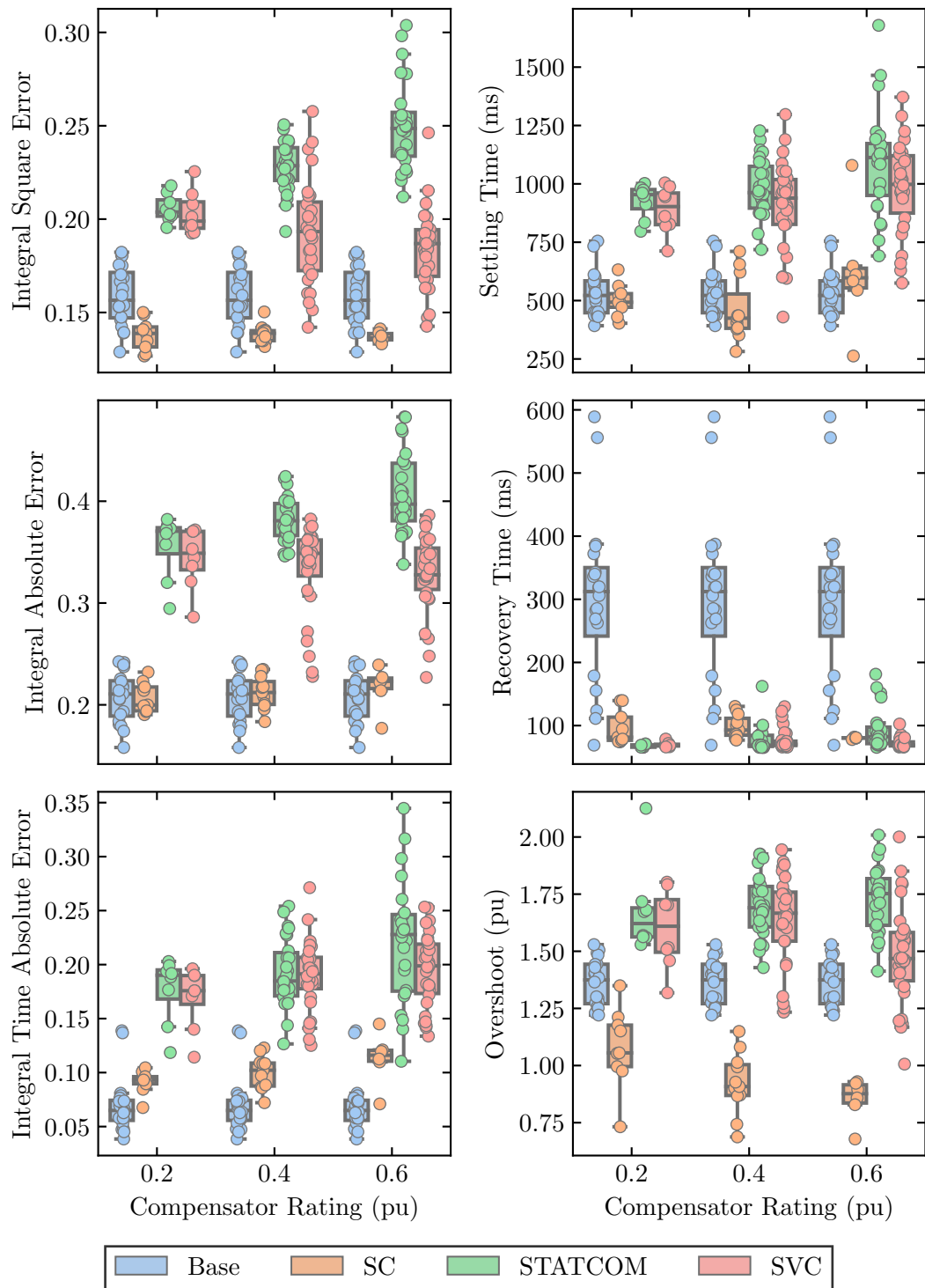


Figure E.5: Box-plots of performance values of measured extinction angle.

E.2 LCC-HVDC Optimal Controller Parameter Values

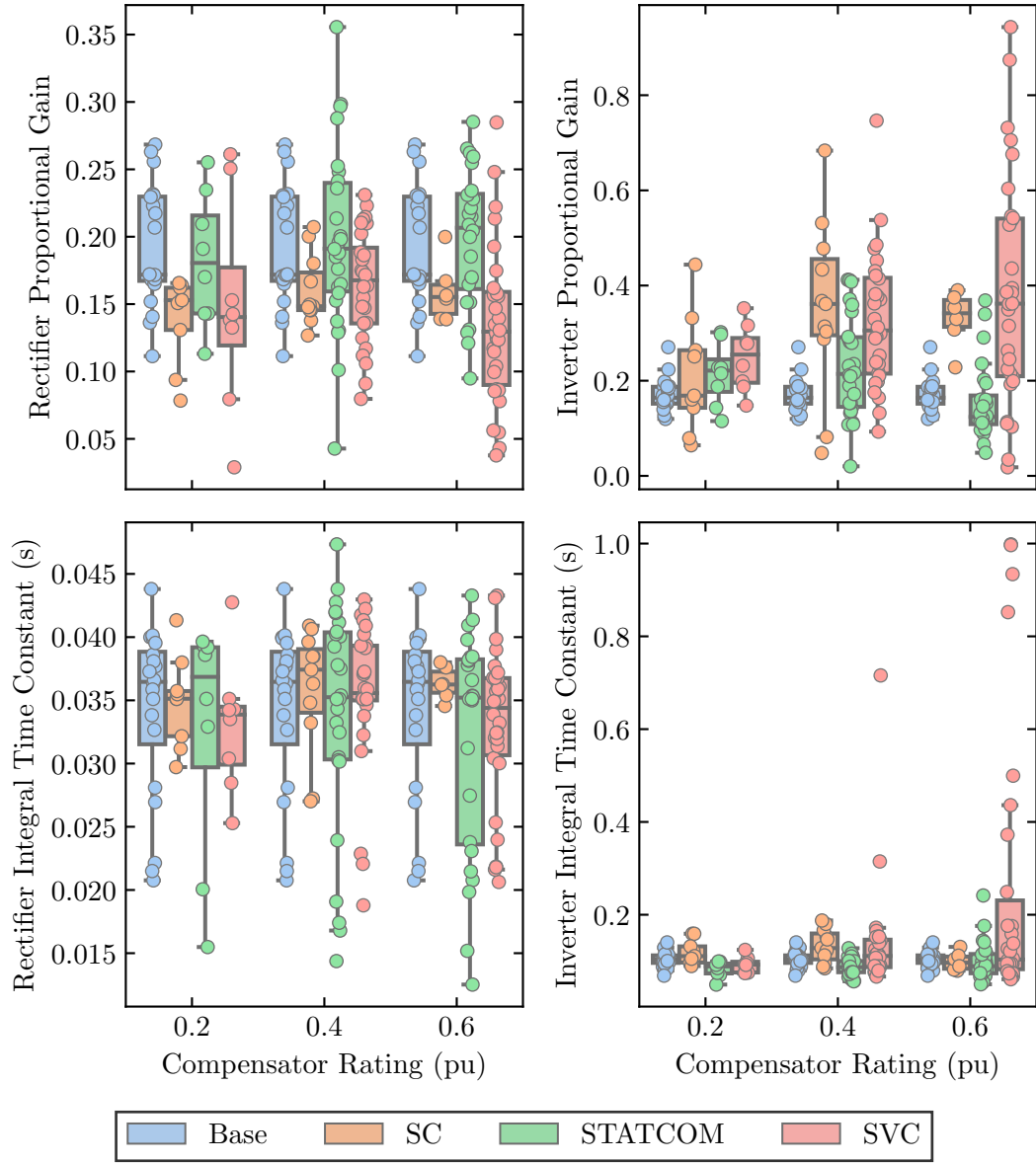


Figure E.6: Box-plots of LCC-HVDC link PI controller optimal parameter values.

Appendix E. Box-plots

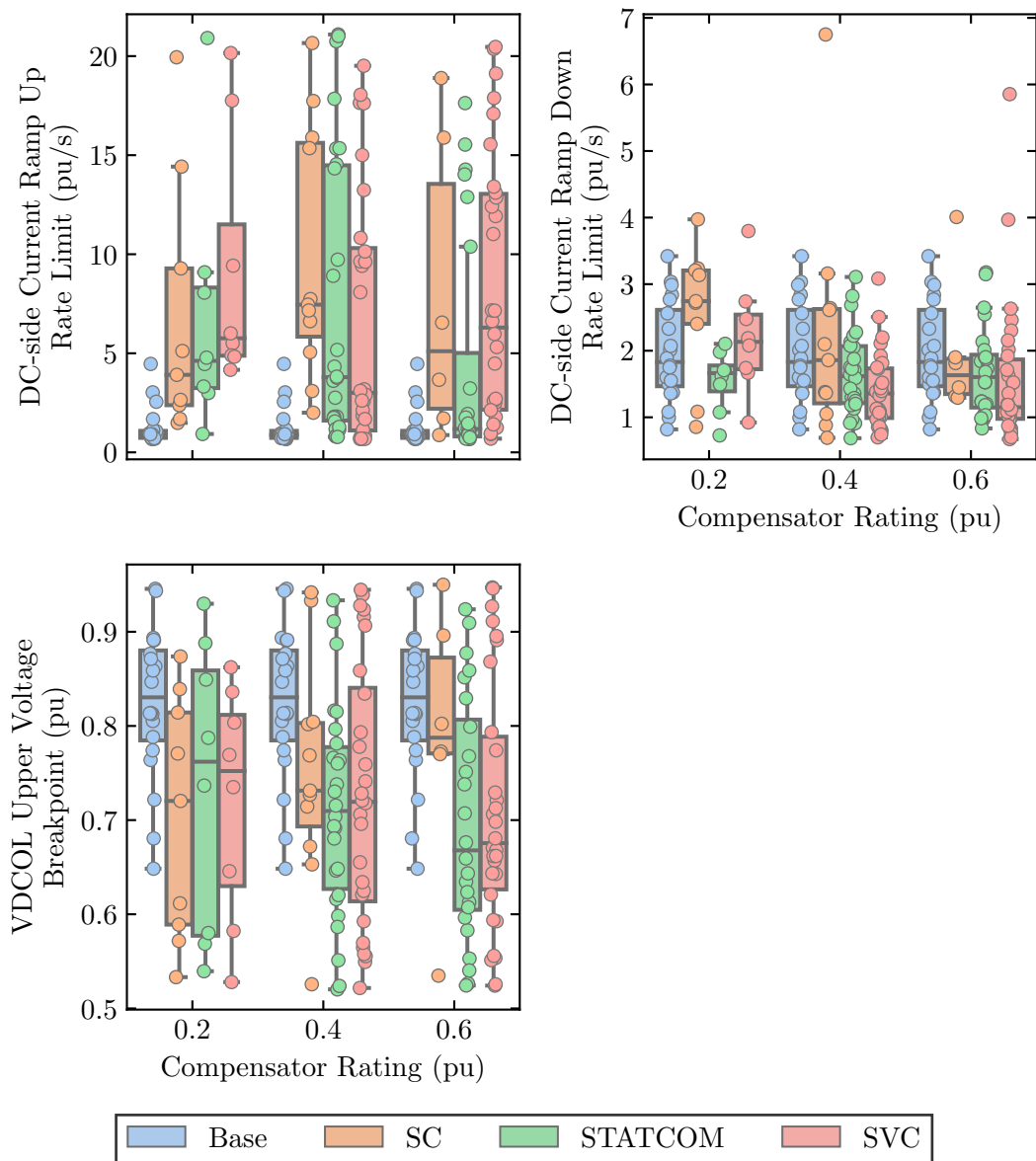


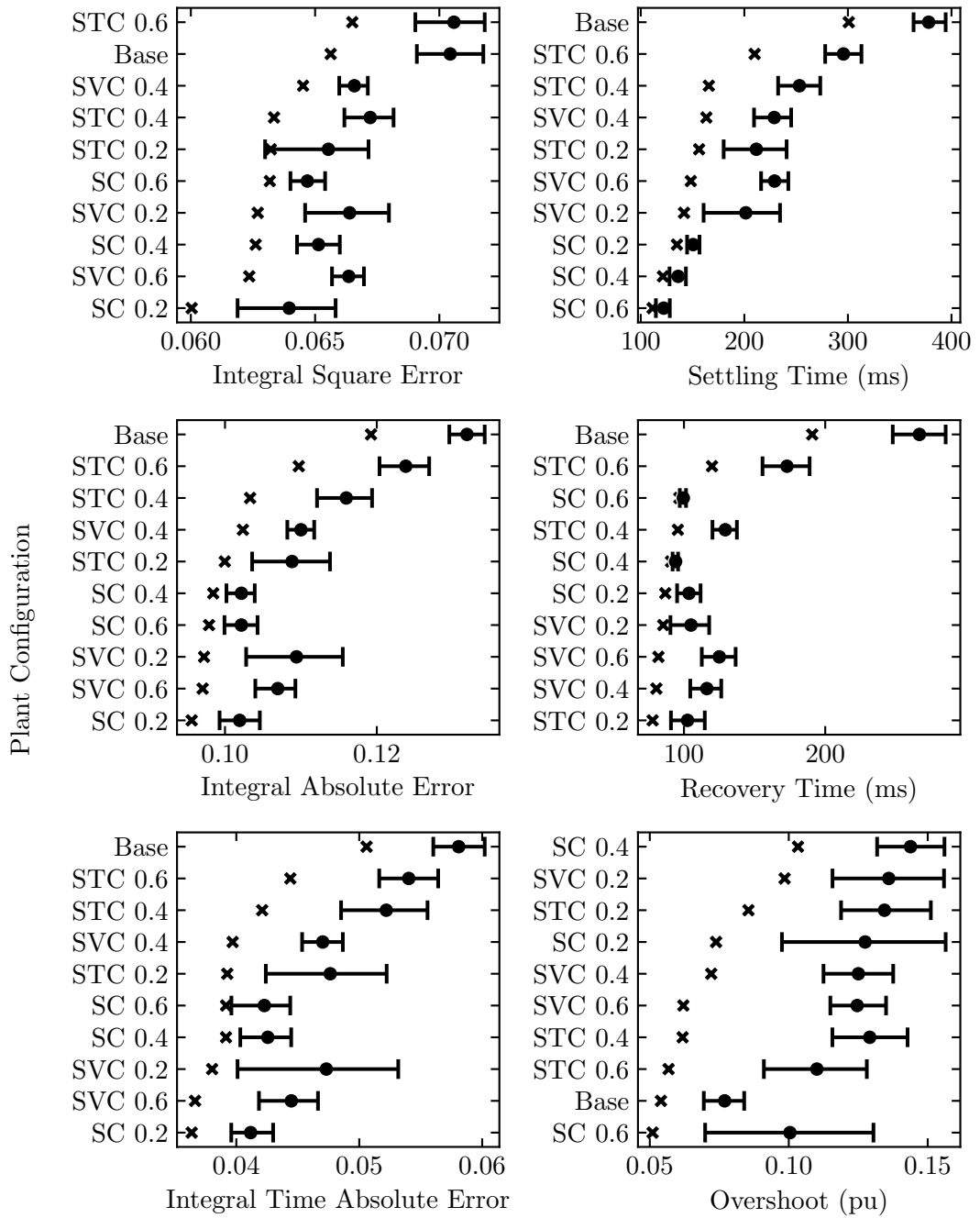
Figure E.7: Box-plots of LCC-HVDC link VDCOL optimal parameter values.

Appendix F

Sample Means and Sample Minima of Performance Values

These plots include observed sample means and sample minima. In addition, the estimated 95% CI of the sample mean is also indicated via intervals. Observed sample minima are indicated by cross markers, and observed sample means are indicated by dot markers. Results are sorted within each plot such that y-axis labels are arranged in ascending order of observed sample minima. In the y-axis labels, “SC” corresponds to synchronous condenser and “STC” corresponds to STATCOM. The ratings of the dynamic compensator equipment are indicated by the numbers “0.2”, “0.4”, and “0.6”—corresponding to 0.2, 0.4, and 0.6 pu ratings respectively—succeeding the “SC”, “STC”, and “SVC” labels.

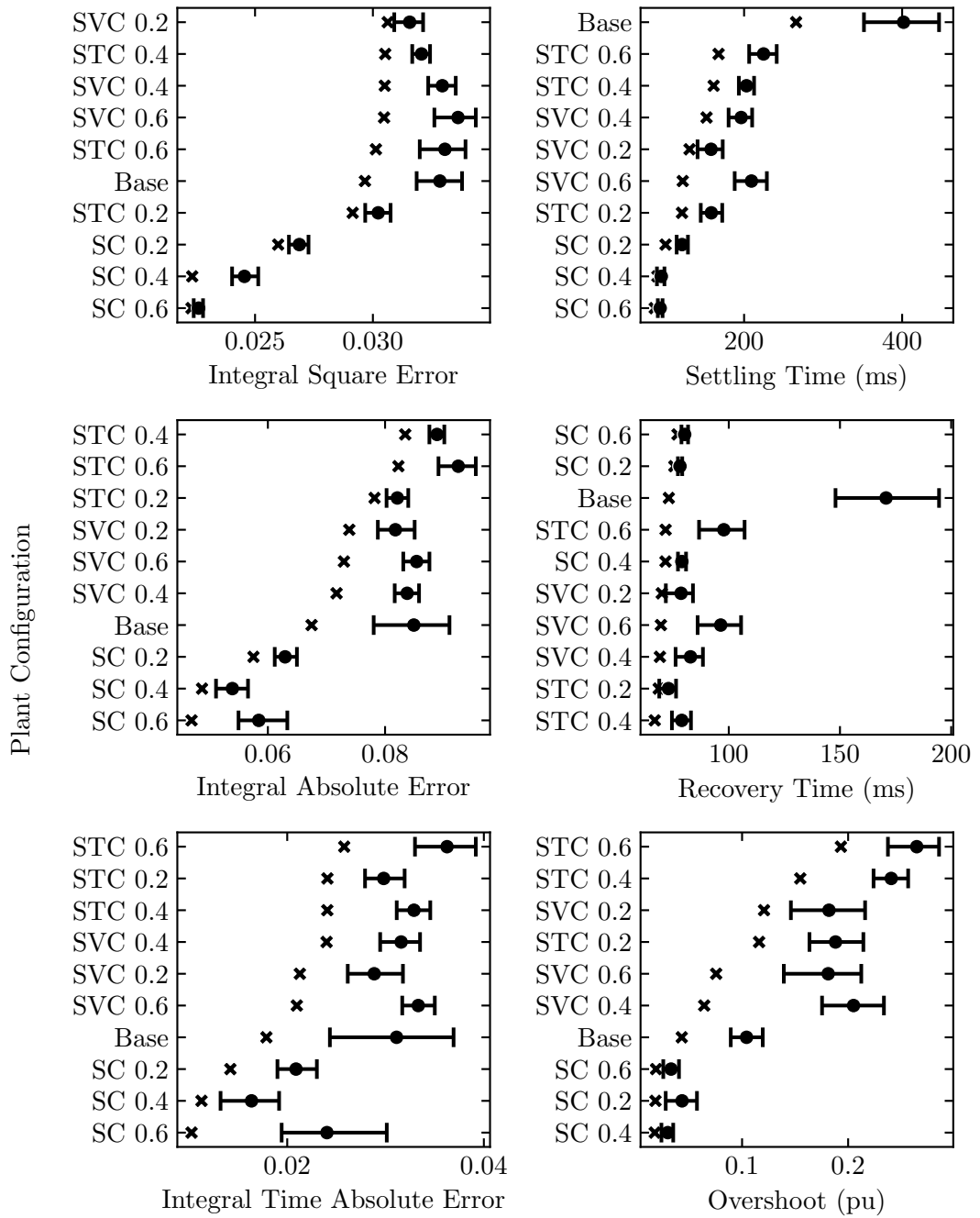
Appendix F. Sample Means and Sample Minima of Performance Values



Plant Configuration Sample Means (with 95% CI), and Sample Minima

Figure F.1: DC-side measured power sample statistics.

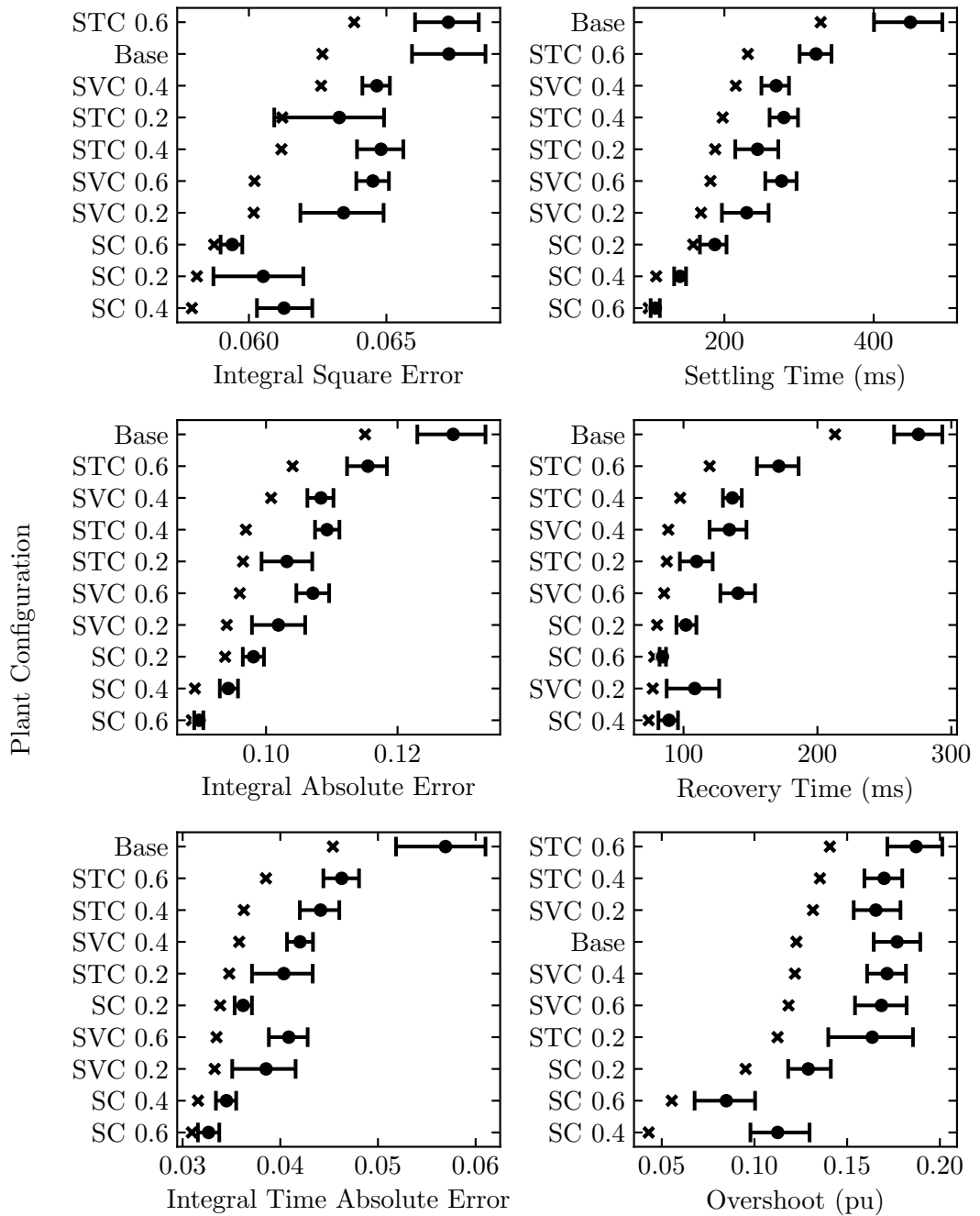
Appendix F. Sample Means and Sample Minima of Performance Values



Plant Configuration Sample Means (with 95% CI), and Sample Minima

Figure F.2: AC-side measured voltage magnitude sample statistics.

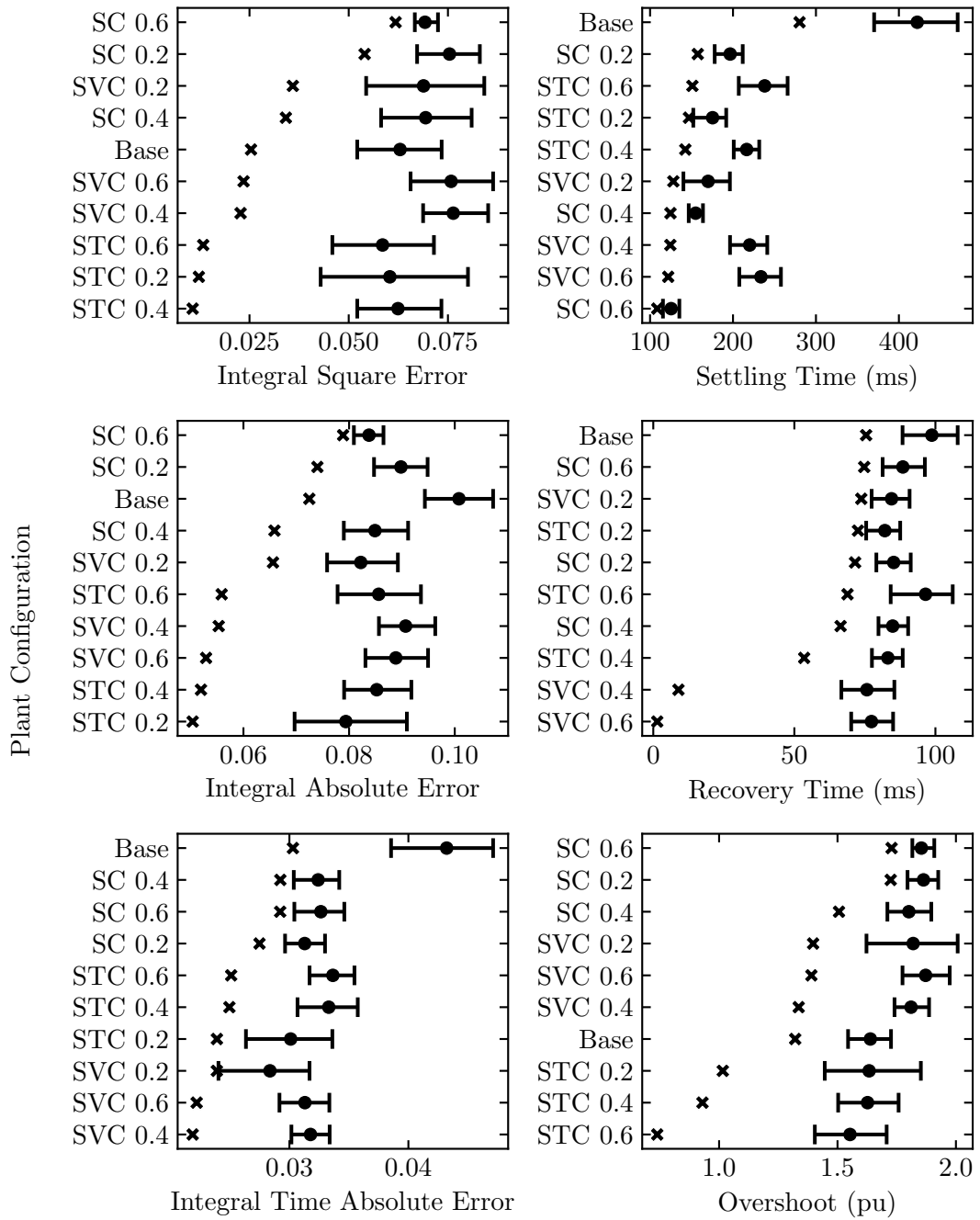
Appendix F. Sample Means and Sample Minima of Performance Values



Plant Configuration Sample Means (with 95% CI), and Sample Minima

Figure F.3: DC-side measured voltage sample statistics.

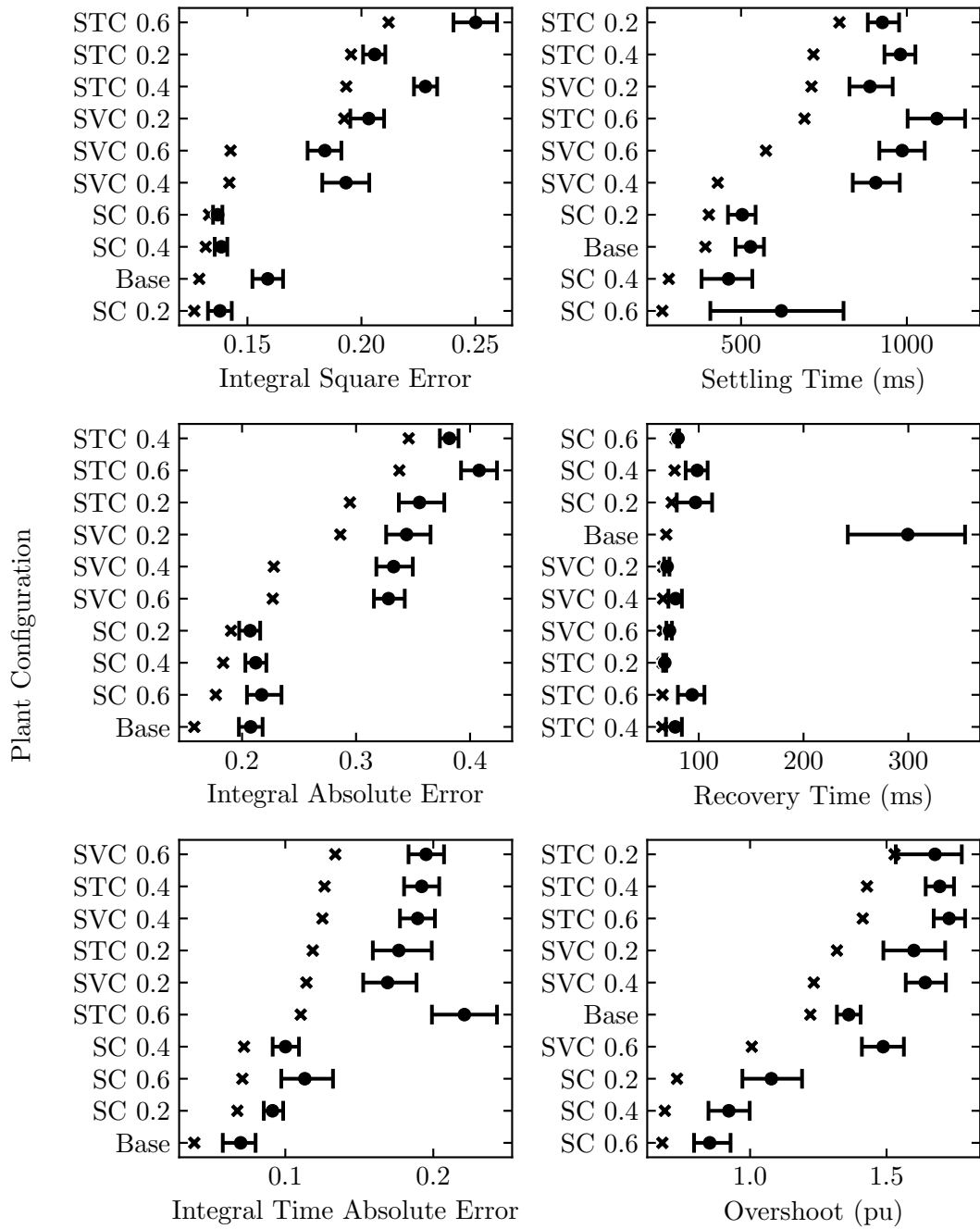
Appendix F. Sample Means and Sample Minima of Performance Values



Plant Configuration Sample Means (with 95% CI), and Sample Minima

Figure F.4: DC-side measured current sample statistics.

Appendix F. Sample Means and Sample Minima of Performance Values



Plant Configuration Sample Means (with 95% CI), and Sample Minima

Figure F.5: Measured extinction angle sample statistics.

Appendix G

Differences between Sample Means of Performance Values

These plots include differences in observed sample means along with the estimated 95% CI of the differences in sample means indicated via intervals. Observed sample mean differences are indicated by dot markers. Statistically significant results are assumed where the value 0 is not within the 95% CI; these results are marked with an asterisk symbol. In the y-axis labels, “SC” corresponds to synchronous condenser and “STC” corresponds to STATCOM. The ratings of the dynamic compensator equipment are indicated by the numbers “0.2”, “0.4”, and “0.6”—corresponding to 0.2, 0.4, and 0.6 pu ratings respectively—succeeding the “SC”, “STC”, and “SVC” labels.

Positive values on the x-axis indicate the right-hand label on the y-axis after the em dash is superior to the left-hand label on the y-axis before the em dash, where superiority is assumed because all performance values are positively valued and are ideally being minimised. For example, consider the IAE interval for “Base — STC 0.2” in Figure G.1. The 0.2 pu rated STATCOM typically results in smaller IAE mean values for DC-side power than the Base study case; so subtraction of the 0.2 pu rated STATCOM IAE values’ sample mean from the Base study case IAE values’ sample mean gives a positive difference.

Appendix G. Differences between Sample Means of Performance Values

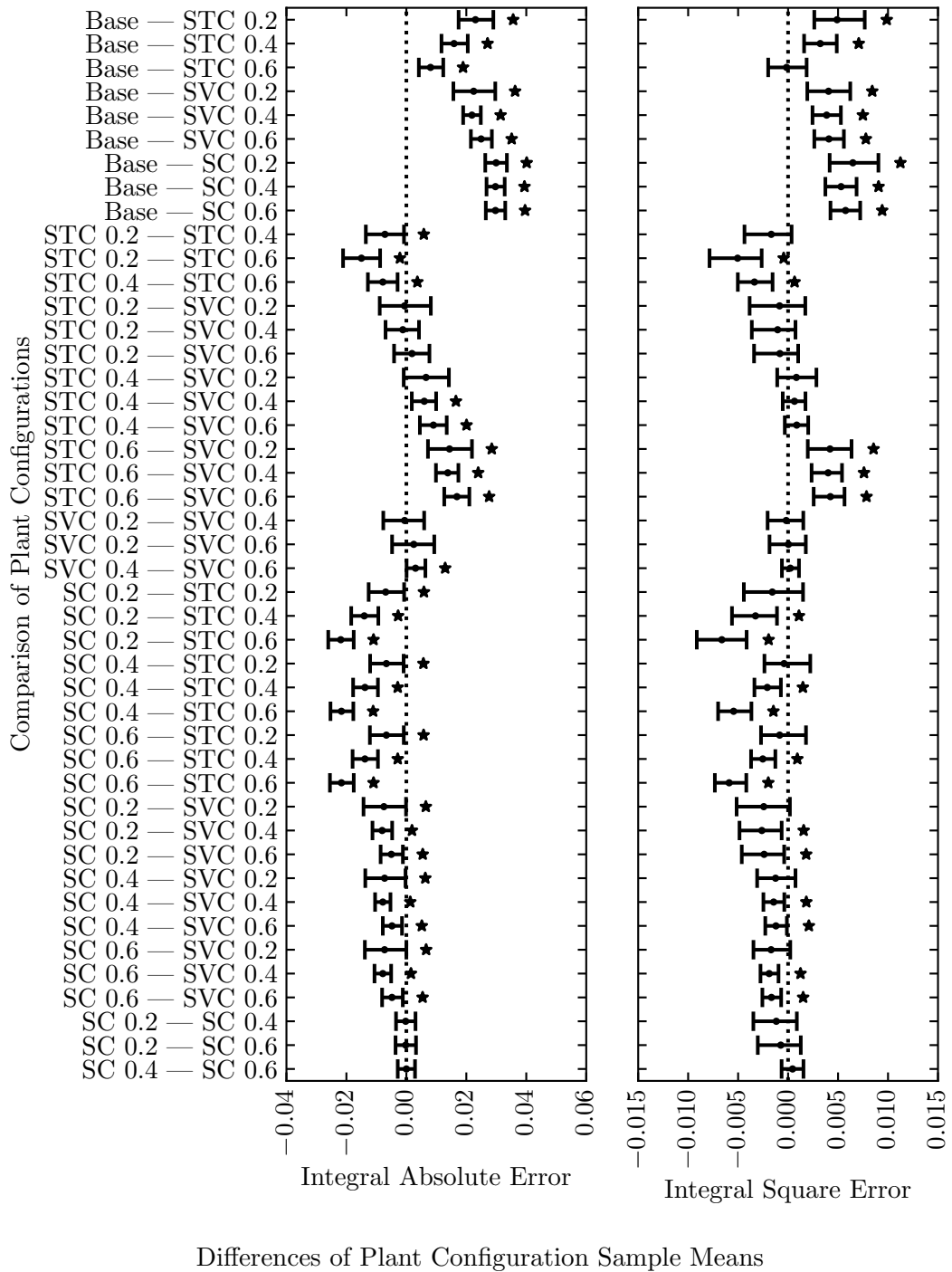


Figure G.1: Differences in sample means of measured DC-side measured power.

Appendix G. Differences between Sample Means of Performance Values

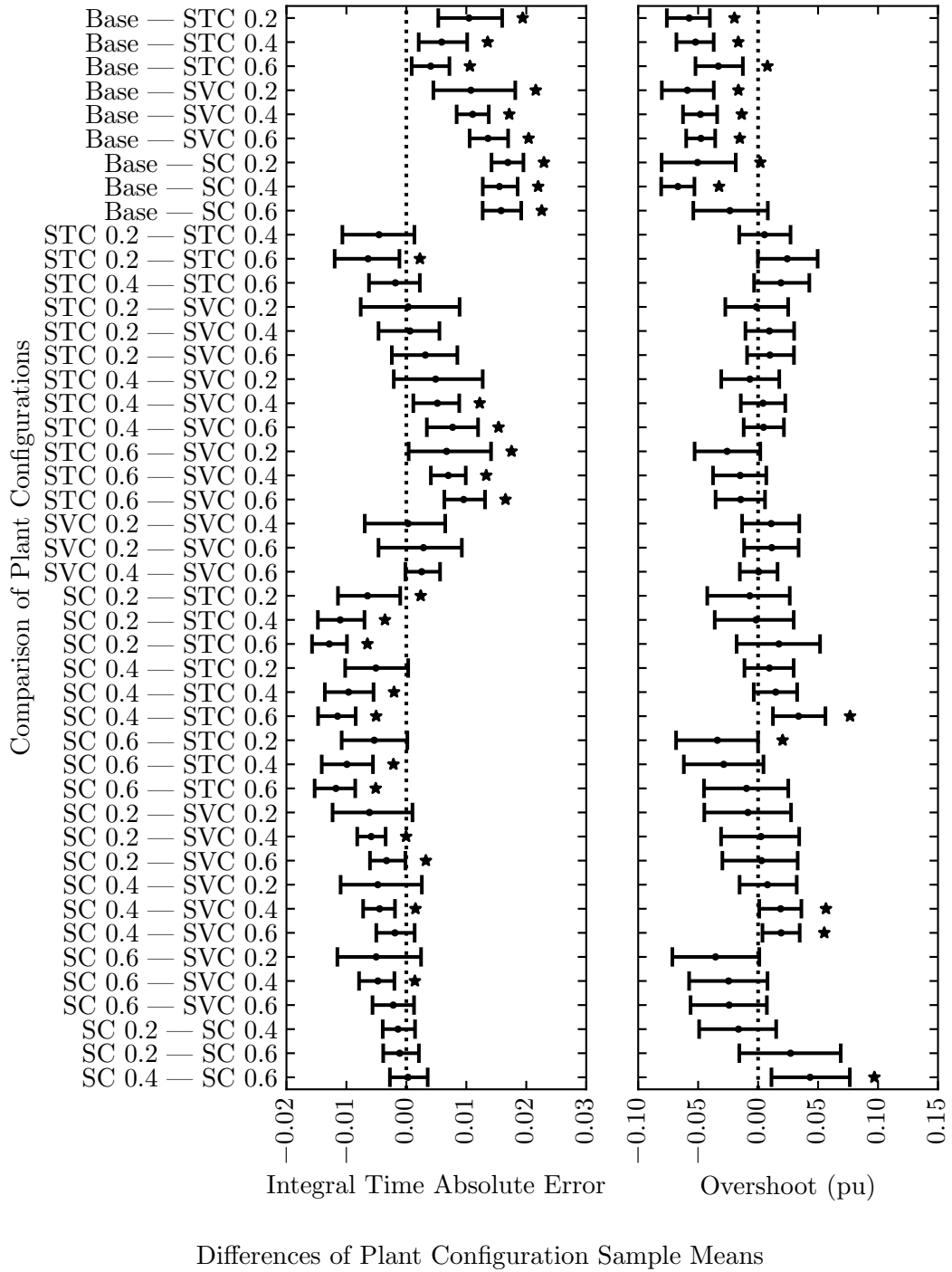


Figure G.2: Differences in sample means of measured DC-side measured power, cont.

Appendix G. Differences between Sample Means of Performance Values

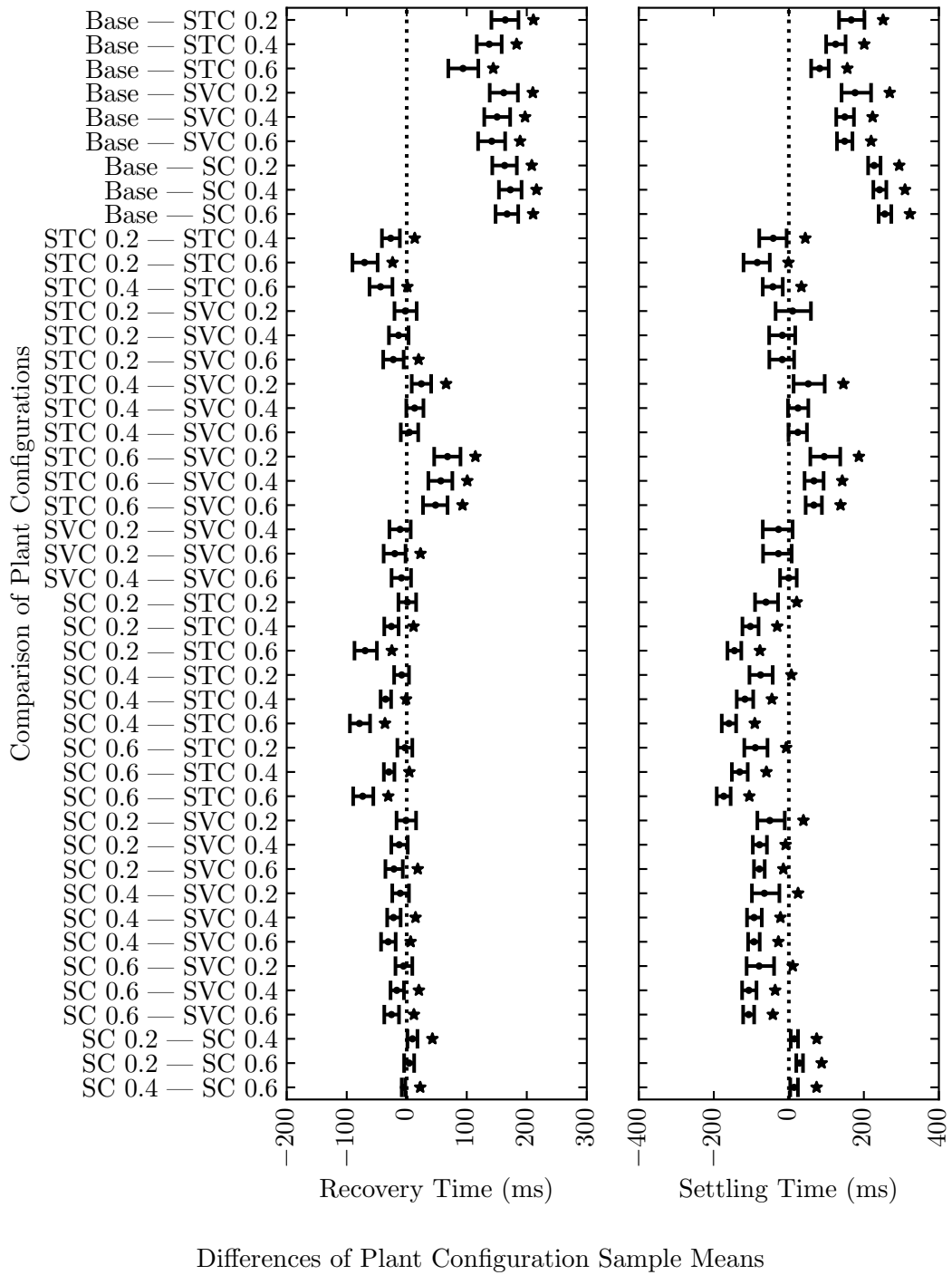


Figure G.3: Differences in sample means of measured DC-side measured power, cont.

Appendix G. Differences between Sample Means of Performance Values

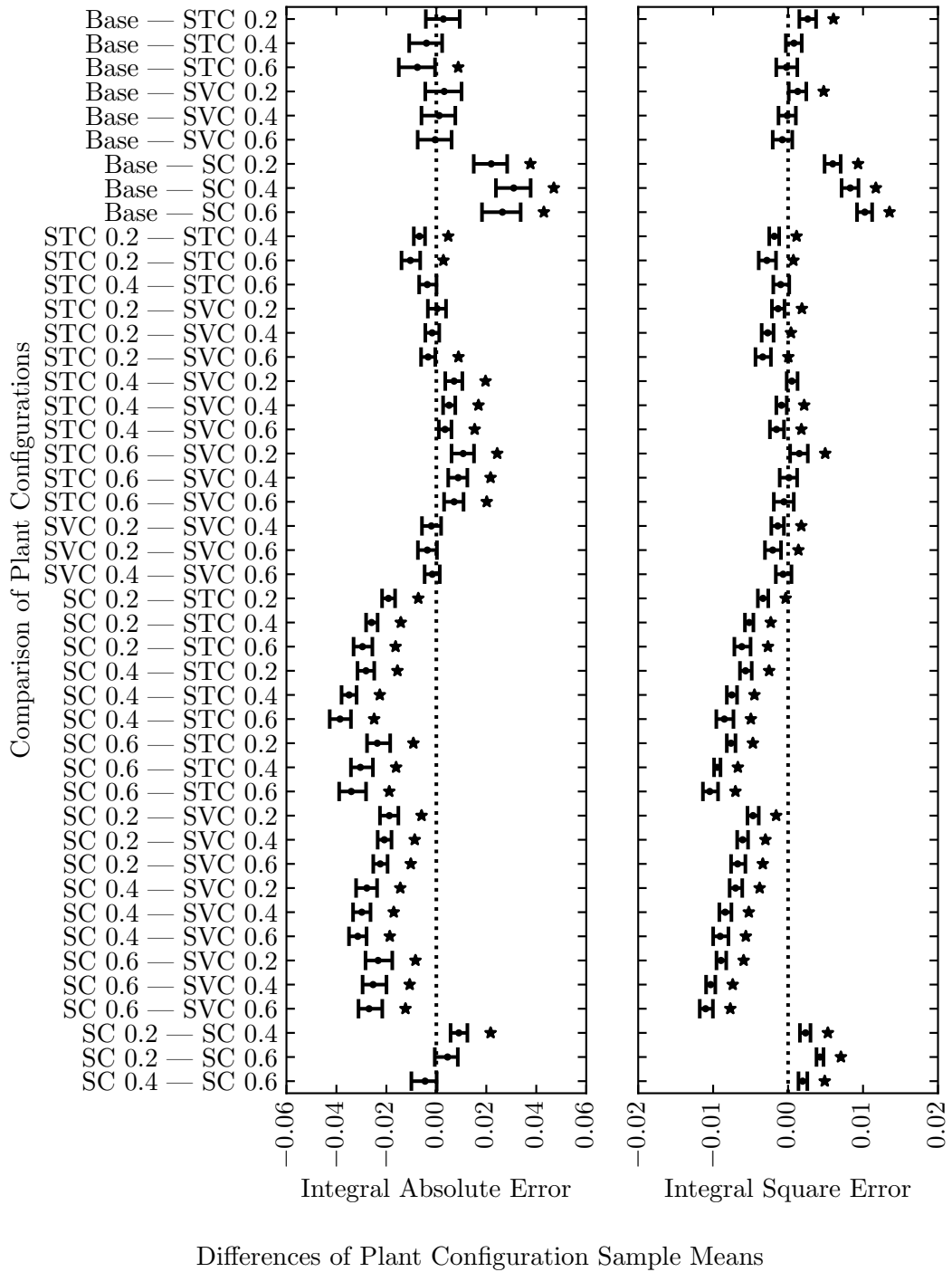
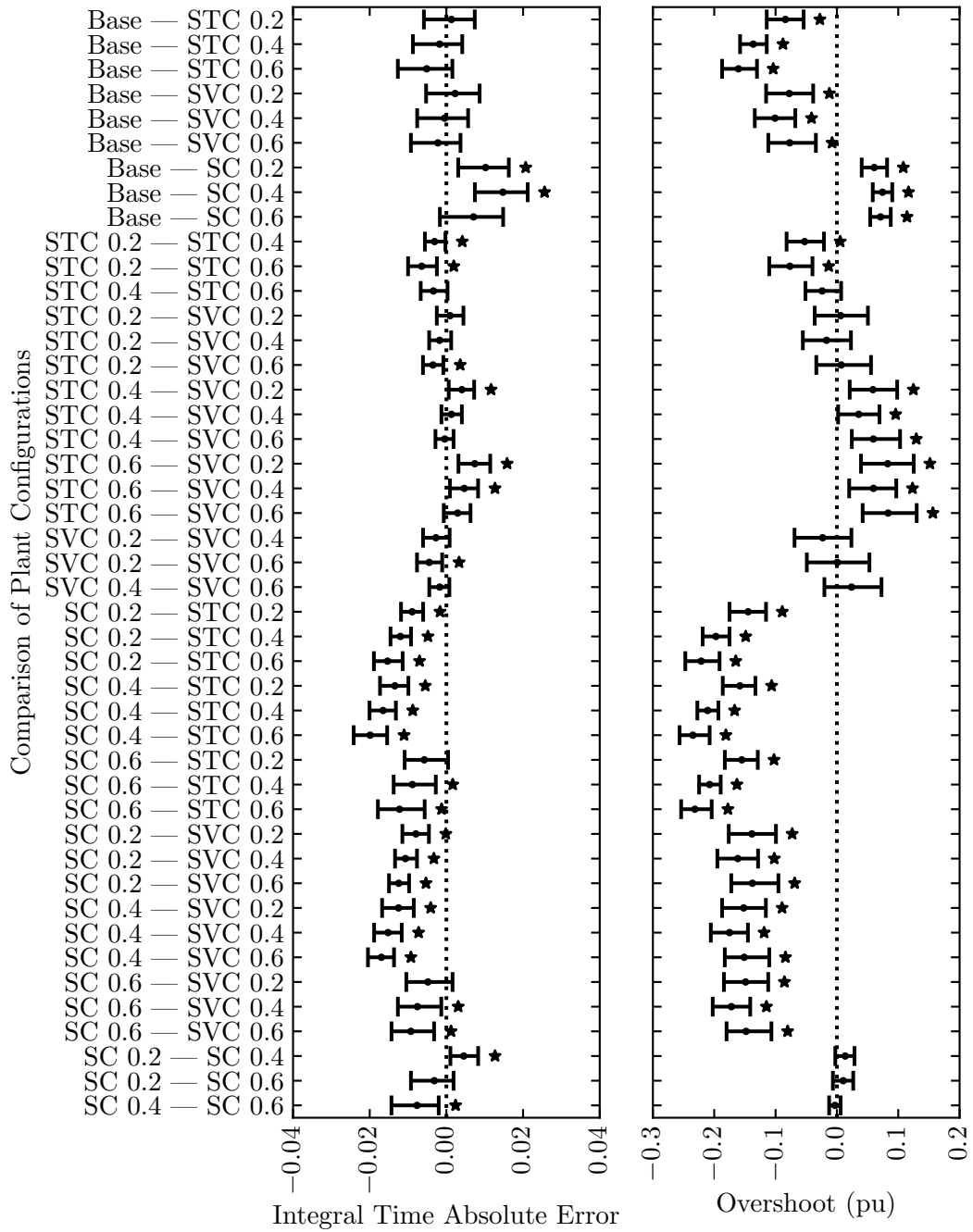


Figure G.4: Differences in sample means of measured AC-side measured voltage magnitude.

Appendix G. Differences between Sample Means of Performance Values



Differences of Plant Configuration Sample Means

Figure G.5: Differences in sample means of measured AC-side measured voltage magnitude, cont.

Appendix G. Differences between Sample Means of Performance Values

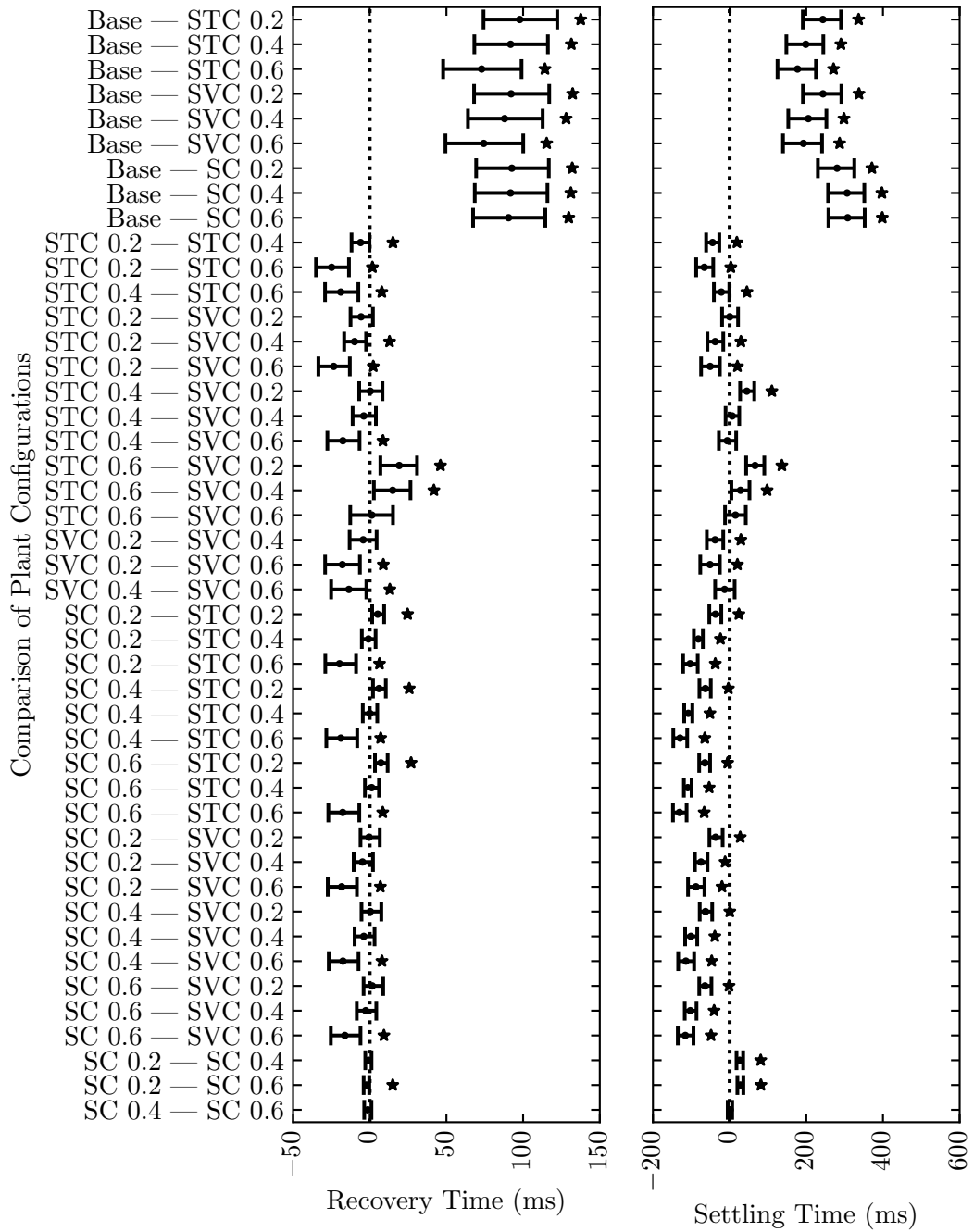


Figure G.6: Differences in sample means of measured AC-side measured voltage magnitude, cont.

Appendix G. Differences between Sample Means of Performance Values

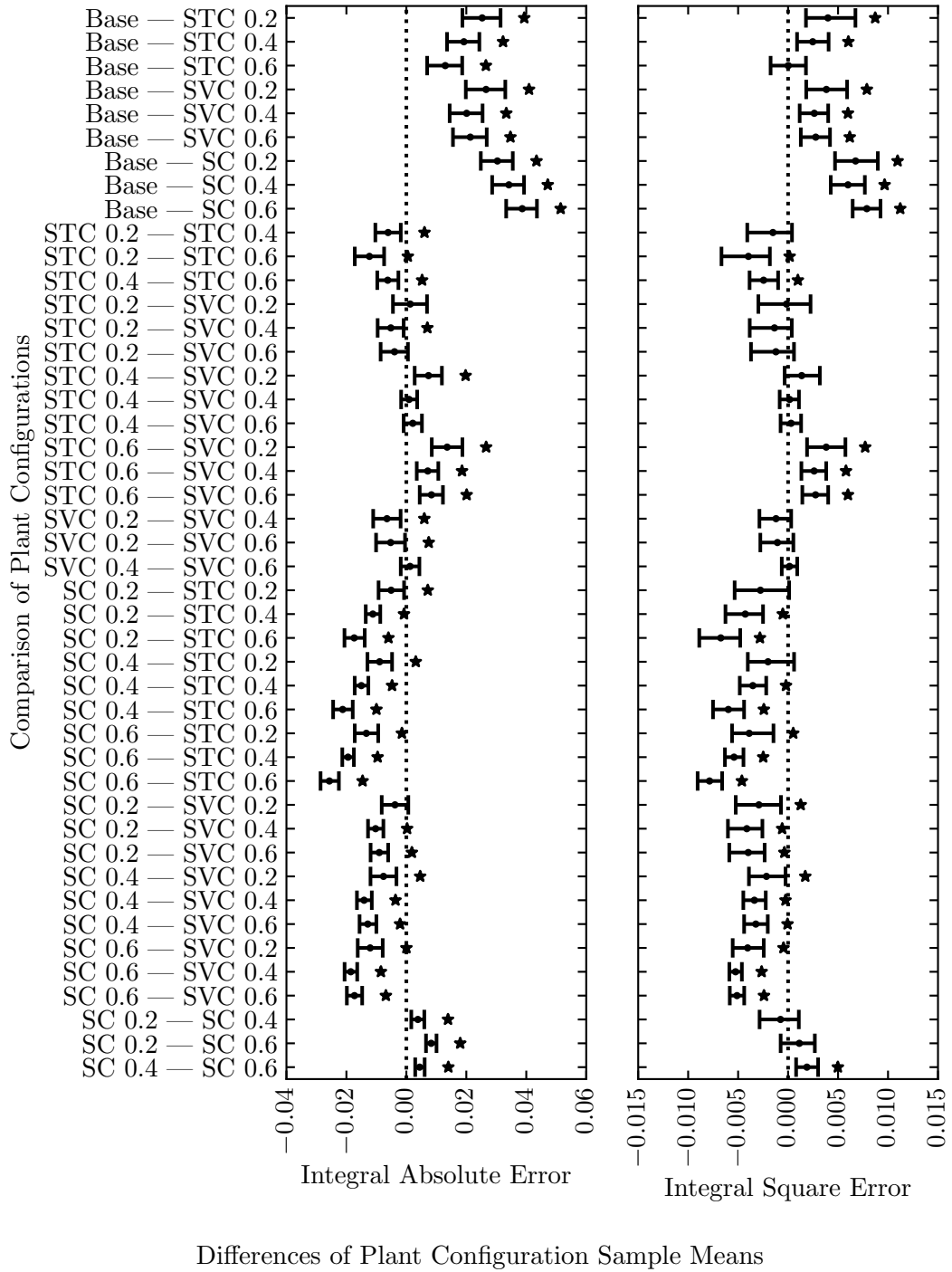


Figure G.7: Differences in sample means of measured DC-side measured voltage.

Appendix G. Differences between Sample Means of Performance Values

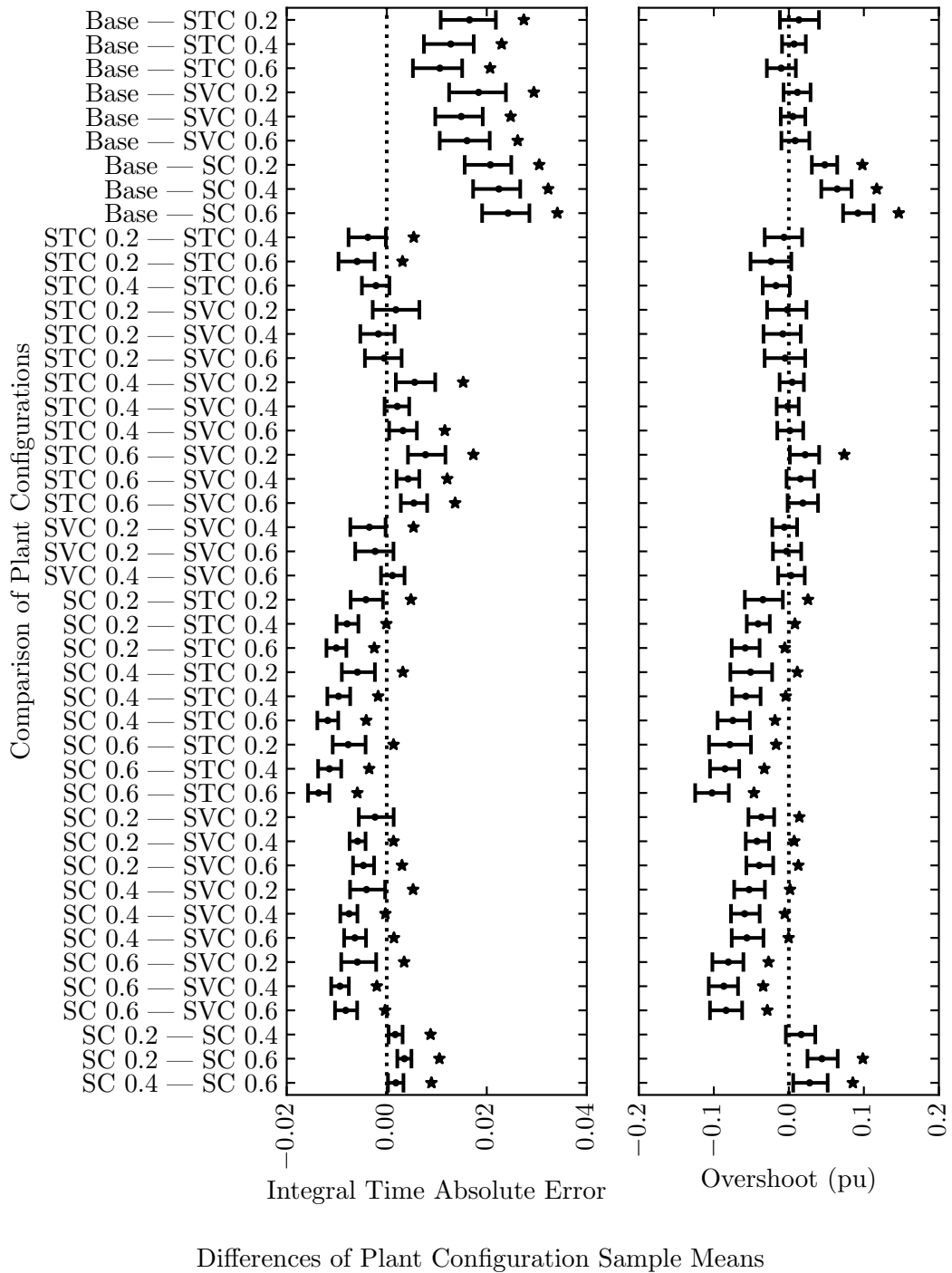


Figure G.8: Differences in sample means of measured DC-side measured voltage, cont.

Appendix G. Differences between Sample Means of Performance Values

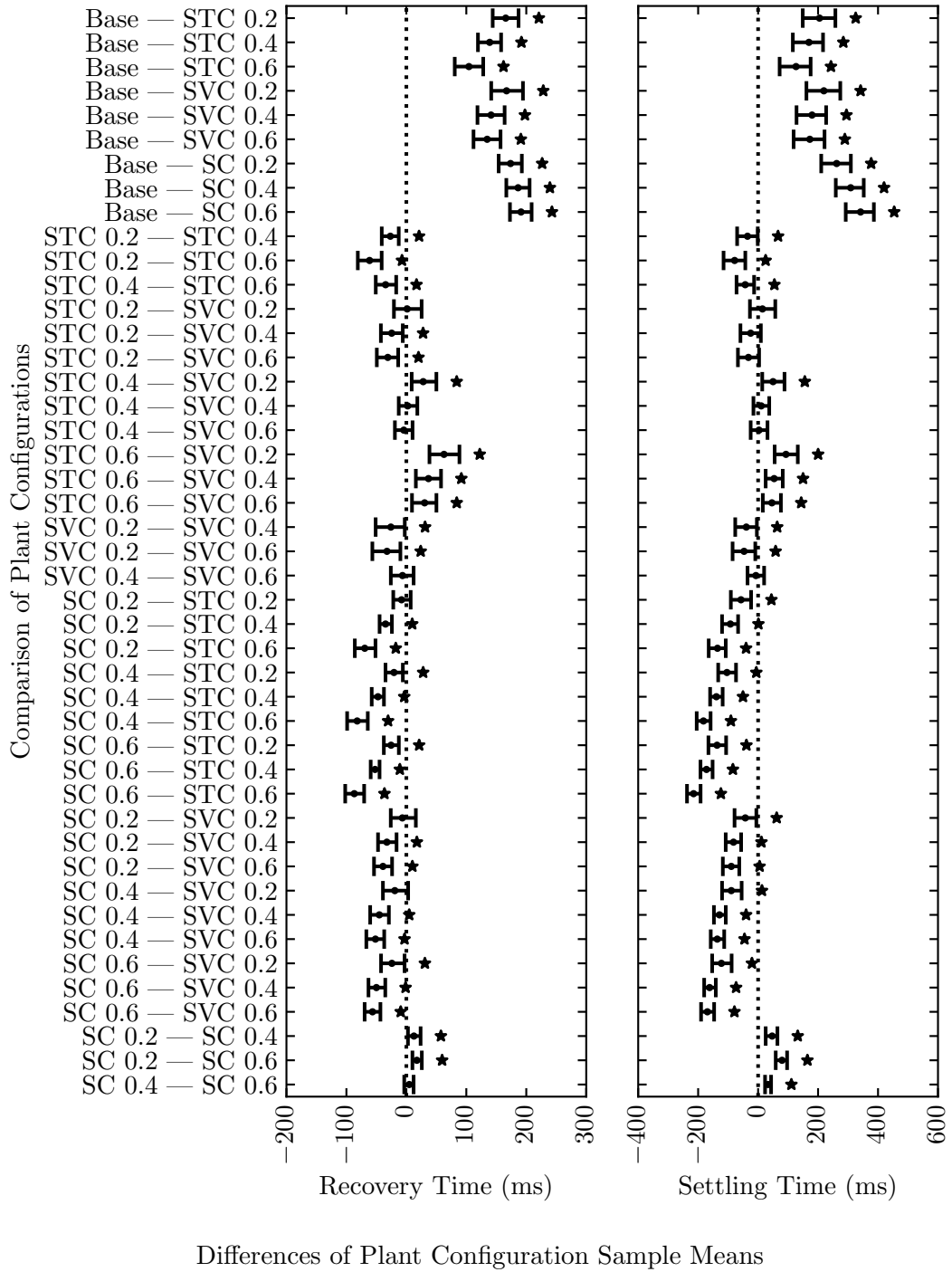


Figure G.9: Differences in sample means of measured DC-side measured voltage, cont.

Appendix G. Differences between Sample Means of Performance Values

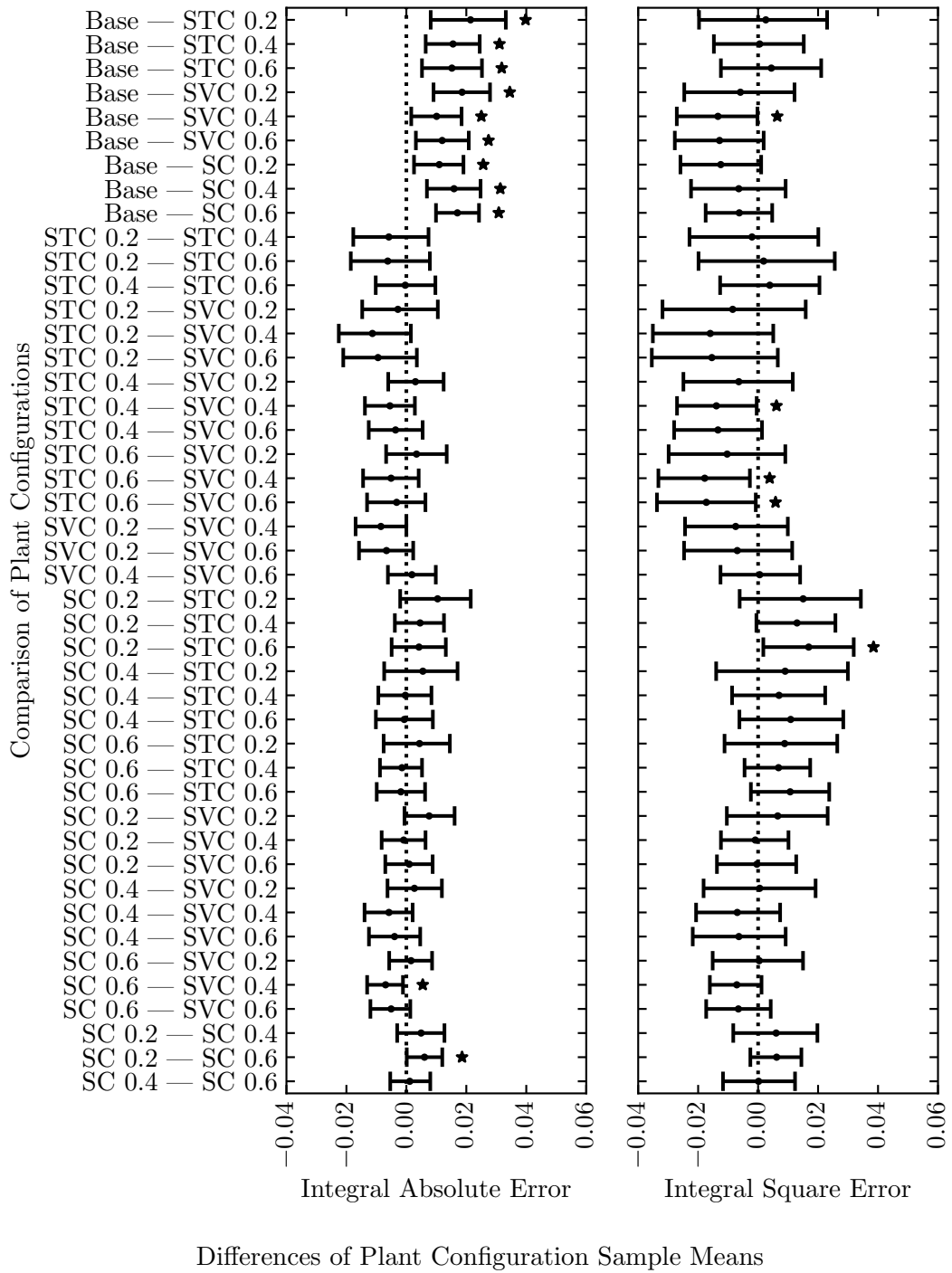


Figure G.10: Differences in sample means of measured DC-side measured current.

Appendix G. Differences between Sample Means of Performance Values

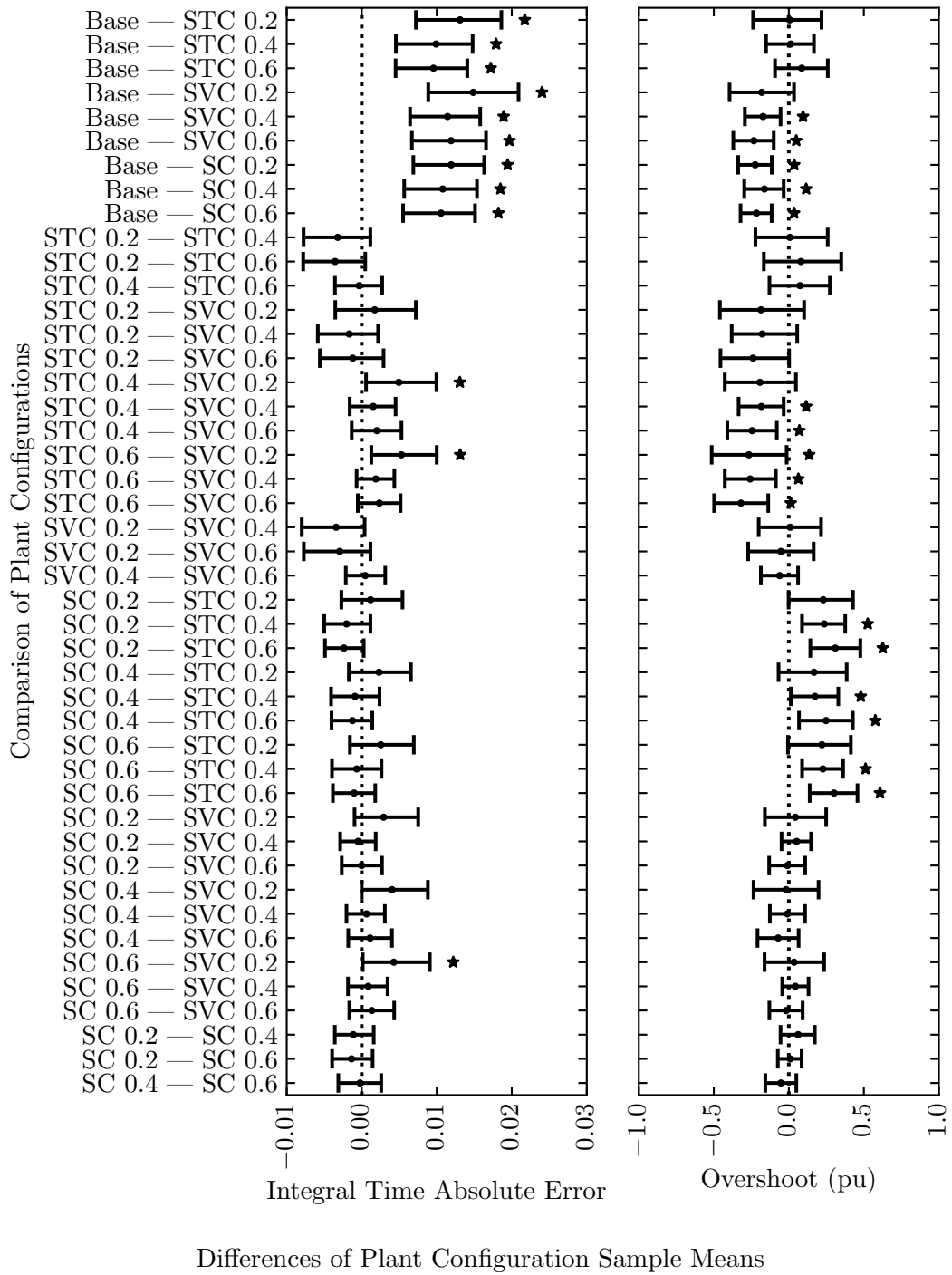


Figure G.11: Differences in sample means of measured DC-side measured current, cont.

Appendix G. Differences between Sample Means of Performance Values

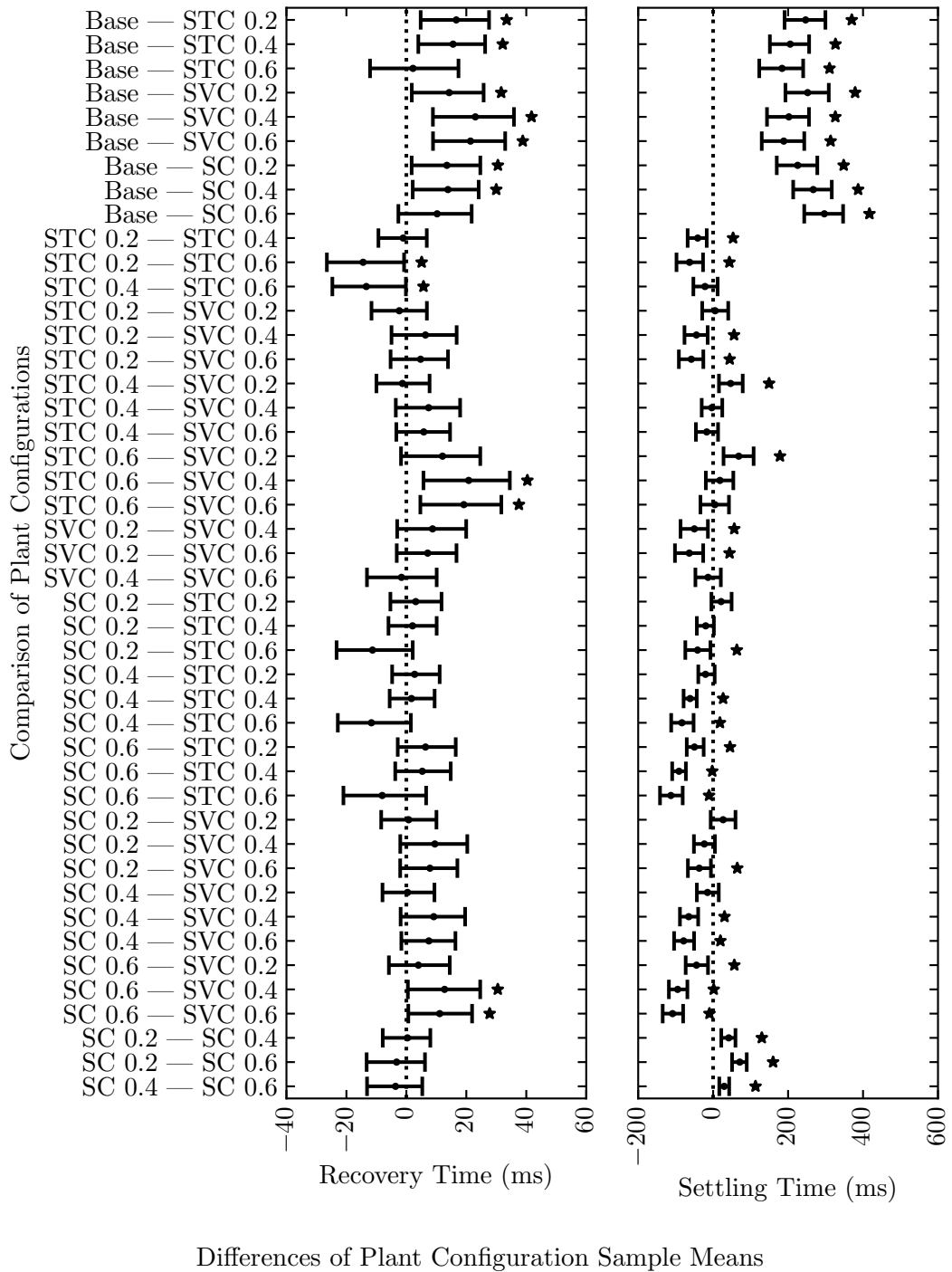


Figure G.12: Differences in sample means of measured DC-side measured current, cont.

Appendix G. Differences between Sample Means of Performance Values

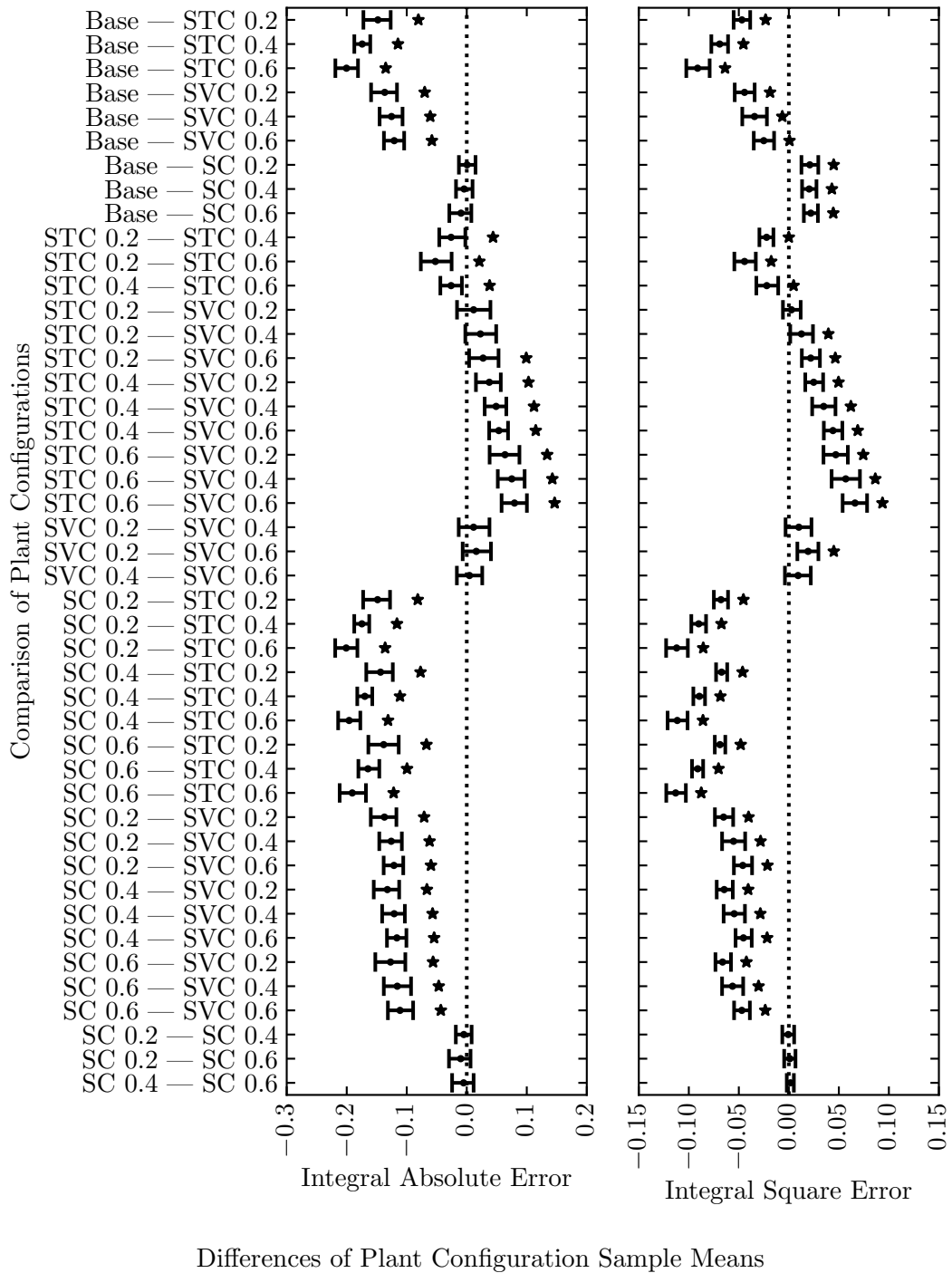


Figure G.13: Differences in sample means of measured extinction angle.

Appendix G. Differences between Sample Means of Performance Values

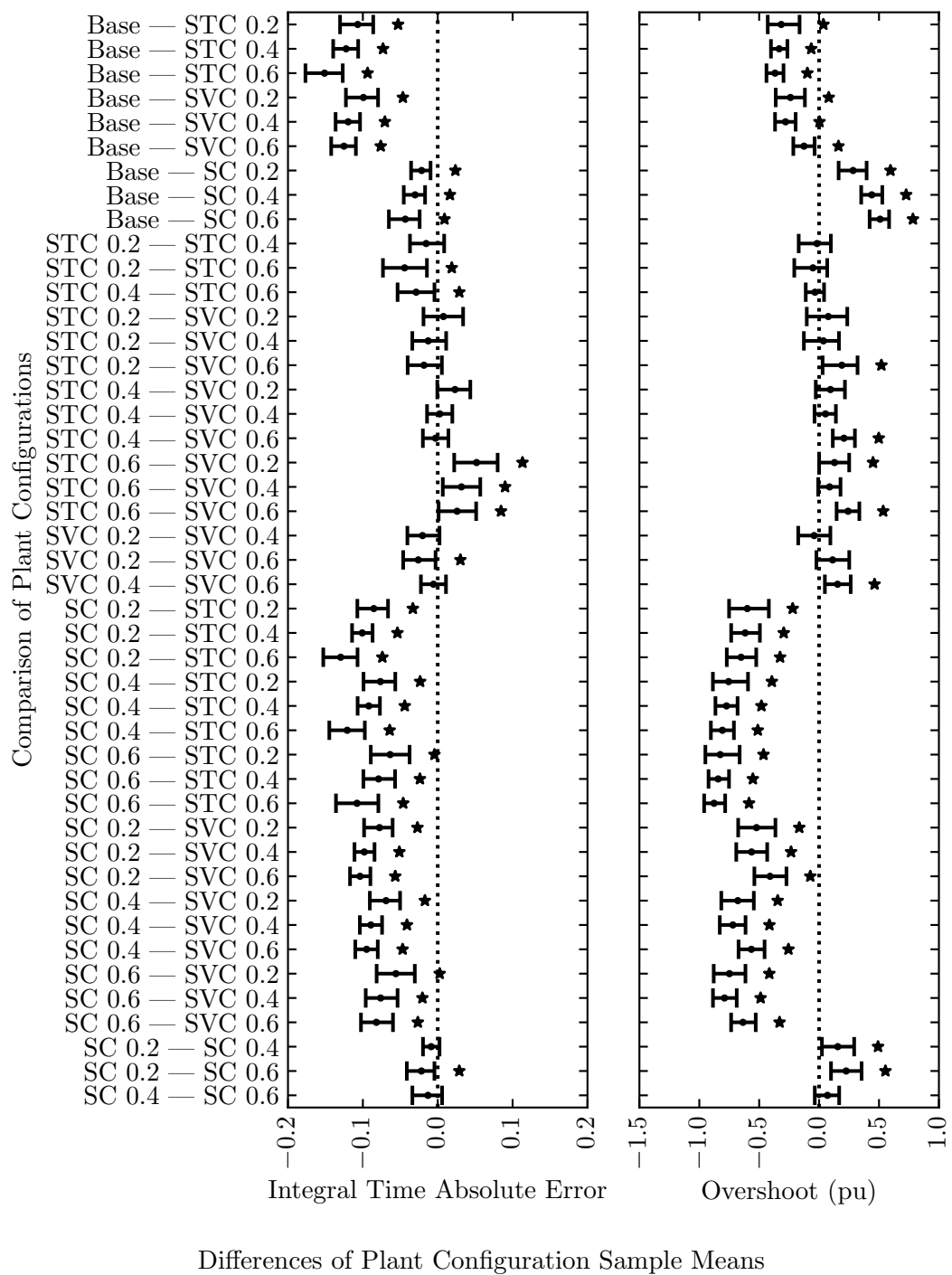


Figure G.14: Differences in sample means of measured extinction angle, cont.

Appendix G. Differences between Sample Means of Performance Values

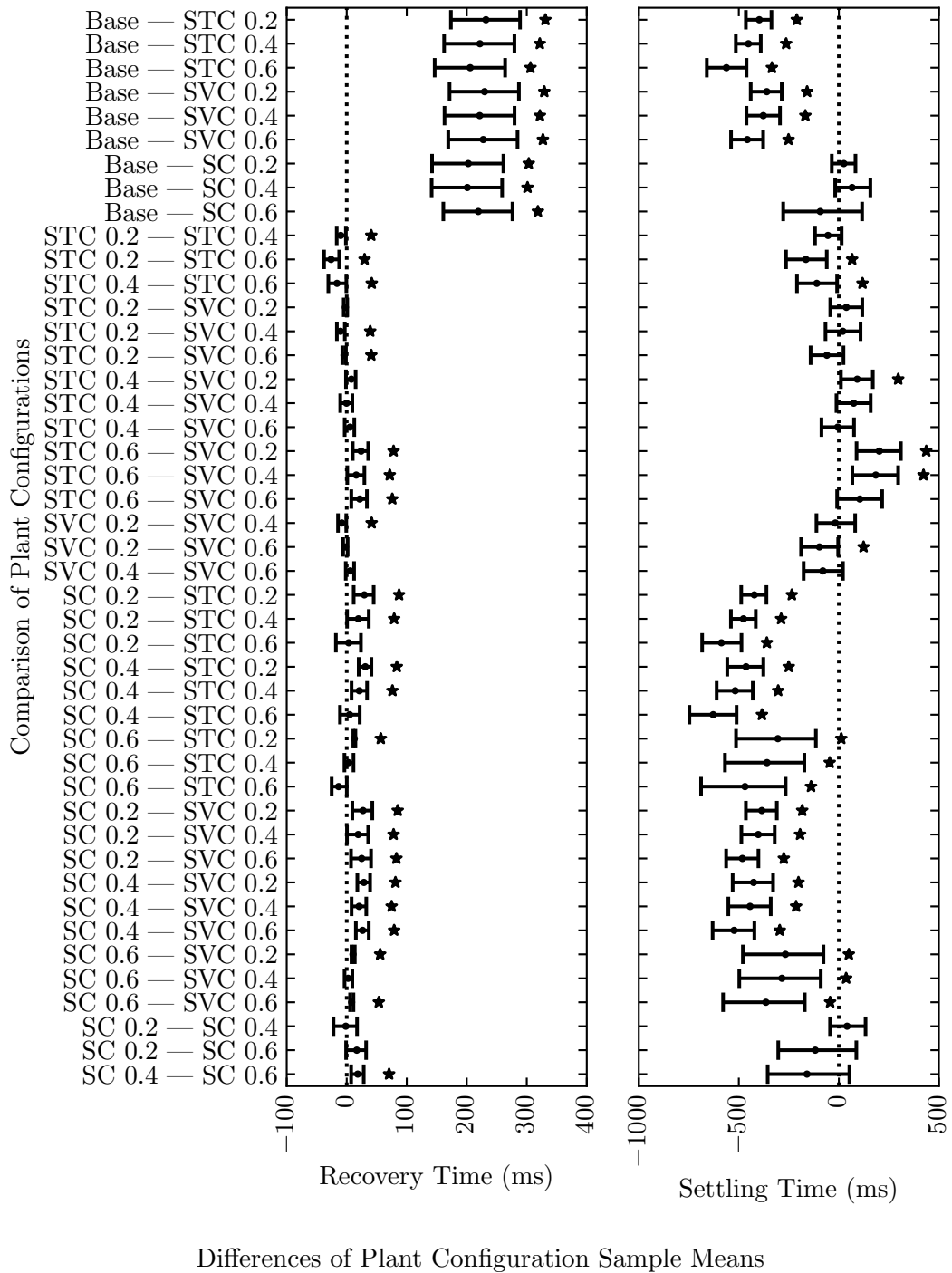


Figure G.15: Differences in sample means of measured extinction angle, cont.

Appendix H

Differences between Sample Minima of Performance Values

These plots include differences in observed sample minima along with the estimated 95% CI of the differences in sample minima indicated via intervals. Observed sample minima differences are indicated by dot markers. Statistically significant results are assumed where the value 0 is not within the 95% CI; these results are marked with an asterisk symbol. In the y-axis labels, “SC” corresponds to synchronous condenser and “STC” corresponds to STATCOM. The ratings of the dynamic compensator equipment are indicated by the numbers “0.2”, “0.4”, and “0.6”—corresponding to 0.2, 0.4, and 0.6 pu ratings respectively—succeeding the “SC”, “STC”, and “SVC” labels.

Positive values on the x-axis indicate the right-hand label on the y-axis after the em dash is superior to the left-hand label on the y-axis before the em dash, where superiority is assumed because all performance values are positively valued and are ideally being minimised. For example, consider the IAE interval for “Base — STC 0.2” in Figure H.1. The 0.2 pu rated STATCOM typically results in smaller IAE minimum values for DC-side power than the Base study case; so subtraction of the 0.2 pu rated STATCOM IAE values’ sample minimum from the Base study case IAE values’ sample minimum gives a positive difference.

Appendix H. Differences between Sample Minima of Performance Values

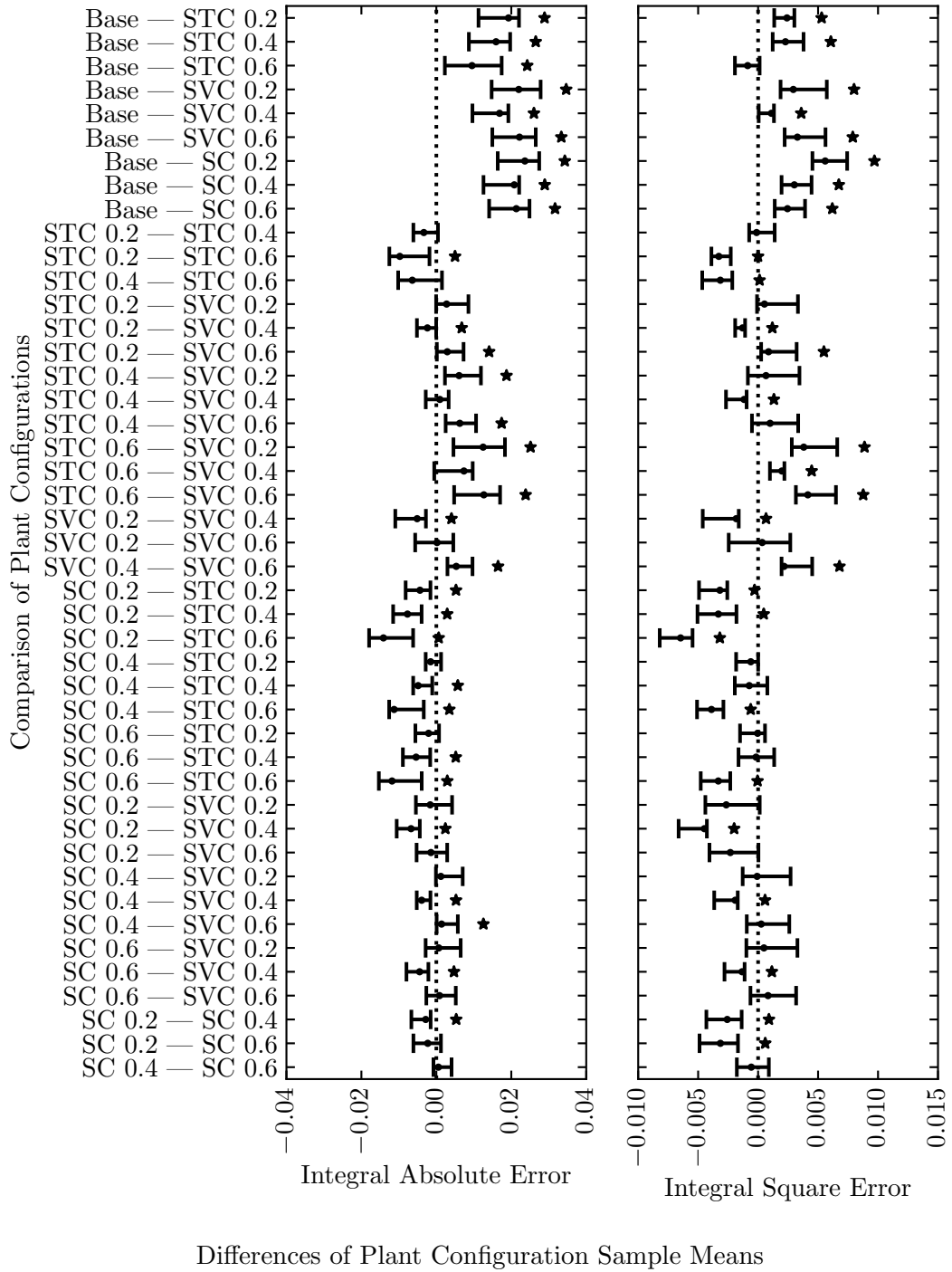


Figure H.1: Differences in sample minima of measured DC-side power.

Appendix H. Differences between Sample Minima of Performance Values

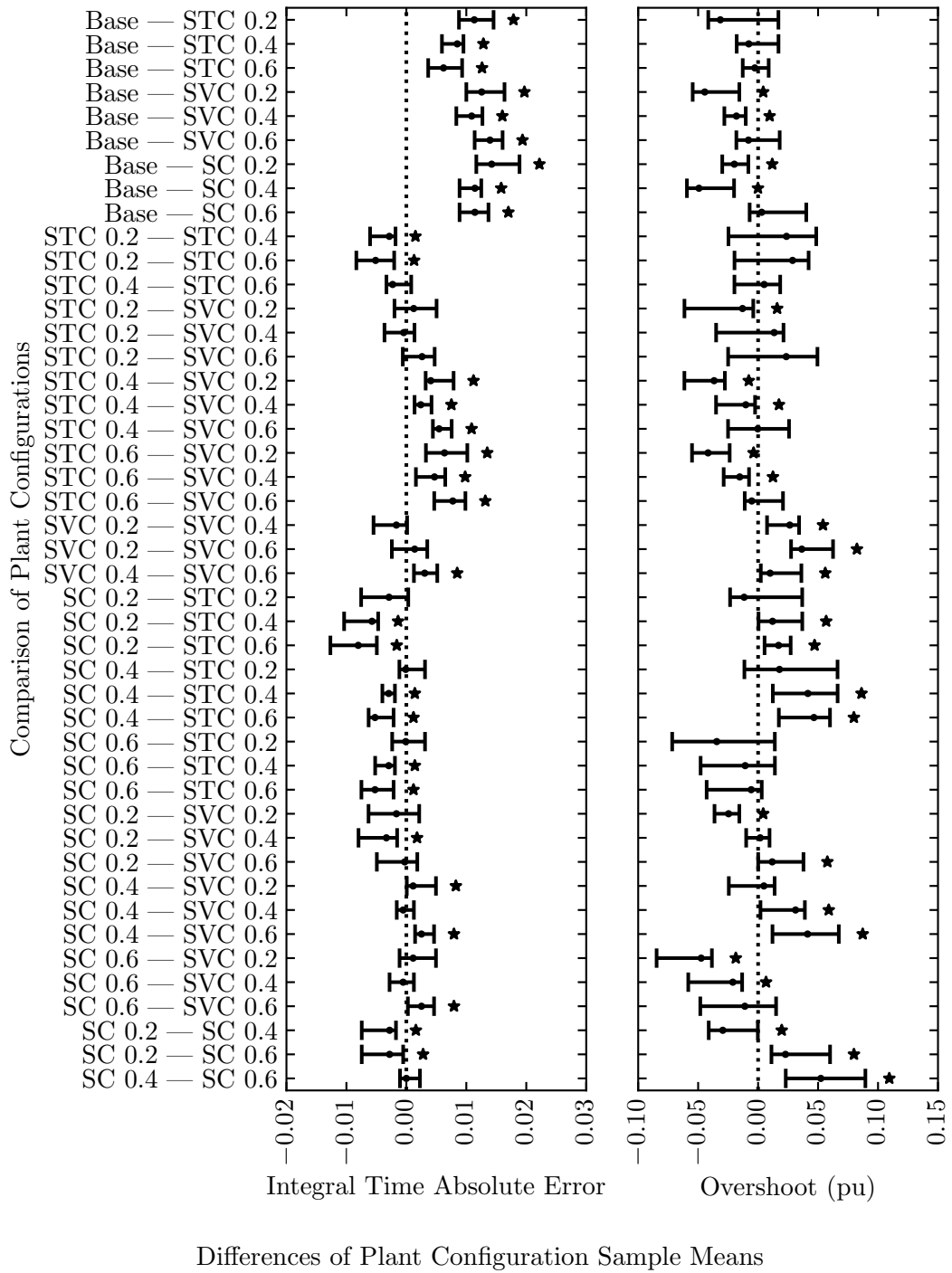


Figure H.2: Differences in sample minima of measured DC-side power, cont.

Appendix H. Differences between Sample Minima of Performance Values

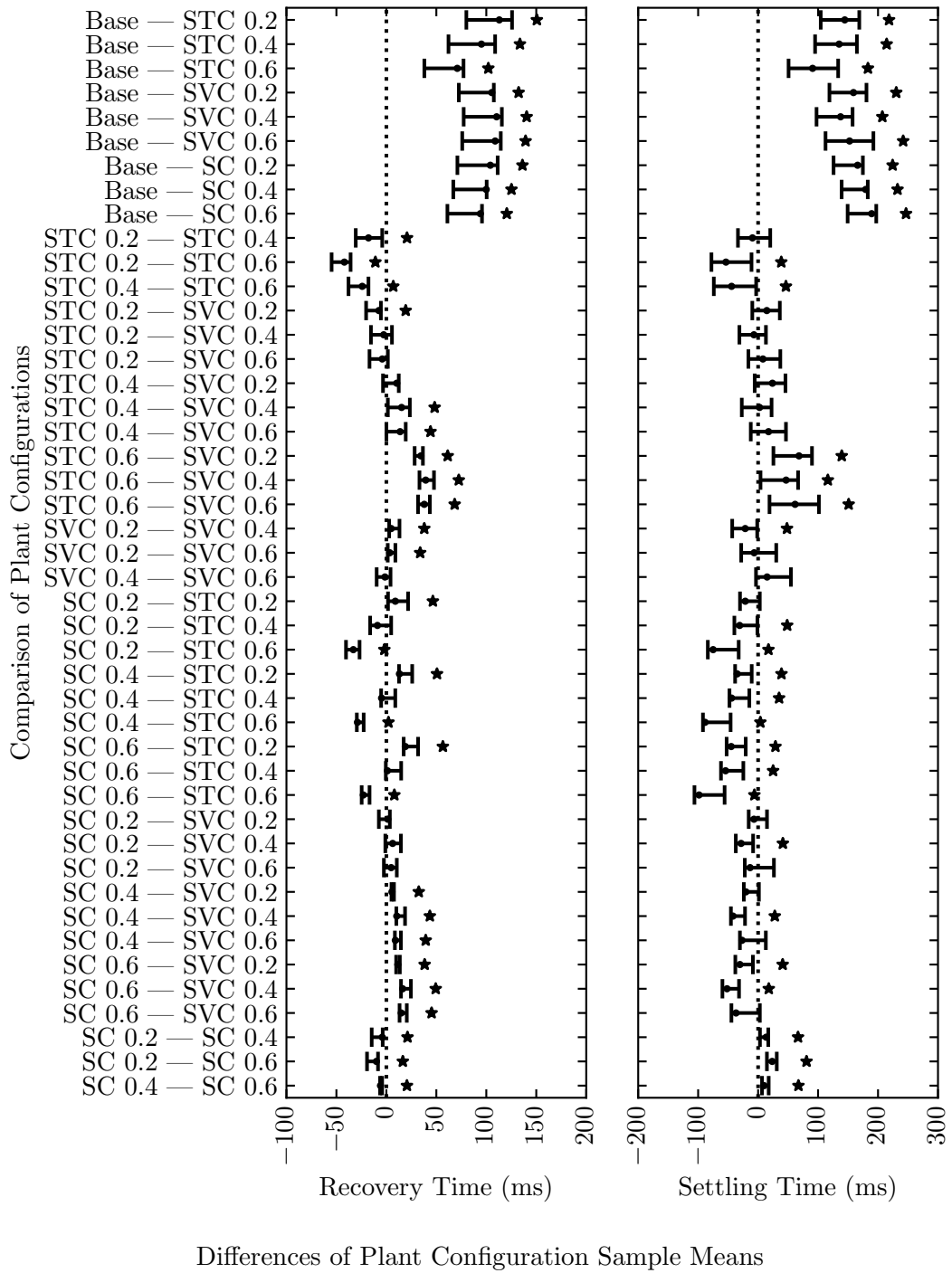


Figure H.3: Differences in sample minima of measured DC-side power, cont.

Appendix H. Differences between Sample Minima of Performance Values

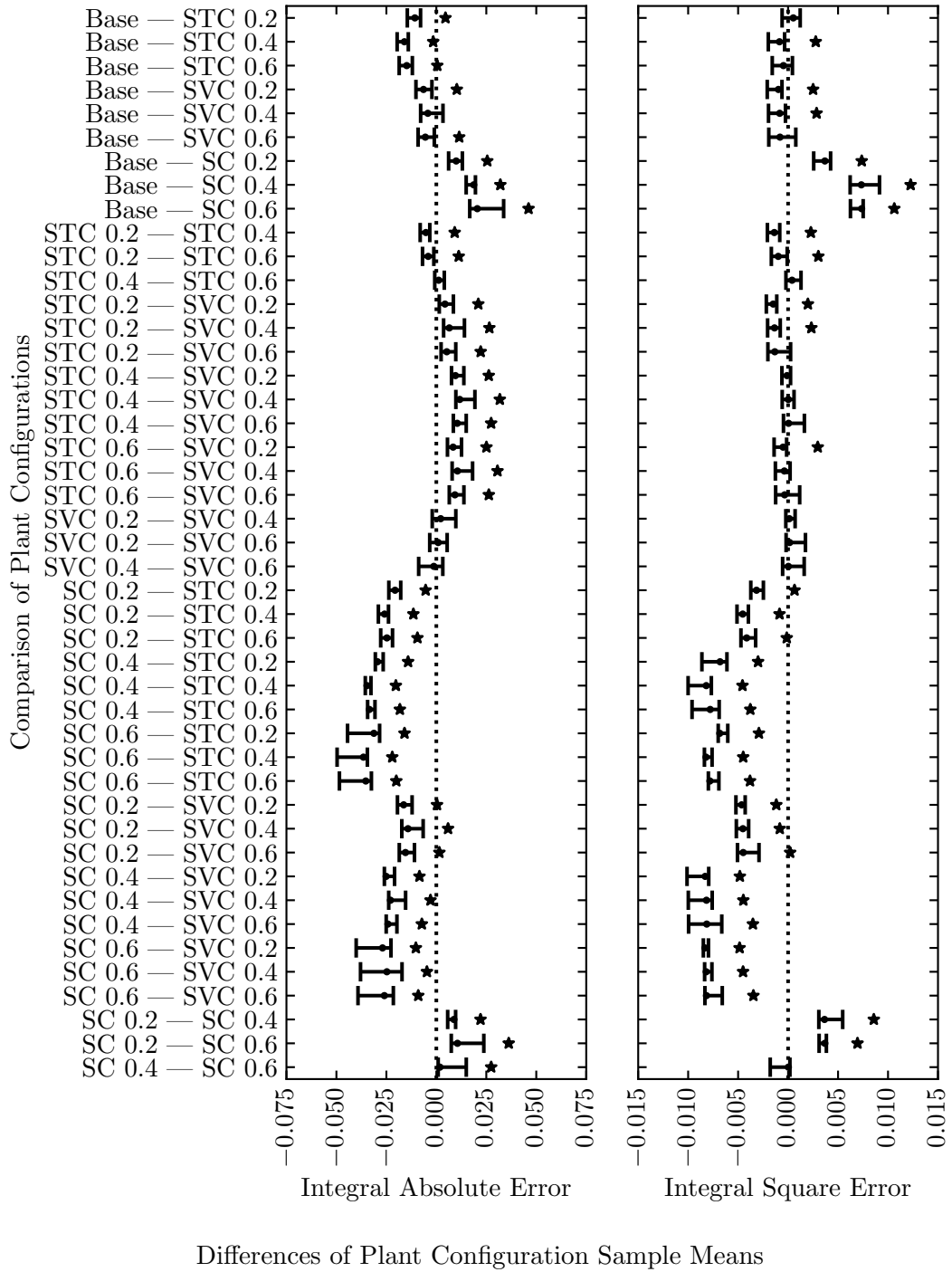


Figure H.4: Differences in sample minima of measured AC-side voltage magnitude.

Appendix H. Differences between Sample Minima of Performance Values

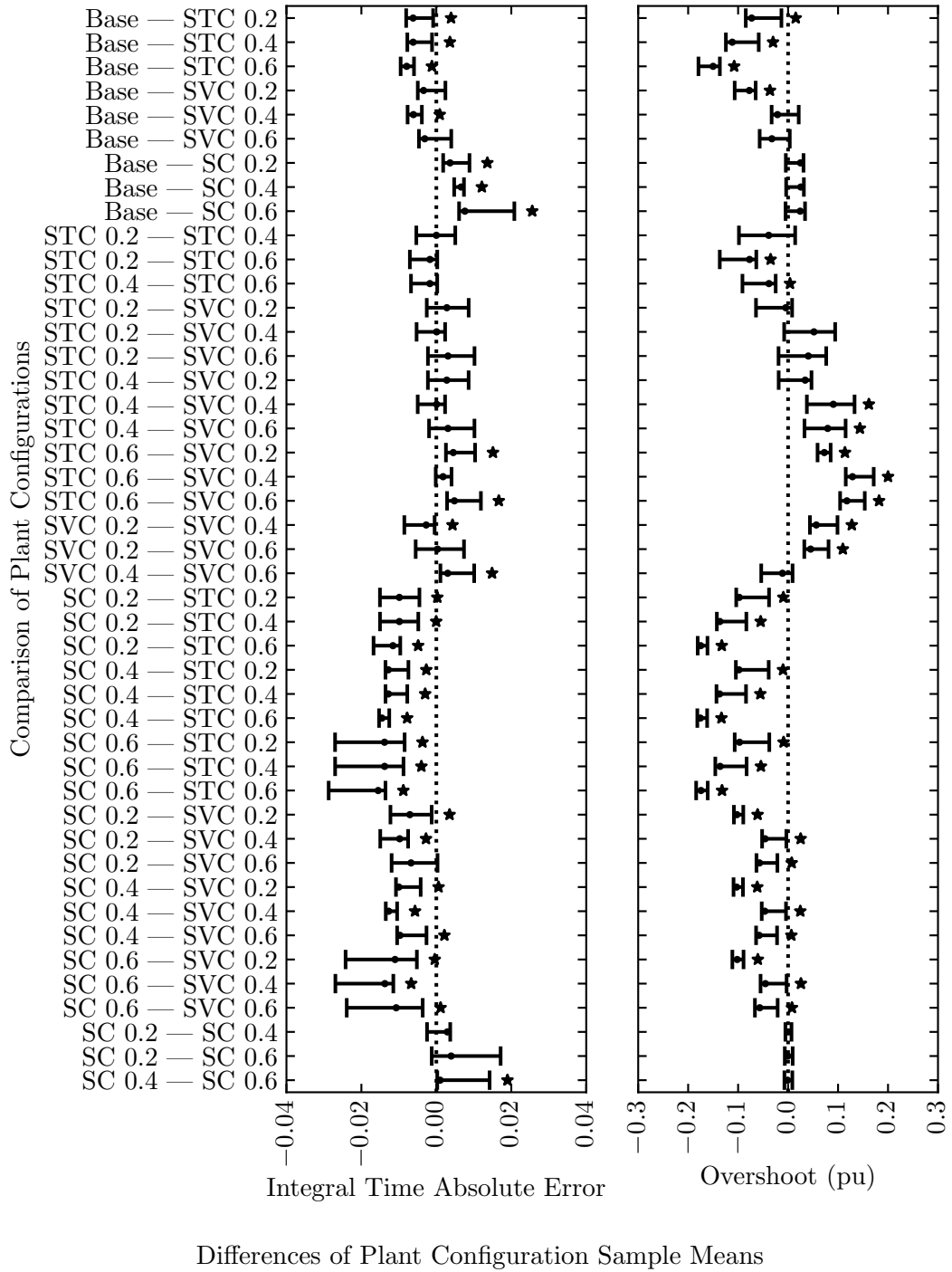


Figure H.5: Differences in sample minima of measured AC-side voltage magnitude, cont.

Appendix H. Differences between Sample Minima of Performance Values

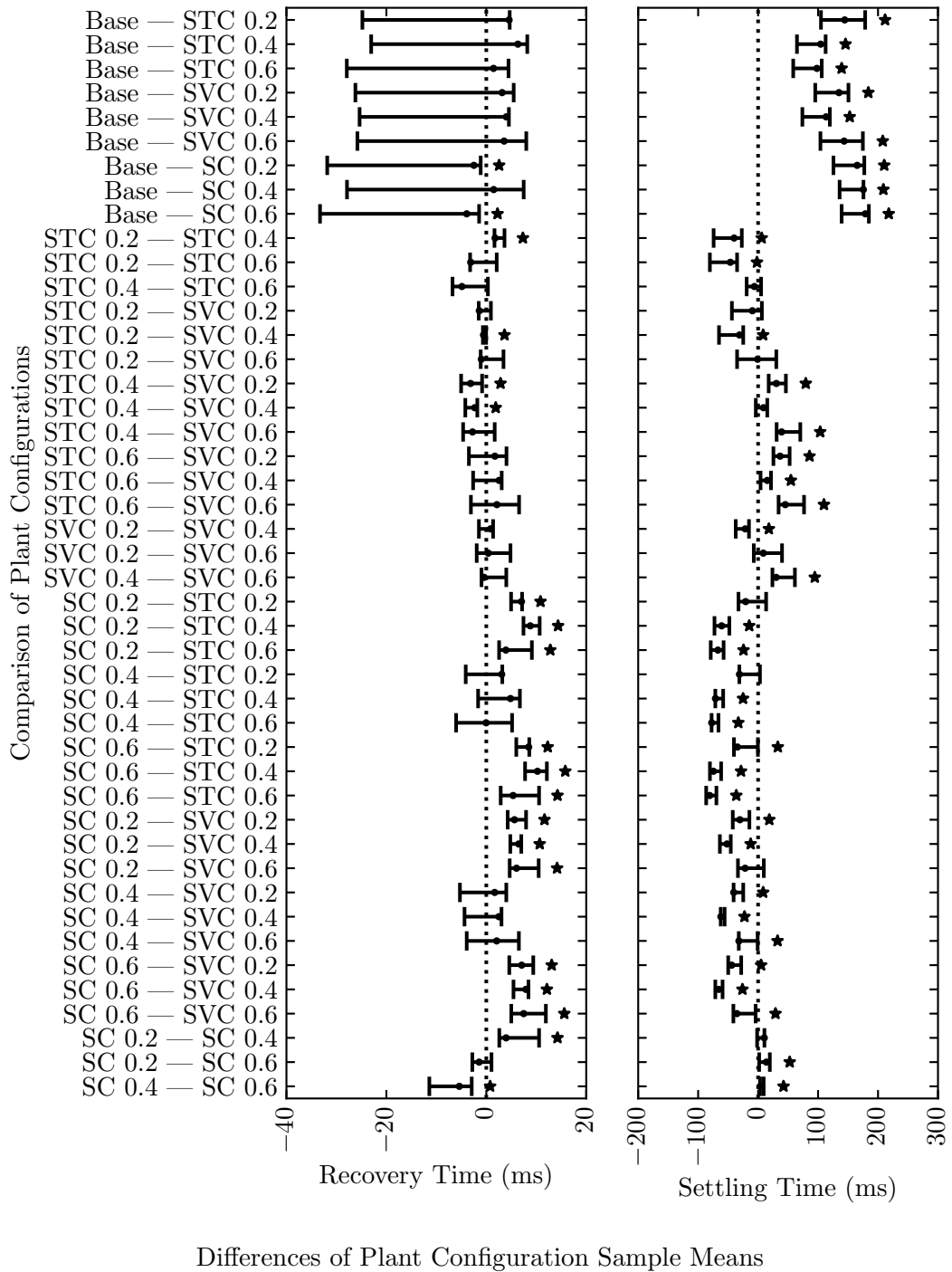


Figure H.6: Differences in sample minima of measured AC-side voltage magnitude, cont.

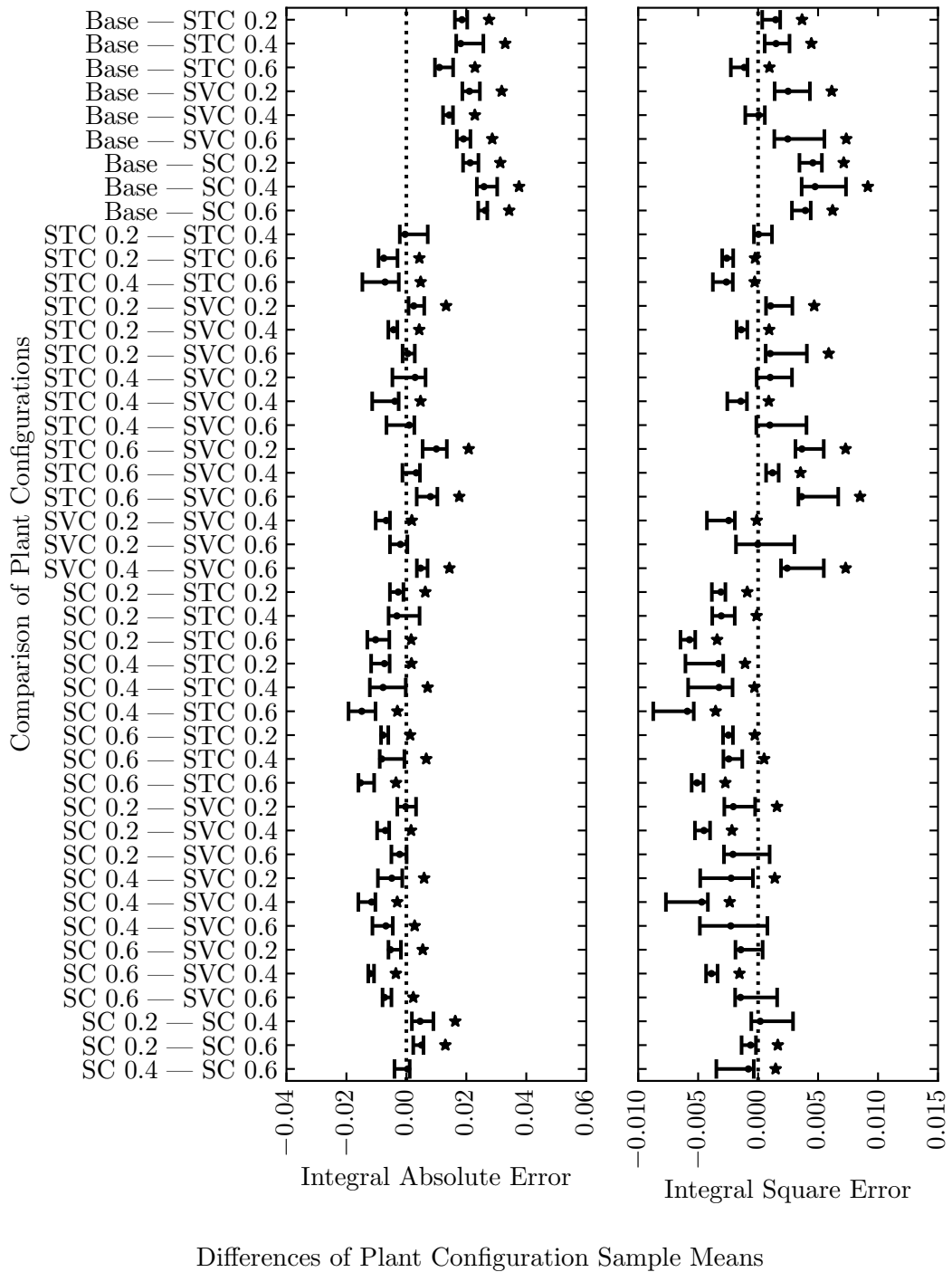


Figure H.7: Differences in sample minima of measured DC-side voltage.

Appendix H. Differences between Sample Minima of Performance Values

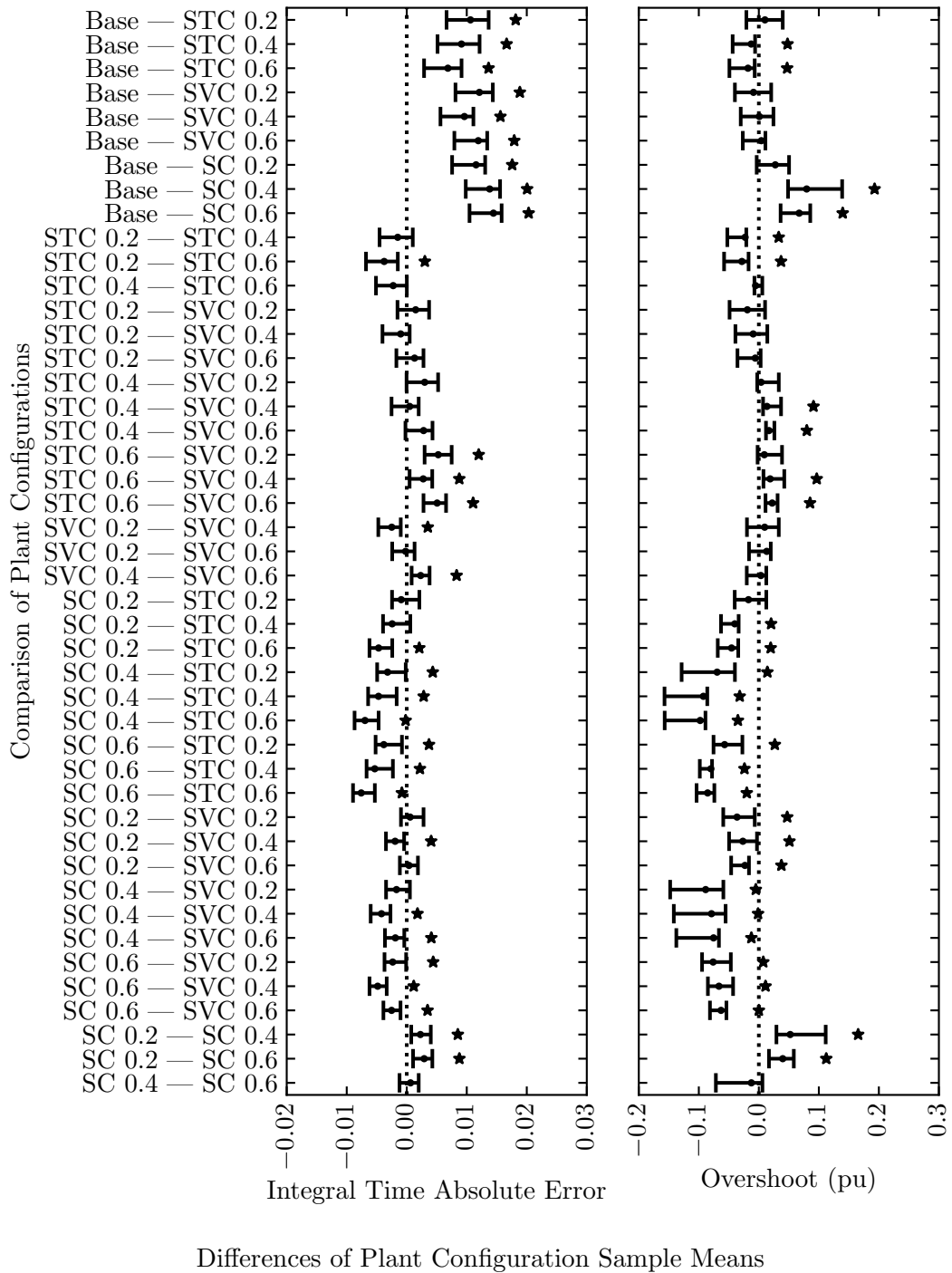


Figure H.8: Differences in sample minima of measured DC-side voltage, cont.

Appendix H. Differences between Sample Minima of Performance Values

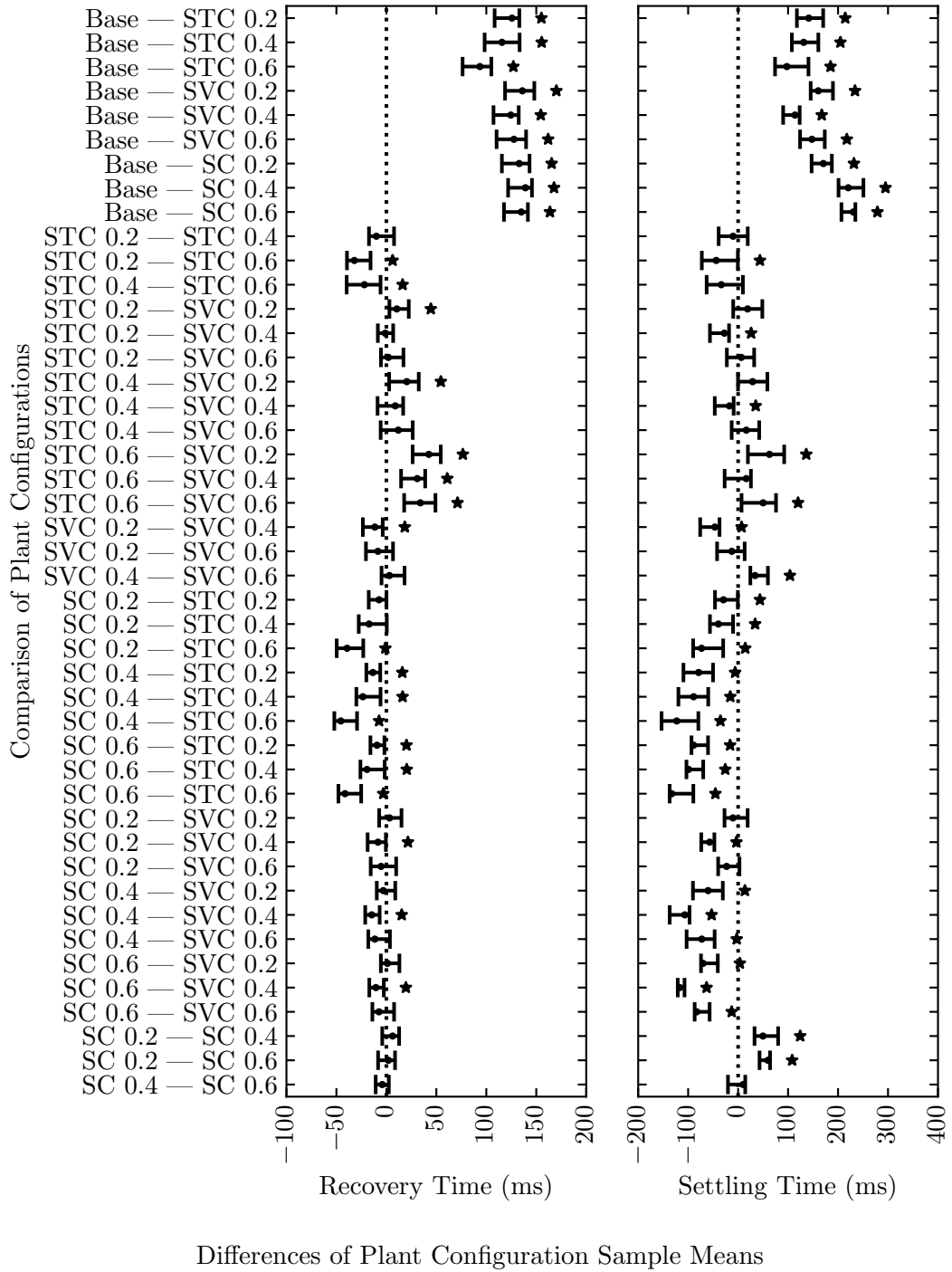


Figure H.9: Differences in sample minima of measured DC-side voltage, cont.

Appendix H. Differences between Sample Minima of Performance Values

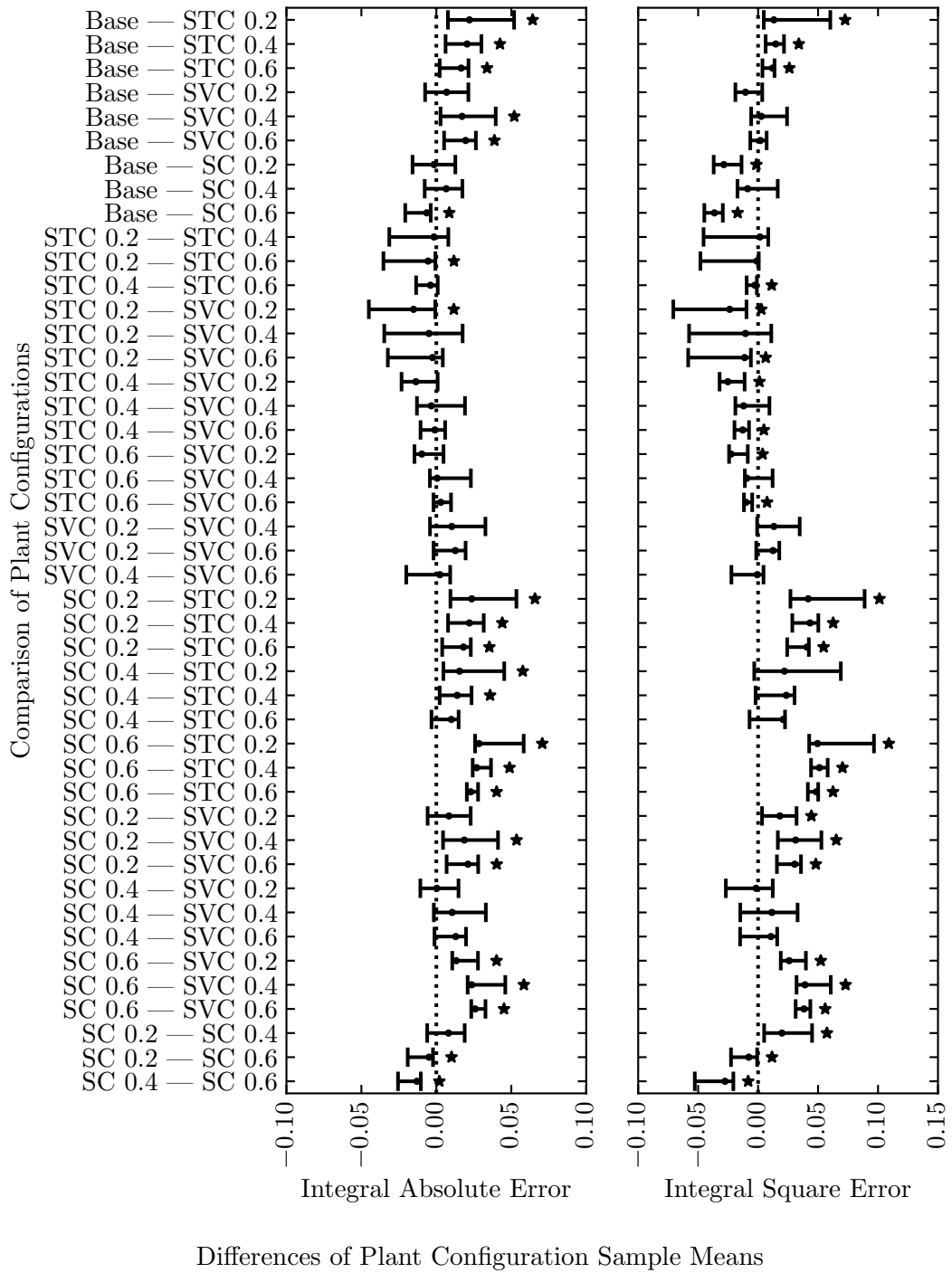


Figure H.10: Differences in sample minima of measured DC-side current.

Appendix H. Differences between Sample Minima of Performance Values

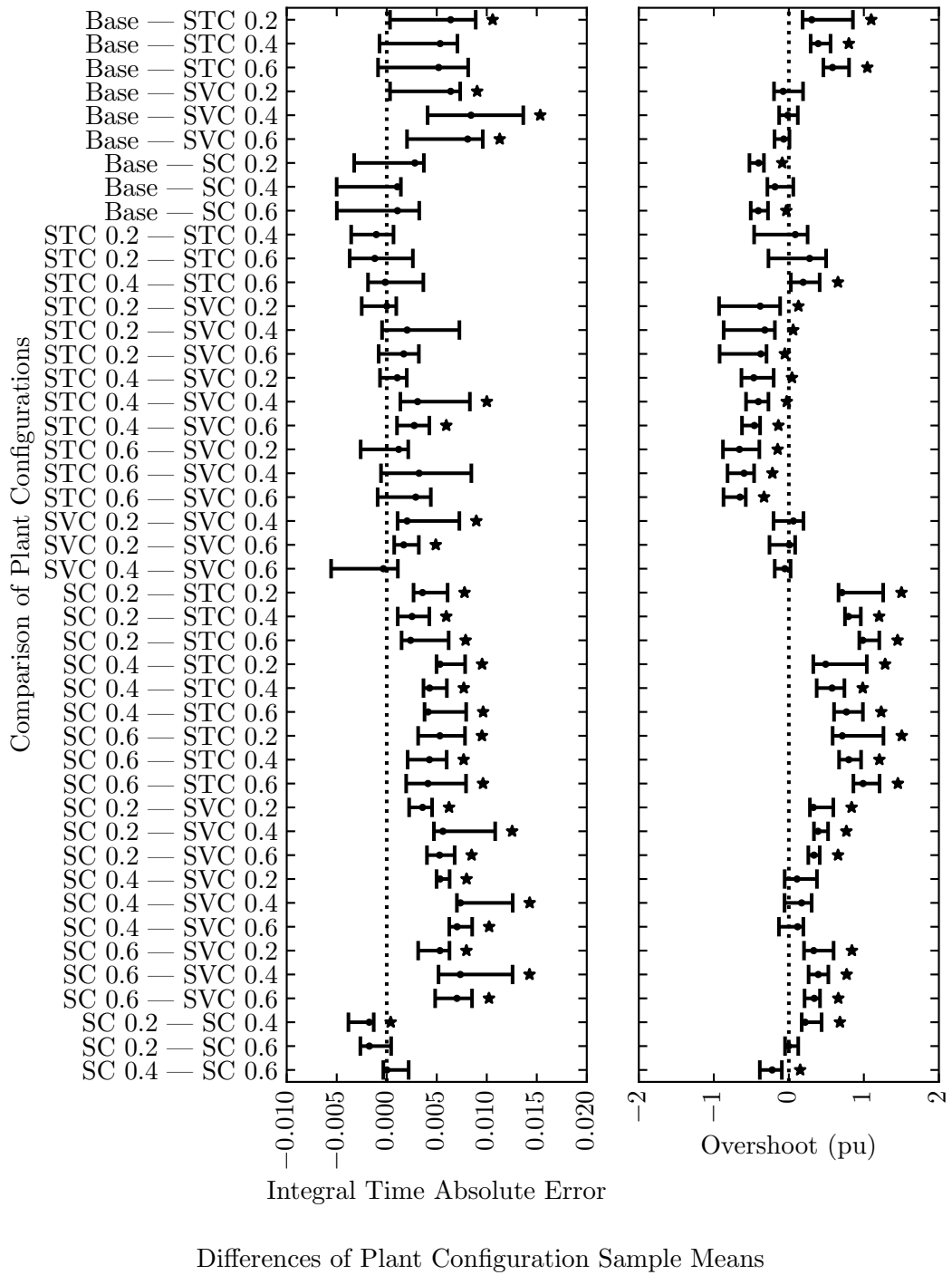


Figure H.11: Differences in sample minima of measured DC-side current, cont.

Appendix H. Differences between Sample Minima of Performance Values

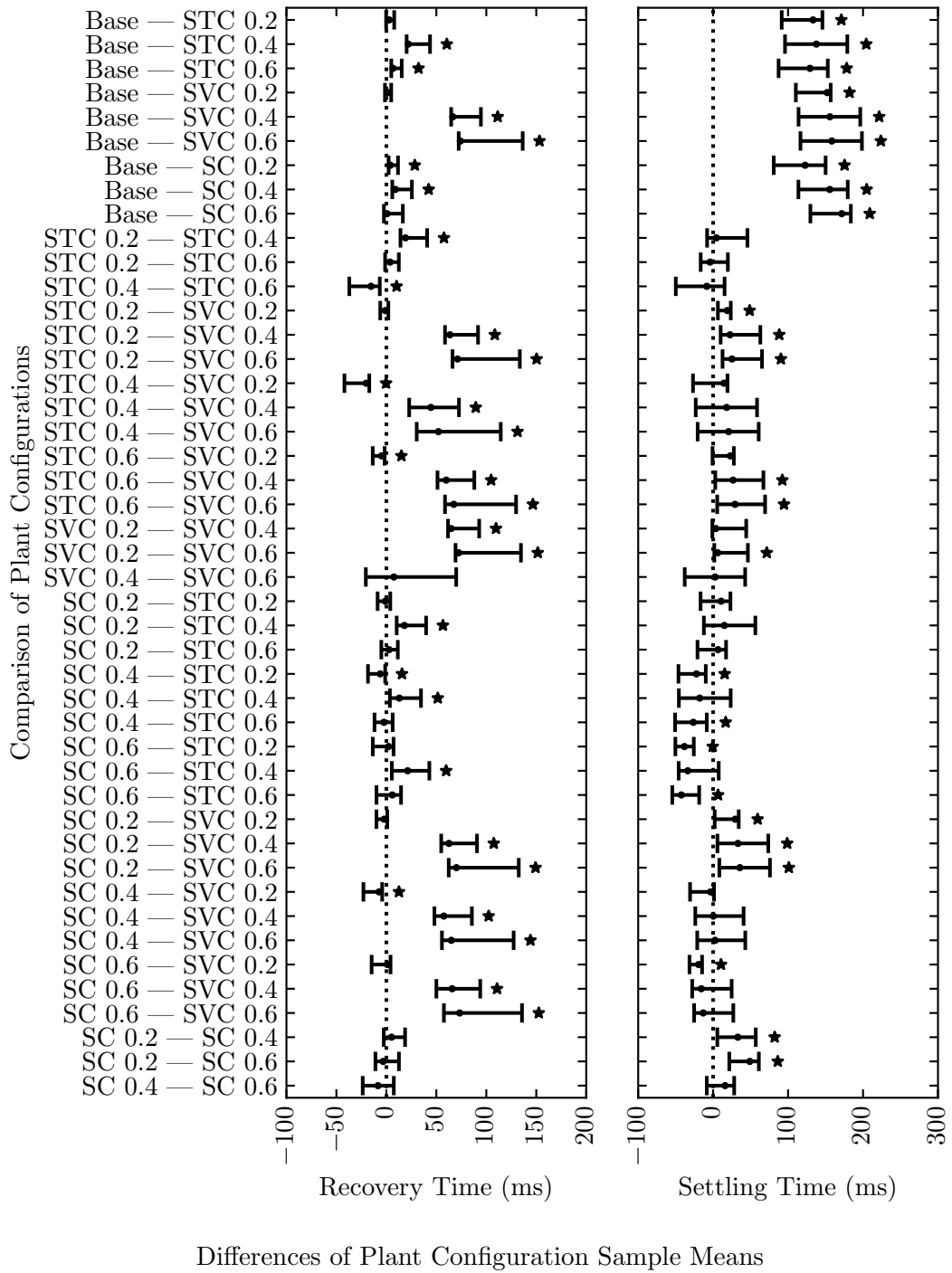


Figure H.12: Differences in sample minima of measured DC-side current, cont.

Appendix H. Differences between Sample Minima of Performance Values

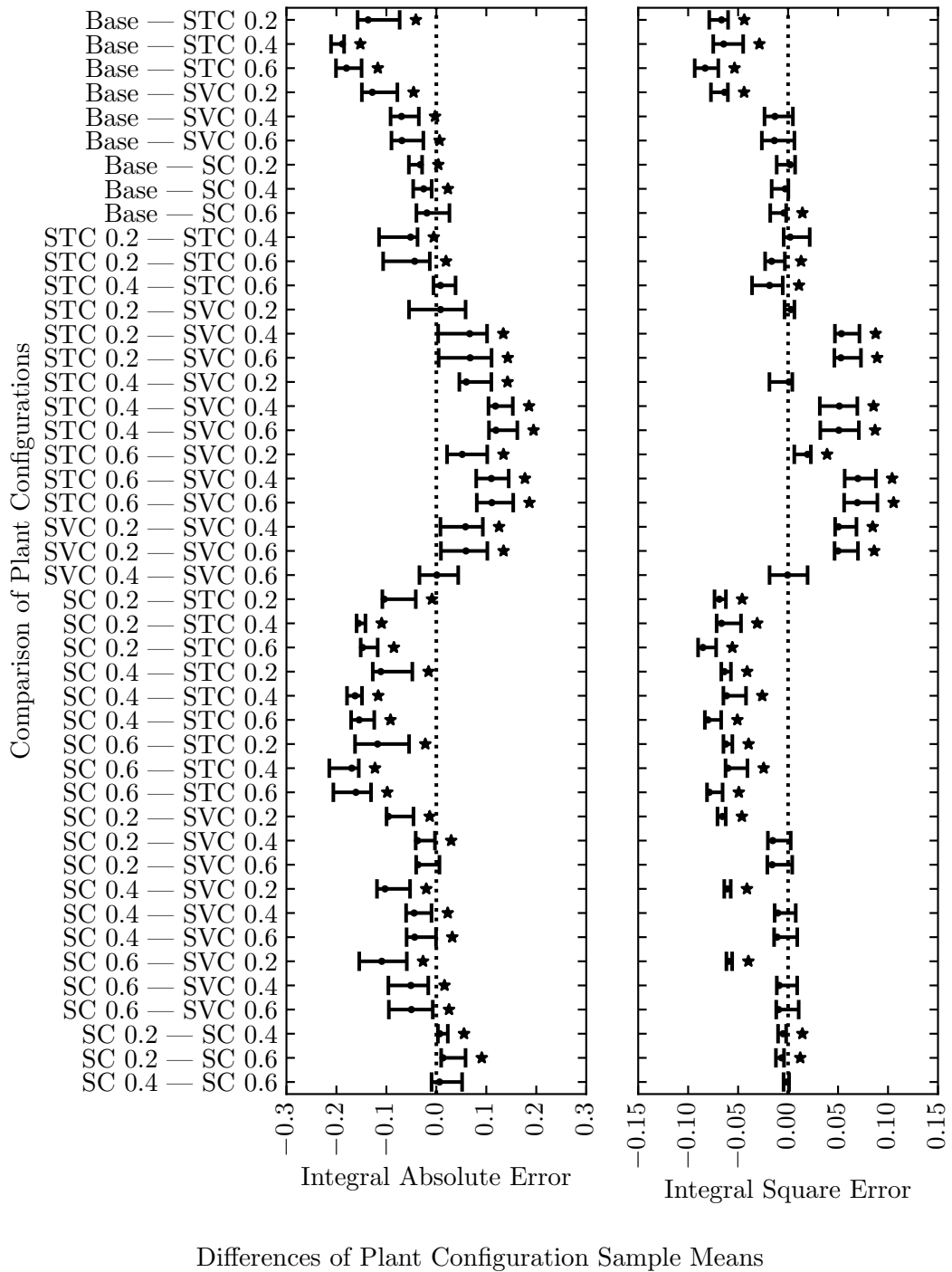


Figure H.13: Differences in sample minima of measured extinction angle.

Appendix H. Differences between Sample Minima of Performance Values

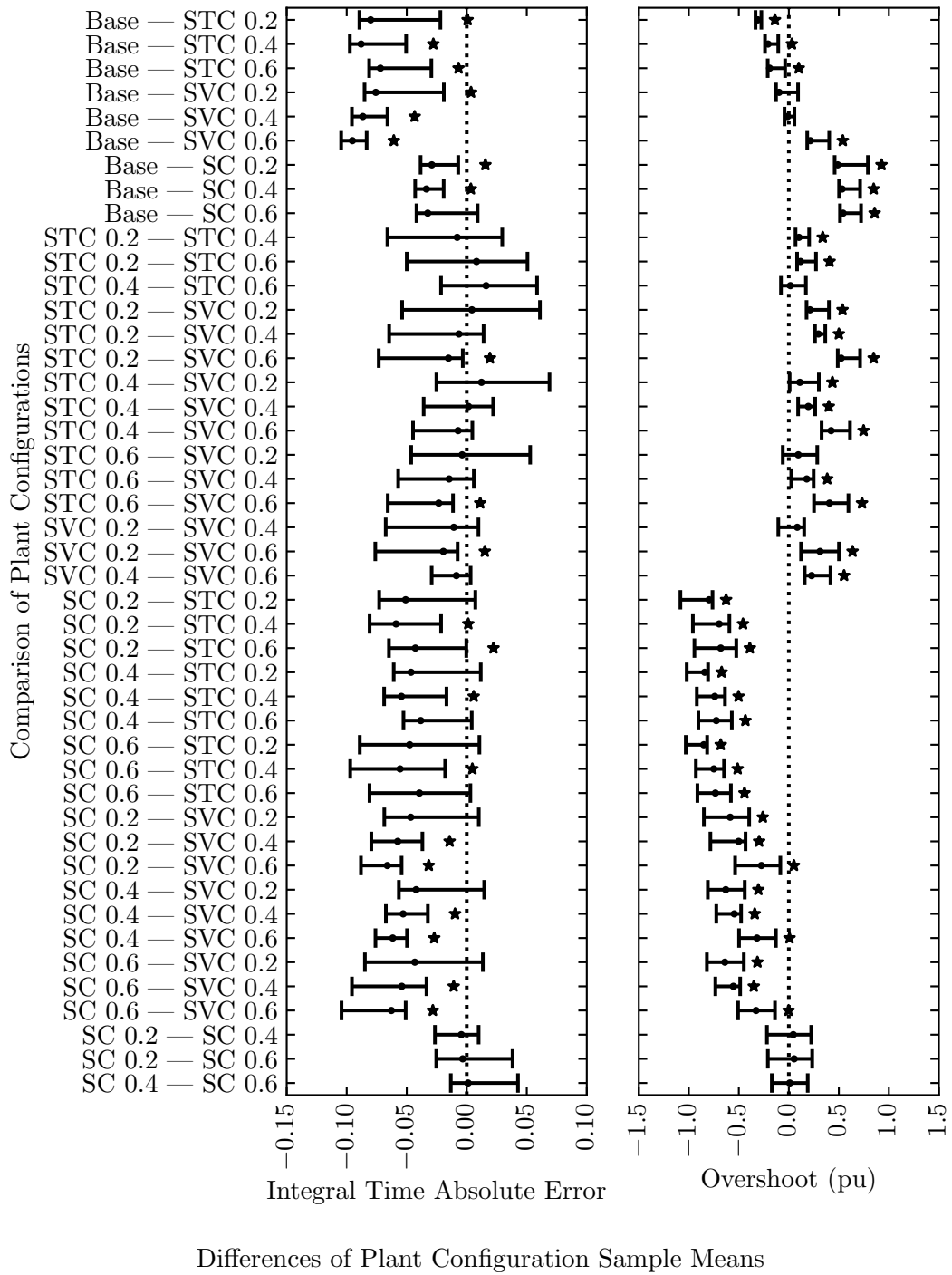


Figure H.14: Differences in sample minima of measured extinction angle, cont.

Appendix H. Differences between Sample Minima of Performance Values

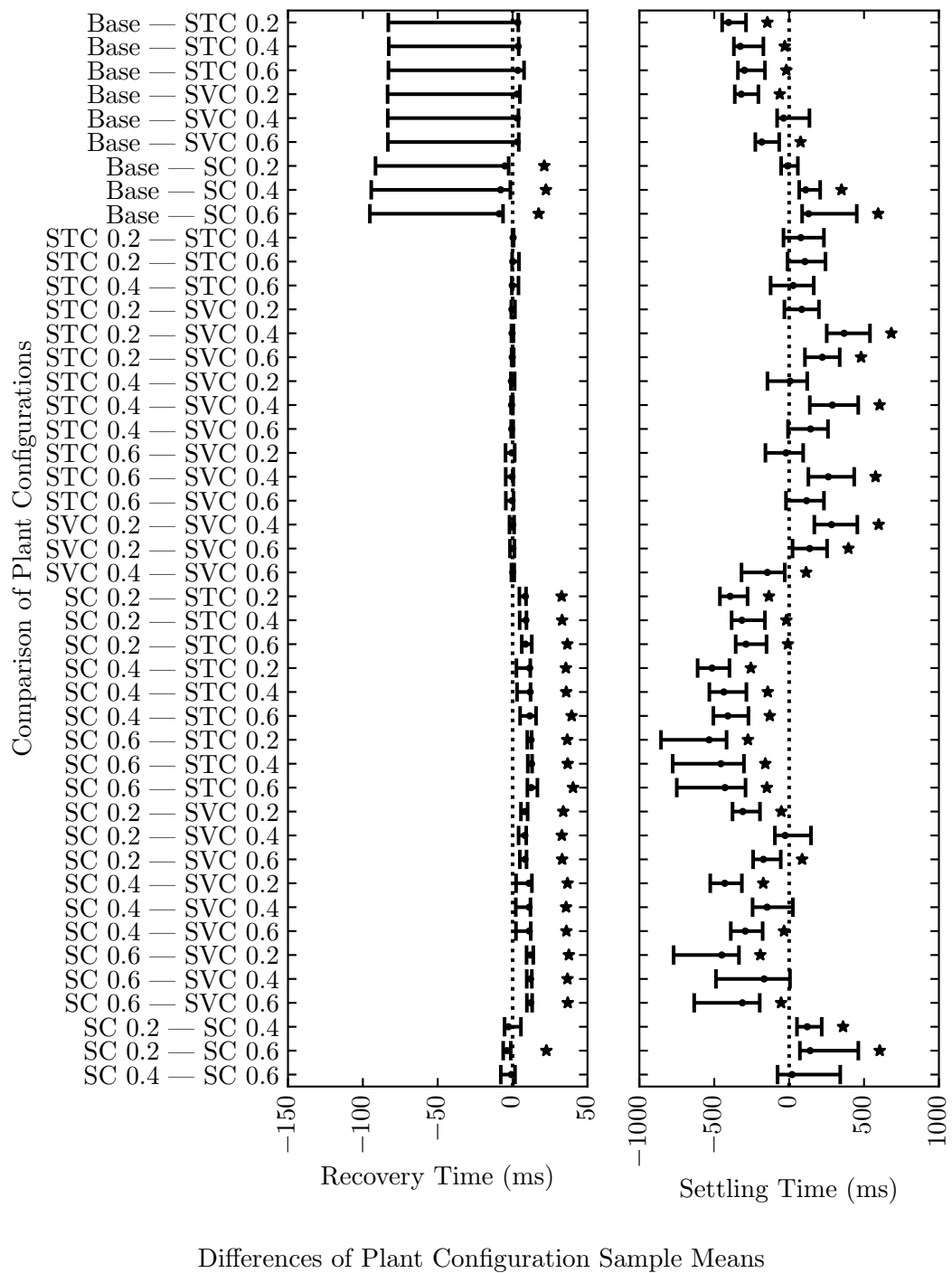


Figure H.15: Differences in sample minima of measured extinction angle, cont.

Appendix I

Associations between Proposed Performance Rankings and Observed Performance Values' Rankings of Sample Means

These plots include observed Kendall's Tau-c associations along with the estimated 95% CI, between proposed Rankings of plant configurations compared to observed plant configuration rank orderings based upon ranks of configurations' sample means. Observed Kendall's Tau-c associations are indicated by dot markers. Statistically significant results are assumed where the value 0 is not within the 95% CI; these results are marked with an asterisk symbol. The orderings in the y-axis labels are defined in Table 4.6. Results are sorted within each plot such that y-axis labels are arranged in ascending order of observed Kendall's Tau-c association.

Appendix I. Associations between Proposed Performance Rankings and Observed Performance Values' Rankings of Sample Means

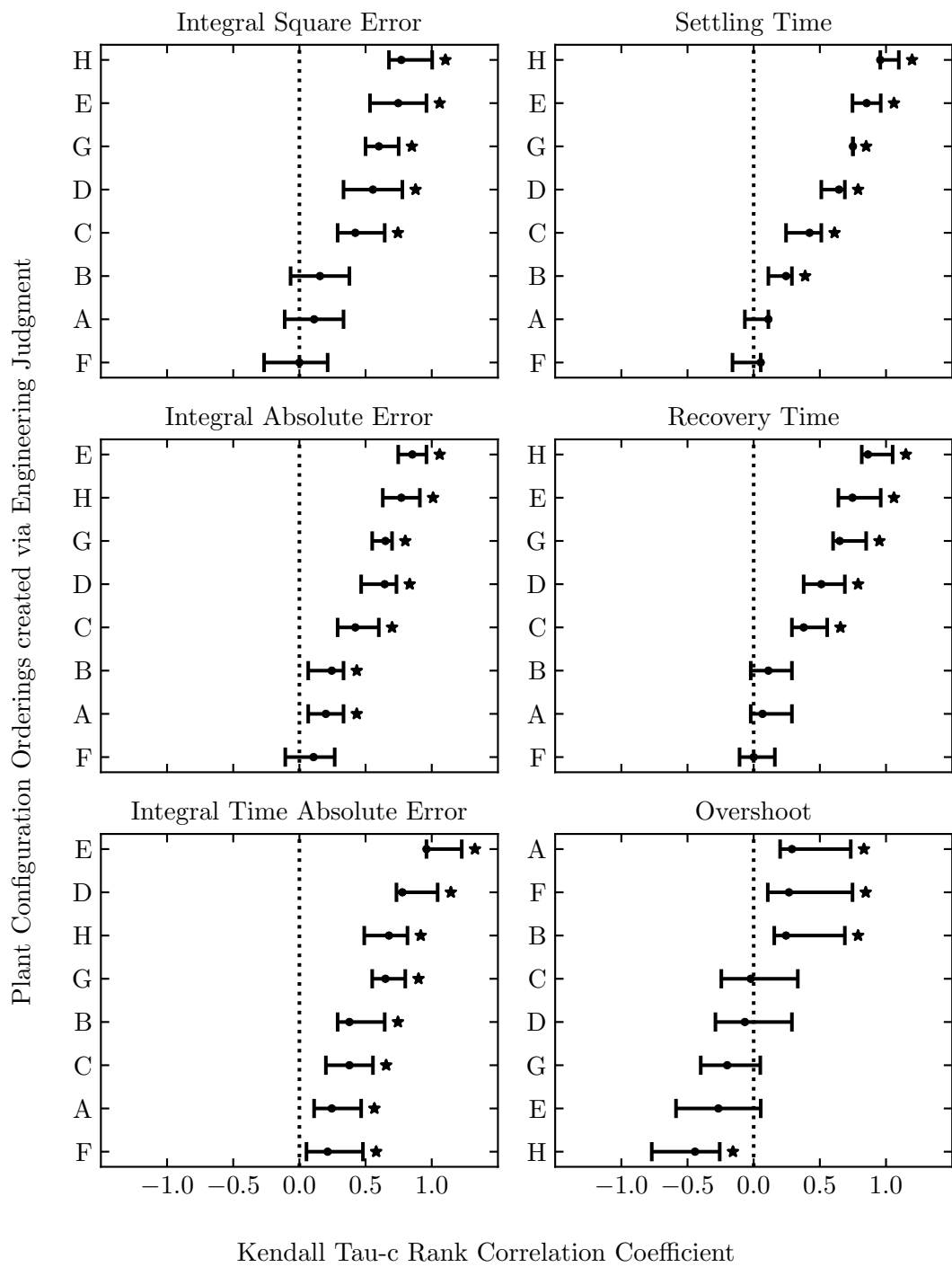


Figure I.1: DC-side measured power associations, depending on sample means.

Appendix I. Associations between Proposed Performance Rankings and Observed Performance Values' Rankings of Sample Means

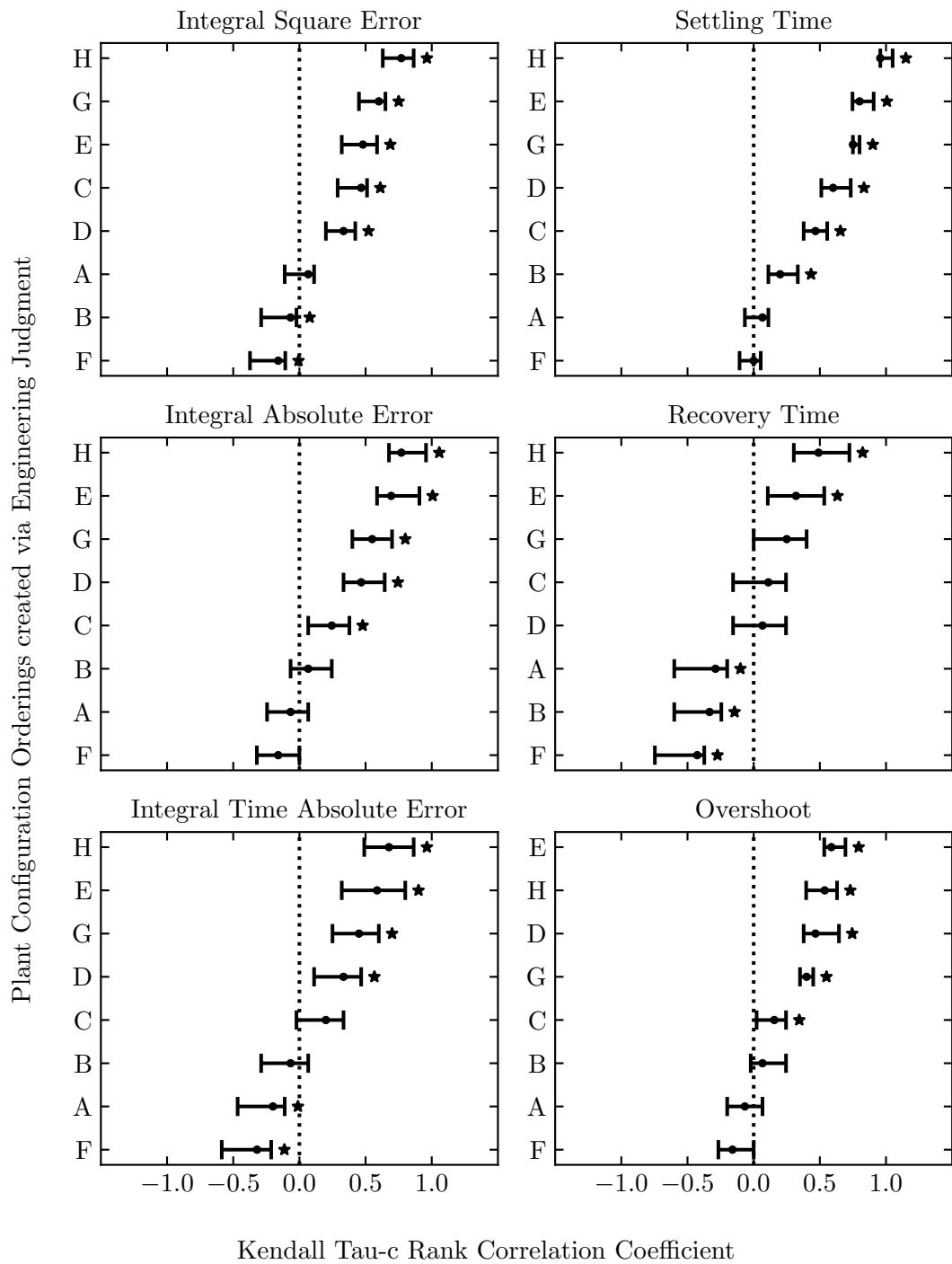


Figure I.2: AC-side measured voltage magnitude associations, depending on sample means.

Appendix I. Associations between Proposed Performance Rankings and Observed Performance Values' Rankings of Sample Means

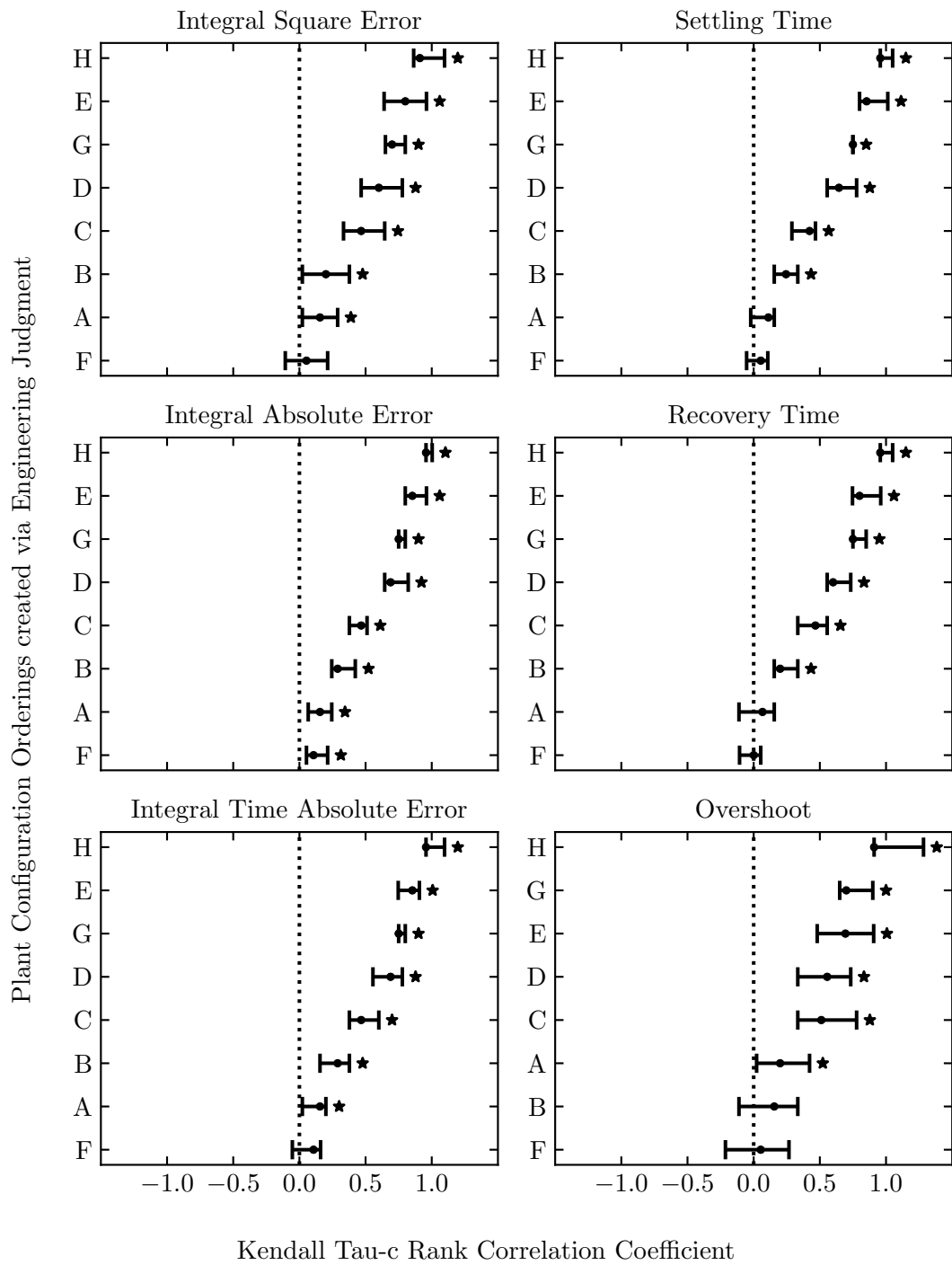


Figure I.3: DC-side measured voltage associations, depending on sample means.

Appendix I. Associations between Proposed Performance Rankings and Observed Performance Values' Rankings of Sample Means

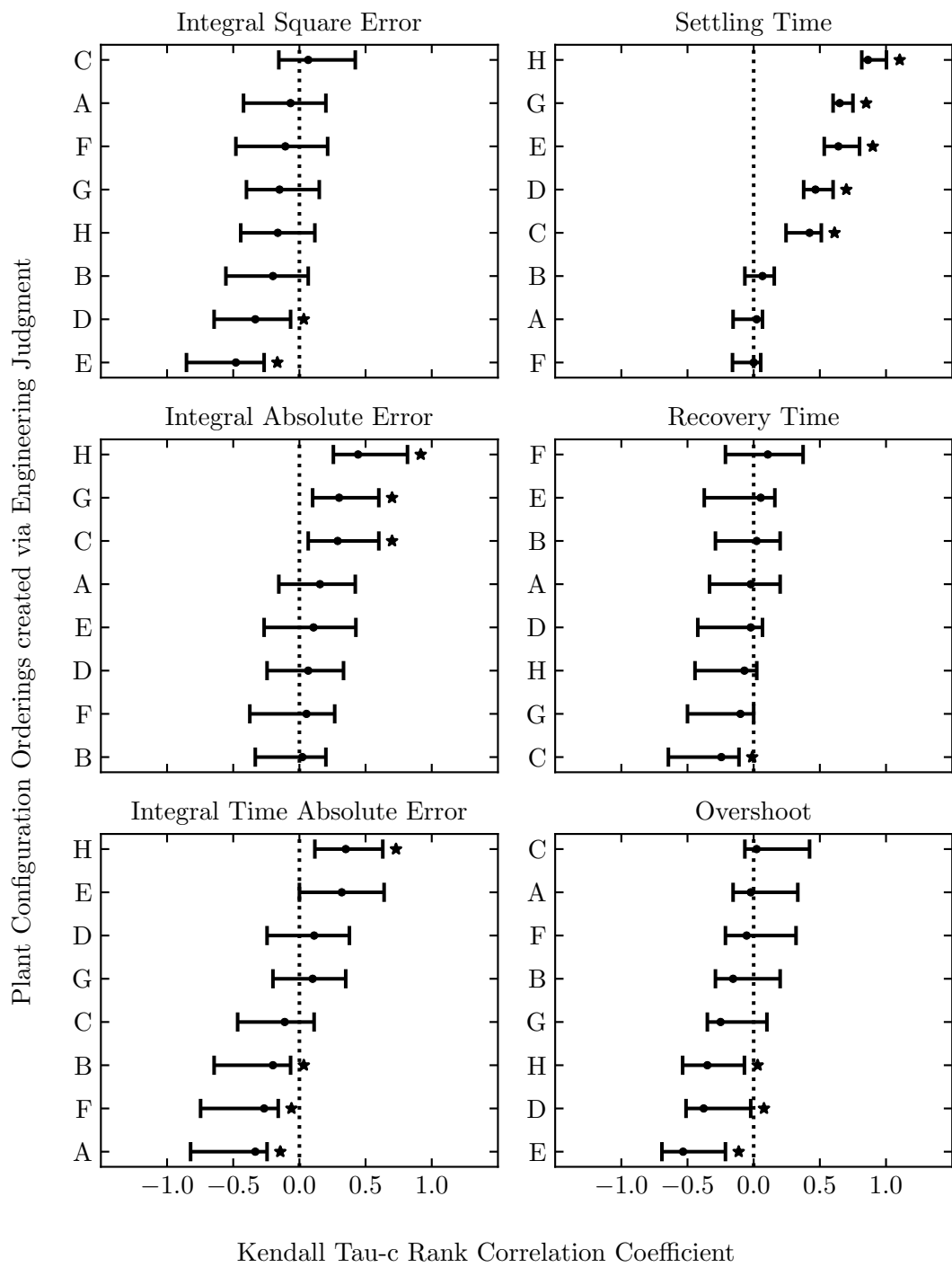


Figure I.4: DC-side measured current associations, depending on sample means.

Appendix I. Associations between Proposed Performance Rankings and Observed Performance Values' Rankings of Sample Means

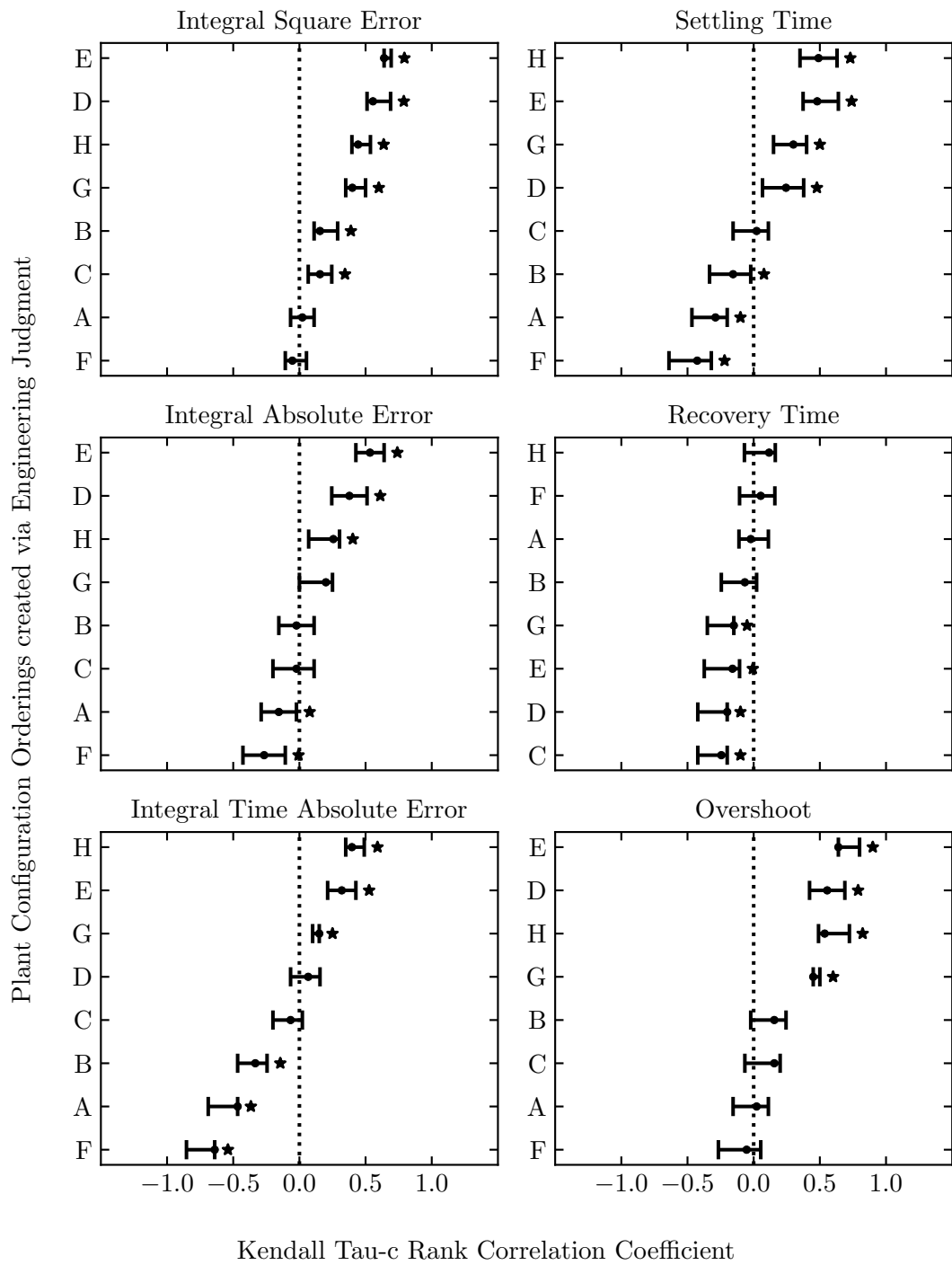


Figure I.5: Measured extinction angle associations, depending on sample means.

Appendix J

Associations between Proposed Performance Rankings and Observed Performance Values' Rankings of Sample Minima

These plots include observed Kendall's Tau-c associations along with the estimated 95% CI, between proposed Rankings of plant configurations compared to observed plant configuration rank orderings based upon ranks of configurations' sample minima. Observed Kendall's Tau-c associations are indicated by dot markers. Statistically significant results are assumed where the value 0 is not within the 95% CI; these results are marked with an asterisk symbol. The orderings in the y-axis labels are defined in Table 4.6. Results are sorted within each plot such that y-axis labels are arranged in ascending order of observed Kendall's Tau-c association.

Appendix J. Associations between Proposed Performance Rankings and Observed Performance Values' Rankings of Sample Minima

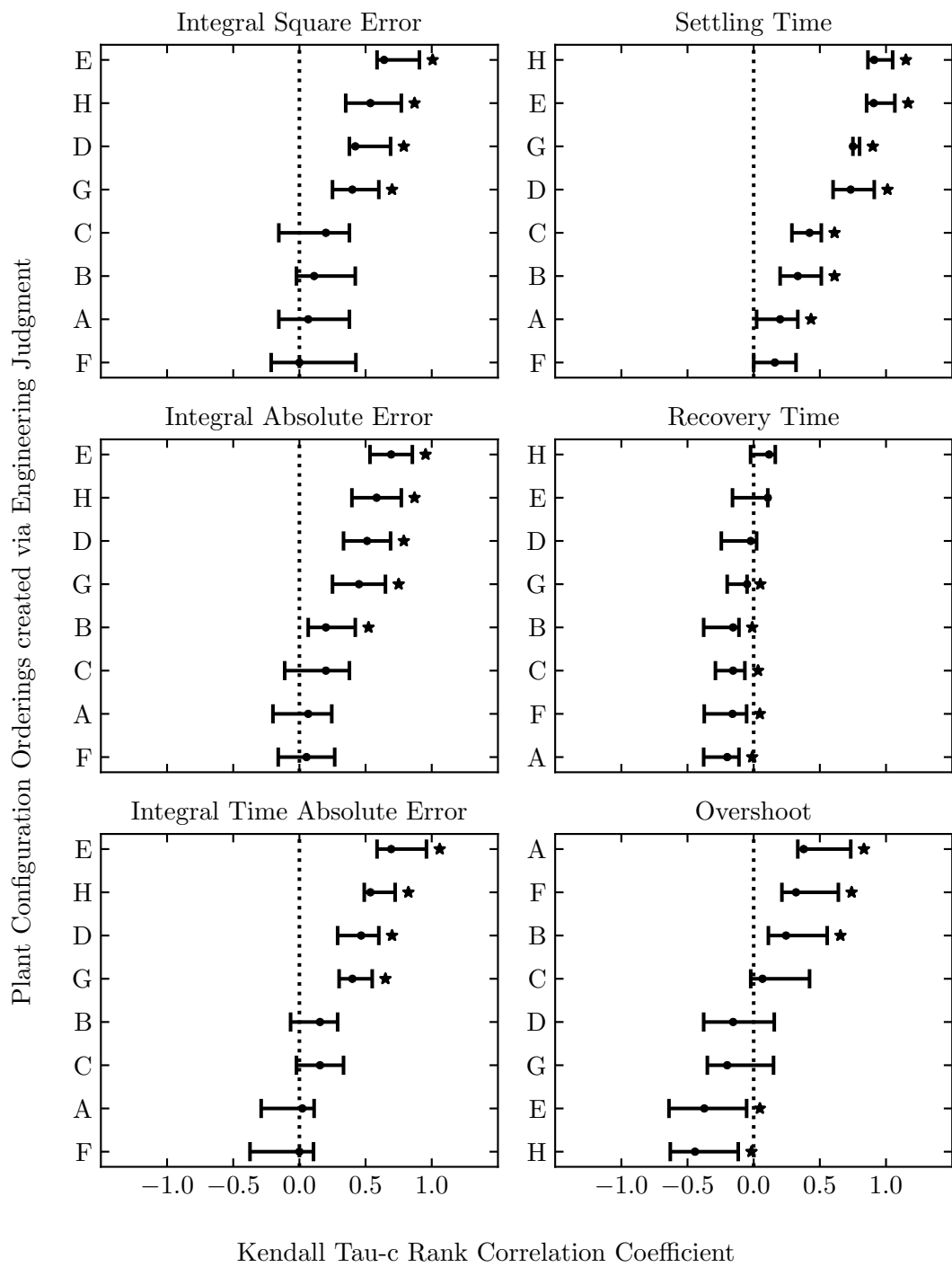


Figure J.1: DC-side measured power associations, depending on sample minima.

Appendix J. Associations between Proposed Performance Rankings and Observed Performance Values' Rankings of Sample Minima

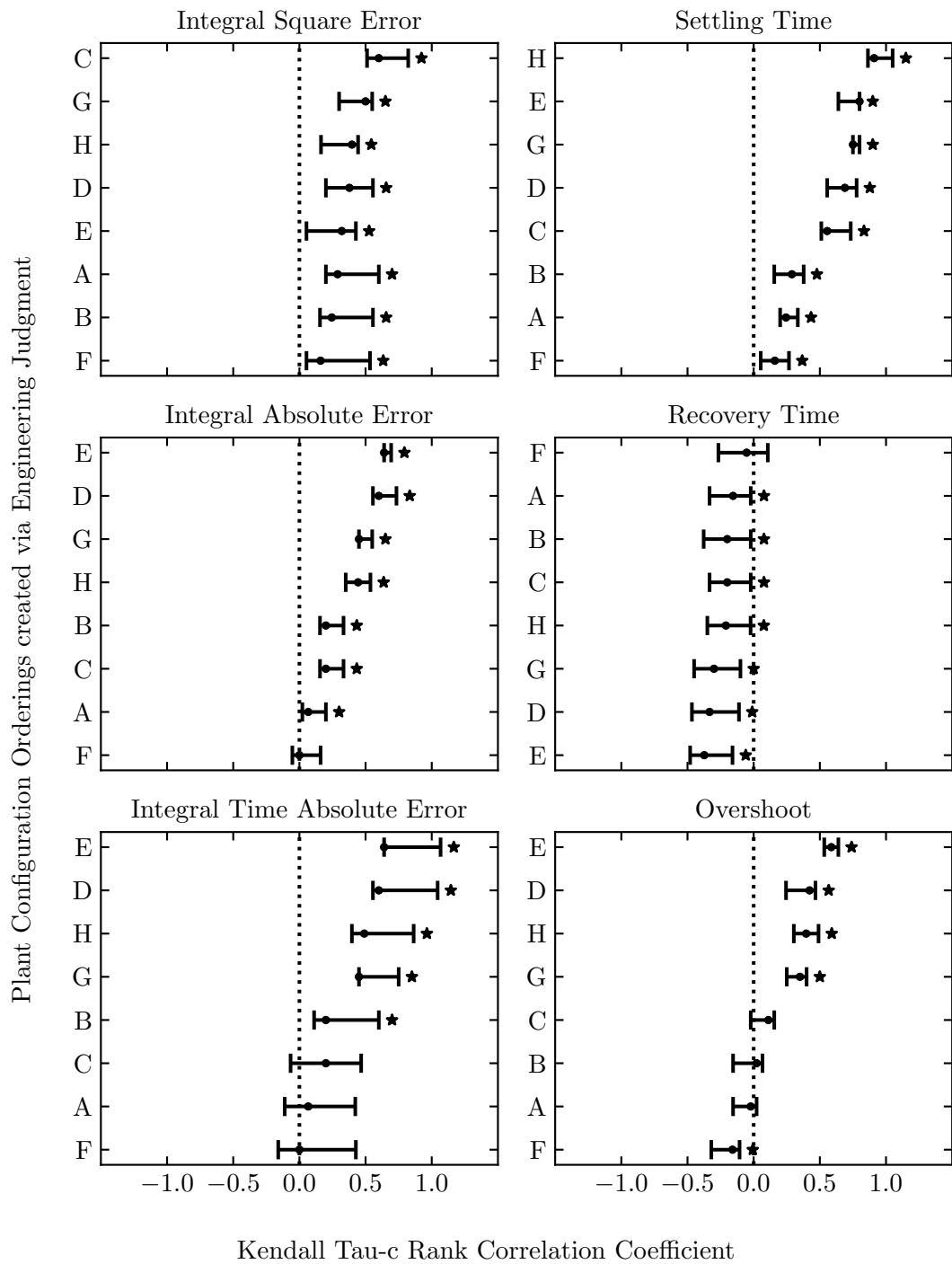


Figure J.2: AC-side measured voltage magnitude associations, depending on sample minima.

Appendix J. Associations between Proposed Performance Rankings and Observed Performance Values' Rankings of Sample Minima

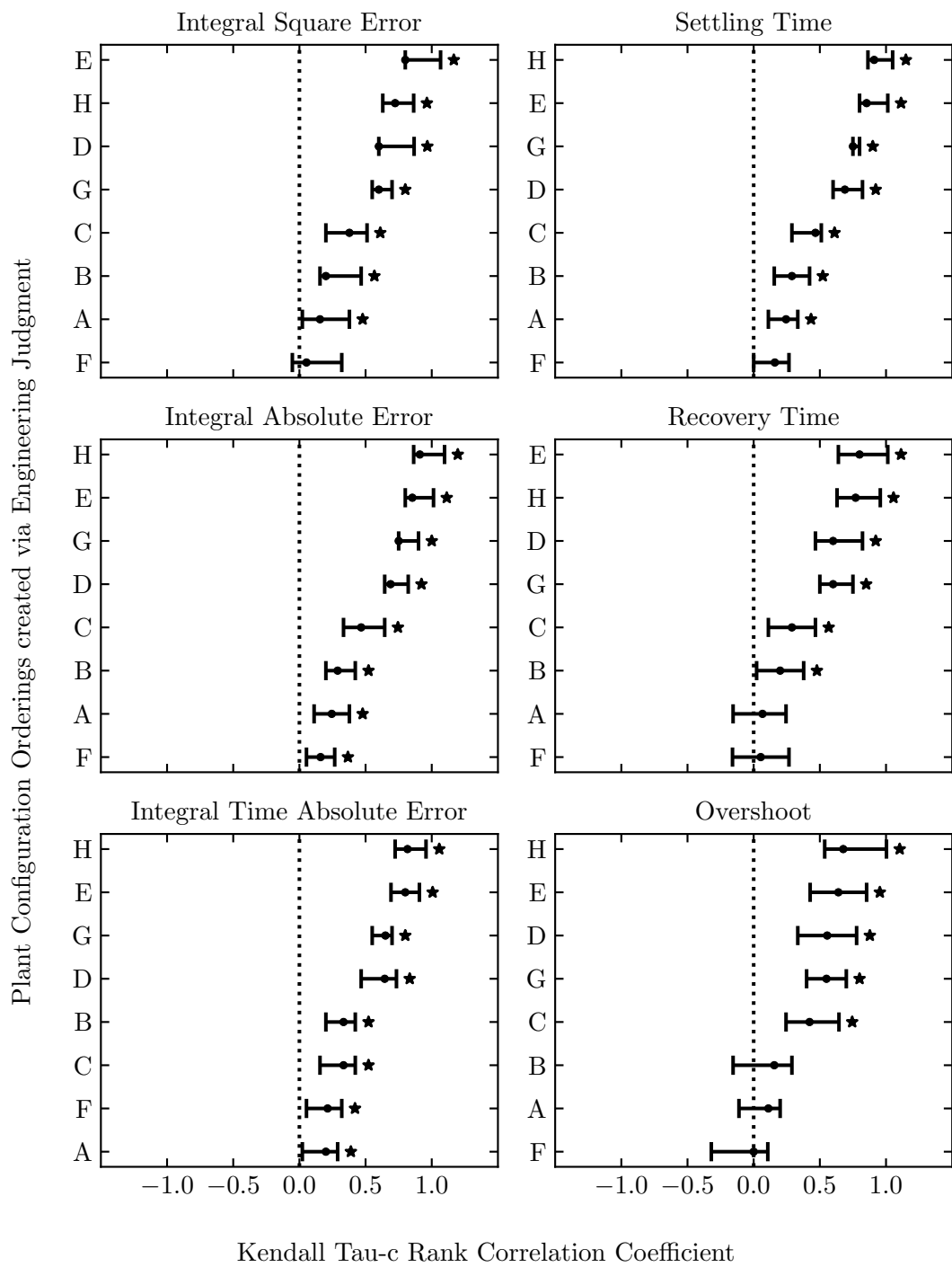


Figure J.3: DC-side measured voltage associations, depending on sample minima.

Appendix J. Associations between Proposed Performance Rankings and Observed Performance Values' Rankings of Sample Minima

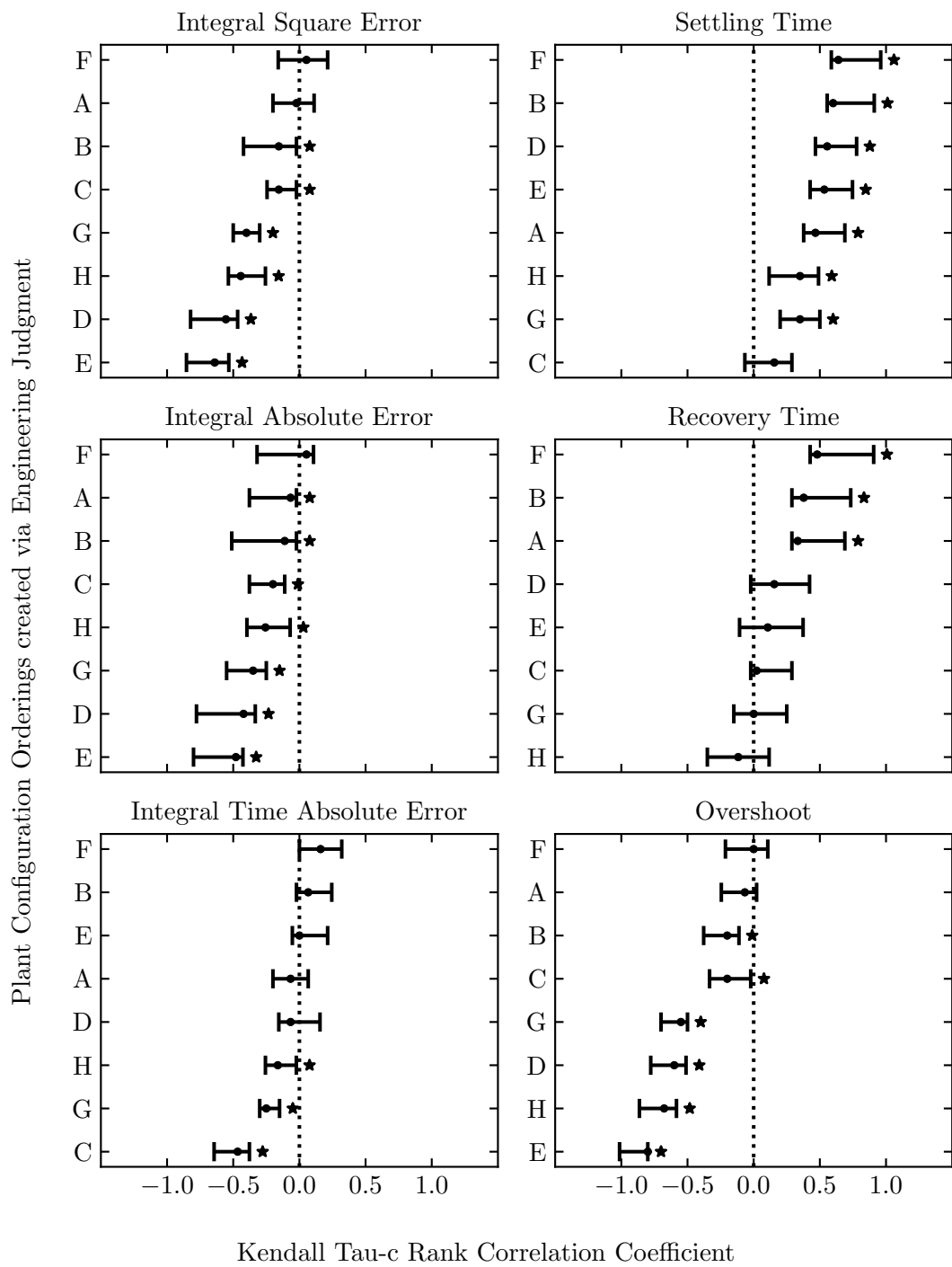


Figure J.4: DC-side measured current associations, depending on sample minima.

Appendix J. Associations between Proposed Performance Rankings and Observed Performance Values' Rankings of Sample Minima

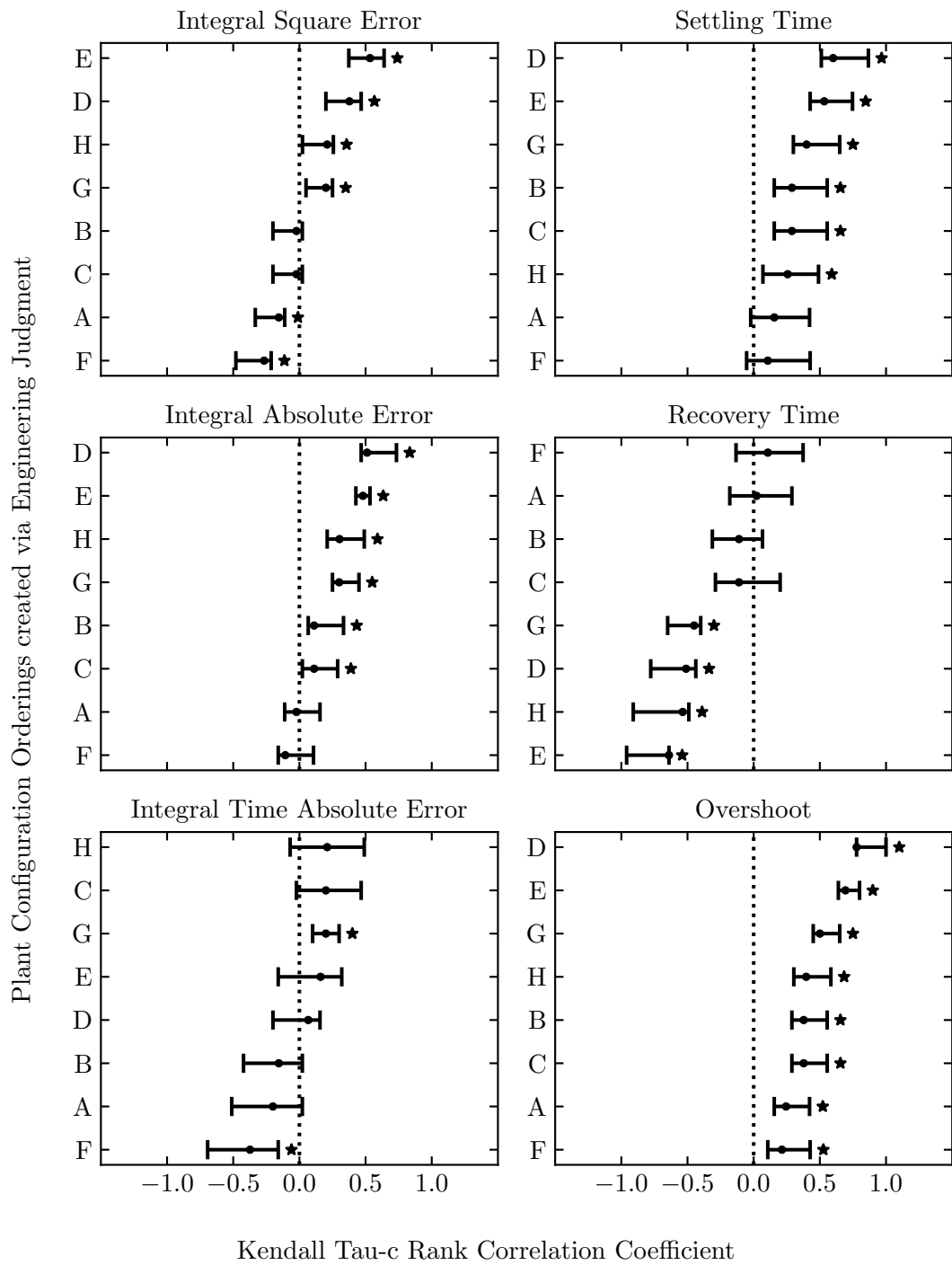


Figure J.5: Measured extinction angle associations, depending on sample minima.